Investigation of failure mechanisms of resistance spot welds in automotive steels using various techniques

Feng Yu

Supervisor: Dr. Hassan Ghadbeigi

A thesis submitted in partial fulfilment of the requirements for the degree of *Doctor of Philosophy*

Department of Mechanical Engineering

Faculty of Engineering

The University of Sheffield

December 2020

ACKNOWLEDGEMENTS

I would like to express my extreme gratefulness to my primary supervisor, Dr. Hassan Ghadbeigi, for all his supervision and support throughout this project. I have received lots of assistance from him who has invaluable expertise on the topic.

I am grateful to my second supervisor, Dr. Christophe Pinna, and industrial supervisor, Dr. Ellen van der Aa, for their useful advises on the project and paper.

I would like to thank Sullivan Smith for his help on sample welding. I would also like to thank Dr. Le Ma and Dr. Peng Gong for sharing their knowledge on steels and their help on sample preparation.

I would also like to thank all my friends for all the support and help I revived from them.

Finally, a great thank to my parents and wife (Xiyu) who are very supportive from the beginning of my PhD life to finish. Thank you for believing in me, supporting me and easing my stress when I got stuck in the difficulties of research problems.

ABSTRACT

Advanced High Strength Steel (AHSS) is popular in automotive industry because of its greater ductility, higher strength, better weight reduction and better crash-energy absorption compared with traditional high strength steels and low carbons steels. Resistance spot welding technique plays a significant role in manufacturing the car body. Body-in-white has a great number of resistance spot welds (around 4000). As a consequence, the performance of resistance spot welded joints directly impacts performance of the whole car body. Nevertheless, limited researches have been made to investigate the effect of deformation evolution on failure mechanism of resistance spot welds of AHSS under different loading conditions, especially for the new grades of dual phase steels (DP1000, etc). It is very necessary to fully understand the performance of resistance spot welds in these materials.

This project aims to investigate the deformation and failure evolution and effect of welding currents on failure mechanisms of resistance spot welds in DP1000 and a type of low carbon steel (reference material) as well as develop a novel and applicable research method of failure mechanisms investigation on spot welds. Novel testing geometries with two half sectioned welds were designed in order to facilitate deformation and failure evolution analysis within the weld section. The testing geometries include three types of macro samples: tensile-shear (TS) samples (tensile and shear condition), coach-peel samples (CP) (tensile and bending condition), U-shape samples (tensile condition) and micro coach-peel samples. The samples with applied three levels of welding currents were tested. Digital image correlation technique was applied to all samples to quantify the deformation evolution of spot weld in the whole testing process. Microstructure morphology and fractography of all samples were studied with optical and scanning electron microscopic technique. Additionally, micro hardness analysis was carried out for samples of different welding currents and materials. Results obtained from experimental techniques mentioned above were correlated with each other, aiming to better understand deformation evolution and the effect of microstructure on failure mechanisms of resistance spot welds.

Results show that the welding current has great influence on failure mechanisms of spot welds in DP1000 steels, but almost no influence was observed in low carbon steel samples. Larger and softer welds are achieved in DP1000 samples with applied higher welding currents, which have lower strength in the welds due to decreasing of the hardness caused by longer cooling and higher temperature in welding. Although increasing welding current also leads to larger weld size in samples in low carbon steels, no strength difference was observed. HAZ and nugget softening as well as nugget size increasing of spot welds in tensile-shear samples in DP1000 steel are the major factors causing the failure modes transition from interfacial failure to pull- out failure. HAZ softening, HAZ bending and plasticity increase in nugget impact the failure mode transition from interfacial failure (IF) to partial interfacial failure (PIF), and then pull-out failure (PF) in spot welds of CP samples and U-shapes samples in DP1000. Spot welds in DP1000 steels have higher failure load than that in low carbon steels. Failure of all samples in low carbon steel is due to necking. The local mechanical properties determination method proposed can provide appropriate data. The findings could help avoid the unexpected failure modes (IF or PIF), thereby enhancing the quality of the welds. The achieved strain distribution maps could provide thresholds of failure in welds under different stress states, which can be used to develop damage model for predicting the deformation and failure behaviour of spot welds.

CONTENT

LIST OF FIGURES

LIST OF TABLES

LIST OF ABBREVIATION

AHSS	Advanced high strength steel
HSS	High strength steel
IF-HS	Interstitial-free high strength
BH	Bake hardening
HSLA	High strength low alloy
DP	Dual phase
CPH	Complex phase
TRIP	Transformation-induced plasticity
MART	Martensitic
TWIP	Twinning-induced plasticity
HF	Hot-formed
TS	Tensile-shear
CP	Coach- peel
CT	Cross-tension
RSWs	Resistance spot welds
BM	Base material
SCHAZ	Subcritical HAZ affected zone
ICHAZ	Intercritical heat affected zone
FGHAZ	Fine grain heat affected zone
CGHAZ	Coarse grain heat affected zone
HAZ	Heat affected zone
IF	Interfacial failure
PF	Pull-out failure
PIF	Partial interfacial failure

DPTS	Dual phase tensile-shear
DPCP	Dual phase coach-peel
DPU	Dual phase U-shape
DPMiCP	Dual phase micro coach peel
LCTS	Low carbon tensile-shear
LCCP	Low carbon coach-peel
LCU	Low carbon U-shape
NSSD	Normalised sum of squared difference

LIST OF NOMENCLATURES

e_{xx}	Strain distribution at X direction
e_{yy}	Strain distribution at Y direction
e_{xy}	Shear strain distribution
f_i	Grey value of the ith pixel in the reference subset
g_i	Grey value of the ith pixel in the target subset
$\sigma_{bending}$	Bending stress (MPa)
M	Bending moment ($N{\cdot}mm$)
F_y	Load (N)
l	Width between loading point and tip of corona bond (mm)
h	Thickness of metal sheet (mm)
b	Width of metal sheet (mm)
S	Section modulus (mm^3)
a	Section area of the spot weld (mm^2)
σ	True stress (MPa)
ε	True strain
P_{max}	Maximum indentation load (GPa)
A	Indenter contact area (nm^2)
h_{max}	Maximum indentation depth (nm)
E_r	Reduced modulus (GPa)
C	Curvature of the loading curve (GPa)
E	Young' s modulus (GPa)
n	Strain hardening exponent
σ_y	Yield strength (MPa)
K	Strength coefficient (MPa/mm)

$\sigma_{0.033}$	True stress when true strain is equal to 0.033 (MPa)
$D_1 - D_5$	Material constants
ε_f	Equivalent fracture strain
σ^*	Stress triaxiality
$\dot{\varepsilon_p}$	Strain rate
T^*	Temperature (K)

1 INTRODUCTION

1.1 Background and motivation

Advanced high strength steels (AHSS) have been widely used in automotive industry as it has better ductility, higher strength and crash-energy absorption ability compared with the traditional automotive steels. The ductility-strength combination of the materials can reduce the weight of car body because that the mechanical properties are not affected at very low thickness [1]. As a consequence, these steels are widely applied in the automotive industry to manufacture crucial components such as wheel rim, structural support, car body panels, structural members, etc[2].

Resistance spot welding is a primary joining method for sheet steels. Relatively low cost and high operating speed make this method important in automotive industry. Usually, a typical car body contains around 4000 spot welds [3]. The microstructure of the spot welds is greatly changed during the welding process. It can be divided into three regions: base material (BM), heat affected zone (HAZ) and weld nugget. It has three typical failure modes, including interfacial failure (IF), partial interfacial failure (PIF) and pull-out failure (PF) modes, each mode has different failure mechanism [4][5]. The performance of resistance spot welds (RSWs) (especially HAZ and FZ) is different with base material and will extremely influence entire performance of the car body.

Although AHSSs bring benefits to automotive industry, problems occur when joining the materials together using resistance spot welding method. The major issue is the effect of welding parameter, especially welding current on how the microstructural morphologies of welds behave under different loading conditions [6], which extremely impacts the performance of car body. Previous researches focused on investigating the failure mechanisms based on the failed welded samples under different loading conditions in automotive steels, including coach-peel tests [5][7][8], tensile-shear tests [4][9][10] and cross-tension tests [6][11], but neglecting the link between the deformation evolution and microstructure of the welds, and how they affect the failure.

Dual-phase steels, which is the most common type in Advanced High Strength Steels (AHSSs), have a microstructure of martensite and ferrite and are widely used for safety parts in car bodies [12]. However, limited researches have been carried out with respect to the failure mechanisms of spot welds in DP1000 [13][14]. Thus, it is essential to develop a new method to study the deformation evolution and failure mechanisms of spot welds in DP1000. The novelty of this project is investigating deformation and failure evolution of the spot weld in DP1000 and the effect of welding currents on weld failure mechanisms.

The motivation is to develop a new method to comprehensively understand the failure mechanisms of resistance spot weld in AHSSs, it is due to the fact that previous method might not provide the information of how the spot weld deformed during loading which is crucial on understanding the associate failure mechanisms, in such way to help improve the performance of welded joints in car body to enhance the passengers' safety. Moreover, the achieved experimental data could help develop FE simulation model to predict the failure of spot weld in AHSS.

1.2 Aims and objectives

The present research aims to investigate the deformation and failure evolution of spot weld under different welding currents and loading conditions and how the welding currents affect failure mechanisms of spot weld in dual-phase steel 1000 (DP1000), while a type of low carbon steel is considered as the reference material. In this project, a new research method will be developed to have a more in-depth understanding of failure of spot weld in steels, and the achieved results could provide data for future FE simulation model development.

Some key objectives are listed below:

- Revealing the deformation and failure evolution of the spot weld - In order to reveal the deformation and damage evolution on the free surface of the spot welds, macro and micro samples with two precisely prepared half spot welds, which were welded with low, medium and high welding currents, were designed based on the standard

tensile-shear, coach-peel and cross-tension samples. A Finite Element technique using ABAQUS/Explicit package is used to determine the optimum geometries of samples to ensure the maximum plastic deformation occurs in the region of interest in the samples.

- Investigation of deformation and failure evolution of the welds - 3D stereo Digital image correlation (DIC) technique is used to quantify the deformation and failure evolution in the tested macro samples during the whole test process. Samples without paint are also tested to correlate the deformation and failure evolution with the achieved strain maps. In-situ tensile test using micro CP samples are carried out.
- Analysis of effect of welding currents on microstructure of the weld section and the associate mechanical properties - The microstructure of welded samples is characterised using standard metallography tests. Microhardness tests are carried out to characterise the mechanical properties of the spot welds.
- Analysis of fracture surface and corresponding microstructural morphology of the weld section and their effect on failure mechanisms - Fractography and microstructural morphology analysis are conducted based on failed samples using optical microscope and Scanning Electron Microscope (SEM).

A better understanding of how welding currents affect the deformation evolution and microstructure of the weld section as well as their effects on failure mechanisms is achieved by linking the corresponding multiscale deformation evolution to the results of metallurgy, fractography and morphology analysis. In addition, an approach to determine the local mechanical properties of different sections of the spot welds is presented, which could provide benefits for damage model development in the future.

1.3 Thesis outline

The structure of the thesis is as follows:

- Chapter 2 - Literature reviews of automotive steels, conventional

joining techniques of car body, conventional testing methods of spot weld failure mechanisms and performance analysis, full-field strain measurement techniques and FE damage models.

- Chapter 3 - Describe and explain the methods of new sample geometries design, deformation evolution analysis of the weld section under multi scales, microstructure and mechanical properties characterisation as well as fractograhy and microstructural morphology analysis.
- Chapter 4 - Present the results obtained according to methods proposed in Chapter 3.
- Chapter 5 - Discuss the results to analyse the deformation and failure evolution and effect of welding current on microstructure of the spot weld as well as their link with failure mechanisms.
- Chapter 6 - Conclusion.
- Chapter 7 - Future work.
- Chapter 8 - Introducing a possible method to characterise the mechanical properties of the weld section to help in future FE damage model development.

2 LITERATURE REVIEW

A detail review of previous literatures was conducted in this chapter in order to identify the shortcomings and develop new approaches to Figure out the issues.

2.1 Automotive steels

Figure 2.1 briefly shows the components in a body-in-white referring to the stage in which components of a car body is joined together[15]. A body-in-white could be made of different types of steels to fulfil different requirements.

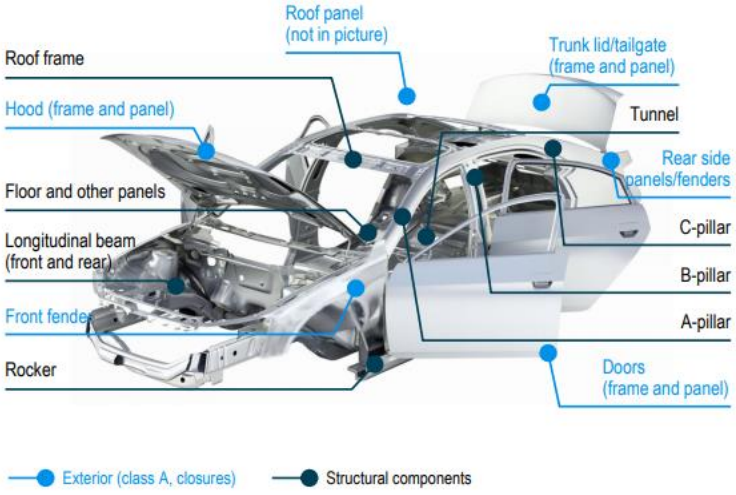

Figure 2.1. Components in body-in-white[15].

Steels are the key materials applied in automotive industry[2]. They can be classified into three categories based on yield strength and tensile strength range[2][16], including low strength steels, high strength steels and Ultra/Advanced high strength steels. The yield strength of low strength steels is less than 210 MPa and the tensile strength is less than 270 MPa, and for the high strength category, the yield strength is between 270 and 550 MPa and the tensile strength is between 270-700 MPa, while the ultra/advanced high strength steels have a yield strength of greater than 550 MPa and a tensile strength in excess of 700Mpa, Figure 2.2 [17][18].

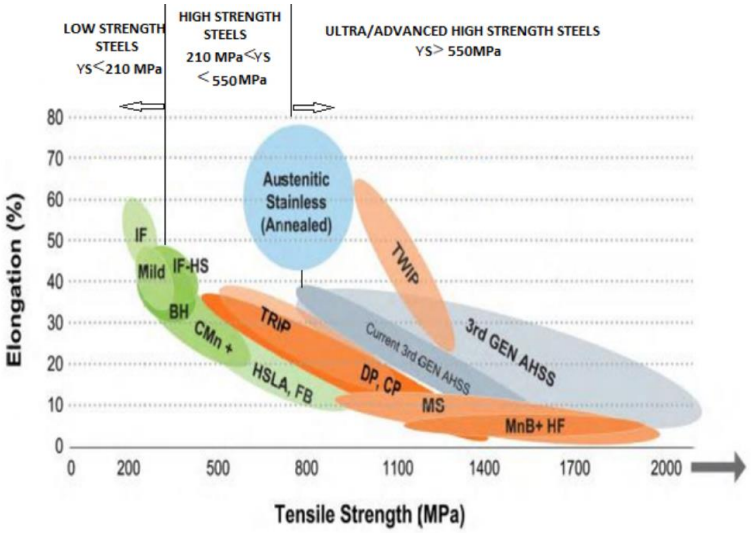

Figure 2.2. Schematic of classification of low, high and ultra/advanced high strength steels based on yield strength and tensile strength[2].

2.1.1 Low strength steel

Steel grades having the carbon content between 0.04%-0.3% and tensile strength lower than 270 MPa are considered as low strength steel [2]. These grades include mild steel and interstitial-free (IF) steel, that mostly contain a ferritic microstructure[2][19]. These are applied to automotive industry for car body parts and panels due to their great formability and deep drawability [2][20].

2.1.2 High strength steels

There are various types of high strength steels (HSS) used in automotive industry, including high strength interstitial-free steels (IF-HS), bake hardening (BH) steels and high-strength low-alloy steels (HSLA). It is reported that application of these grades can help to reduce the mass of the car body by about 19% while a better strength and structure performance can be achieved[2].

IF-HS steels have a ferritic microstructure, and carbon and nitrogen contents are controlled to achieve a high formability. Due to the high formability, these grades are usually used to manufacture rear and front door inner and rear floor panel of car body in automotive industry [21]. BH steels,

which have a basic ferritic microstructure, are treated by bake hardening process [22], where strain aging is applied to enhance the strength of formed steel parts in a low temperature (150-200 degree) paint baking stage [22]. It basically results in migrating the interstitial atoms (carbon and/or nitrogen) to dislocation produced during forming operation to increase the strength and dent resistance in steels [22]. It is usually applied into making automotive outer body because of its high strength, high formability and dent resistance [22]. High Strength Low Alloy (HSLA) steels are a type of steels that have better mechanical properties and greater corrosion resistance than carbon steels. The strength and corrosion resistance of HSLA steels are increased by adding micro-alloying elements, such as manganese, copper, nickel, niobium, chromium, titanium, and calcium, etc. [23]. HSLA steels are often used in some load application components of automotive due to their sufficient strength [2].

2.1.3 Advance High Strength Steels

The AHSS are developed to fulfil the requirements of today' s vehicles for strict safety regulations, emission reduction and economical cost [24]. These materials have superior strength and ductility balance and can reduce the weight of body-in-white as well as improve the passengers' safety [24]. These grades of steels improve the formability, strength range and crash-energy absorption compared with conventional HSS [12]. The usage of AHSS in vehicles increased to 8% of the entire body in 2011 and it is expected to rise to 15% in 2020. This exhibits a wide spread trend of AHSS usage in automotive industry [12].

All AHSS are produced by controlling the rate of cooling from the microstructure of austenite plus ferrite or austenite [12]. As shown in Figure 2.1, AHSS are divided into different grades based on their microstructure and relative strength levels, such as dual phase (DP), complex phase (CP), transformation-induced plasticity (TRIP) and martensitic (MART), twinning-induced plasticity (TWIP) steel, hot-formed (HF) steel and manganese-boron steel [2].

Dual phase steels consist of a combination of ferrite and martensite phases

produced through controlled cooling rate to transform some austenite to ferrite with slow cooling and some austenite to martensite with rapid cooling, Figure2.3 [2][25]. These grades of steels show great mechanical properties, such as great ductility-strength combination, continuous yielding behaviour and formability compared with conventional high strength steels [25][26], their ductility-strength combination is quite valuable as it will not affect the mechanical properties even in very low thickness [27]. Hence, they can help reduce the weight of vehicles [27]. In this case, DP steels are widely applied in safety automotive components, including car body panels, B-pillars, bumpers and roof rails [2].

Multiphase or complex phase (CP) steels contain a mixture of ferrite, bainite pearlite and martensite, Figure 2.3. Its yield strength is higher when the tensile strength is at same level with dual phase steels. CP steels have great energy absorption and high residual deformation and are used in frame rails, transverse beams, rocker outer and rocker panels, etc. [2].

Transformation induced plasticity (TRIP) steels have a multiphase structure containing retained austenite within the matrix of ferrite, bainite and martensite. A controlled phase transformation method is used to produce TRIP steels with slow and rapid cooling rates as shown in Figure 2.3. They have sufficient carbon content, which is higher than DP steels, in order to make retained austenite stable below room temperature [2]. TRIP steels are applied to manufacture roof rails, B-pillar upper, front and rear rails due to its high strength and elongation [28].

Martensitic steels (MS) contain fully martensitic phases. They are produced by rapid cooling to transform austenite into martensite as shown in Figure 2.3. A 100% martensite structure can be obtained in a continuous annealing line by water quenching. They have high tensile strength up to 1700MPa [2][18]. They are used in bumper reinforcements, bumper beams, rocker outer and side intrusion, etc [2].

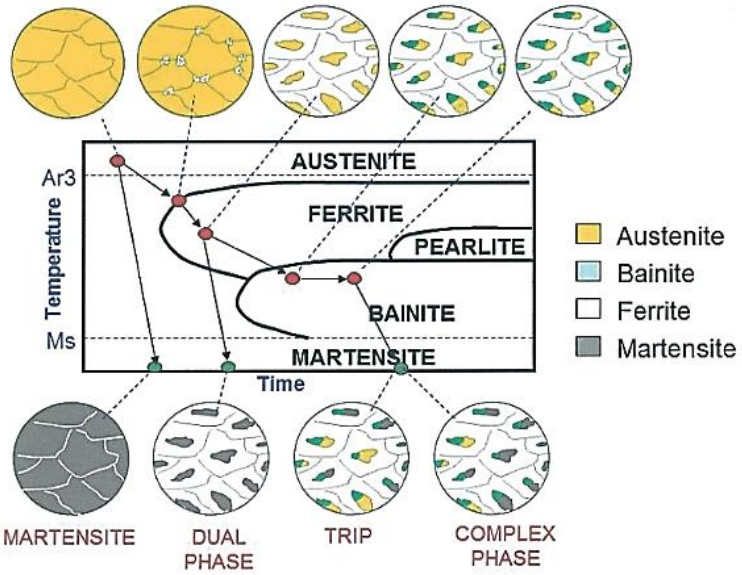

Figure 2.3. Time-temperature –transformation (TTT) diagram for carbon steel [29]**.**

Twinning-Induced Plasticity (TWIP) steels only consists of austenite at room temperature which are developed by adding high manganese content (15-30%) in the chemical composition of the alloy [30]. They have large uniform elongation (60%) over a wide range of strain rates and extremely high tensile strength (>1000 MPa). It also has high strain hardening rate because of deformation twinning [30]. Consequently, they are usually used for A-Pillar and door impact beam, etc. [2].

Manganese-boron steels are tempered boron-alloy steels offering great tensile strength up to 1650MPa and good elongation (around 5%) after hot forming and controlled cooling process. The high strength is caused by controlling cooling to get the martensitic structure [2]. The carbon and manganese content as well as very low boron content (between 0.001%-0.005%) also make a contribution to the strength [31]. It is normally used for A-Pillar and B-Pillar, etc. [2].

2.2 Mechanical properties characterisation of the weld section

In order to analyse the failure mechanism and simulate failure process of welded samples, it is essential to determine the mechanical properties of

welded samples. These properties include true stress-strain curves and hardness of different regions of the welded joint.

2.2.1 Hardness test

The relation of hardness and other mechanical properties are close, including strength and ductility. The hardness is a common parameter to evaluate the quality of materials [32][33]. The hardness test can be classified into two types including macro-indentation testing and micro-indentation testing specified in standard ISO 14577 [34]. Macro-indentation tests are characterized by indentation loads L in the range between $2N$ and $30\,kN$ while micro-indentation tests are specified by indentation loads $L < 2N$ and penetrations $h > 2\mu m$. There are several similar hardness test methods developed according to the actual or projected indent surface area, indent depth and indentation load within a certain time, such as Brinell, Meyer, Vickers and Rockell, etc. [33]. Vickers test is commonly used for both macro and micro harness tests among them. It can be applied into measuring metallic and non-metallic materials including steels, ceramics and polymers [32][35][36][37].

Figure 2.4 shows the indenter and indentation of Vickers test. The indenter is often a squared pyramid shape with 136 degree angle for the opposite side and the hardness value is computed based on the indenter load and projected surface area. The hardness value is calculated as the following equation [32]:

$$H_v = \frac{P}{A_s} = 2P\frac{\sin(\frac{136^o}{2})}{g_n d^2} = 0.1891\frac{P}{d^2}$$

Equation 2.1

where H_v is the Vickers hardness, MPa, P is the indentation load, kgf, g_n is standard acceleration due to gravity; d is the mean diagonal length of indentation, mm.

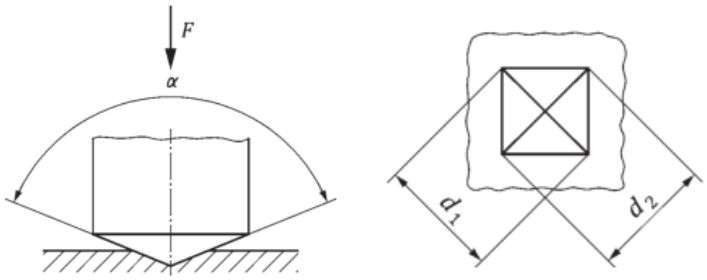

Figure 2.4. Vickers indenter and indentation [32]**.**

2.2.2 Nanoindentation

Nanoindentation has been implemented to characterise Young' s modulus and hardness of materials [38][39]. Force and depth can be continuously measured during indentation and provide accurate load-depth data under submicron scale. Then, the Young' s modulus and hardness can be determined based on the loading and unloading load-depth data as well as the data of indentation area [39]. Methods have also been developed to determine constitutive relations of materials by determining the strain hardening exponent n and strength coefficient K or FEM method according to the Nanoindentation data [40][41][42]. Thus, Nanoindentation is an effective technique to determine the mechanical properties of materials that are not able to be characterised by conventional uniaxial tensile test, such as thin polymer film and different regions of spot welds [41][43].

Determination of Young' s modulus E and hardness is briefly introduced as follows. Although, several different shapes of indenters are applied for indentation including conical, pyramid and Berkovich tips, the principle of extracting E and H are similar. Figure 2.5a shows the Schematic of indentation using Berkovich tip under peak load and after unloading, while Figure 2.5b shows loading and unloading load-depth curve and corresponding energy fractions. The Young' s modulus E is determined by the reduced modulus $E_r$and elastic modulus of the indenter E_i:

$$\frac{1}{E_r} = \frac{1-v^2}{E} + \frac{1-v_i^2}{E_i}$$

Equation 2.2

Where v is the Poisson ratio of the material and v_i is the Poisson ratio of the indenter. E_i is the Young' s modulus of indenter. E_r is determined by a series of calculations using the parameters shown in Figure 2.5a and b developed by researchers [44].

Hardness can be calculated from its normal definition in equation 2.3:

$$H = \frac{P_{max}}{A}$$

Equation 2.3

where P_{max} and A are the peak load and the projected area of indentation[44].

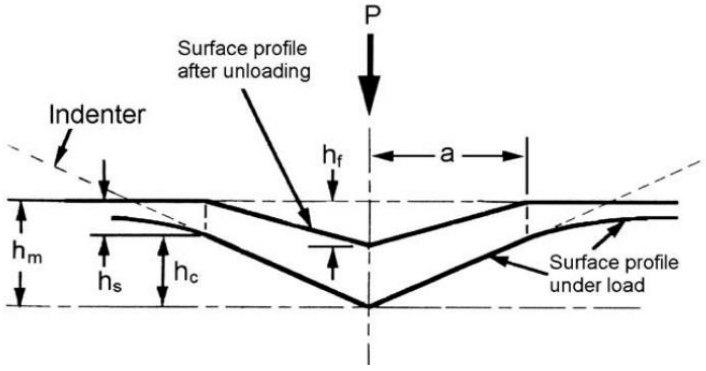

(a)

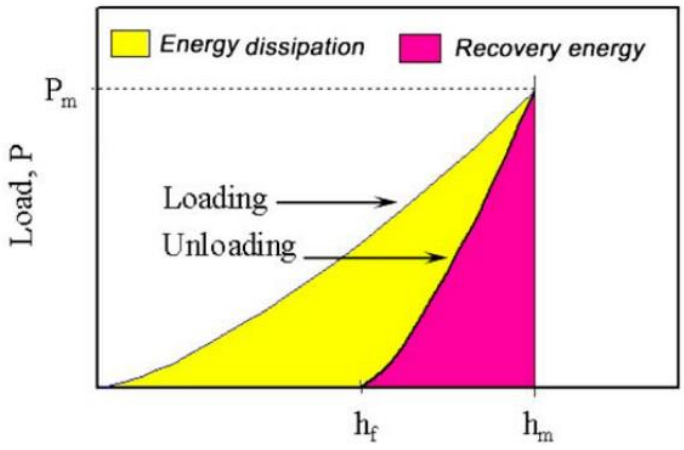

(b)

Figure 2.5. (a) Schematic of nanoindentation, (b) schematic of loading and unloading load-depth curve and corresponding energy fractions [38]**.**

2.2.3 Uniaxial tensile test

Uniaxial tensile test is simple and effective to understand the stress-strain relationship of a metallic material. Various mechanical properties can be characterised though such method, including Young' s modulus, yield strength, tensile strength, strain hardening and true stress-strain curves, etc, referring to the standard ISO 6892[45]. Standard specimen or standard subsize specimen are applied to the test depending on the requirements, as shown in Figure 2.6. The length change needs to be measured along the gauge highlighted with G in Figure 2.6.

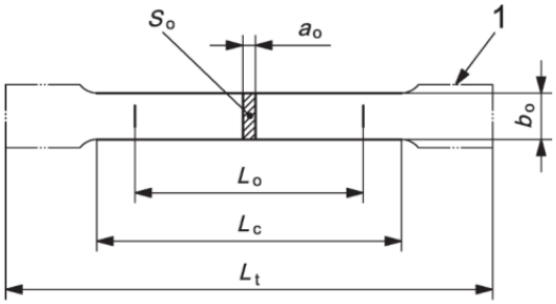

Figure 2.6.Schematic of standard tensile test specimen [45]**.**

Engineering stress-strain relationship can be directly calculated through achieved data from the test, as shown in Figure 2.7. Young' s modulus is slope of linear portion of the curve while yield strength is determined by a 0.2% strain offset method referring to the standard ASTM E8, Figure 2.7 [46]. Moreover, necking, which occurs in ductile materials [47], happens after the maximum load point as the strength increase by strain hardening (caused by increase resistance of dislocation movement) is no longer withstand the stress produced by loading. The stress and strain are calculated from:

$$\sigma_e = P/A$$

Equation 2.4

$$\boldsymbol{\varepsilon_e = \Delta l / l}$$

Equation 2.5

where $\sigma_e, P \text{ and } A$ are engineering stress, load and cross section area of the sample while $\boldsymbol{\varepsilon_e}, \Delta l \text{ and } l$ are engineering strain, length change and initial length of the gauge.

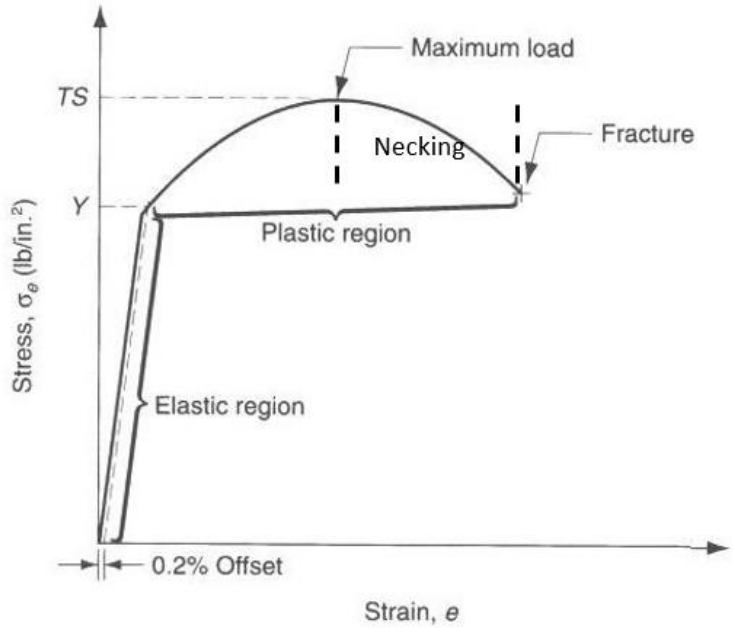

Figure 2.7. Schematic of engineering stress-strain curve.

True stress-strain relationship can be calculated according to engineering stress-strain curve considering the area change during testing. True stress, σ_t, and strain, ε_t, are calculated by the following equations before necking [48]:

$$\sigma_t = \sigma_e(1 + \varepsilon_e)$$

Equation 2.6

$$\varepsilon_t = \ln(1 + \varepsilon_e)$$

Equation 2.7

A power law used to represent the flow curve [48] can be utilized to calculate the true stress-strain relationship after necking as below:

$$\sigma_t = K\varepsilon_t^n$$

Equation 2.8

Where K is strength coefficient and n is strain hardening exponent.

2.3 Joining techniques

Several permanent or semi-permanent joining techniques are available to join the metallic or non-metallic parts together. The semi-permanent joining methods are designed to join the parts for a certain time, including using mechanical fasteners such as nuts and bolts and washers, knock-down fittings and screws, where a flexibility in assembly and disassembly is required without

damaging the parts. The permanent joining methods includes permanent mechanical fastening, welding, friction stir welding, laser welding and resistance spot welding [49]. These methods can permanently join the metallic or non-metallic parts together and hardly be separated [50]. Joining methods that are commonly applied in assembling a car body include bolts, self-piercing riveting, mechanical clinching, laser welding and spot welding [51][52][53]. The following sections give a general review of the selected permanent techniques used in carbody construction.

2.3.1 Self-piercing riveting

Self-piercing riveting (SPR) is permanent joining technique used to connect two or more sheets together in car body construction. It can be applied into different materials including aluminium alloy and steel sheets [54][55]. Figure 2.8 shows the SPR process wherein the rivet is driven through the upper sheet materials and deformed the lower sheet into a die. During the process, the gap between two sheets is closed and an interlock is formed. There are several advantages for SPR including no pre-drilled holes, low noise and no surface treatment [54]. However, the method has high equipment and tooling cost, low connection strength and is not suitable for materials that has low ductility or brittle materials [56].

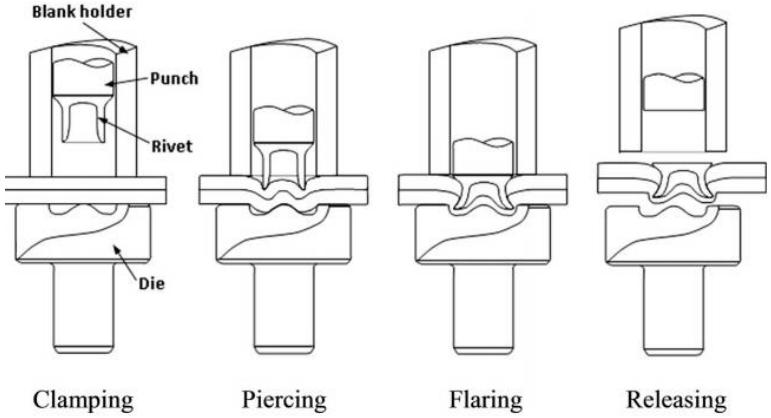

Figure 2.8. Schematic of a SPR process [54]**.**

2.3.2 Mechanical clinching

Mechanical clinching is usually used to join non-ferrous sheet materials

used in car body construction including aluminium alloys and magnesium alloys [57][58]. These materials can not to be joined effectively by other joining techniques due to their low electrical resistance high strength [57]. Figure 2.9 shows the process of mechanical clinching. An interlock is formed between two sheets through punching the sheet materials into a die in order to join the sheets together [59]. Mechanical clinching has some advantages, including no surface preparation, no additional parts (bolts, screws and rivets), high efficiency and low –energy consumption [57][59]. However, clinching has some disadvantages including extremely high force requirement and inapplicability in sheet materials of low ductility [58].

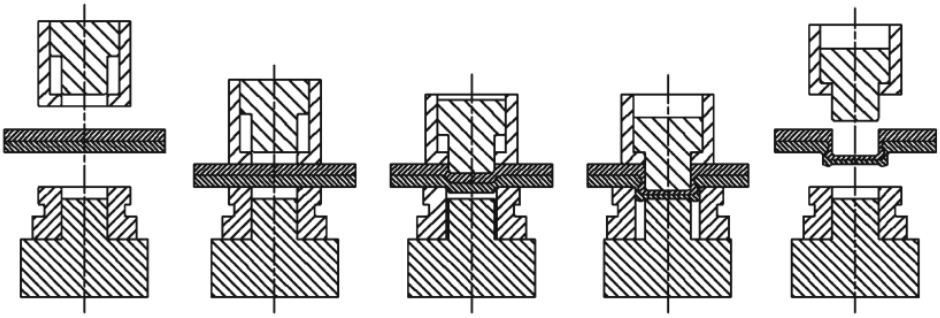

Figure 2.9. Schematic of a mechanical clinching process [59]**.**

2.3.3 Laser welding

Laser welding is a technique using laser beam to join metal pieces or thermoplastics together. It can be used to weld steel, aluminium and titanium [60][61][62]. Additionally, laser welding is commonly applied into welding automotive components, such as gears and transmission components. The high concentrated laser beam is targeted on the workpieces to melt the material around the beam, Figure 2.10 [63][64]. Welds can be created with or without filler metal. The advantages of laser welding are high welding speed, low energy input and small heat affected zone (region that is not melted but its microstructure is varied by the heat generated in the welding process between weld and base metal) [65]. However, it also has several disadvantages restraining its application, such as safety issues caused by direct or indirect exposure to the laser radiation, low energy conversion efficiency, high requirement of laser beam position accuracy, humping and porosity [64].

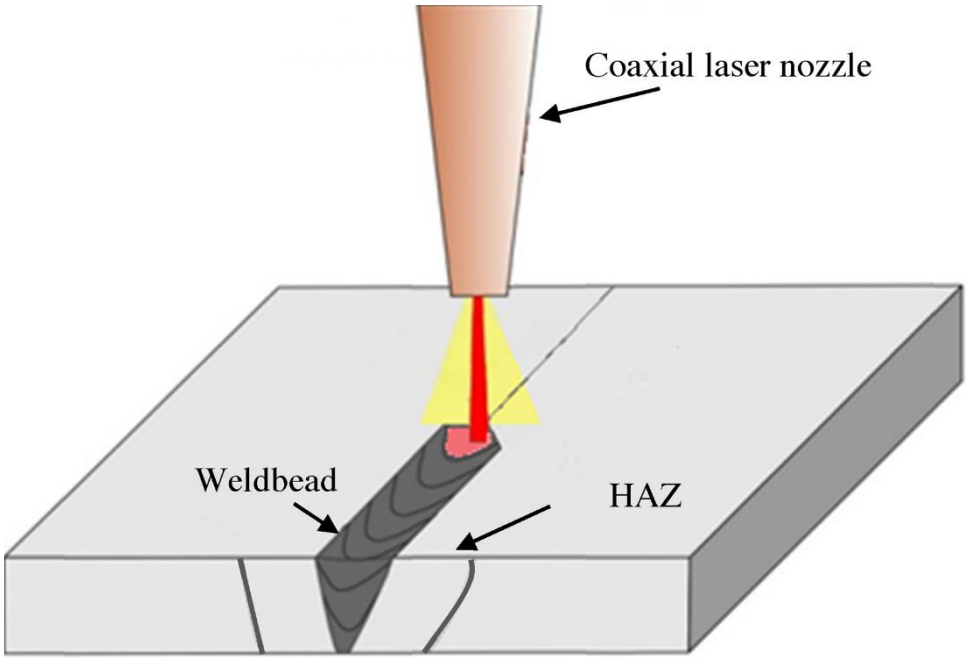

Figure 2.10. Schematic drawing of laser welding process [63]**.**

2.3.4 Resistance spot welding

Resistance spot welding (RSW) is popular in joining metal sheets and is commonly used in assembling car bodies due to it is the most economical, flexible, time efficiency joining technique used in automotive industry [66][67]. Additionally, the joint made is uniform and has higher loading capacity compared with riveted and clinched joints and the operation is highly automatic. A car body is made of automotive steels with thousands of spot welds [66]. Therefore, the failure mechanisms of spot welds are crucial to be investigated [68].

Figure 2.11 presents the fundamentals of a resistance welding machine circuit wherein two electrodes made of copper alloy locate at upper and lower sides of the workpieces due to its low resistance allowing heat generated in the workpieces. The workpieces are pressed by the electrodes. During welding process, the workpieces experience two stages including melting and solidification between two metal sheets [69]. The region around the contacted surfaces of two metal sheets first melted at start of welding process and the melted volume becomes larger as more heat generated, and then the

solidification will fuse the two metal sheets together [70]. The heat generation during welding refers to the following equation:

$$Q = I^2RTK$$

Equation 2.9

Where Q is heat, I is welding current, R is resistance of workpieces, T is welding time and K is heat losses.

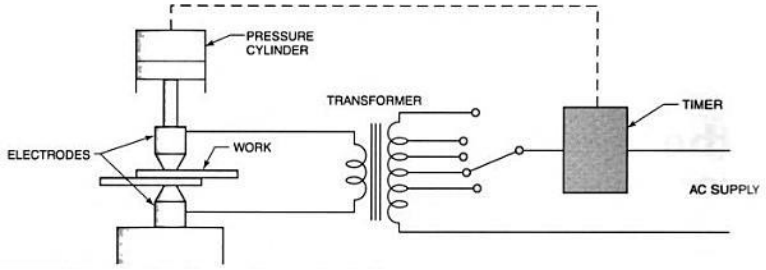

Figure 2.11. Schematic of RSW principle [69]**.**

The resistance spot welding process results in three microstructural zones as shown in Figure 2.12: weld nugget, heat affected zone (HAZ) and base metal (BM) [71][72][73].

The temperature experienced of any spot welds in steels is the key factor to characterise the different regions of a spot weld as metal phase transformation happens in the weld resulting in different microstructure due to different temperature level caused by heat generated during welding process and different cooling rates [74].

The nugget is created by heating the materials over the temperature that all ferrite is transformed to austenite (Ac_3) and being cooled down rapidly from the liquid phase. Phase transformation may occur in this region. All the materials are melted in this region [70].

The HAZ is the region surrounding the weld nugget. It can be divided into four regions, (i) coarse grain heat affected zone(CGHAZ) where the temperature is well above Ac_3 but lower than the temperature in the nugget, new phases may form during rapid cooling in this zone and grains slightly grow up [43], (ii) fine grain heat affected zone (FGHAZ) where the temperature is just above Ac_3, new phases may form and almost no grain grows in this zone as the cooling rate is faster than CGHAZ [43], (iii) intercritical heat affected zone

(ICHAZ), where the temperature is between Ac_3 and temperature that ferrite begins to transform to austenite (Ac_1), some of the ferrite transforms to austenite and partial phase transformation may occur in this zone after cooling [70], (iv) subcritical heat affected zone (SCHAZ) where the temperature is below Ac_1, it is difficult to identify this region due to that there is almost no visible microstructural changes [75]. In hence, mechanical properties of BM, HAZ and nugget vary from each other.

In addition, a thin line-like bond within the HAZ ahead of the notch tip (highlighted in blue squares in Figure 2.12) is the called corona bond which is a solid phase bonding formed by pressure of two electrodes [76][77].

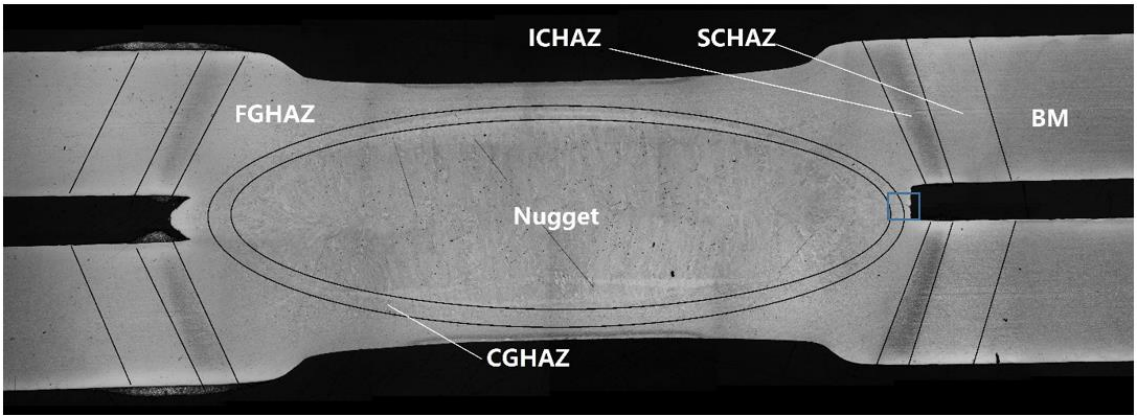

Figure 2.12. Schematic of weld section showing nugget, CGHAZ, FGHAZ, ICHAZ, SCHAZ and BM.

2.4 Effect of grain size

The size of grains in polycrystalline metals has great effect on their mechanical properties, including yield strength, tensile strength and hardness [78]. The Hall-Petch relation, as shown in equation 2.10, indicates that increase in average grain size results in decrease in mechanical properties in ferrous materials, as found by researchers in pure iron sample [78], a high manganese austenitic steel [79] and a type of martensitic steel [80], which is due to the decrease of area fraction of grain boundaries leading to lower stress to develop the crack [81].

$$\sigma_y = \sigma_i + K_y d^{-1/2}$$

Equation 2.10

Where σ_y is yield strength, σ_i is friction resistance of dislocation movement within the polycrystalline grains, K_y is Hall-Petch slope and d is average grain size [80].

The increase in grain size primarily occurs during the heating process in steels, when recovery and recrystallization are complete and further heating can increase the size of grains [82]. It is worth noting that recovery is a process that energy stored in deformed grains can be reduced through rearranging or removing defects in their crystal structure occurring in lower temperature than recrystallization [82]. Recrystallization is a process that distorted grains in metals through cold work are substituted by new grains having more stable state when being heated above recrystallization temperature [83]. The increase of grain size can be enhanced by higher temperature and longer heating time while the presence of other particles can slow down the grain growth [84]. A general relationship is used to describe the grain growth, equation 2.11 and the constant K is expressed by equation 2.12.

$$D^m - D_0^m = K \cdot t$$

Equation 2.11

$$K = K_0 \cdot \exp(-\frac{Q}{R \cdot T})$$

Equation 2.12

Where D is current grain size, D_0 is initial grain size, K is proportional constant depending on thermodynamic temperature T and activation energy Q, R is universal gas constant, t is heating time at a given temperature and m is a material exponential coefficient [84].

2.5 Failure modes and failure mechanisms of spot welds

2.5.1 Fracture mechanisms of metals

Metallic materials fail through two main different fracture mechanisms, depending on their mechanical and microstructural properties, including brittle fracture and ductile fracture [85]–[90].

Transgranular and intergranular fracture are two types of brittle fracture which is a type of fracture without appreciable prior plastic deformation.

Transgranular fracture, which is also called transgranular cleavage, is a rapid crack propagation along a particular crystal plane [91]. It is because of the local stress is sufficient to overcome the cohesive strength of the material [91]. The crack does not propagate along the grain boundary but rapidly goes through grains, Figure 2.13a, and generates reflective, flat and bright facets on the fracture surface shown in Figure 2.13b [91][92].

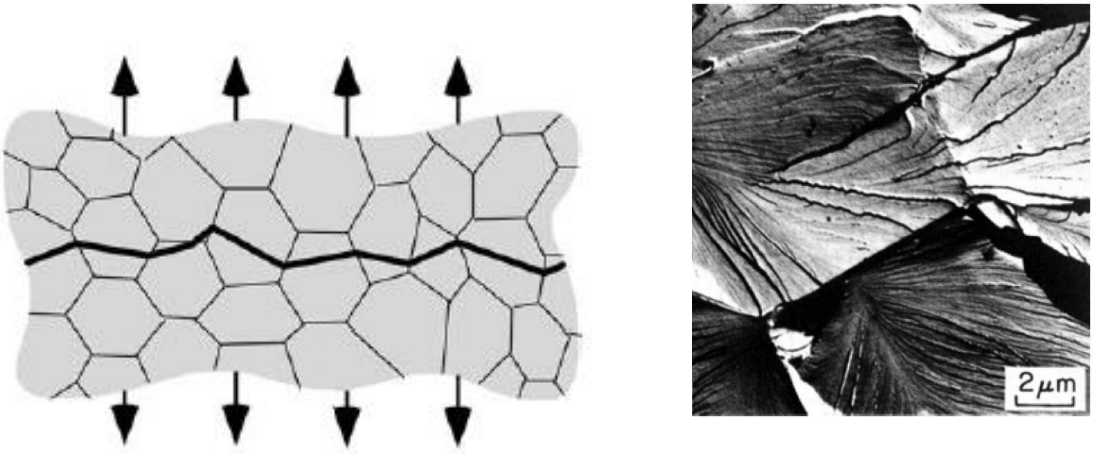

(a) **(b)**

Figure 2.13. (a) Cleavage and (b) Crack path [91]**.**

Another type of brittle fracture is called intergranular fracture wherein the crack goes along the grain boundaries of the material resulting in a fracture of jagged looking with shining surfaces and straight edges as shown in Figure 2.14 [91]. Intergranular fracture can be induced in several ways, including impurity elements in the grain boundaries [93], hydrogen embrittlement in the material [94] and increase of carbon as well as manganese contents which may strengthen the grain boundaries [95].

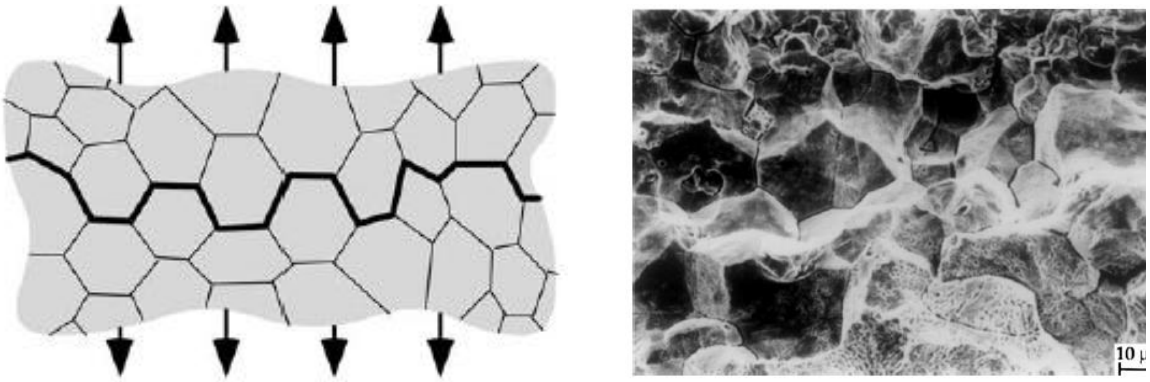

(a) **(b)**

Figure 2.14. Intergranular fracture (a) crack path, (b) intergranular fracture in a type of steel [91]**.**

In contrast to fast crack propagation in brittle fracture, ductile fracture is associated with nucleation, growth and coalescence of the voids [96][97], which can be induced by tensile or shear loads. Figure 2.15a-c shows the mechanism of ductile fracture due to tension. There are three stages during a ductile fracture process, firstly, microvoids nucleate at an inclusion or second-phase particles, Figure 2.15a, secondly, the voids grow in size by further plastic strain and hydrostatic stress, Figure 2.15b. Lastly, adjacent voids coalesce with each other and lead to ductile fracture, Figure 2.15c [91]. Due to the presence of voids during the ductile fracture, the produced fracture surface is shown in Figure 2.16a. In contrast to ductile fracture due to the applied tensile loads, shear fracture occurs when a shear loads is applied. As shown in Figure 2.15d, when the material is dominated by shear stress state, voids can form in smaller particles compared with ductile fracture and subsequent growth may cause interaction between neighbouring voids and finally causing shear failure [98]. Shear fracture can produce elongated dimples, Figure 2.16b.

A low energy absorption and rapid failure process indicate that brittle fracture is very dangerous and has to be avoided [99]. In contrast to brittle fracture, ductile fracture experiences larger plastic deformation and needs much more applied energy, which means it is able to absorb more energy [91]. Thus, failure due to ductile fracture is preferred in automotive.

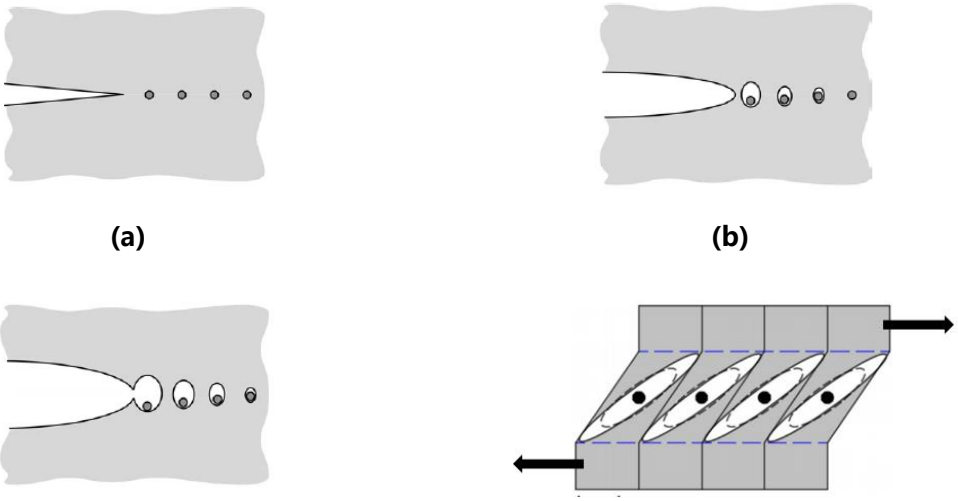

Figure 2.15. Mechanisms of ductile crack propagation (a) initial state, (b) nucleation and growth of voids (c) voids coalescence (d) shear fracture [91][100]**.**

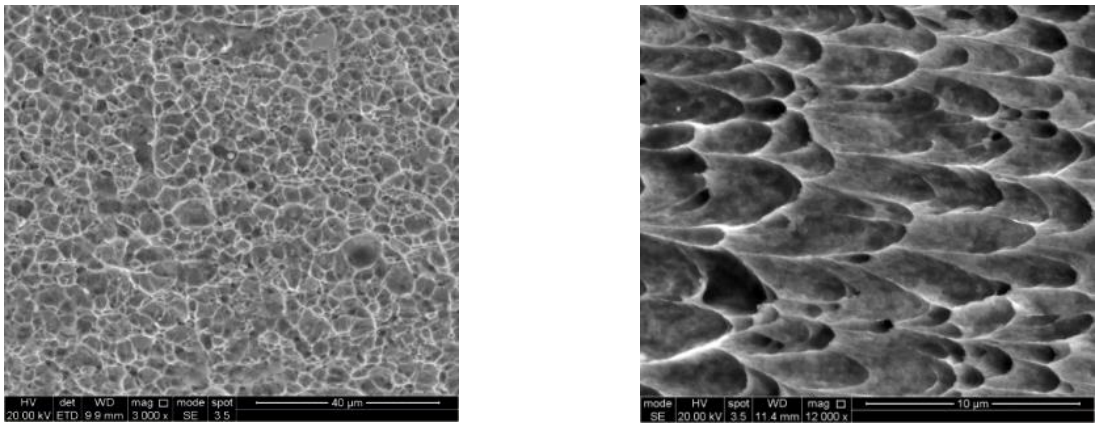

Figure 2.16. (a) Microvoids observed in ductile fracture surface resulted by tension in welds of DP1000, (b) elongated dimples observed in shear fracture surface in welds of DP1000.

2.5.2 Failure modes in resistance spot welds

The failure modes of RSWs have been classified into three types: pull out failure (PF), interfacial failure (IF) and partial interfacial failure (PIF) [101]. The pull out failure includes nugget pull out failure and sheet pull out failure. The

crack paths of all failure modes are highlighted in Figure 2.17. For nugget pull out failure, the crack initiates from inner side of metal sheet within HAZ and propagates along thickness direction, highlighted by green arrow in Figure 2.17. In sheet pull out failure, the crack initiates within base metal and propagates through thickness direction of the sheet as highlighted by white arrow in Figure 2.17. In this way the whole weld is pulled off the metal sheet. However, in the case of partial interfacial failure, the crack initiates from the tip of corona bond and propagates along interface of the nugget before deflecting its path to the thickness direction of the sheet, as highlighted by blue line in Figure 2.17, part of materials within the nugget is pulled out in this mode. In the case of interfacial failure, the crack initiates at the corona bond tip and propagates through the interface of the nugget to divide the welded sheets into two pieces, as highlighted by yellow line in Figure 2.17 [102].

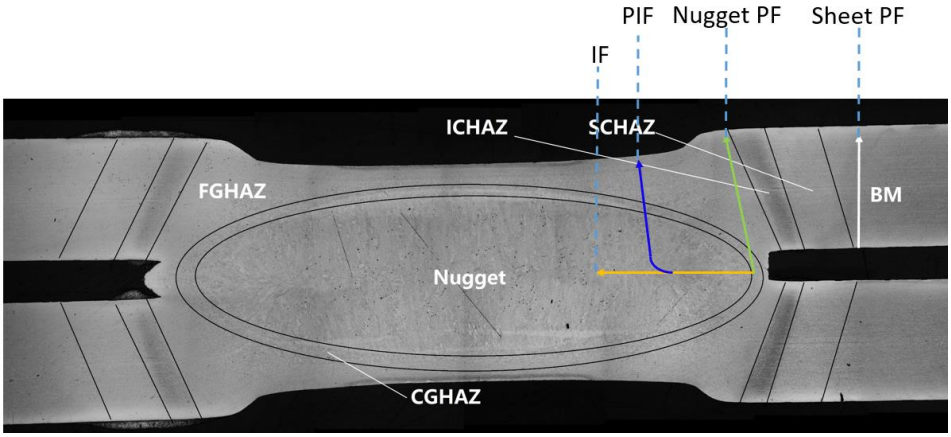

Figure 2.17. Schematic of different failure modes in RSWs.

2.5.3 Failure analysis of resistance spot welds

There are several standard tests reported to assess the structural integrity and strength of spot welds including cross-tension test, tensile-shear test and coach-peel test representing tensile, tensile/shear and tensile/bending loading conditions, respectively [103][104]. [105]Researches were carried out using failed resistance spot welds in different types of automotive steels, showing that steels types, welding current and loading conditions could affect the failure mechanisms of the spot welds and failure modes.

In cross-tension test, two sheets are overlapped and perpendicular to each

other and a weld is made at the centre of the overlapped region referring to the standard EN ISO 14272:2001 . Subsequently, a tensile load is applied normal to the sheet surface to assign tension stress state to the weld [6][106].

In a study of IF and DP steels welded CT samples, different failure modes were observed at different zones of the weld, Figure 2.18b, wherein PF happens in zone 1- and zone 2, PIF and IF happens in zone 3 [101]. Specifically, as shown in Figure 2.19, IF260, DP450 and DP980 steels welded CT samples of same welding parameters was tested, however, the failure modes and failure mechanisms are different. Weld in DP450 steel fails via sheet PF mode as mentioned above in zone 1 caused by ductile fracture, weld in IF260 steel fails via nugget PF failure in zone 2 caused by ductile shear fracture, weld in DP980 steel fails via PIF caused by semi-brittle fracture. In addition, Dancette et al. reported the failure modes change from nugget PF or PIF to a mixed failure (nugget PF and sheet PF) in welds in DP590 when increasing the nugget size by increasing the welding current [11].

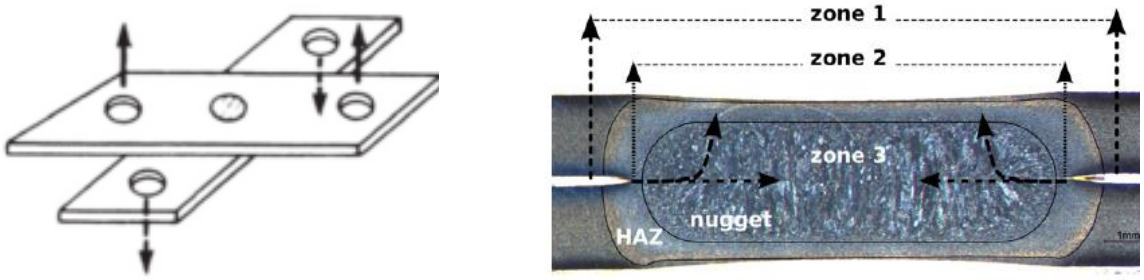

(a) **(b)**

Figure 2.18. Description of failure modes of cross-tension test [67][101]**.**

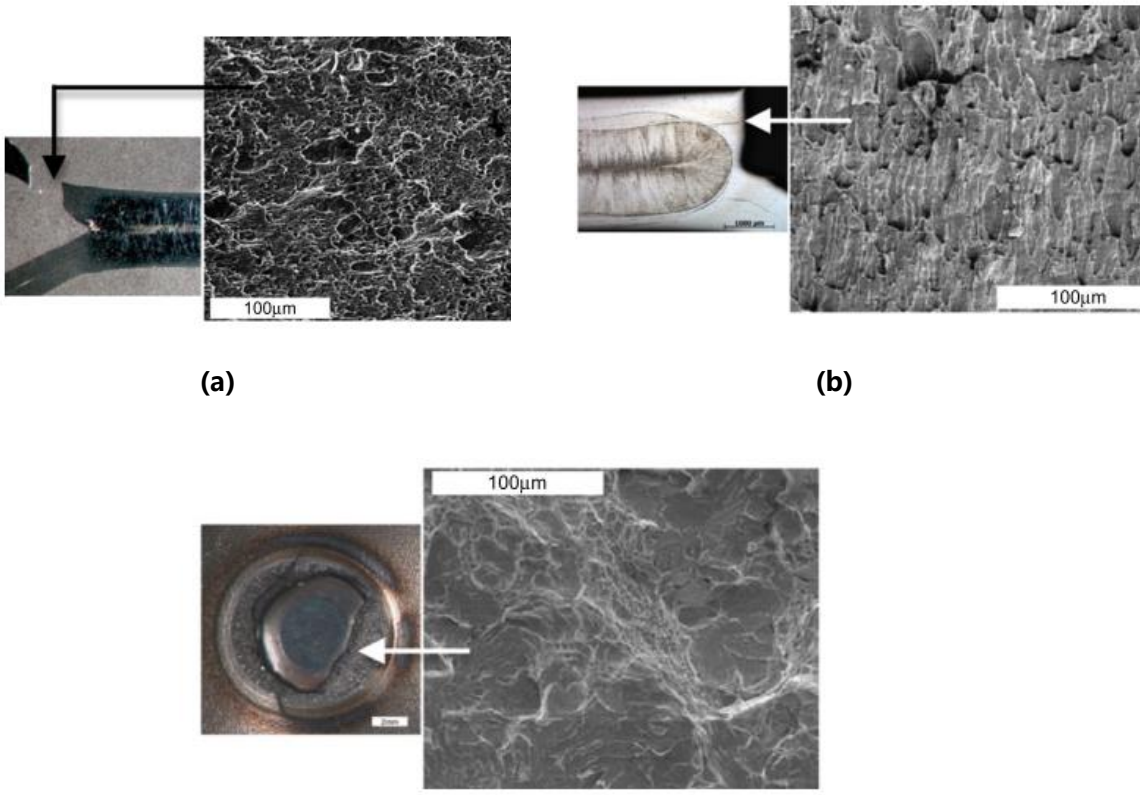

Figure 2.19. SEM images, (a) PF in BM in Dp450, (b) PF in HAZ in IF260, (c) PIF in DP980 [101].

As shown in Figure 2.20, in tensile-shear test, part of the two sheets are joined together, a spot weld locates in the centre of the overlapped region while a tensile load is applied to the sample to assign a shear stress state to the weld referring to standard EN ISO 14273:2001 [107].

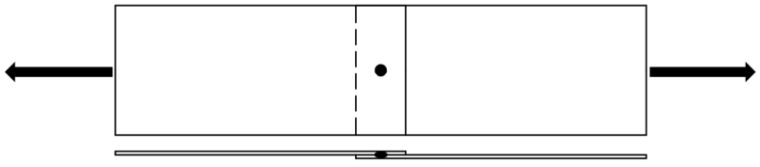

Figure 2.20. Schematic of tensile-shear sample.

Previous researches also show that material types and welding currents can influence the failure mechanisms and failure modes of spot welds under tensile-shear loading condition. Dancette et al. reported the failure modes

transition from IF to PF when increasing the nugget size by increasing the welding current for spot welds in IF260 or DP590 steels [11]. Different failure mechanisms were also observed for welded sample failed via same failure modes in different steels. For the welds failed via IF mode, as shown in Figure 2.21, the crack goes through the interface of the nugget and in-plane shear was observed in the central part of the nugget while out-of-plane shear on flank side in DP980 reported by researchers [11][108]. However, it is different for the welds failed via IF in B1500 steel, as shown in Figure 2.22, where brittle fracture is the dominant factor of failure with some ductile fracture[109]. The difference of failure mechanisms was also observed in welds failed via PF mode in different steels. Ductile fracture caused by necking was observed to be the reason inducing sheet PF mode in DP450 steel and a type of low carbon steel [104][11]. An example of cross section surface and fracture surface of the weld in low carbon steel is shown in Figure 2.23 [104]. However, welds in a type of grade 1000 high strength steel failed via sheet PF showed ductile fracture with brittle facets [110]. Moreover, necking in BM and subsequent shear fracture were observed in weld in DP780 resulting in sheet PF [111]. The relation between peak load and nugget size was also investigated by researchers including DP600 and low carbon steels, showing an increase of peak load as increasing nugget size by increasing welding current, and then decrease of peak load was observed due to the presence of expulsion (molten metal ejection) when further increasing the welding current [105][112][113].

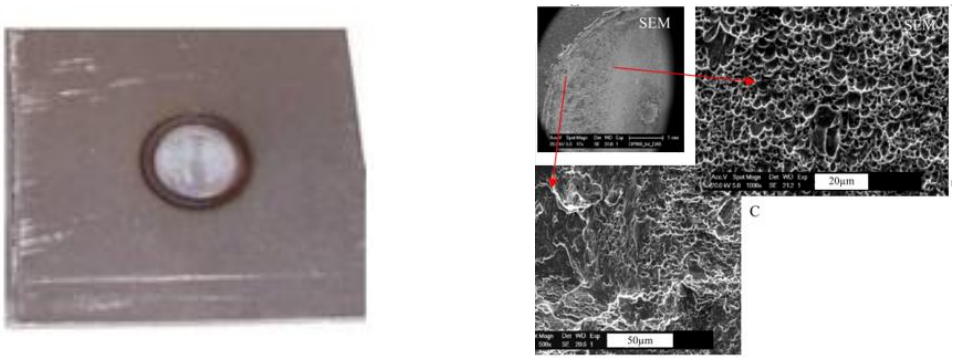

(a) **(b)**

Figure 2.21.Microstructure of IF region of RSWs in DP980 [11].

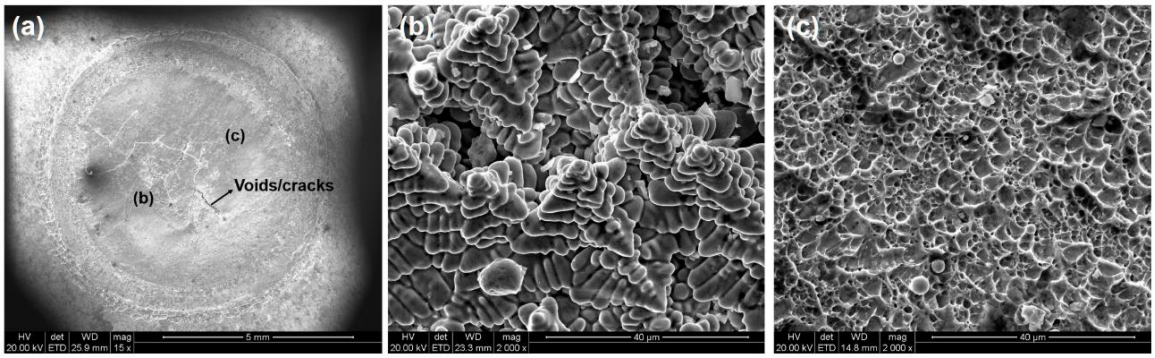

Figure 2.22. SEM fracture surfaces in tensile-shear sample via IF in RSWs of B1500**, (a) overview of fracture surface, (b) brittle fracture surface and (c) ductile fracture surface**[109]**.**

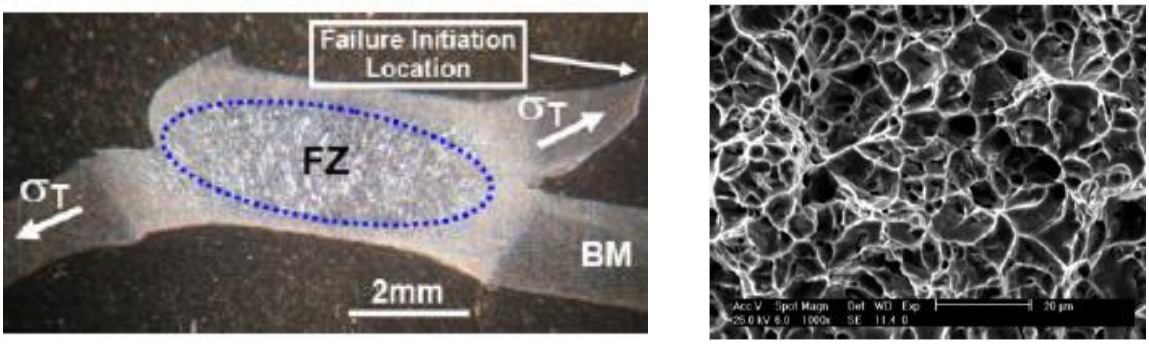

(a) **(b)**

Figure 2.23. Cross-section surface of TS sample failed via PF (a) and fracture surface indicated by the arrow (b) in RSWs of low carbon steel [104]**.**

The geometry of coach peel samples is shown in Figure 2.24, referring to standard EN ISO 10447: 2007 [114]. Two sheets are bended to 90 degrees and joined together by resistance spot welding, then a tension load is applied to the two legs of the sample [104][115][5].

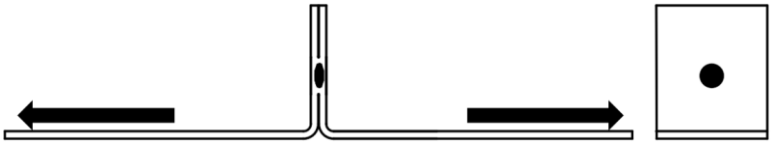

Figure 2.24. Geometry of coach-peel sample.

Researches also show that material types have influence on the failure mechanisms for welds under coach-peel loading condition. And limited

researches were done on the influence of welding parameters, especially welding current, to the failure mechanisms [5] [8] [104].

Researchers reported the failure mechanisms of coach-peel samples of different materials such as low carbon steel [104] and several types of Advance High Strength Steels [5]. Figure 2.25 shows an example of the fracture surfaces of IF and PF modes in RSWs of a type of low carbon steel [104]. For IF mode, the crack initiates from the notch tip by the side of the loading legs and goes through the nugget, clear grain boundary can be seen indicating quasi-cleavage fracture, Figure 2.25b. For PF mode, those elongated dimples and voids in Figure 2.25d shows failure under shear and bending condition. In contrast, PF mode with different failure mechanism was observed in weld of HSLA grade 50 steel, including notch tip blunting and ductile fracture, was also reported by Zuniga [8]. Moreover, PIF was observed in spot weld in TRIP780 [5].

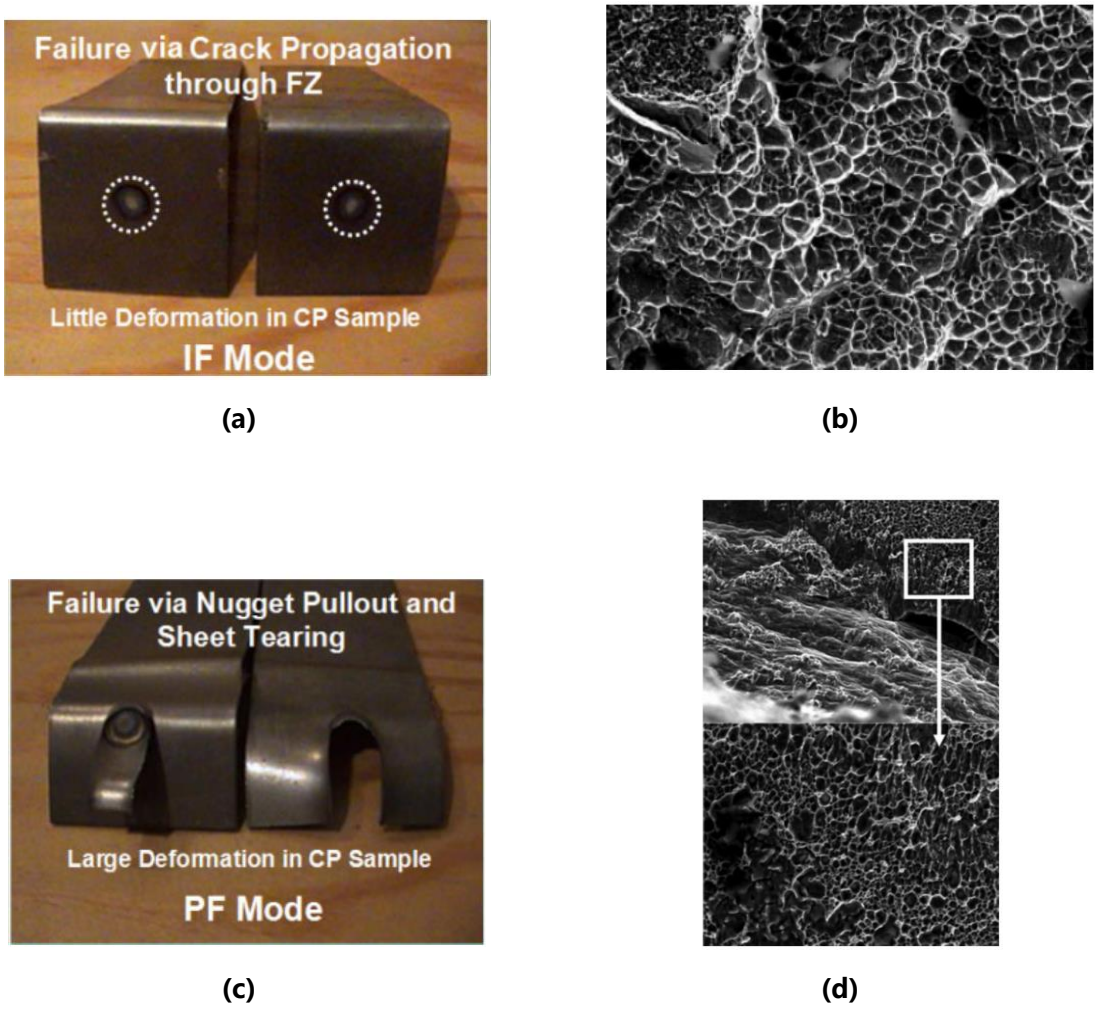

Figure 2.25. Failure modes of coach-peel sample, (a) interfacial failure, (b) fracture surface of IF, (c) pull-out failure and (d) fracture surface of PF of RSWs in low carbon steel [104]**.**

Previous researches indicated that material types, welding currents and loading conditions could affect the failure mechanisms of spot welds. Fractography analysis of failed welds and microstructure analysis were used to investigate the underlying failure mechanisms while load-displacement curves were used to assess the performance of welds. However, deformation evolution within different weld zones under different loading conditions and welding currents have not been studied by the previous researchers. It could provide detailed information on how the different regions of the weld behave during loading, which can be correlated with microstructure of the corresponding region to achieve a more comprehensive and better

understanding of the failure mechanisms.

Previous researches showed that steel types could influence the failure mechanism of spot weld, which could be due to the different types of steels consist of different microstructure. In-situ testing technique was applied by researchers under microscopic scale to investigate the effect of microstructure on damage of steel samples. Ghadbeigi et al. investigated the deformation evolution in DP1000 steel using in situ tensile test implemented under SEM, they clearly identified influence of ferrite and martensite phases on the damage nucleation through continuously obtaining the micrographs of the region of interest during loading [1]. Sawanishi et al. carried out in situ test under SEM to study the effect of pulsed welding current on strength properties using a sectioned DP980 welded joins, they found the pulsed current can improve the ductility of the nugget according to observation of microstructure as well as crack propagation in nugget [116]. The mentioned researches show that microscopic in situ test is an effective technique to investigate how the microstructure impacts the failure mechanism of the sample, which is due to such testing method can continuously record the deformation and damage evolution of region of interest under micro scale providing detailed information to study the effect of microstructure on crack initiation and propagation.

2.6 Modelling of deformation and damage in RSWs

The fracture of resistance spot welds was found to be mostly ductile fracture. To simulate the ductile fracture in metal, two types of model were applied, one is coupled model and the other is uncoupled model [117].

The coupled model can simulate the strength loss induced by the damage initiation attribute to micro void nucleation, growth and coalescence [117]. It can be divided into two categories micromechanical based coupled models and continuum damage mechanics (CDM) based coupled model. The micromechanical based model usually optimizes the microstructure with plastic potential and computational cells of the homogenized medium and the evolution equations [117]. On the other hand, the continuum damage

mechanics based model usually use internal damage variables, the evolution of these variables were depicted phenomenologically to fit the experimental observations [118].

The most common used coupled model used in simulating ductile failure is Gurson-Tvergaard-Needleman (GTN) model.

Gurson model was developed and proposed by Gurson [119]. He introduced plastic potential used for porous materials, the damage parameter used was void volume fraction. Then, Tvergaard and Needleman made a modification based on Gurson model, the critical strain for localization, the coalescence of voids and interaction between voids were taken into account. This new model was called Gurson-Tvergaard-Needleman model [120].

It has been integrated in ABAQUS software package [121]. The model is defined as follows [122]:

$$\emptyset = \frac{\sigma_{\mathrm{eq}}^2}{\sigma^{*2}} + 2q_1 f^* \cosh\left(\frac{3}{2} q_2 \frac{\sigma_{\mathrm{m}}}{\sigma_*}\right) - (1 + q_3 f^{*2}) = 0$$

Equation 2.13

Where σ^* is the current flow stress of the matrix, σ_{eq} is the macroscopic von Mises stress, σ_{m} is the hydrostatic stress, q_1, q_2 and $q_3 = {q_1}^2$ are parameters. The void volume fraction function [122], f^* is defined as:

$$f^*(f) = \begin{cases} f, & for\ f \leq f_c \\ f_c + \dfrac{\frac{1}{q_1} - f_c}{f_f - f_c}(f - f_c), & for\ f_c \leq f \leq f_f \end{cases}$$

Equation 2.14

Where f, f_c, f_f are void volume fraction, critical void volume fraction and void volume fraction at failure. The voids growth rate is the sum of voids growth $\dot{f}_g$ and the new voids nucleation $\dot{f}_n$ [122].

$$\dot{f} = \dot{f}_g + \dot{f}_n$$

Equation 2.15

$$\dot{f}_g = (1 - f) tr\dot{\varepsilon^{pl}}$$

Equation 2.16

$$\dot{f_n} = A\dot{\varepsilon_M}^{pl}$$

Equation 2.17

$$A = \frac{f_n}{S_n\sqrt{2\pi}}\exp[-\frac{1}{2}\left(\frac{\varepsilon_M^{pl} - \varepsilon_N}{S_N}\right)^2]$$

Equation 2.18

In which $tr\dot{\varepsilon^{pl}}$ is the volume plastic strain rate S_N is the mean quantity of voids nucleation, f_n is the second phase particles volume ratio and ε_N is mean strain at voids nucleation.

GTN model has already been coupled into FE software, however though it can completely characterize the ductile damage process, the calibration of parameters, including f_0 (initial volume fraction), f_c, f_f, ε_N, S_N, f_n, q_1, q_2 and q_3, are very hard [123]. Researchers used 'trial-error' method to calibrate these parameters based on experimental data, which is very complicate and time consuming [124][125].

Comparing with coupled model, the uncoupled model can be more computation efficiency. It formulates the damage evolution empirically or semi-empirically according to certain macroscopic variables including the tensile stress, hydrostatic stress and equivalent plastic strain, which are most relevant to damage initiation and evolution [117]. However, due to the plastic internal variables are not coupled to damage variables D, and there is no feed back to elastic-plastic behaviour of the material, it is only satisfied to predict the fracture initiation[118].

Johnson-Cook damage model is one of the typical uncoupled models [126] and based on the plastic strain. It is an empirical model combining strength with strain rate and temperature. Although, the model does not use loading history, it is proved to be proper for solving dynamic problems of a wide range of applications. These problems includes tension, shear, impact, explosive acceleration and penetration of metals [127][128].

Johnson-Cook failure proposed by Johnson and Cook [129] and given in the following equation:

$$\varepsilon_f = [D_1 + D_2\exp(D_3\sigma^*)]\left[1 + D_4\ln\left(\dot{\varepsilon_p}^*\right)\right][1 + D_5T^*]$$

Equation 2.19

where $D_1 - D_5$ are material constants, ε_f is failure strain, σ^* is stress triaxiality, $\dot{\varepsilon_p}^*$ is strain rate and T^* is temperature [130].

Although, as an uncouple damage model, J-C damage model can only accurately predict the initiation of fracture, it is very cost efficiency compared to GTN model as only 5 constants are needed to be calibrated, including $D_1 - D_5$, and these constants can be determined through experiments without iterative parameter calibration process [130][131], thereby the constants could be determined by the experimental data. Furthermore, it can be combined with the built-in Abaqus Ductile Damage model to predict the damage evolution [132]. In this case, J-C model was selected to simulate the damage of spot welds.

2.7 Full field strain measurement

Several strain measurement techniques have been applied to analyse the full field strain evolution on specimens due to more detailed information collection ability than typical uniaxial strain measurement techniques and their convenience and suitability to investigate the heterogeneous and anisotropic materials as well as structure properties of a sample. These techniques includes geometry moiré, moiré interferometry, speckle interferometry, grid method or digital image correlation (DIC) [133]–[135]. They can provide quantitative measurement of displacement, which can be used to improve the performance of materials or structures. It is very helpful to research the failure mechanism of a welded sample as the complex microstructure within different regions of a weld varies the mechanical properties leading to complex deformation behaviour during loading.

2.7.1 Grid method

Grid method is used to measure in-plane displacement components of plastic deformation on specimens. It features a great balance between measurement resolution and spatial resolution [136]. In this technique, a grid of different size pitches is printed onto the surface of the specimens as shown in Figure 2.26. The printed grids are normally vertical and horizontal lines [137].

Various approaches have been used to apply grids onto the surface of materials. Electron beam [138], electro-polishing [139], electro-resist method [140], photolithography [141]and deposition [142] have been used to create micro-grids and paint spray has been used to create greater grids [143]. After creating the pitches, CCD cameras or scanning electron microscopes are used to capture images during the test process to obtained undeformed and deformed images of grids [136][138]. Lastly, the phase change caused by illumination is linked with displacement and strain fields to calculate the displacement and strain using different techniques mentioned by researchers [134] [136] [137]. However, the preparation of grid needs substantial work and procedures for obtaining the displacement and strain are complex.

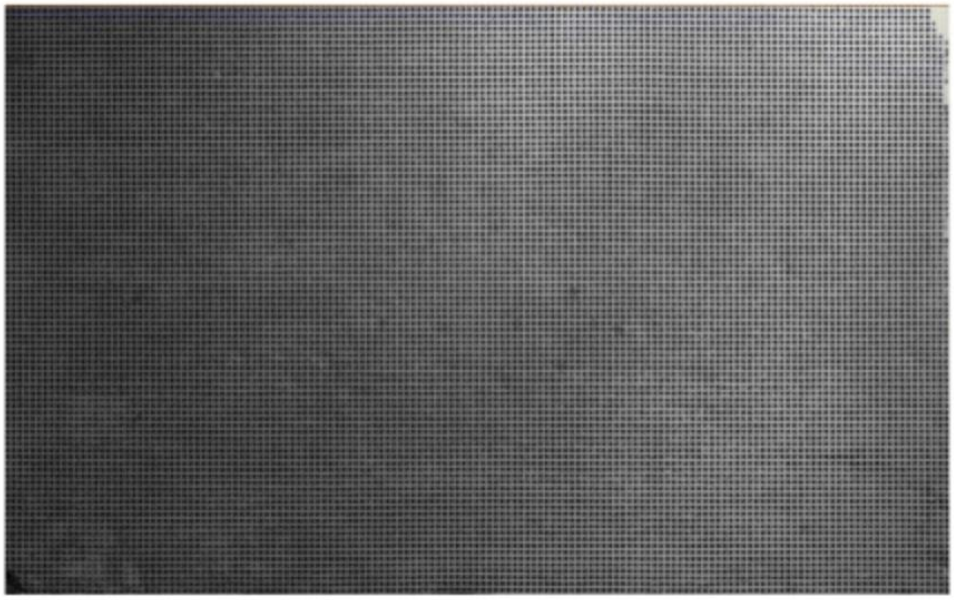

Figure 2.26. Sample printed with grid [143]**.**

2.7.2 Moiré interferometry

Moiré interferometry is a very popular technique for analysing strain field in mechanics [144]. Its development history has been concluded by the researchers [145]. It has very high sensitivity in measuring in-plane displacement but very low sensitivity in measuring out-of-plane displacement. Reliable strain distribution can be calculated based on in-plane displacement field [146]. It is superposition of two collimated laser beams to provide interference and fringes, Figure 2.27. Moiré interferometry has the same

principal with geometrical moiré method. The difference is that it has much greater grating frequency [147]. This created gratings is called a 'virtual' grating, to show the difference with the 'physical' grating in geometrical moiré [146]. Based on the gratings created by the laser beams, the strain distribution data can be calculated by the methods given by the researchers based on the deformed and undeformed grating images [144] [147].

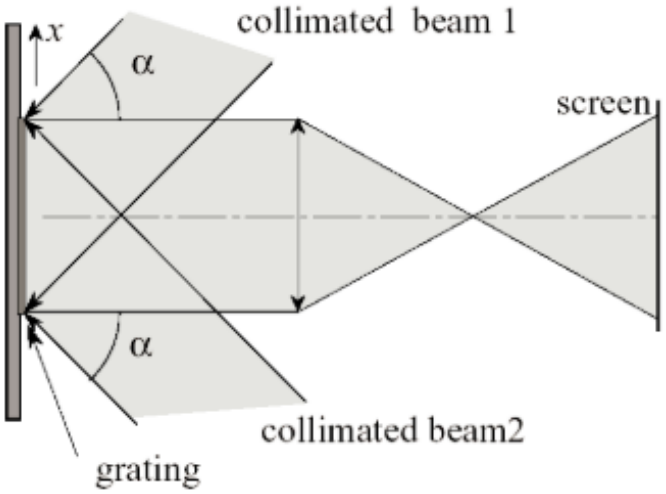

.

Figure 2.27. Schematic of moiré interferometry.

2.7.3 Digital image correlation

Digital image correlation (DIC) technique, which is a powerful and flexible tool, has been widely applied in experimental mechanics to measure full field displacement and strain variation [148]. It was first developed in the 1980s by researchers from the University of South Carolina and being continuously improved [149]–[155].

The principle of DIC is simple, it is basically tracking the change of pixels in a subset between deformed and undeformed images of the sample to obtain the displacement as shown in Figure 2.28 [156]–[159]. A subset is a sub-image used to discretize the image and track the displacement between deformed and undeformed images as shown in Figure 2.28.

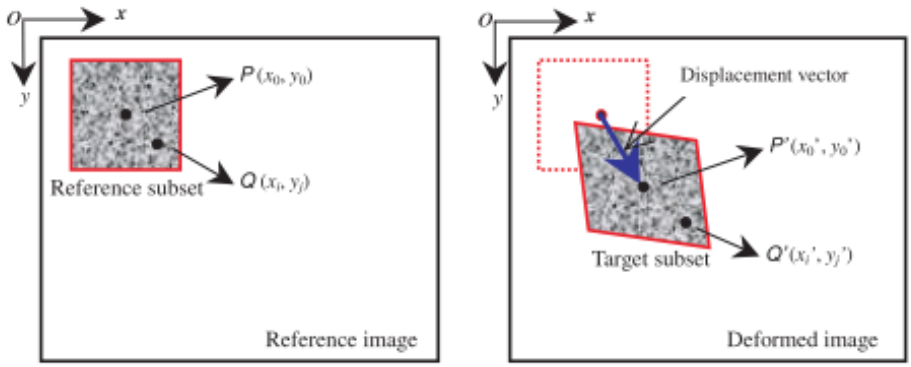

Figure 2.28. Schematic of a reference subset in undeformed image and a target subset in deformed image [148].

The DIC techniques can be implemented in 2D and stereo setups. 2D DIC is only capable of measuring in-plane displacement while 3D DIC can measure both in-plane and out-of-plane displacement [155][157].The set-up of apparatus of 2D-DIC system is shown in Figure 2.29 [148]. A charge-coupled device (CCD) camera is connected to the software. Sufficient illumination is provided by light sources close to the sample. Additionally, the specimen has to be perpendicular to the camera and the camera has to be horizontal.

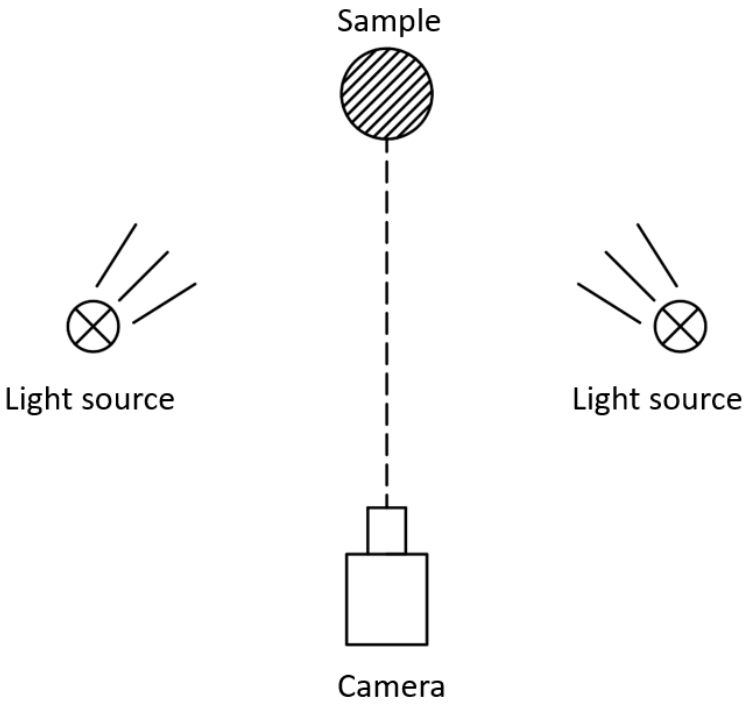

Figure 2.29. Schematic of Apparatus set-up of 2D-DIC system.

The 3D DIC system set-up is shown in Figure 2.30. The stereo angle, which

is the angle formed between two cameras and the sample, should be between 15° to 35° to ensure a good depth of focus [160]. Knowing the imaging parameter and orientation for each camera, a 3D space can be generated by the correlation algorithm for measuring out-of-plane displacement [161]. Although, the 3D DIC system can measure the out of plane displacement, the calculated strain is in-plane strain. The sample needs to be at the centre line of two cameras to ensure same distance between sample and two cameras in order to keep identical stereo angle.

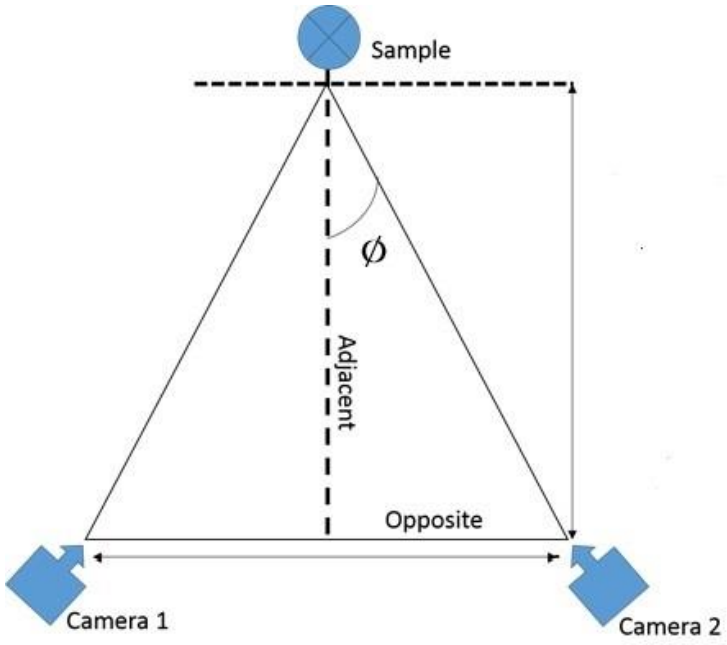

Figure 2.30. Schematic of the 3D DIC setup.

In order to implement an experiment using DIC, interest area of the sample needs to be properly prepared with random speckle patterns. The speckle can be prepared by various methods, such as stamps, spray cans, printer toner, fine powder and air brush [156], etc. The accuracy of DIC measurement can be influenced by many factors, such as quality of speckle pattern, camera lens distortion, shape functions, sub-pixel image registration algorithms and subset size [148] [162]–[167].

The speckle pattern needs to have high contrast, random distribution, isotropy, proper size and stability to ensure accurate DIC measurements [168]–[172].

In order to locate the reference subset between deformed and undeformed image, the correlation criterion is of great importance [173]. Three correlation criterions are commonly used, including cross correlation (CC) criterion, sum of square difference (SSD) criterion and Least Square Matching (LSM), these criterion evaluates the similarity between reference subset in undeformed image and subset of same size in deformed images in the area of interest to locate the target subset (reference subset in the deformed image) by determining the centre point P, shown in Figure 2.28, through calculating the correlation coefficient based on grey values of each pixel [173]–[175]. In this case the in-plane displacement vector could be obtained according to the position of P in reference and target subsets.

In cross correlation criterion, the location where has the maximum value of the cross-correlation coefficient is used to determine location of target subset in the deformed image [174]. CC criterion can be classified into four types, including cross-correlation (CC) criterion, zero-mean cross-correlation (ZCC) criterion, normalised cross-correlation (NCC) criterion and zero- mean normalised cross-correlation (ZNCC) criterion. CC is the basic form having the lowest accuracy while NCC and ZCC are improved forms which can bear the scale change or offset change of intensity of the deformed images. ZNCC is the most recommended form which is insensitive to offset and scale changes of the intensity of deformed images with high accuracy [176]–[179].

SSD criterion [176] can also be classified into four types, including sum of square difference (SSD), zero-mean sum of square difference (ZSSD), normalised sum of square difference (NSSD) and zero-mean normalised sum of square difference (ZNSSD). Unlike CC criterion which is matching the speckle pattern having the maximum CC coefficient, SSD is matching the subset in the deformed image having the minimum coefficient. Similar with CC criterion, ZNSSD is the most recommended form which is insensitive to offset and scale changes of intensity of deformed images [176][177] .

Least Square Matching is according to minimize the squared differences of the grey values of the subset in the correlated windows between deformed and undeformed images [180]–[182]. Both radiometric (brightness and contrast)

and geometric (translation, rotation or complex geometric transformation) corrections are considered which give Least Square Matching high accuracy [174][183].

Shape function is used to determine the deformation mode of reference subset in the deformed images, in other word to determine the position of an arbitrary point Q around the center point P in the target subset, Figure 2.28. Transformation matrix is used to determine plastic deformation of the subset, including zero-order shape function (pure translation) in equation 2.20, first-order shape function (translation, rotation, shear and normal strain) in equation 2.21 and second-order shape function (considering strain gradients) size in equation 2.22. First-order shape function can produce reliable results in low gradient deformation field with large template size while second-order shape function produces reliable results in high gradient deformation field with large template size [130] [131].

$$\begin{bmatrix} x' \\ y' \end{bmatrix} = \begin{bmatrix} 1 & 0 & u \\ 0 & 1 & v \end{bmatrix} \begin{bmatrix} x \\ y \\ 1 \end{bmatrix}$$

Equation 2.20

$$\begin{bmatrix} x' \\ y' \end{bmatrix} = \begin{bmatrix} 1+u_x & u_y & u \\ v_x & 1+v_y & v \end{bmatrix} \begin{bmatrix} x \\ y \\ 1 \end{bmatrix}$$

Equation 2.21

$$\begin{bmatrix} x' \\ y' \end{bmatrix} = \begin{bmatrix} \frac{1}{2}u_{xx} & u_{xy} & \frac{1}{2}u_{yy} & 1+u_x & u_y & u \\ \frac{1}{2}v_{xx} & v_{xy} & \frac{1}{2}v_{yy} & v_x & 1+v_y & v \end{bmatrix} \begin{bmatrix} x^2 \\ xy \\ y^2 \\ x \\ y \\ 1 \end{bmatrix}$$

Equation 2.22

where (x, y) is the local coordinate of the center of the undeformed subset, (x', y') is the coordinate of the center of the subset after deformation, u and v are the displacement of the center the subset, v_x, v_y, u_x and u_y are the corresponding first order displacement gradients, v_{xx}, v_{xy}, v_{yy}, u_{xx}, u_{xy} and u_{yy} are the corresponding second order displacement gradients.

Subset size has been found to be the most important factor in measurement accuracy of DIC. It is due to that subset size directly determine the area of subset being utilized to trace the displacement change between deformed and undeformed images and needs to be manually selected by users in plenty of DIC softwares [148]. The subset size is supposed to be large enough to obtain enough information to make the subset distinguishable compared with other subsets, however, small deformation is neglected which leads to large errors. A small subset size can better capture the underlying deformation, but might not be distinctive enough from other subsets [148][184]. Normally, a subset containing around 3-5 speckles is considered to be optimum [185].

The lens distortion is very common when applying wide-angle lens or zoom lens into the DIC system. It can induce measurement errors on spatial position of measured points and displacement [167]. Subpixel image registration algorithms is used to measure sub-pixel displacement change between deformed and undeformed images in order to further improve the accuracy of DIC measurement [186]. Several subpixel registration algorithms have been developed by researchers, such as correlation coefficient curve-fitting [187][188], gradient-based methods [189][190], double Fourier transformation [191], Newton-Raphson iteration [159], genetic algorithms [192][193] and artificial neural network methods [194]. These algorithms can enhance the measurement accuracy to subpixels from 0.01 to 0.5 pixel [186].

Some work has been done to assess the accuracy of DIC technique under macro or micro scales showing that a reasonable accuracy is achieved. Chu et al. compared 2D strain results with experimental mechanics and reported that the errors in the deformation determination were less than 10% for strain values ranging from 0.01 to 0.03 [150]. Wang compared strain measurements between 2D DIC and extensometer technique and found that DIC technique provides accurate results and more strain information (major and minor strain) [195]. Quantitative error assessment was also made in stereo based deformation measurements showing that the experimental measurements were in excellent agreement with theoretical predictions [196]. Wang et al. studied the error of DIC technique under SEM and found that tiny errors were

obtained (about 2 pixels difference) [197]. A quantitative error analysis was done by Ghadbeigi et al. between DIC and micro grids techniques at microstructure scale, results showed that DIC technique is appropriate to measure local strain at microstructure scale as the error values was between 0% and 34%, which is accepteable, compared with grid method [138].

DIC technique was selected as full field strain measurement method in this project and Lagrange strain tensor was used to obtain the strain distribution as it is an appropriate strain tensor used in calculating large deformation [198]. Unlike grid method or moiré which need substantial work to get the relevant information about displacement and can only be applied in 2D displacement measurement [133], although, DIC technique needs proper surface preparation and careful calibration, it is the most popular technique for full field displacement and strain measurement due to its simple experimental setup, simple post-process operation, high accuracy and wide range of applicability for diverse materials and structures [156]. Additionally, it can be applied into measuring both in-plane and out-of-plane displacement.

2.8 Strain tensors

It is essential to select an appropriate strain tensor to compare the strain values obtained from DIC technique, which is due to the fact that different strain tensors could have different performance at small strains or large strains.

There are several strain tensors used in DIC software, including Green-Lagarangian, Engineering. Henchky strain and Euler-Almansi strain tensors. These four strain tensors are known as Seth-Hill family [199].

Green-Lagarangian strain tensor is a finite strain measure describing the difference between a given displacement and a rigid body displacement locally [199], which is used to calculate large strains. The lagrangian strain formulation is as follows

$$\mathbf{E} = \frac{1}{2}(\boldsymbol{C} - \boldsymbol{I})$$

$$\mathbf{C} = \boldsymbol{F}^T\boldsymbol{F}$$

Where $\boldsymbol{F}$ is the deformation gradient and $\mathbf{C}$ is right Cauchy-Green

deformation tensor.

Engineering strain $\mathbf{E} = \boldsymbol{C}^{1/2} - \boldsymbol{I}$ is also known as Cauchy strain, which is a ration of total length to initial length. It usually used to measure small strains and can be compared to the strain obtained by strain gauges[199].

Hencky strain tensor $\mathbf{E} = \frac{1}{2} ln\boldsymbol{C}$ is also known as true strain tensor, it might have problem in larger strain measurement and severe shearing[199].

Euler-Almansi strain tensor $\mathbf{E} = \frac{1}{2}(\boldsymbol{I} - \boldsymbol{C}^{-1})$ is also used to measure finite deformation, which is obtained based on Eulerian coordinate. However, it could change under rigid body motion and affect the accuracy of strain measurement[200].

In conclusion, Green-Lagarangian strain tensor was selected to achieve the strain from DIC technique.

2.9 Summary

The failure behaviour of the spot welds of low or high strength steels can be well understood due to the simple microstructure in BM. However, for advanced high strength steels, the microstructure is more complex and consists of several phases such as martensite, bainite and ferrite, which affect the mechanical properties of the spot welded section. Dual-phase steels are the most common type of AHSS and have high strength and high ductility that makes them desirable for crash resistance and weight reduction, thus they are very useful in automotive industry [201]. Several researches were conducted on spot welds in several grades of dual-phase steels including DP450, DP590, DP780 and DP980 steels as mentioned above, effect of steel grades, welding current and loading conditions on failure modes of spot weld was studied according to failed samples. However, there is no researches were carried out with respect to the knowledge of failure mechanisms linked to local deformation evolution and microstructural morphologies of different regions of welds for advanced automotive steels, and especially for high strength AHSSs. This is important since a better and more comprehensive understanding of failure mechanisms can be achieved through analysing how the deformation evolves within each region, which contains different

microstructure, of weld section through the test process. The achieved results could help improve the performance of spot weld and provide data for future FE model development.

In the following chapter, new sample geometries and new experimental methods will be developed to study how deformation evolution and microstructure of the weld with different welding currents and loading conditions influence the failure behaviour of spot welds of DP1000 and a type of low carbon steel (reference material) under macro and micro scales with help of DIC technique. Microhardness test on different sections of spot weld will be made to characterise the mechanical properties. Microstructural morphology and fractography analysis will be conducted to study the effect of microstructure on failure mechanisms of spot welds. The obtained results will be correlated with each other to analyse the deformation and failure behaviour of the welds and effect of welding current on failure mechanisms of spot weld with applied different loading conditions.

3 METHODOLOGY

As stated in the chapter 2, to the best of author' s knowledge, deformation evolution and its relation with and microstructure have been neglected by previous researches, which could be important to achieve a better understanding of the failure mechanisms of welds. This chapter aims to obtain deformation and damage evolution of the weld section and correlate it with relevant fracture mode and microstructure in order to analyse the failure mechanisms of spot weld with applied various weld currents and loading conditions.

3.1 Design of new sample geometries

A dual phase steel (DP1000) and a low carbon steel (reference material) with a sheet thickness of 1.2mm were used in this project with the given microstructural morphology of Figure 3.1. Martensitic grains are the white phase and ferritic grains are the darker regions in the micrograph of DP1000, Figure 3.1a, and a pure ferritic microstructure is observed in low carbon steel, Figure 3.1b. Standard tensile tests based on ASTM E8 standard [46] were conducted to determine the mechanical properties of the as received materials, Table 3.1.

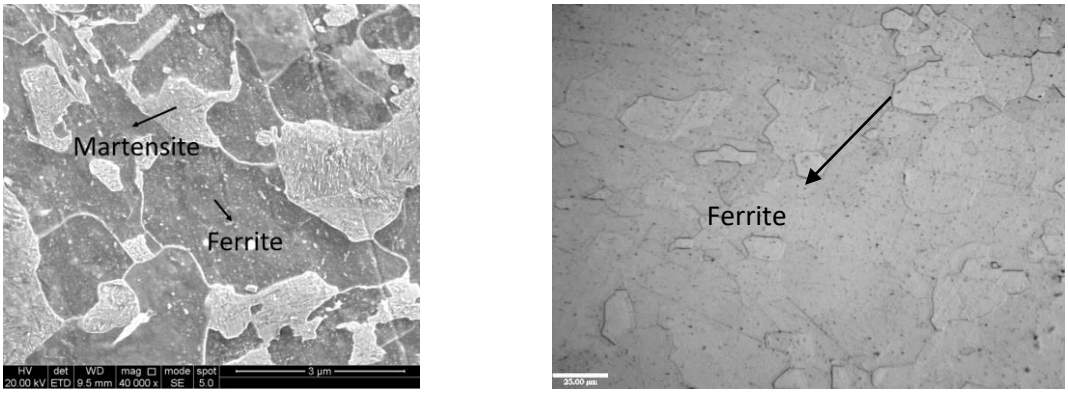

(a) **(b)**

Figure 3.1. (a)Microstructure of the DP1000 sheet used showing a ferritic-martensitic structure with the bright phase to be a martensite grain and the darker phase to be a ferrite grain and (b) microstructure of the low carbon steel sheet used showing a pure ferritic strcuture.

Table 3.1. Mechanical properties of the materials.

	YS(MPa)	UTS(MPa)	Elongation (%)
DP1000	690	1048	16.9
Low carbon steel	155	276	53.1

As explained previously, developing new sample geometries was necessary in order to reveal the deformation and damage process in the welds and it was needed to be able to correlate the deformed microstructure with them. Therefore, to design the macro samples with half welds (sectioned through the centre of the weld) was useful. In this case, the deformation and damage evolution could be correlated with the microstructural morphology of the weld. In addition, it was helpful to view the variation of microstructure in weld section during the test process. In hence, micro sample which can be tested under SEM should also be considered. As mentioned at end of section 2.5.3, DIC technique was used to analyse the deformation and damage evolution, however, only 2D DIC could be used to analyse the SEM images considering the existed testing equipment, indicating that too much out-of-plane displacement could lead to

large error on the results. Additionally, as the maximum principal strain obtained was in 2 dimensions, it was crucial to reduce the out-of-plane displacement so that 2D maximum principal strain could be an indicator of failure. Thus, a double weld setup for macro and micro samples was considered to achieve a similar stress state and to reduce the out-of-plane displacement within the weld section.

A set of new sample geometries, Macro CP, Micro CP, TS and U-shape samples, was designed for the sake of investigating deformation and failure mechanisms that traditional samples are not able to get access to, as reported in literatures [104], [106], [108], [202], and investigating the possibility of implementing in-situ quantitative measurement of local deformation fields within the weld section.

The new test geometries were developed based on standard tensile-shear (TS), coach-peel (CP) and cross tension (CT) samples [105][107][114], wherein double half welds were produced at the edges instead of placing a single weld at the middle of the section, as shown in Figure 3.2. A Finite Element (FE) parametric study was carried out using Abaqus/Explicit package in order to determine the ideal dimension of the samples to satisfy the stress state for the required failure modes and to ensure the maximum plastic deformation occurs at the free surface of the nugget along the polishing line on the onset of fracture. In order to continuously record the deformation and damage process of samples, DIC technique was selected. It is critically important that maximum plastic deformation and failure occurs within the field of view where the strains can be calculated than any point in the material beneath the surface as DIC technique is based on recording images of deformed samples.

The material properties of the weld section and the base material for the FE simulation were selected from published literatures [203]–[205]. The Gurson-Tvergaard-Needleman (GTN) model was implemented as the failure criteria according to the reported results of coach-peel and tensile-shear tests shown in the literatures [206][207]. The parameters of GTN model were obtained from the work of author' s Master project, which focused on simulation of damage of spot weld in DP1000, and listed in table 3.3. Although,

the parameters of HAZ and nugget could be different for this project as the welding parameters are different, it is important to note that the FE simulation was done to perform a qualitative study for the dimensional analysis of the samples rather than prediction of failure in the researched materials. A C3D8R element was selected and the elements of the weld section were refined to get a more accurate result. The loading conditions can refer to Figure 3.8. Figure 3.3 shows the predicted strain field before crack initiation in the designed geometries wherein a mesh refinement was applied around the weld nugget and the maximum plastic strain was observed at the free surface of TS sample (Figure 3.3a), Macro-CP (Figure 3.3b) samples and U-shape samples(Figure 3.3c align the cut section. The final designed geometries are in Figure 3.2 while all dimensions of all samples are in Table 3.2).

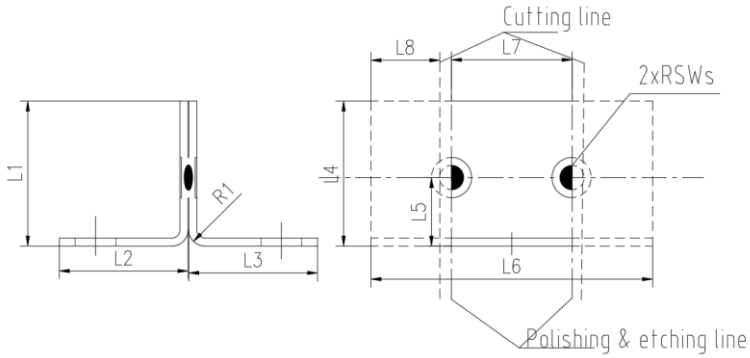

(a)

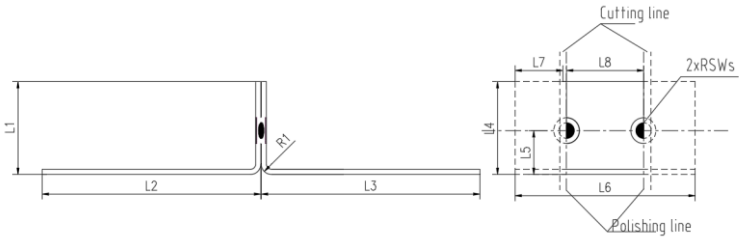

(b)

Figure 3.2. Geometry of samples, (a) micro-CP sample, (b) macro-CP sample, (c) TS sample and (d) U-shape sample.

Continue to next page.

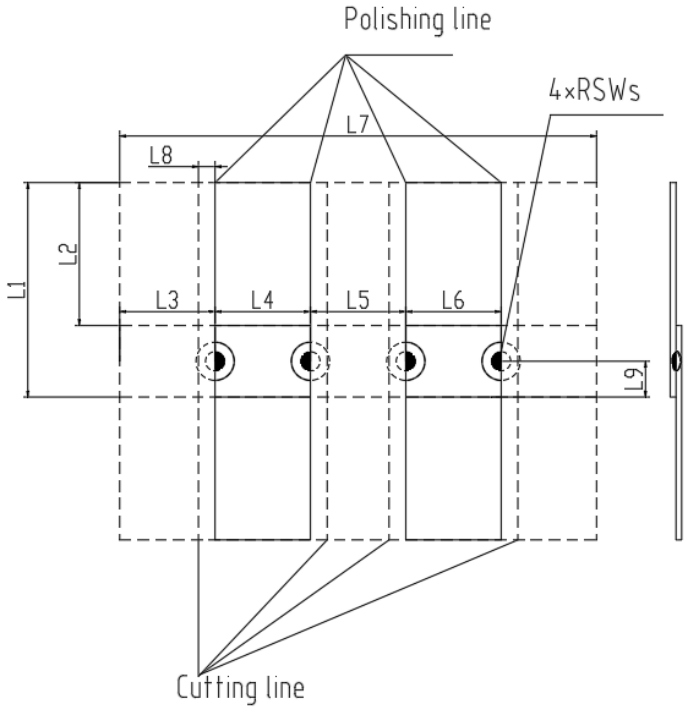
Polishing line
4×RSWs
L7
L8
L2
L1
L3
L4
L5
L6
L9
Cutting line

(c)

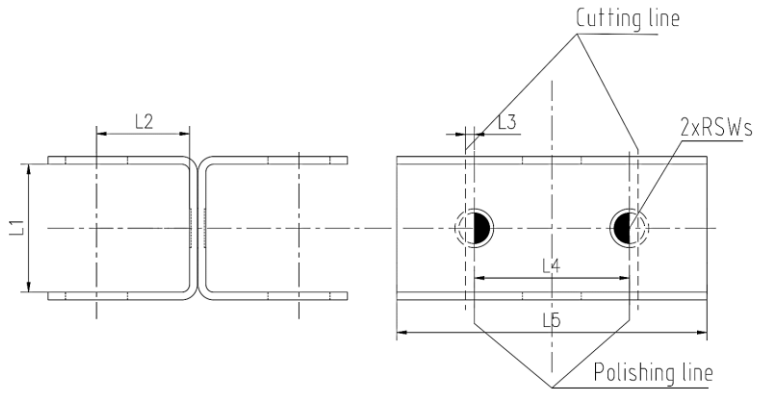
Cutting line
L2
L3
2xRSWs
L1
L4
L5
Polishing line

(d)

Table 3.2. Dimension of all samples.

	Dimensional parameters (mm)									
Sample geometry	L1	L2	L3	L4	L5	L6	L7	L8	L9	R1
Micro-CP	19	14.5	14.5	19	10	45	15	14	-	4
Macro-CP	23	40	40	23	12	50	14	20	-	4
TS	45	30	20	20	20	20	100	1	7.5	-
U-shape	18	12	1	20	40	-	-	-	-	-

Table 3.3. Parameters of GTN model for each region of spot weld in DP1000.

	q_1	q_2	q_3	f_N	s_N	ε_N	f_C	f_F
BM	1.5	1	2.25	0.02	0.11	0.35	0.15	0.25
HAZ	2.7	1	7.29	0.02	0.11	0.35	0.25	0.3
Nugget	2.7	1	7.29	0.02	0.11	0.35	0.35	0.4

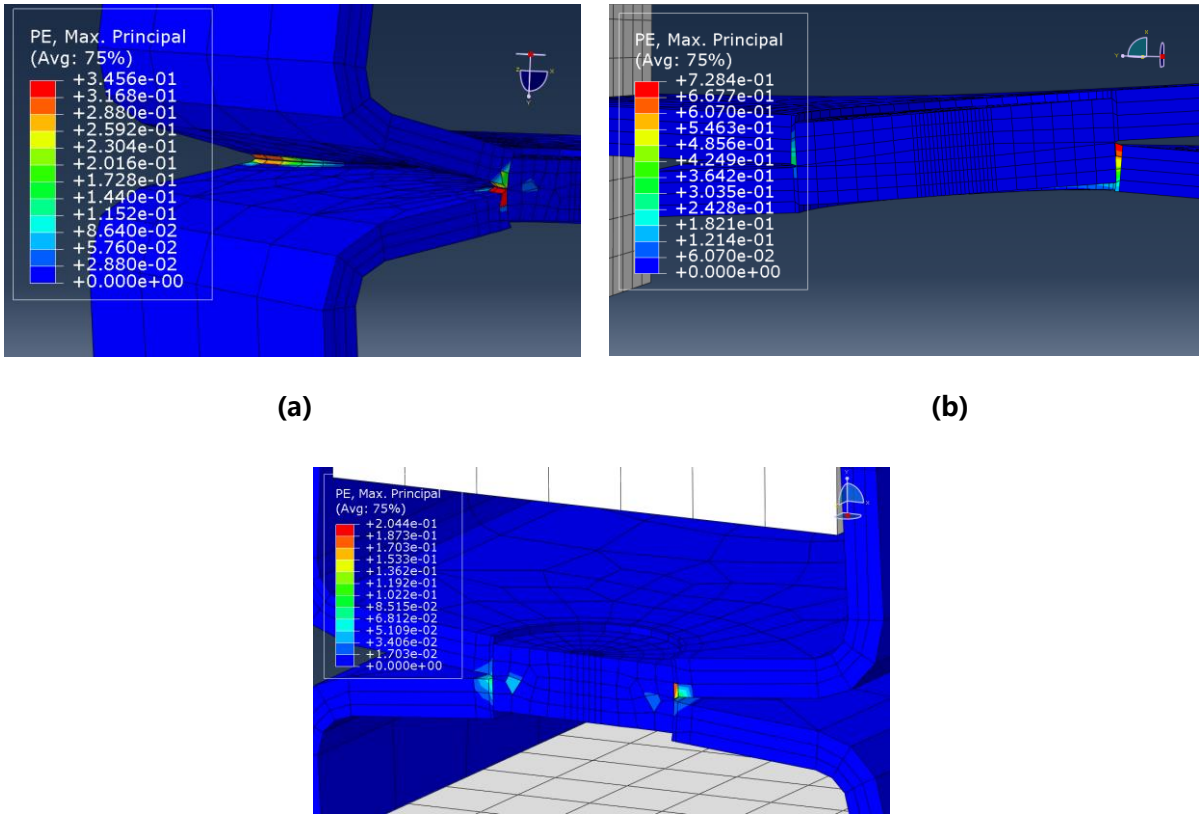

Figure 3.3. Maximum principal strain distribution, (a) macro-CP , (b) TS and (c) U-shape samples.

3.2 Sample fabrication

A sheet cutter and a bending machine were used to produce macro and micro CP samples and TS samples. A bespoke bending rig was designed to produce U-shape samples, Figure 3.4a. Welding jigs were designed to weld Micro and Macro CP samples, TS samples and U-shape samples, Figure 3.4b. This provided a good consistency in the dimensional accuracy of the parts since any variations of the selected parameters in Figure 3.2 could affect the stress state and consequently the observed failure modes. The samples were welded using a Kawasaki ZX165U welding Robot at The Welding Institute (TWI), shown in Figure 3.5.

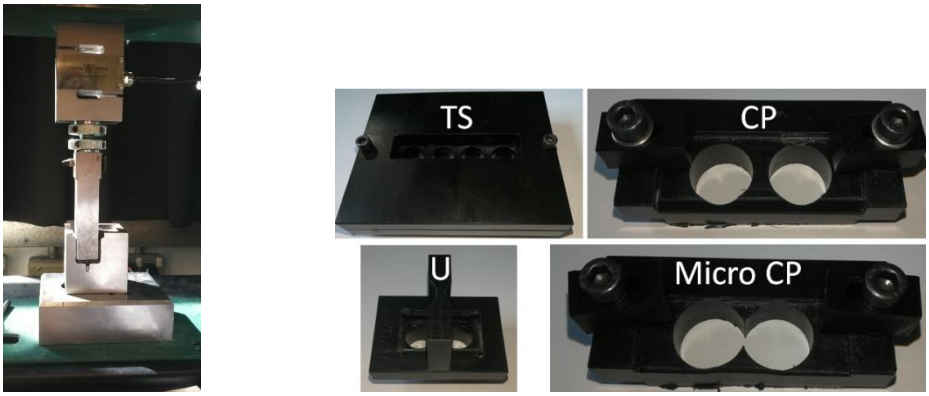

(a) **(b)**

Figure 3.4. (a) Bending rig for manufacture U-shape samples and (b) welding jigs for each type of sample geometries.

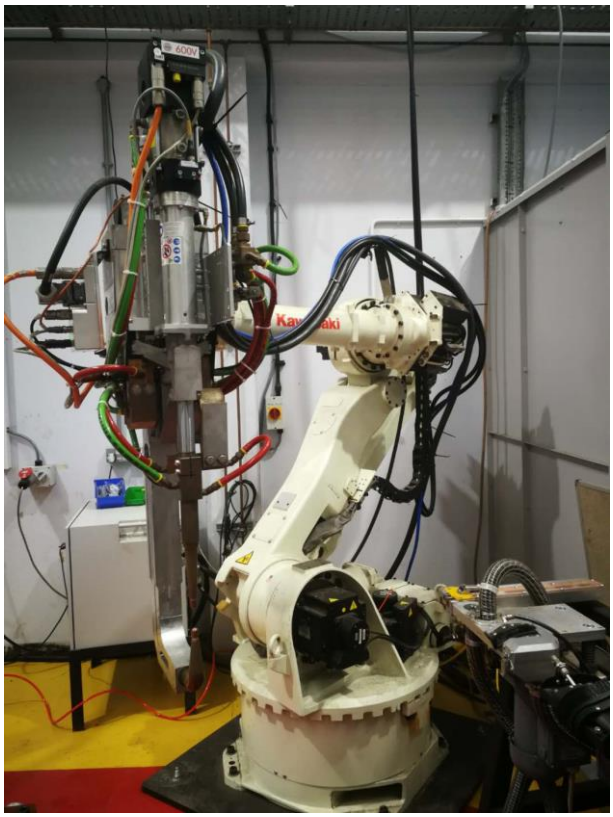

Figure 3.5. Kawasaki ZX165U welding Robot.

For the macro scale samples (TS, CP and U), the welding parameters were selected and kept constant except varying welding current according to the data sheet given by TATA Steel and standard BS EN ISO 18278 [208] for the given sheet thickness 1.2mm, in order to avoid any unexpected welding issues

affecting the weld quality, such as defects inside the nugget, expulsion (the ejection of molten metal during welding), etc. Additionally, in order to make the samples failed via different failure modes to investigate the failure mechanisms, a critical nugget size required to obtain PF mode was calculated according to standard ANSI/AWS/SAE D8.9-97 [209] which is $4\sqrt{t}$ and t is the thickness of sheet. A critical nugget size of around 4.3mm was calculated. Welds of larger nugget sizes were obtained to ensure that different failure modes can be achieved. Considering the standards ANSI/AWS/SAE D8.9-97 and BS EN ISO 18278, three levels of welding current were determined. The nugget sizes of low carbon steel samples were made same with DP1000 samples as reference. The selected welding parameters and achieved nugget diameters of DP1000 and low carbon steel samples are given in Table 3.4 and 3.5 and several samples for each type were made to evaluate variations in the results. Moreover, Three repeats of each set were done.

Table 3.4. Welding parameters of TS, macro-CP, U-shape and micro-CP samples in DP1000.

Sample	Welding force, kN	Welding current, kA	Welding time/ms	Holding time/ms	Nugget size/mm
DPTS-L	4	5.5/5.7	320	200	3.8
DPTS-M	4	6.5/6.7	320	200	4.8
DPTS-H	4	7.7/7.9	320	200	5.9
DPCP-L	4	5.5/5.7	320	200	3.8
DPCP-M	4	6.5/6.7	320	200	4.8
DPCP-H	4	7.7/7.9	320	200	5.9
DPU-L	4	5.5/5.7	320	200	3.8
DPU-M	4	6.5/6.7	320	200	4.8
DPU-H	4	7.7/7.9	320	200	5.9
DPMiCP-L	4	5.5/5.7	320	200	3.8
DPMiCP-M	4	6.5/6.7	320	200	4.8
DPMiCP-H	4	7.7/7.9	320	200	5.9

Table 3.5. Welding parameters of TS, macro-CP, U-shape and micro-CP samples in low carbon steel.

Sample	Welding force, kN	Welding current, kA	Welding time/ms	Holding time/ms	Nugget size/mm
LCTS-L	4	6.1/6.3	320	200	3.8
LCTS-M	4	7.4/7.6	320	200	4.75
LCTS-H	4	7.7/7.9	320	200	5.85
LCCP-L	4	6.1/6.3	320	200	3.8
LCCP-M	4	7.4/7.6	320	200	4.75
LCCP-H	4	7.7/7.9	320	200	5.85
LCU-L	4	6.1/6.3	320	200	3.8
LCU-M	4	7.4/7.6	320	200	4.75
LCU-H	4	7.7/7.9	320	200	5.85

After welding, the samples were cut along the predefined lines (indicated through dashed lines in Figure 3.2) using Wire-EDM, followed by manual mechanical polishing (indicated in Figure 3.2) to remove the thermally affected layer generated by the Wire-EDM process. As the thickness of thermal affected zone is in micron level [210][211], thus the samples were cut up to the cutting line and around 1mm material was left for polishing to remove the affected zone. Grinding paper was used to prepare the macro samples, while grinding paper and water based diamond polishing suspension were used to prepare the micro samples in order to reveal the microstructure. The sample dimensions were continuously measured during polishing stage to ensure the cut section passes through the centreline of the weld and remaining weld nuggets were equal in size at both sides of the sample. Examples of unprepared and prepared samples for each type are shown in Figure 3.6. The sizes of welds of all tested samples were measured using an optical desktop microscope shown in the results section.

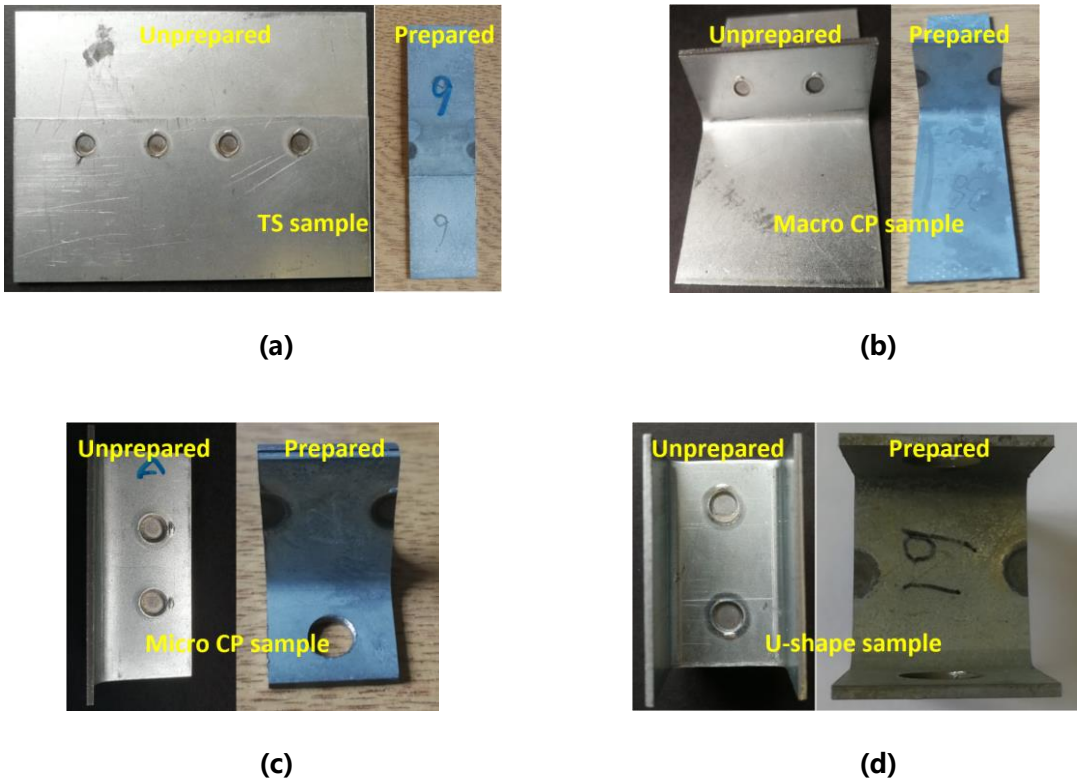

Figure 3.6. Examples of unprepared and prepared samples of each type, (a) TS samples, (b) macro CP samples, (c) micro-CP samples and (d) U-shape samples.

3.3 Deformation and failure analysis at macro scale

In order to clearly reveal deformation and damage evolution of the weld section of the samples, an optical DIC system was used combined with the macro-scale experiments (Macro CP， TS and U-shape samples) at the quasi-static loading rate of 1mm/min using a servo-electric tensile testing machine in order to avoid the effect of inertia force. The setup of experiment is shown in Figure 3.7, as out-of-plane displacement was observed in some pre-tests, a 3D stereo setup was used to avoid the effects on the results. However, as speckle patterns needed to be performed onto free surface of weld section which might cover some information regarding to each region of the weld section, in order to correlate the deformation and damage evolution with the corresponding regions of the weld section, tests of samples without paints were also conducted. Three samples with painted speckle patterns for each welding current of TS, macro CP and U-shape samples were tested to

determine the variation of the results and to obtain high quality results.

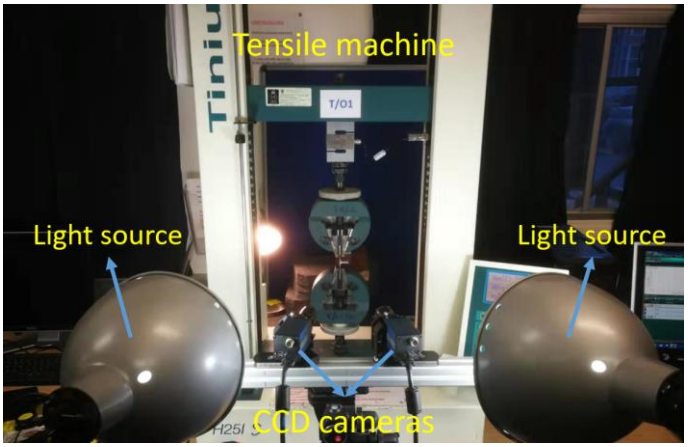

Figure 3.7. 3D stereo DIC system set-up.

In order to achieve a high quality speckle pattern, which is one of the most significant factor of deformation characterisation using DIC, an air-brush spray with a fine nozzle was used. The speckle patterns were generated on the cut surface of the samples wherein the weld zones are exposed, an example of each type of sample is shown in Figure 3.8. VIC 3D DIC system from Correlation Solutions, which has a normalised sum of squared difference correlation criteria [212], was used for the image acquisition and analysis of deformed images as the criterion is not sensitive to scale change of intensity in deformed images. The correlation criteria is shown in the following equation

$$\mathrm{NSSD} = \sum \left(\frac{f_i}{\sqrt{\sum f_i^2}} - \frac{g_i}{\sqrt{\sum g_i^2}}\right)^2$$

Equation 3.1

Where f_i and g_i are the grey values of the ith pixel in the reference subset.

An image acquisition rate of 4Hz was used and about 240 images/mm were taken per test, which is sufficient to capture the deformation variation under a quasi-static loading condition. To evaluate the effects of DIC parameters and determine the proper subset size, a sensitivity analysis was also performed to assess potential errors in strain calculations, including a systematic error analysis and subset size dependency analysis. Specifically, subset size dependency analysis was carried out in relation to maximum principal strain by decreasing the subset size from a large value and by

checking the convergence of the value of maximum principal strain, meanwhile keep the step size as one third of subset size as a smaller step size could increase the noise on the strain field and an optimal step size is between 25% and 50% of the subset size recommended in the literatures [213][214]. To analyse the systematic error of strain measurement, ten static images before testing were used as there is no deformation in the area of interest. The subset sizes were also checked to ensure there were enough random features (around 5 speckles) within the selected subsets as stated in literature [185]. The DIC parameters were then determined as shown in Figure 3.8, at the region of interests. The Lagrangian strain tensor components were extracted from the analysed images giving the expected large deformation of the material.

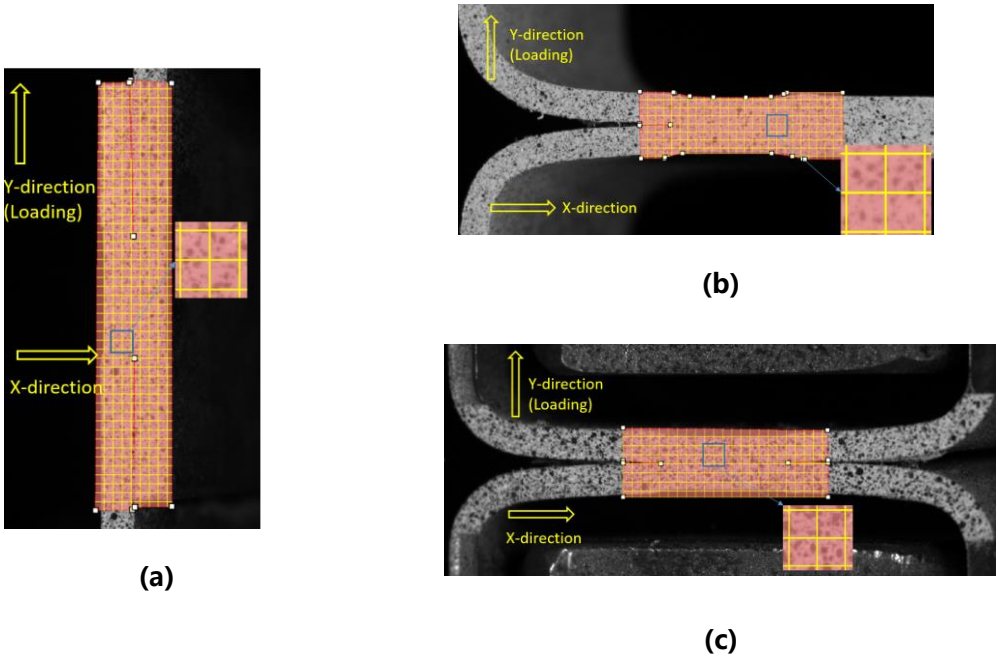

Figure 3.8. (a) TS samples, (b) macro-CP samples and (c) U-shape samples with the generated speckle patters showing the size of the selected subsets together with the loading direction.

3.4 Microstructural deformation and failure analysis

To determine the local deformation distribution within the microstructure of the weld nugget, Micro-CP samples (Figure3.2a) were fabricated based on the previously described procedures to achieve a mirror polish at the cut

sections of the welds[215]. The polished surfaces were then chemically etched with 2% Nital Solution [215] in order to reveal the microstructure caused by the welding process, Figure 3.9. In-situ experiments were conducted using 5 kN Deben MICROTEST tensile stage inside the chamber of a CamScan Scanning Electron Microscope (SEM) and deformed microstructures were continuously observed during the test, Figure 3.10. The samples were loaded at a rate of 0.2mm/min and stopped loading every 0.2mm for imaging, consecutive micrographs were taken at a magnification of 50x in order to include the area of interest in the field of view as shown in Figure 3.9, including the weld nugget and HAZ. It should be noted that the images were taken after around 3 minutes relaxation of the stopped stage to avoid the effect of stress relaxation[216] which might lead to deformation within the area of interest. The obtained micrographs were analysed by DIC technique in which the random patterns developed by the etched microstructures were used as the speckle pattern for the image correlation [1]. Similar method with macro test in section 3.3 was used to analyse the errors and determine the proper subset size. Beam shift error, which is random and time dependent, occurs due to the electron beam drift and could be larger at higher magnification[217]. It has been reported that error of absolute strain value due to beam shift is small enough (0.004) to be neglected under a relatively low magnification (500x)[138]. Since the testing magnification was set to 50x and the plastic deformation was studied which had large strain value, the error could be small enough to be ignored. In such way, the full field strain evolution was obtained to analyse the effect of microstructure on failure mechanisms of the weld section.

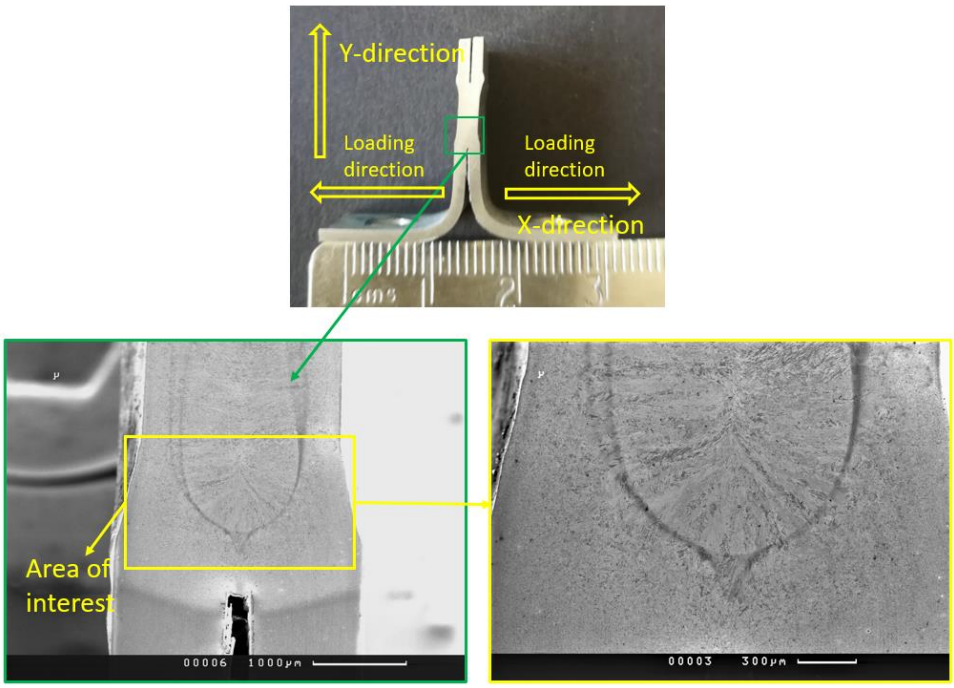

Figure 3.9. Area of interest including the crack initiation and propagation.

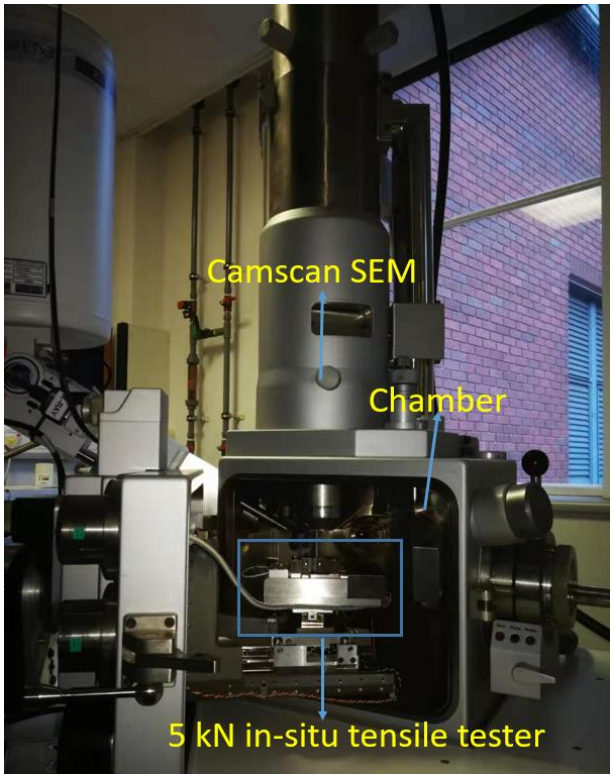

Figure 3.10. Set-up of in-situ testing of micro-CP samples.

3.5 Microhardness characterisation

In order to analyse the influence of welding current on hardness profile of

BM, HAZ and nugget for welded samples, Vickers microhardness test was implemented on the samples with applied low, medium and high welding current using a Struers DuraScan micro/macro hardness tester. The samples made of DP1000 and low carbon steels were cold mounted and mirror polished before the hardness measurement to minimise the effects of surface smoothness on hardness measurement, examples of two types of materials are shown in Figure 3.11. Indents were performed on the cut surface of non-tested samples. The corresponding parameters of hardness measurement were selected (Table 3.5) to obtain a certain number of indents in the welded regions (BM, HAZ and nugget) according to the minimum spacing (3.5*diagonal length of the indent) between two indents specified in standard E92-17 to ensure a sufficient number for comparison [37].

Table 3.6. Parameters of Vickers micro hardness test.

Material type	Indent force/N
DP1000	0.5
Low carbon steel	0.2

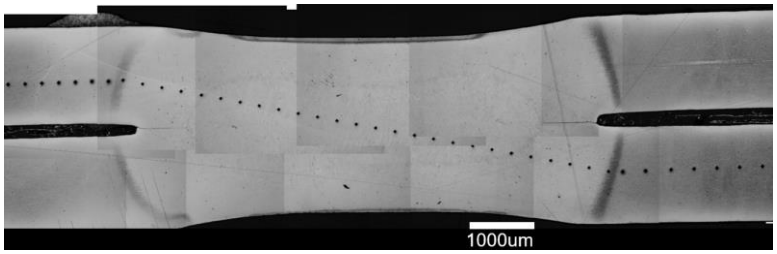

(a)

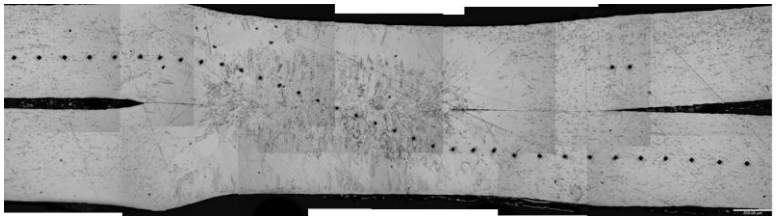

(b)

Figure 3.11. Examples of sample preparation for Vickers micro hardness indentation and indents location on the sample surface, (a) DPCP and (b) LCCP samples.

3.6 Fractography and microstructural morphology analysis of the spot weld

Fractography, morphology analysis of broken TS, macro-CP and U-shape samples of the tested materials (DP1000 and low carbon steel) were conducted using a Nikon optical microscope and Inspect F50 Scanning Electron microscope, in order to investigate the effect of microstructure of weld section on the fracture process and fracture surfaces of the samples.

Metallography analysis on the free surface of the non-tested samples was conducted to characterise the microstructure within BM, HAZ and nugget of the weld and study the effects of microstructure on the failure.

To conduct the Fractography analysis of the failed welded sample. One sample of samples in each type and each welding current in DP1000 and low carbon steel was selected. The fracture surfaces of these samples were cleaned in an ultrasonic bath using isopropanol, and then dried by dryer, in order to avoid damage and oxidation to the surface, and microscopic images were taken using SEM with different magnifications to clearly identify the features on the fracture surface, in such way to study the fracture mechanisms.

These samples were then cold mounted, slightly grinded to remove the deformed sites, polished and etched with 2% Nital solution to reveal the metallic phases, Figure 3.12. Carbon coating was applied to the etched sample to eliminate the charging effects [218]. Microscopic images of the several positions where along the crack path were captured with different magnifications using optical microscope and SEM to clearly study the correlation between microstructural morphology and the fracture surface to better understand the fracture mechanisms.

Finally, the obtained results were correlated with measured strain distribution maps as well as deformation evolution of welded samples to investigate the possible failure mechanisms in relation to the applied welding currents.

(a)

(b)

(c)

Figure 3.12. Etched (a) TS, (b) macro-CP and (c) U-shape samples.

4 RESULTS AND DISCUSSION

According to the methods proposed in section 3, results were obtained based on the developed samples. The welds were characterised by comparing the weld size, the microstructure and corresponding microhardness of each region of the weld section. Subsequently, the results of deformation and damage evolution as well as fracture surface and corresponding microstructural morphology were presented for TS, CP and U-shape samples in DP1000 and low carbon steels.

4.1 Weld characterization in DP1000

4.1.1 Weld size measurement

Weld sizes of TS, CP and U-shape samples were measured using Dinolight desktop microscope before experiments. Due to the difficulty of measuring the size of nugget without destructing the whole weld, the radius of two weld indents upon the welds as shown in Figure 4.1 were measured for DPTS, DPCP and DPU samples after sample preparation, instead of the nugget size. The measured radius of the welds in the produced samples was found to vary between ± 0.04mm in each groups as shown in Figure 4.1. This small variation is believed to not affect the failure and deformation of the welded samples helping to avoid the possible effect of unsymmetrical loading on two welds in the samples.

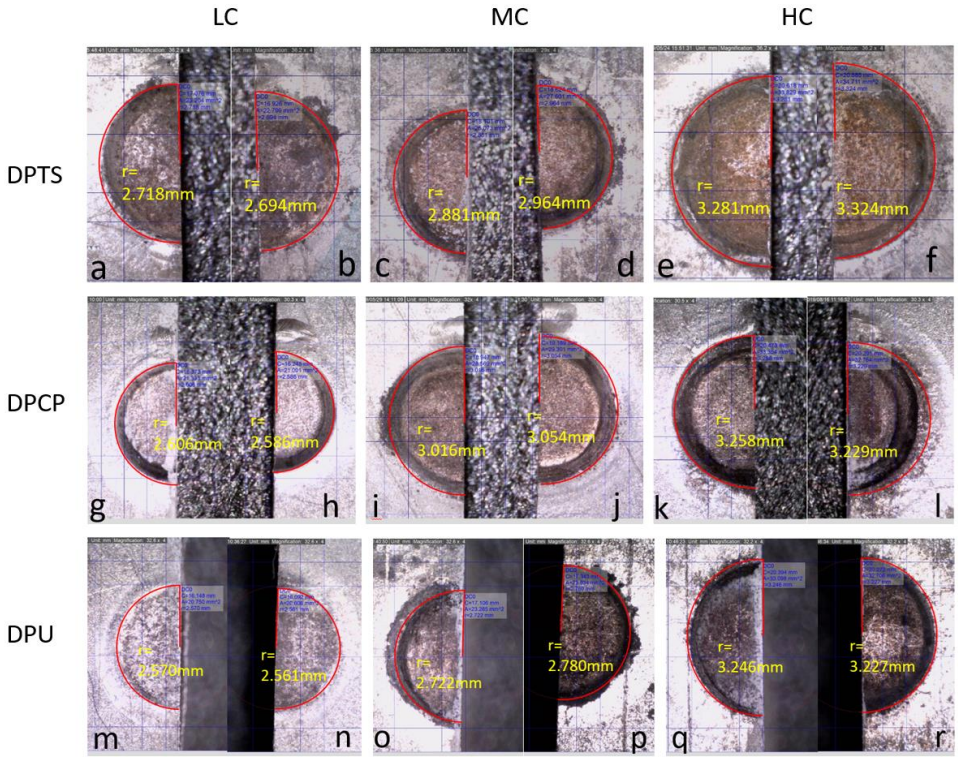

Figure 4.1. Examples of Weld size measurement for two welds for (a) and (b) DPTS-L, (c) and (d) DPTS-M, (e) and (f) DPTS-H, (g) and (h) DPCP-L, (i) and (j) DPCP-M and (k) and (l) DPCP-H samples, (m) and (n) DPU-L, (o) and (p) DPU-M and (q) and (r) DPU-H samples after sample preparation.

4.1.2 Microstructure characterization of spot weld

Figure 4.2 depicts the microstructure of different regions of spot weld in DP1000 with applied low, medium and high welding currents. The microstructure of base metal (BM), subcritical heat affected zone (SCHAZ), intercritical heat affected zone (ICHAZ), fine grain heat affected zone (FGHAZ), coarse grain heat affected zone (CGHAZ) and nugget are shown by purple, blue, green, yellow, orange and red squares in Figure 4.2a followed by micrographs with high magnification in the squares of same colours in Figure 4.2. It is worth noting that the microstructure of BM and SCHAZ are not significantly different because that no phase transformation within this zone as the temperature of SCHAZ during welding process is below AC_1 [70], except the presence of tempered martensite [43] [219], thus micrographs of SCHAZ were not shown in

Figure 4.2.

The base material is composed of ferrite and martensite. Martensite appears brighter and ferrite appears darker in SEM micrographs. The peak temperature of ICHAZ is between AC_1 and AC_3 [70], therefore some of ferrite transform into austenite within this range, and then austenite transforms to martensite due to rapid cooling. Thus the volume fraction of martensite within this region is higher than that in base metal as shown in Figure 4.2g, I and q. FGHAZ is located between ICHAZ and CGHAZ with a temperature of around AC_3. In this zone, all or most of the ferritic phase is transformed to austenite and subsequently transformed to martensite due to rapid cooling but little grain growth as shown in Figure 4.2f, k and p. The peak temperature of CGHAZ adjacent to nugget is over AC_3. Longer cooling time due to higher temperature induces grain growth leading to coarser lath shape martensitic microstructure [43], as shown in Figure 4.2e, j and o. The formation of lath martensite might be due to a low carbon content [43]. The nugget directly contacting the electrode has the highest peak temperature where all ferrites are transformed to lath like martensite, Figure 4.2d, i and n. The centre of the nugget where is the last solidified shows smaller grains, Figure 4.2c, h and m.

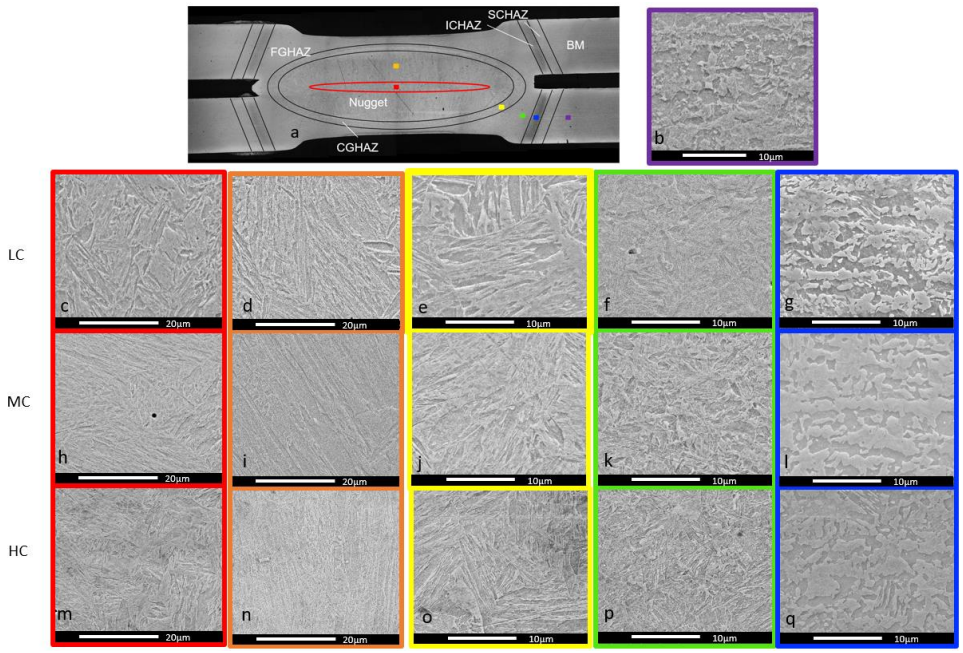

Figure 4.2. Microstructure characterization of spot weld with applied low. medium and high welding current in DP1000, (a) image indicating different regions of weld section; (b) base metal; (c), (d), (e), (f) and (g)micrographs of different regions of weld with applied low welding current; (h), (i), (j), (k) and (l)micrographs of different regions of weld with applied medium welding current; (m), (n), (o), (p) and (q)micrographs of different regions of weld with applied high welding current, indicated in image (a) with same color.

4.1.3 Microhardness characterization

Figure 4.3 shows an example of microhardness indents on the cross section of welded samples carried out according to the described approach in the previous chapter. Figure 4.4 shows the microhardness profiles of different regions of the spot weld under low, medium and high welding currents, indicated by black, green and blue lines, respectively. The hardness of BM is similar for all the samples, which is around 316 VHN, highlighted in green bars in Figure 4.4. The hardness of welds with each welding current shows similar trends. Sudden drops are observed in SCHAZ in samples, this could be due to tempering effect of martensite in SCHAZ reducing the strength, highlighted with light yellow bar in Figure 4.4. The hardness increases dramatically in ICHAZ

which could be due to the increasing volume fraction of martensite, highlighted in light orange bar in Figure 4.4. The hardness of FGHAZ is the highest while that of CGHAZ is slightly smaller, highlighted in orange bar in Figure 4.4. Nugget has slightly smaller hardness than CGHAZ, highlighted in light blue bar in Figure 4.4. According to the achieved results, the hardness is lower at higher welding current leading to better ductility and formability at higher welding currents.

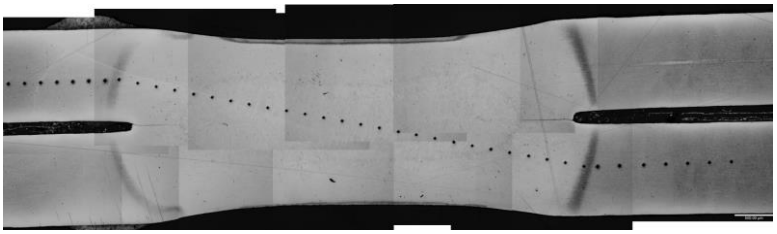

Figure 4.3. Microhardness indents of DPCP sample for BM, HAZ and nugget.

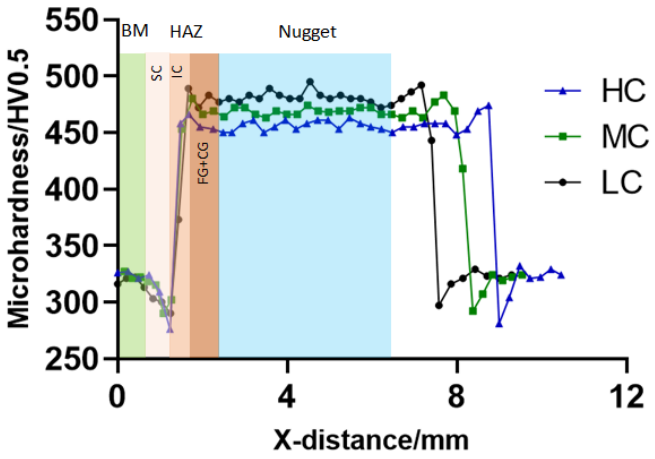

Figure 4.4. Comparison of microhardness of spot welds under low welding current, medium welding current and high welding current.

4.2 Weld characterization in low carbon steel

4.2.1 Weld size measurement

Figure 4.5 shows the measured weld size of LCTS, LCCP and LCU samples with each welding current using optical microscope. Same with DP1000 sample that the indent radius was measured instead of the nugget size. The maximum difference of the measured radius in the samples is around 0.05mm, which is

believed not to affect the failure and deformation results.

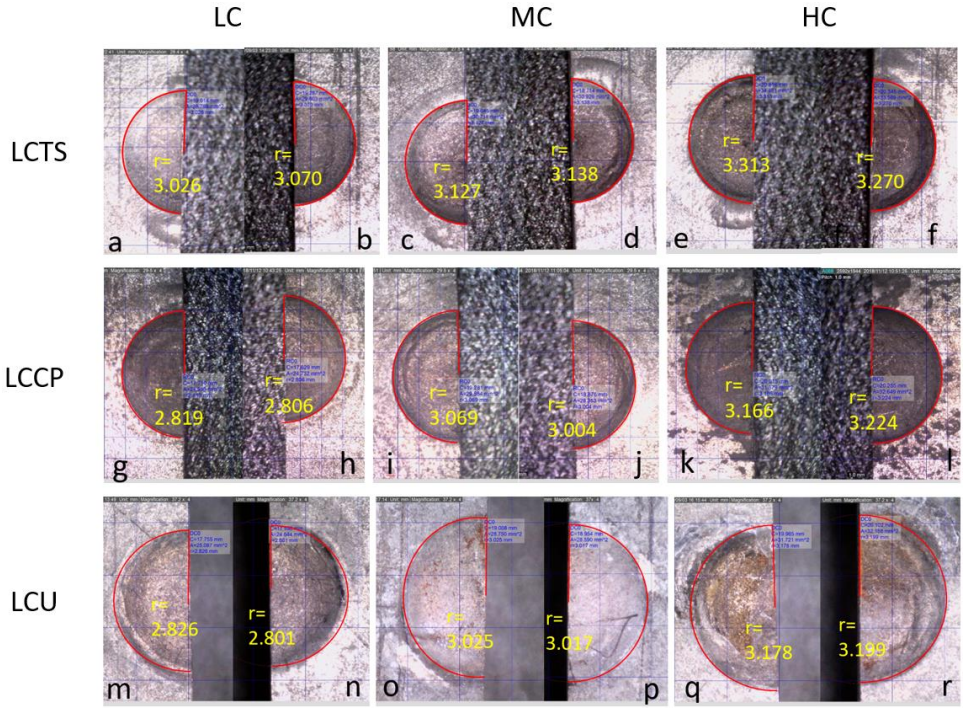

Figure 4.5. Examples of Weld size measurement for two welds for(a) and (b) LCTS-L, (c) and (d) LCTS-M , (e) and (f) LCTS-H, (g) and (h) LCCP-L, (i) and (j) LCCP-M, (k) and (l) LCCP-H, for (m) and (n) LCU-L, (o) and (p) LCU-M and (q) and (r) LCU-H samples after sample preparation.

4.2.2 Microstructure characterization of spot weld

Microstructure of BM, HAZ and nugget of weld section with low, medium and high welding current in low carbon steel was characterised as shown in Figure 4.6. Microstructure shown in Figure 4.6b indicates that there is only ferrite within BM. Micrographs of HAZ around the indents were obtained along the direction from BM to nugget, highlighted in green, yellow and blue squares in Figure 4.6c, d and e. No phase transformation is observed which could be due to the low carbon content of BM in spite of high cooling rate [220]. Ferrite grain growth is observed along the direction from BM to nugget, shown in Figure 4.6 b, f, i, l and r, due to the higher temperature and longer cooling time. Coarse ferrite is observed in the nuggets, which is plate like microstructure indicated with white arrows, similar microstructure was observed in weld in a

low carbon steel by researcher in literature [220], Figure 4.6 r, s and t. Smaller ferrite are observed in the central portion of nugget, highlighted in green square in Figure 4.6u.

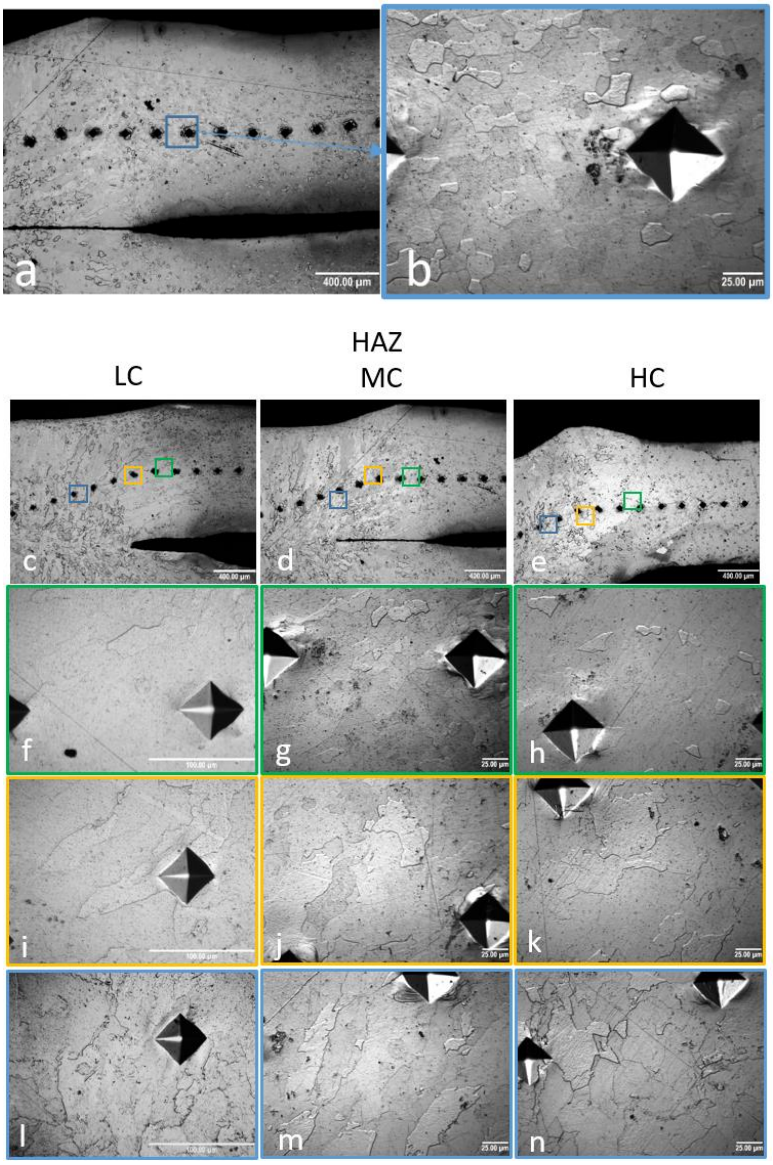

Figure 4.6. Microstructure characterisation of weld section in low carbon steel sample, (a) and (b) BM, (c-e) HAZ of welds with low, medium and high welding currents, (f-n) higher magnification micrographs according to indents in HAZ , (o-q), (r-t) and u nuggets of welds with low, medium and high welding currents.

Continue to next page.

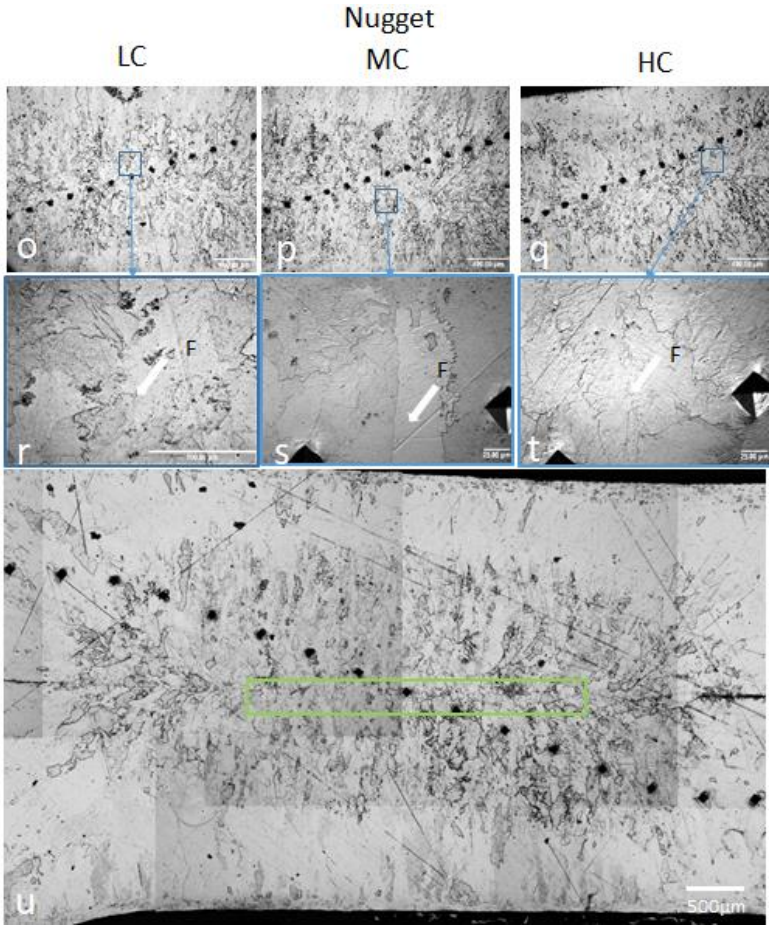

4.2.3 Microhardness characterization

The indent path is shown in Figure 4.7. Figure 4.8 reveals the microhardness of different regions in spot welds under low welding current, medium welding current and high welding current. The microhardness of BM, HAZ and nugget is similar for samples with applied low, medium and high welding currents indicating that welding current has almost no influence on the mechanical properties of HAZ and nugget due to only ferrite is in HAZ and nugget. Then, microhardness increases in HAZ and nugget owing to higher cooling rate resulting in higher dislocation in ferrite grains[220].

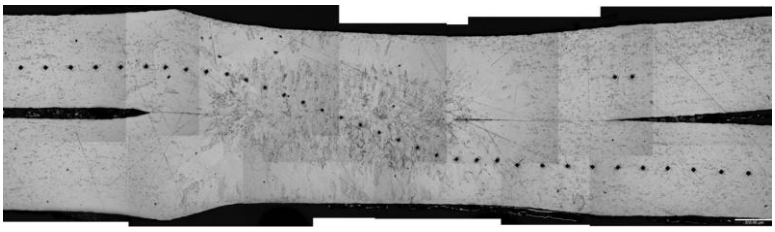

Figure 4.7. Microhardness indent path of low carbon steel samples.

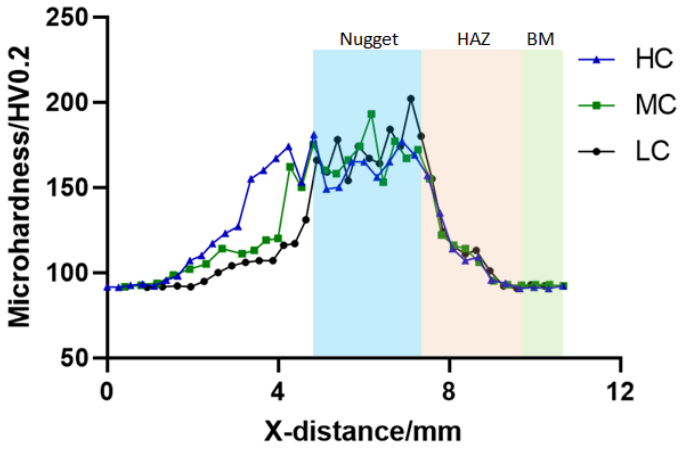

Figure 4.8. Comparison of microhardness of spot weld in low carbon steel samples under low welding current, medium welding current and high welding current.

4.3 Metallography and microstructural morphology analysis of the welds

The characterisation of microstructural morphology of the samples produced by the applied low, medium and high welding currents indicated that the microstructure of different weld zones were greatly affected. Larger weld size were obtained through higher welding current, Figure 4.1 and 4.5, due to the fact that higher welding current input can generate larger amount of heat between two steel sheets resulting in bigger size of melted zone.

Martensite with shorter and smaller size locates in the central portion of the nugget of DP1000 while longer and larger size of martensite grains are in the surrounding areas as shown in Figure 4.2. This phenomenon was also reported by Bouzeki et al. on DP780 spot weld[221]. Similar distribution of grain size is also observed in nugget of low carbon steels shown in Figure 4.6u. This phenomenon could be due to the forming process of nugget during spot welding. The formation of microstructure in the nugget is very similar to the casting process where the molten metal starts the solidification process from the boundaries of the mould with grains growing towards the centre of the liquid pool generating long and large grains [70]. This is schematically illustrated in Figure 4.9 where the melt pool is generated directly beneath the contact points of the electrodes and the weld is subsequently cooled down.

The heat generated by the welding current dissipates to the environment, the water cooled electrodes and the base material, as shown by the red arrows in Figure 4.9.

The solidification of nugget consists of two stages: nucleation of a solid phase and subsequent grain growth. This occurs when the temperature decreases below the liquidus temperature of the alloy at the exterior of the nugget followed by the grains growth towards the centre of the nugget. The direction of grain growth is along the orientation of heat dissipation. Due to the faster cooling rate of nugget close to the water cooling electrodes, longer columnar grains form at upper and lower side of the nugget while the columnar grains are shorter at where cooled through air and base metal, which was also reported by S Dancette in the weld of DP980 [108]. The martensite in nugget of DP1000 sample as well as ferrite in nugget of low carbon steel sample in the central portion have smaller size than the surroundings. This could be due to the microsegregation of alloying elements in the nugget, the materials at circumference of nugget first solidified which contains the least proportion of alloying elements or other chemical elements, these elements segregated extensively to the centre of the nugget during solidification, the liquid material last solidified contains the highest concentration of the these chemical elements [222]. Therefore, these elements could increase the number of grains during solidification leading to smaller grain size[222]. The central portion of nugget shows a long and narrow shape, highlighted with red ellipses in Figure 4.1a and green square in Figure 4.6u. It is because that the solidification in the normal direction to the electrode surfaces is faster than that of horizontal direction due to a higher cooling rate in vertical direction, which may squeeze the last portion of liquid material towards the faying face of the nugget along vertical direction before solidified.

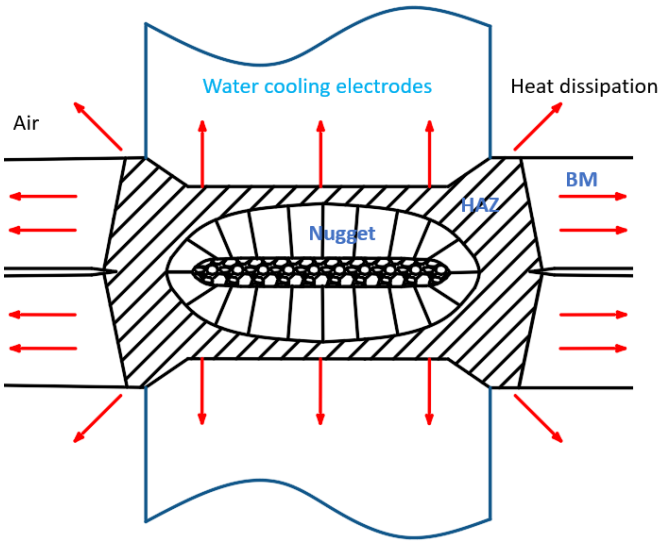

Figure 4.9. Schematic of nugget structure and method of cooling.

The hardness increases from the base metal to the centre of the nugget in DP1000 sample shown in Figure 4.4, that could be linked to the presence of different microstructure and possibly residual stress within different zones caused by microstructure of base material and heat treatment approach [112]. It is reported that the temperature of HAZ can reach as high as between AC_1 and AC_3 or above AC_3 while the material in the nugget is fully melted and rapidly cooled from above AC_3 [43], which is similar with quenching process, leading to phase transformation, as shown in micrographs of Figure 4.2. The hardness drop in SCHAZ is due to tempering effect on the local hardness of the material as the temperature is below AC_1. The higher volume fraction of martensite in ICHAZ leads to hardness increase. The grains in CGHAZ grows to larger size than the recrystallized grains in ICHAZ due to a lower cooling rate, slightly reducing the hardness.

The observed reduction of microhardness of nugget and HAZ with higher welding currents indicates that the spot welds with applied higher welding current have a better ductility and slightly lower strength. The increasing welding current from 5.5kA to 7.7kA results in rise of thermal energy input from 23J to 46J in the material that can prolong the heating process and decrease the cooling rate leading to reduction of the dislocation within martensite and grain growth, consequently reducing the hardness. This has also been reported for the case of DP600 [223]. And then, as reported by researchers that hardness

of steels has a linear positive correlation with yield strengths [224]. Moreover, steels with low strengths commonly show better ductility known as strength-ductility trade-off [225]. Additionally, it was found the hardness drop from FGHAZ to nugget is 18 VHN in weld of high welding current, which is larger compared to MC (14 VHN) and LC (11 VHN) cases. Thus, the difference of ductility between HAZ and nugget under higher welding current is larger.

In contrast, the hardness of weld in low carbon steel samples is shown in Figure 4.8. Hardness increases from BM to nugget for sample under same welding current. As only coarse ferrite is observed in HAZ and nugget, thus the increase of hardness in weld could be due to the increase of dislocation density within ferrite during welding process by higher cooling rate [226]. Almost no difference is observed when increasing the welding current, which might be due to that no phase transformation is in HAZ and nugget. Much lower hardness is obtained in BM, HAZ and nugget comparing to weld in DP1000 samples with each welding current indicating the weld in low carbon steel is more ductile.

4.4 Validation of developed sample geometries

In order to validate the developed TS, CP and U-shape samples, a FE simulation was carried out to obtain the maximum principal stress distribution at the cross section of weld section of full and half weld samples under each loading condition, as shown in Figure 4.10. The material used was DP1000 and the properties were obtained from literature [203]–[205]. In this case, the obtained stress state could be used to conduct qualitative comparison. The stress distribution contours were obtained at two stages of loading for each group, shown in Figure 4.10. The selection of displacement point of first stage is around yielding and the second stage is within plastic deformation.

Stress concentration in cross section surface for full weld and half weld TS, CP and U-shape samples all locates at the notch tip, white arrows in Figure 4.10. The stress values at region of stress concentration of half weld samples are smaller than full weld samples. This could be due to that BM between two half welds of the designed samples dispersed the applied load. And this issue has

more effect on U-shape samples with half welds as the highest stress value is not on the cross section of the weld, Figure 4.10 c_3 and c_4. Although this issue shows the effect on stress state, similar stress patterns at cross section surfaces of full weld and half weld samples and same location of stress concentration are observed for designed samples.

Above all, the weld section of designed TS and CP samples could show similar deformation and failure behaviour with conventional full weld samples, but for U-shape samples, there might larger difference between full and half weld samples.

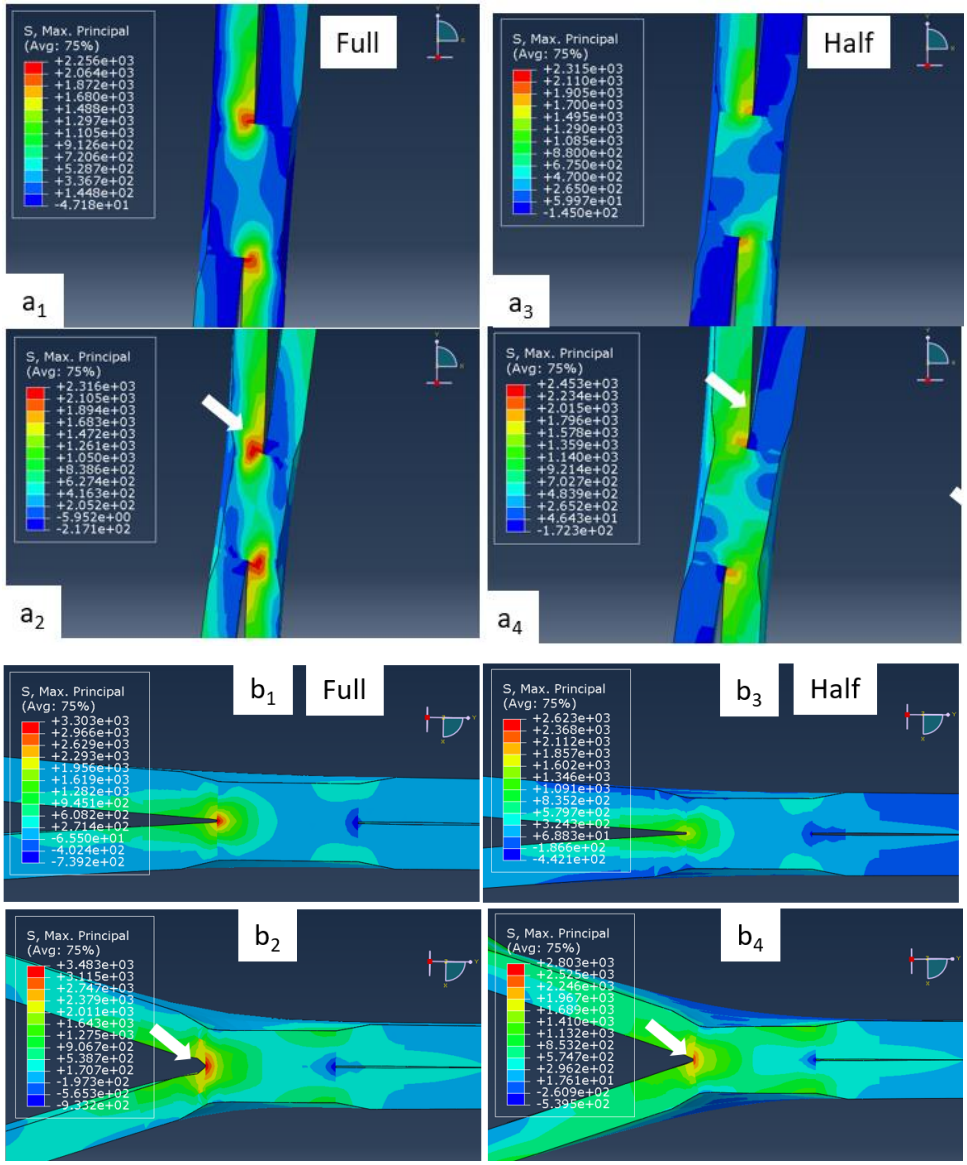

Continue to next page

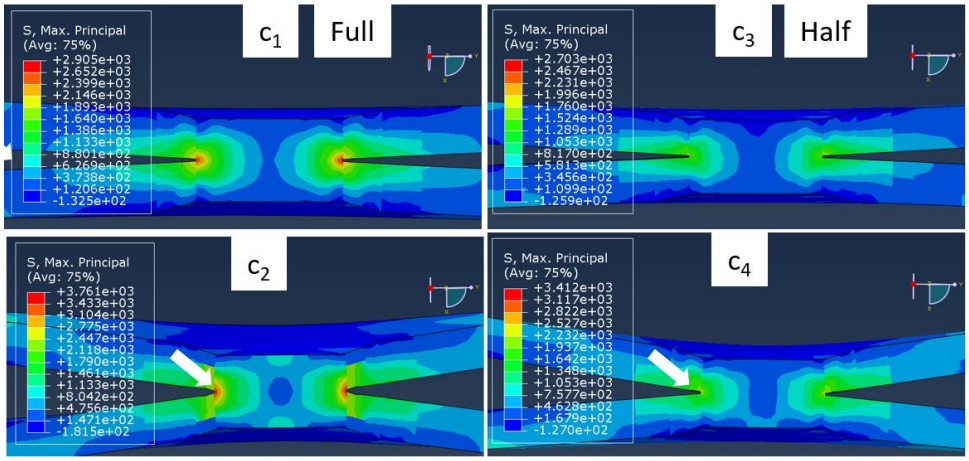

Figure 4.10. Comparison of maximum principal Stress distribution between full and half weld (a) TS, (b) CP and (c) U-shape samples at two stages of loading. a_1, a_3, b_1, b_3, c_1, c_3 are the first stage while a_2, a_4, b_2, b_4, c_2, c_4 are the second stage.

4.5 Failure mechanism analysis of spot weld under mixed tensile/shear loading condition

4.5.1 Deformation and failure analysis of welds under mixed tensile/shear loading condition (results)

The section shows results of deformation and failure of DPTS and LCTS samples. Four samples were tested for each welding current. Three samples of each welding current were painted with speckle patterns while one sample was tested without speckle patterns.

Figure 4.11a Load-displacement curves of tensile-shear samples using low carbon steels. Lines in black indicate the samples LCTS-L with high welding current, lines in green indicate the samples LCTS -M with medium welding current while the green lines show samples LCTS-L with a lower welding current. Samples of higher welding current have higher failure load and longer displacement indicating a better energy absorption ability. It can be seen that two drops after the highest load in some of the curves, indicated with blue arrows in Figure 4.11a, which could be due to the failure of two half welds were not starting simultaneously as the position of failure could be slightly different

with each other, indicated with black arrows in Figure 4.10b.

Figure 4.11b shows the load-displacement curves corresponding to the tensile-shear tests implemented using samples with low (DPTS-L), medium (DPTS-M) and high (DPTS-H) welding currents. The lines in black indicate the DPTS-L samples while the DPTS-M and DPTS-H tests results are shown with the yellow and green curves.

Figure 4.11c shows average maximum load and corresponding average displacement with the standard deviation for DPTS and LCTS samples. The standard deviation are small compared to the load and displacement which might indicate the load-displacement curves of DPTS and LCTS samples shows reasonable consistency. Additionally, DPTS have much higher maximum load and slightly longer displacement than that of LCTS samples which might indicate that DPTS samples reveals better energy absorption ability.

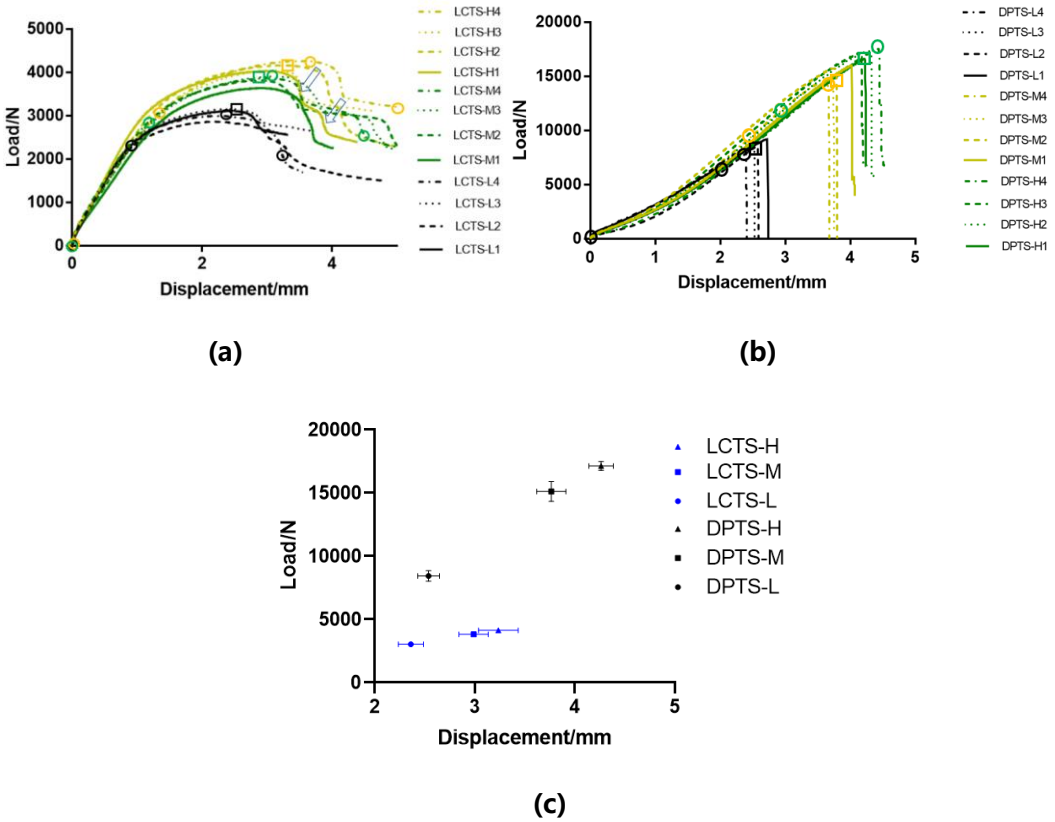

Figure 4.11. Load-displacement curves of tensile-shear samples in (a) Low carbon steel and (b) DP1000 steel with low, medium and high welding currents. The highlighted squares show the failure point of the samples with paint, the highlighted circles show process of failure of the samples without paint, (c) average maximum load vs average displacement with standard deviation for samples with each welding current.

The failed tensile-shear samples are shown in Figure 4.12. It is clear that DPTS-L samples fail via IF mode while DPTS-H samples fails via PF mode. DPTS-M samples fail via IF in two samples while the other two samples show a combination of IF and PF modes . In contrast, all LCTS samples fail via PF mode shown in Figure 4.12b.

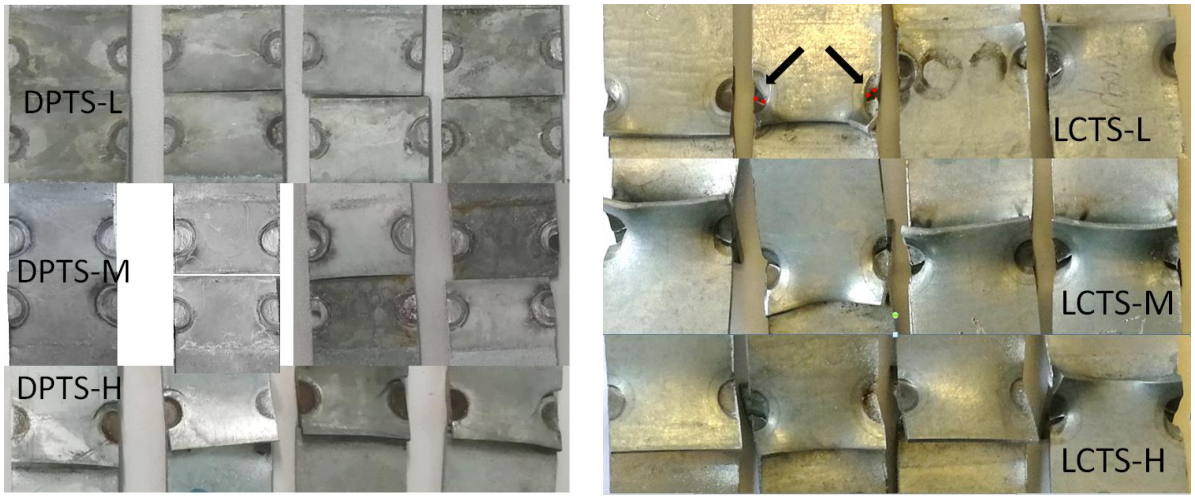

(a) **(b)**

Figure 4.12. Failed tensile-shear samples, (a) DP1000 and (b) low carbon steel, under three differnet welding current

Figure 4.13 shows deformation and failure process of spot weld of LCTS-L, LCTS-M and LCTS-H samples, where the samples were grinded to make the deformation more visible. The images are obtained at different stages in load-displacement curves of LCTS-L4, LCTS-M4 and LCTS-H4 samples, the displacement stages are indicated in black, yellow and green circles in Figure 4.11a representing before testing, around yield point, highest load before failure and final failure.

Deformation evolution of all LCTS samples is similar. Local deformation occurs within the HAZ leading to bending and necking followed by fracture within HAZ causing PF mode failure, highlighted in blue and yellow squares in Figure 4.11. However, although, the failure occurs in HAZ, the deformation within nugget around corona bond tip could be smaller in sample with applied higher welding current based on the observed the deformation bands, Figure 4.13d, h and l.

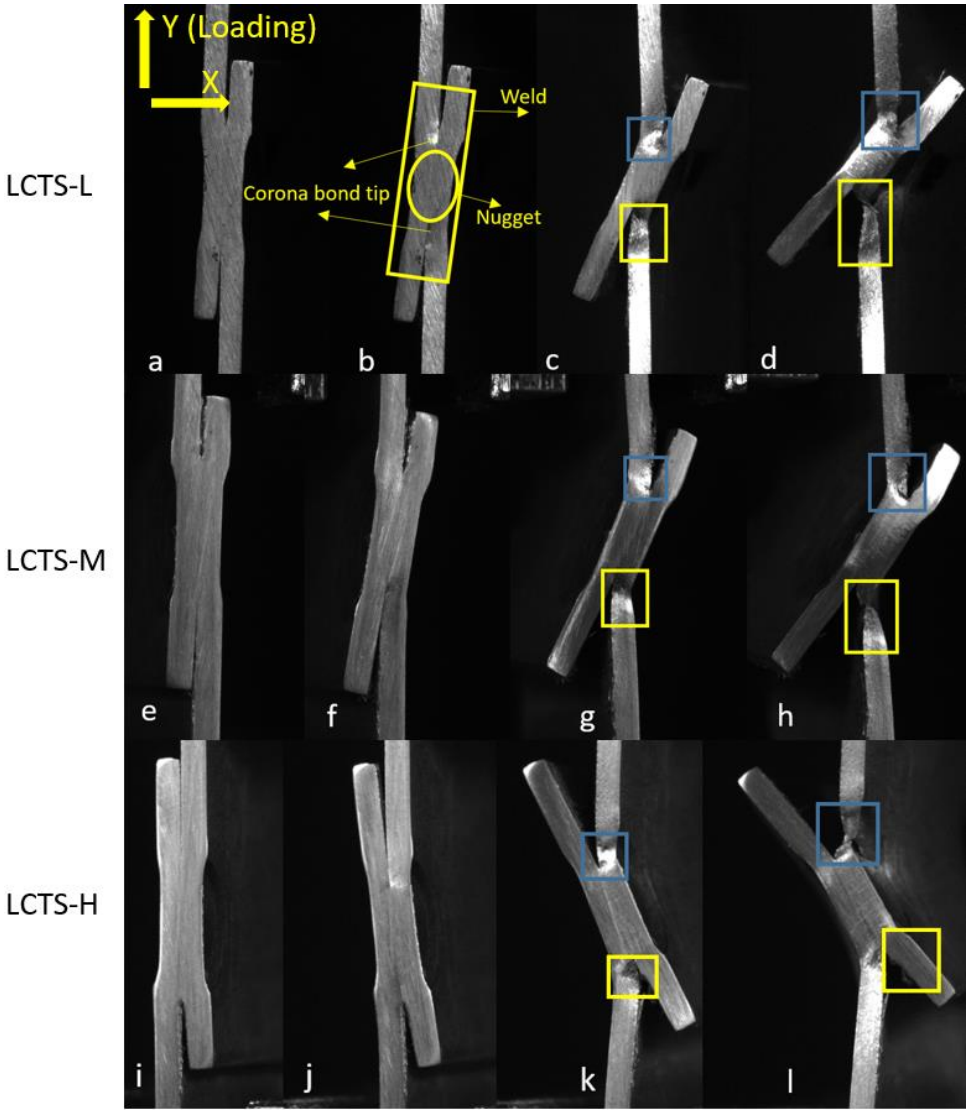

Figure 4.13. Images of deformation and failure process of LCTS-L4, LCTS-M4 and LCTS-H4 samples without paint, (a), (e) and (i) image before testing, (b), (f) and (j) around yield point, (c) (g) and (k) highest load and (d), (h) and (l) final failure.

The evolution of deformation in the tested samples is shown in Figure 4.14. The images shows different stages of loading indicated in load-displacement curves of DPTS-L4, DPTS-M4 and DPTS-H4 samples using black, yellow and green circles in Figure 4.11b representing before test, around yielding, just before final failure and final failure. Different failure modes are observed that DPTS-L sample and DPTS-M sample fail via IF (Figure 4.14d and h) while DPTS-H sample fails via PF (Figure 4.14l).

Figure 4.14a, b, c and d reveals the deformation evolution and failure of

DPTS-L sample wherein the nugget is shown by the ellipse and the corona bond tips (indicated in Figure 4.14b). The local deformation in the material makes the surface to become dull and some deformation bands become visible. The results show that deformation first starts from the nugget near the corona bond tips and propagates towards the centre of the nugget leading to IF mode by when the shear deformation bands are observed on the interface of nugget, Figure 4.14b and c. There is almost no deformation at upper and lower legs of the sample comparing with sample before testing, Figure 4.14d.

Figure 4.14h shows that DPTS-M failed through IF mode, however, plastic deformation is observed within nugget and HAZ around corona bond tips and at the boundaries of HAZ. During loading, the deformation initially occurred at the boundaries of HAZ, highlighted in Figure 4.14f, with the observed sign of out-of-plane deformation. Then, deformation is localised and transferred to the nugget at some point during test leading to failure, yellow arrows shown in Figure 4.14g and h. It should be noted that although the failure passed through the nugget, the deformation bands within the nugget is not as visible as in Figure 4.14d, which might be due to bending deformation in HAZ around the corona bond tips.

DPTS-H sample failed via PF mode as shown in Figure 4.14l. Similar with DPTS-M sample, deformation localisation is initially observed around the boundaries of HAZ, highlighted with blue squares in Figure 4.14j, and then transferred to nugget around the corona bond tips, yellow arrows shown in Figure 4.14k. However, the plastic deformation located around boundaries of HAZ is much larger than that adjacent to the nugget, Figure 4.14k, which might be due to the large deformation localisation around the HAZ boundaries reducing the load that transfers to nugget. Additionally, large bending deformation is also observed at upper and lower legs of DPTS-H sample.

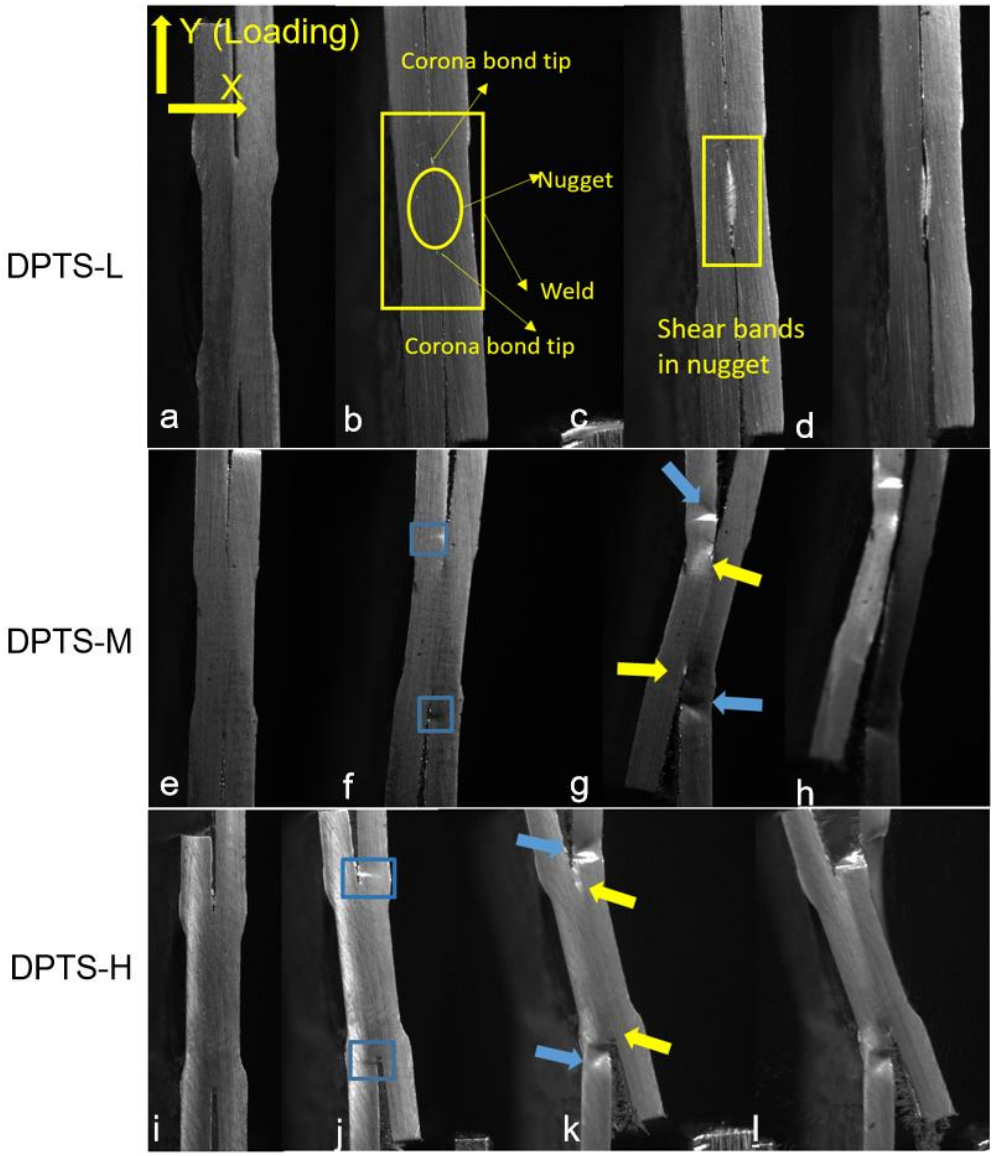

Figure 4.14. Images of deformation and failure process of DPTS-L4, DPTS-M4 and DPTS-H4 samples without paint, (a), (e) and (i) image before testing, (b), (f) and (j) around yielding, (c) (g) and (k) just before final failure and (d), (h) and (l) final failure.

The out-of-plane displacement at the nugget zone of the tested samples are shown in Figure 4.15 wherein the maximum measured out-of-plane displacement at the onset of failure is less than 0.05mm of DPTS-H sample while that is around 0.15mm in LCTS sample. This confirms the minimal image distortion. It is because the image captured under SEM in in-situ test is a projection of real object, thus the smaller out-of-plane displacement is the more similar the captured deformed image is with the real deformed object,

reducing the error caused by out-of-plane displacement. Additionally, the maximum in-plane displacement are 0.31mm and 0.65mm at the onset of failure, as out-of-plane deformation is much smaller, the in-plane maximum principal strain could be an indicator on failure of the samples.

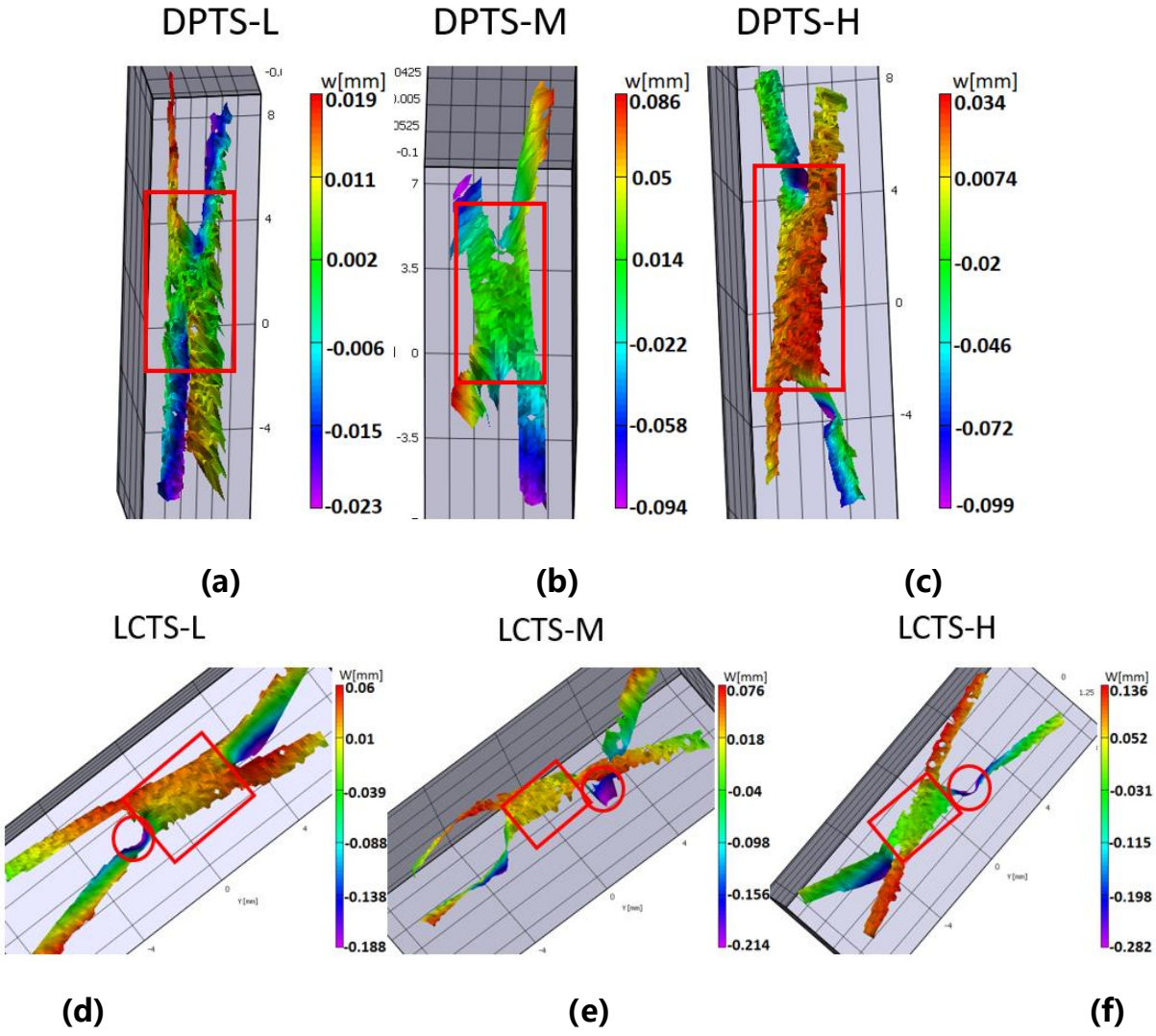

Figure 4.15. (a), (b) and (C) out-of-plane displacement of DPTS-L, DPTS-M and DPTS-H samples while (d), (e) and (f) out-of-plane displacement of LCTS-L, LCTS-M and LCTS-H samples.

To measure the deformation during the test, DIC system was used as explained in section 3.3. In order to determine the optimum accuracy for the measured strain, subset size dependency study was conducted to get the most proper subset size as it is the key factor impacting the accuracy of strain measurement. A random sample was selected as representative for the study

and the subset size changed from 39 to 19 while keeping the overlap as constant to keep the density of data points in each subset for displacement calculation consistent [227] and maximum principal strain was calculated. Assuming that when the error of measured strain between each two subset sizes is constantly below 5%, the corresponding subset size is acceptable. Figure 4.16 shows the effects of subset size to maximum principal strain where the maximum principal strain keeps increasing by decreasing the subset size, and subsequently the error are smaller than 5% when subset size decreases to 23 pixels. Thus, subset size of 23 pixels was chosen for all DPTS and LCTS samples with physical size of 310 micron and 322 micron as well as spatial resolution of 13.5micron/pixel and 14micron/pixel. Additionally, systematic error of strain measurements were analysed for DPTS and LCTS samples, Figure 4.17. These errors were usually come from calibration and correlation algorithm. Ten images of unloaded sample were used to carry out the analysis. The maximum strain values are around 0.003% indicating an ignorable error in strain measurement.

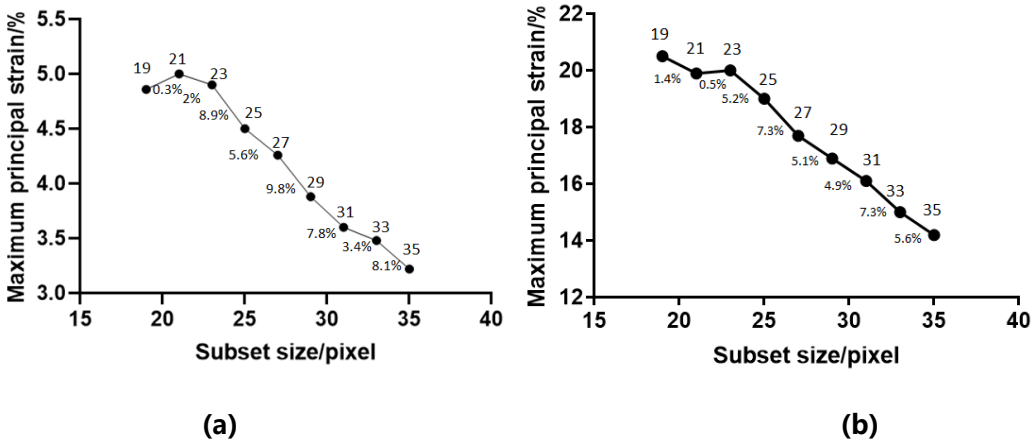

Figure 4.16. Subset size dependency on measured strain of (a) DPTS sample and (b) LCTS sample.

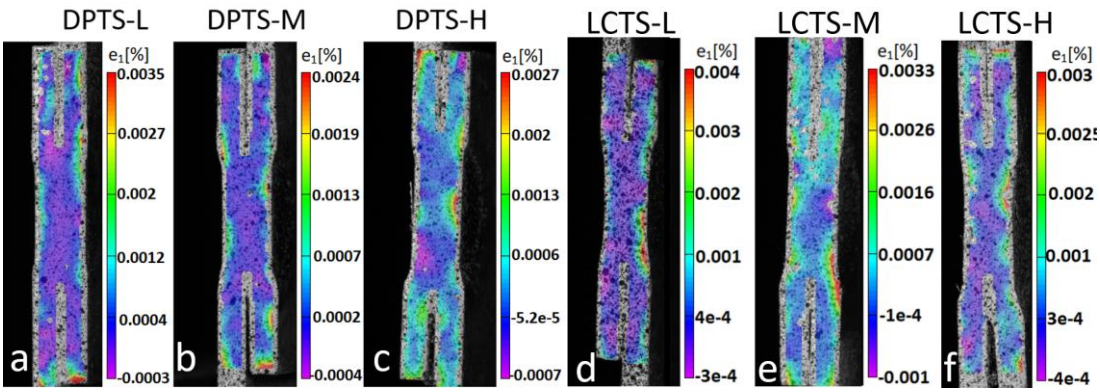

Figure 4.17. Uncertainty analysis, systematic error of maximum principal strain of (a) DPTS-L, (b) DPTS-M, (c) DPTS-H, (d) LCTS-L, (e) LCTS-M and (f) LCTS-H samples.

Similar strain maps were observed for the samples tested under same welding current, therefore analysis of one of the samples tested with each condition is provided here. Figure 4.18 reveals the strain distribution in the LCTS samples with applied low (L2), medium (M2) and high (H2) welding currents around plastic deformation initiation and highest load before failure (highlighted in displacement in Figure 4.18). The Lagrangian strain tensor were calculated for X (normal to the loading referring to Figure 4.13a) (Figure 4.18a, e, i, m, q and u) and Y (parallel to the loading referring to Figure 4.13a) (Figure 4.18b, f, j, n, r and v) directions as well as shear strain component in XY orientation (Figure 4.18c, g, k, o, s and w). Figure 4.18d, h, l, p, t and x show the distribution of maximum principal strain in the tested samples with low, medium and high welding currents, respectively.

At low welding currents, shear deformation occurs in HAZ around the corona bond tips and propagates into the centre of the nugget, Figure 4.18c and g. The materials around the HAZ and the interface between the HAZ and BM are severely deformed leading to large plastic strain in Y direction, and then the strain concentration in HAZ in Y direction induces local necking which could be the main factor of PF failure, Figure 4.18b and f, this is because that it plays the most important role in maximum principal strain values as shown in Figure 4.18d and h. The cases of LCTS-M and LCTS-H samples are similar with LCTS-L sample. However, larger measured maximum principal strain is observed in samples with higher applied welding current at highest load as

shown in Figure 4.18 h, p and x.

Additionally, failure strain could be determined according to the maximum principal strain at highest load before failure, which is around 20%, 24.8% and 32.4% for low/medium/high current samples, Figure 4.18h, p and x.

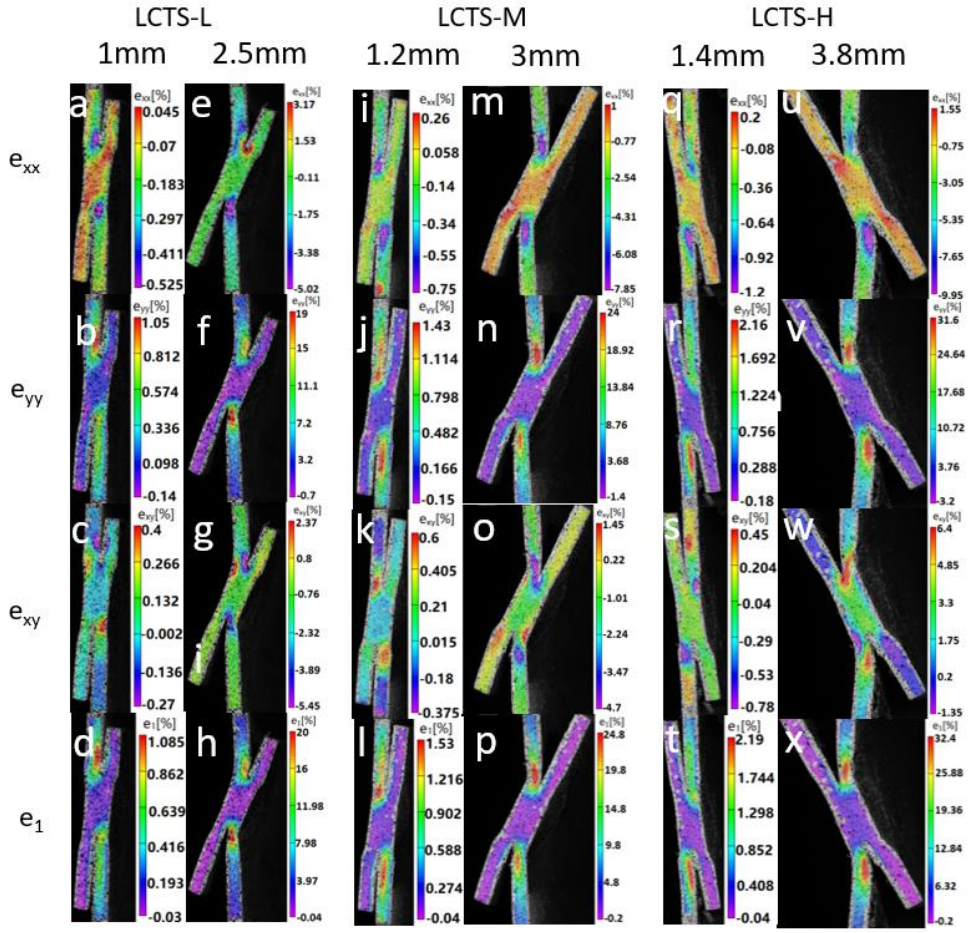

Figure 4.18. Distribution and evolution of strain components (including strain maps around yielding (1, 1.2 and 1.4mm) and at failure (2.5, 3 and 3.8mm)) for (a-h) LCTS-L2, (i-p) LCTS-M2 and (q-x) LCTS-H2 samples showing the strain components normal (a, e, i, m, q, u), e_{xx}, aligned to the loading direction (b, f, j, n, r, v), e_{yy}, shear (c, g, k, o, s, w), e_{xy}, and maximum principal strain (d, h, l, p, t, x), e_1.

The distribution and evolution of measured strain components are extracted at the points around plastic deformation initiation and the points before final failure of DPTS-L2, DPTS-M2 and DPTS-H2 samples, indicated by displacement in Figure 4.19.

In low welding current, at the point around plastic deformation initiation, the local strain concentration occurs around the corona bond tips while there is almost no deformation in the centre of nugget referring to maximum strain distribution in Figure 4.19d. Such deformation localisation is owing to strain concentration in X and shear directions, Figure 4.19a and c. Before final failure, the deformation in shear direction grows from the corona bond tip to the centre of the nugget, Figure 4.19 c and g. Though the deformation in X direction becomes larger, it still locates around the corona bond tips, Figure 4.19a and e. Meanwhile, considering the maximum principal strain shown in Figure 4.19h, shear strain values produces great contribution to the failure which might indicate that failure of DPTS-L sample is caused by shear stress.

However, this is different for DPTS-M sample, although it fails via IF mode, different strain patterns are observed in Figure 4.19. Negative strain in X direction concentrates at HAZ and grows to a larger absolute value indicating necking in HAZ, Figure 4.19i and m. According to shear strain distribution in Figure 4.19k and o, shear deformation first occurs around the corona bond tip and propagates into the nugget, however, there is almost no shear within the centre. Deformation in Y direction localises at HAZ and nugget leading to necking around HAZ and BM, Figure 4.19j and n. Considering maximum principle strain distribution in Figure 4.19i and p, strain concentration observed in Y and shear direction within HAZ, causes opening of the corona bond as well as necking around HAZ and BM, which plays the most important role to failure

Strain distribution maps of DPTS-H sample in Figure 4.19 shows different mechanism with medium current sample. Strain distribution in X direction shows an increasing compressive deformation around HAZ and BM indicating necking phenomenon, Figure 4.19q and u. This is caused by deformation localisation developed in Y direction indicated by strain concentration in Y direction shown in Figure 4.19r and v. Unlike low and medium current samples, shear deformation initiates and develops in HAZ and BM, Figure 4.19s and w. According to maximum strain distribution shown in Figure 4.19t and x, there is no deformation in nugget and the large plastic deformation within HAZ and BM in Y direction is most likely to lead to necking and subsequent PF mode, Figure 4.19i and k.

Additionally, failure strain could be determined according to the maximum principal strain at highest load before failure, which is around 4.5%, 6% and 17.3% for low/medium/high current samples, Figure 4.19h, p and x.

Comparing the samples under three levels of welding currents, the relative rotation and subsequent bending of the loading legs are larger with higher welding current. Shear deformation plays an important role in IF failure of DPTS-L sample, while the weld section of DPTS-H sample takes much larger plastic deformation in HAZ leading to a different mode of failure identical to PF mode. Moreover, although the weld sizes of LCTS samples are same with DPTS samples, no failure modes transition is observed, which could be related to different mechanical properties of weld section due to different microstructure.

In conclusion, increasing the welding current leads to a transition of localised deformation from wtihin the nugget to HAZ causing failure modes change from IF to PF, and the strain dominating the failure changes from shear strain to strain in Y direction.

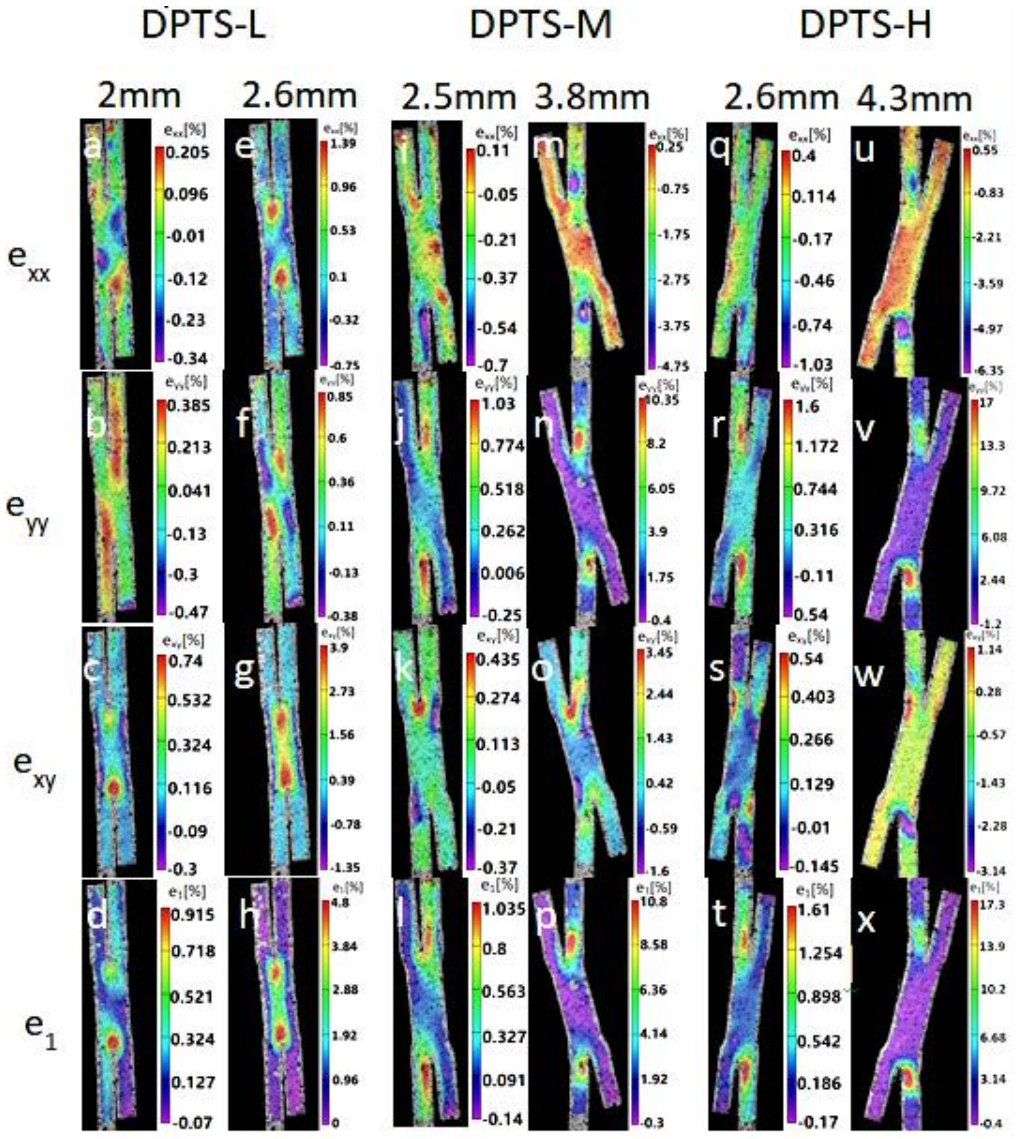

Figure 4.19. Distribution and evolution of strain components for (a-h) DPTS-L2, (i-p) DPTS-M2 and (q-x) DPTS-H2 samples showing the strain components normal (a, e, i, m, q, u), e_{xx}, aligned to the loading direction (b, f, j, n, r, v), e_{yy}, shear (c, g, k, o, s, w), e_{xy}, and maximum principal strain (d, h, l, p, t, x), e_1.

4.5.2 The effect of welding current on fracture mechanism of welds under mixed tensile/shear loading condition (results)

Fractography analysis and microstructural morphology analysis were conducted as shown in Figure 4.20, 4.21 and 4.22 for LCTS samples with low, medium and high welding currents.

In samples with low welding current, deformation bands highlighted with yellow square in Figure 4.20a reveals large plastic deformation due to tensile loading which also leads to local necking as the out-of-plane deformation is observed, highlighted in blue square in Figure 4.20a. Deep elongated dimples on the fracture surface, highlighted in green square in Figure 4.20a, and local shear bands around the crack path, Figure 4.20b might indicate that the PF failure of LCTS-L sample is very likely to be caused by necking due to tensile loading. This mechanism could be confirmed by micrographs of microstructural morphology, Figure 4.20b. The ferrite grains within HAZ are severely stretched resulting in large plastic deformation and local necking highlighted in yellow square in Figure 4.20b. Meanwhile, the local shear bands with severely elongated ferrite grains along the crack path, highlighted in green square in Figure 4.20b, could be caused by stretch.

Similar mechanisms are observed in samples with applied medium and high welding currents shown in Figure 4.21 and 4.22.

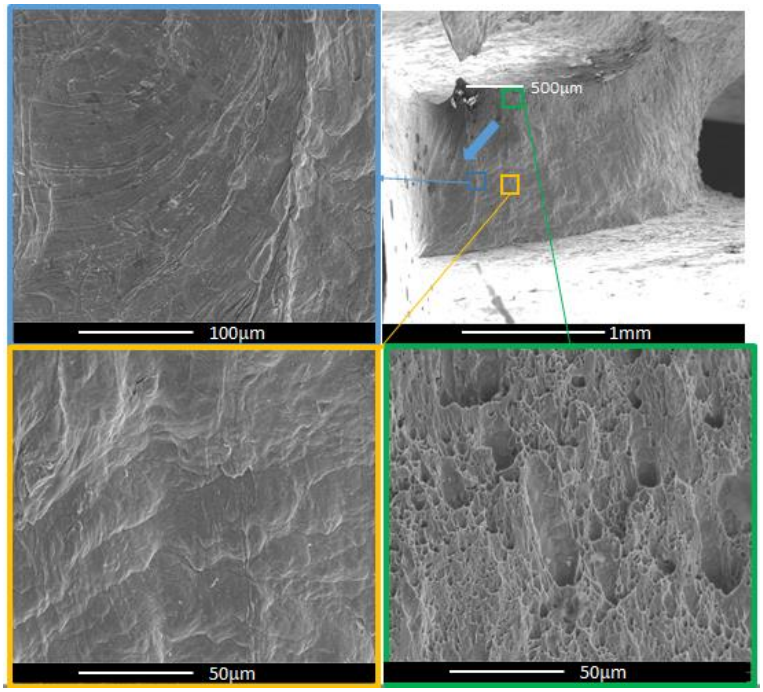

(a)

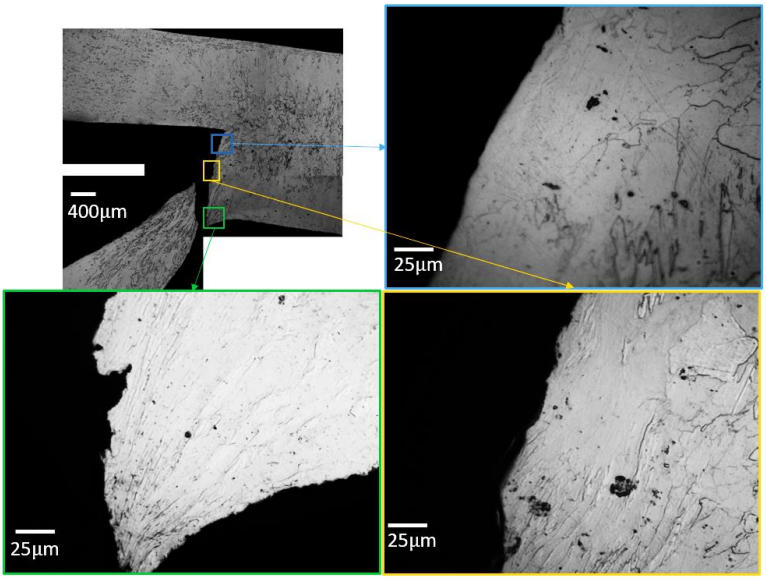

(b)

Figure 4.20. Fracture surfaces (a) and microstructural morphology (b) of LCTS-L samples showing domination of necking.

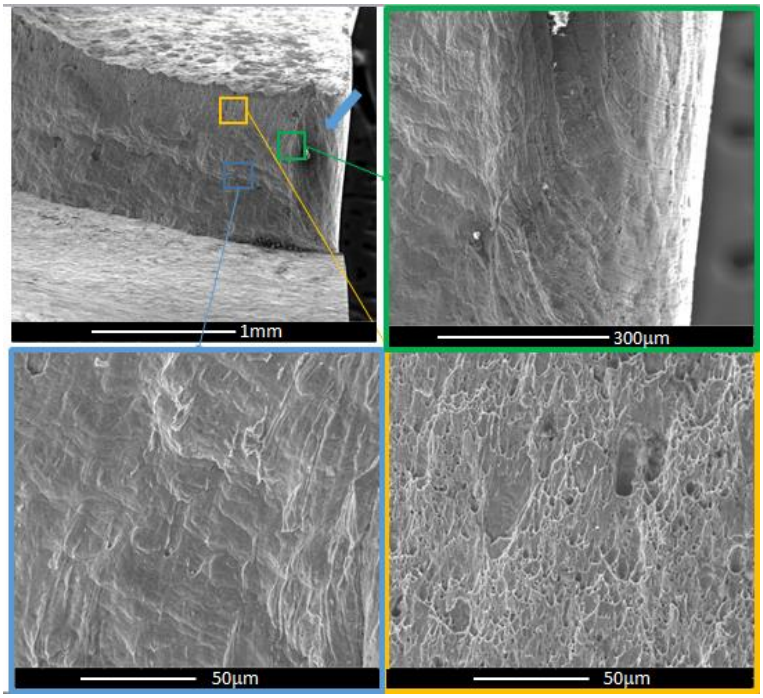

(a)

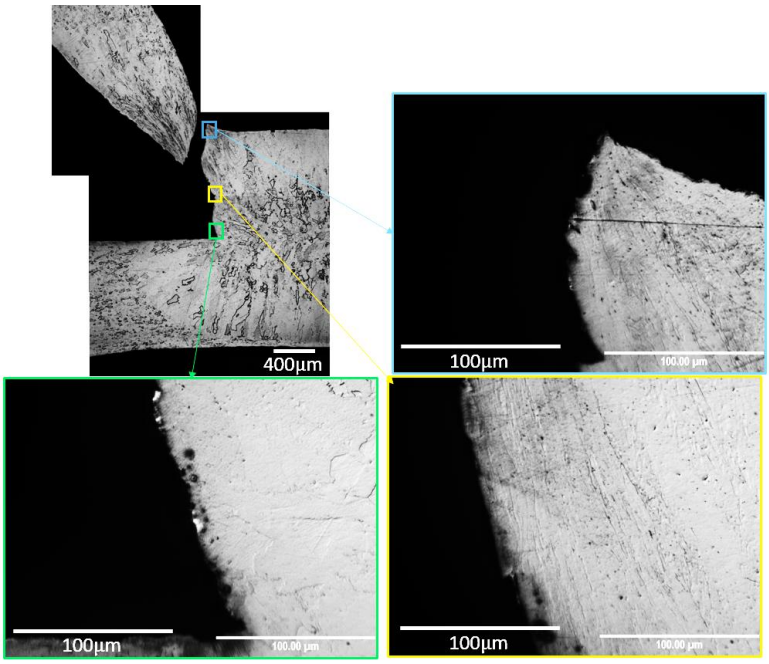

(b)

Figure 4.21. Fracture surfaces (a) and microstructural morphology (b) of LCTS-M samples showing domination of necking.

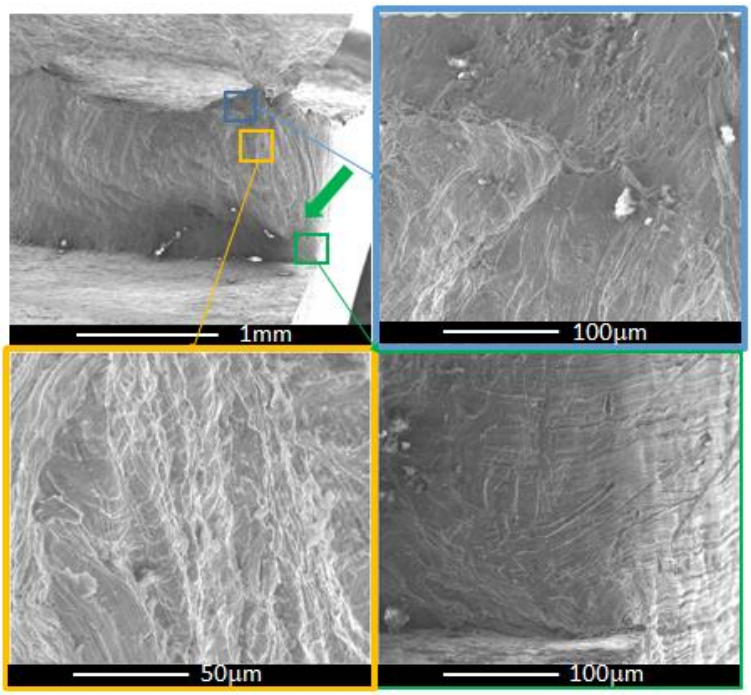

(a)

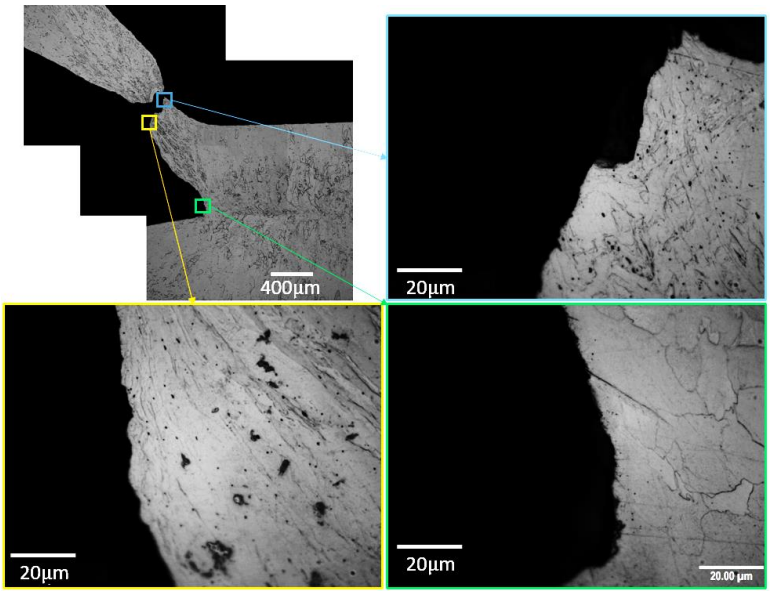

(b)

Figure 4.22. Fracture surfaces (a) and microstructural morphology (b) of LCTS-H samples showing domination of necking.

Figure 4.23 shows micrographs of fracture surface morphology of DPTS-L sample. The majority of the facture surface in DPTS-L sample is covered with elongated dimples indicating an in-plane shear fracture as expected

highlighted in blue ellipse in Figure 4.23a. Although in-plane shear failure dominates the fracture, the flank side of the nugget (highlighted in yellow ellipse in Figure 4.23a) shows complex fracture surface indicating change of stress state results in out-of-plane shear. The elongated martensitic laths (highlighted in blue, yellow and green squares in Figure 4.23b) confirm that shear failure dominates the fracture.

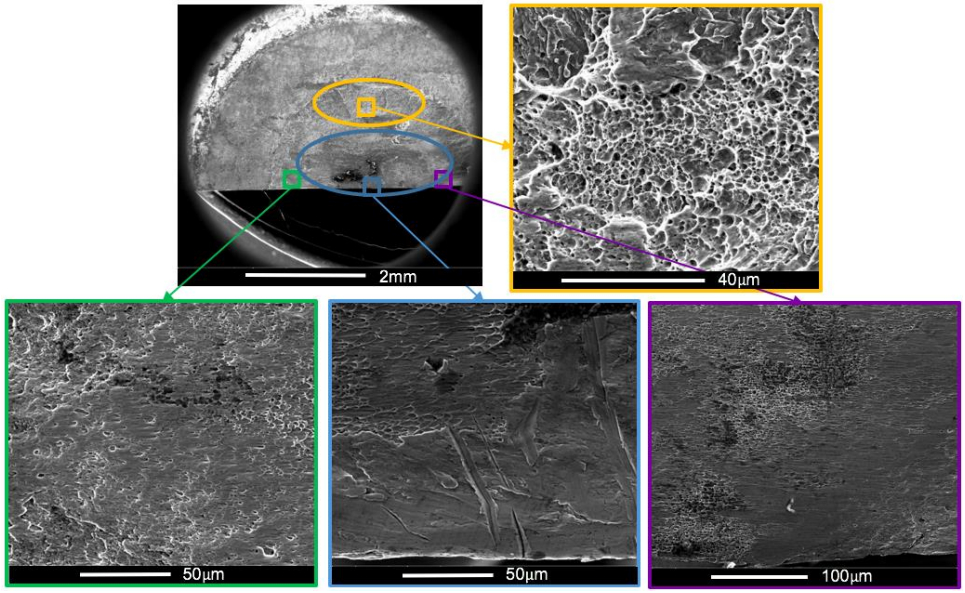

(a)

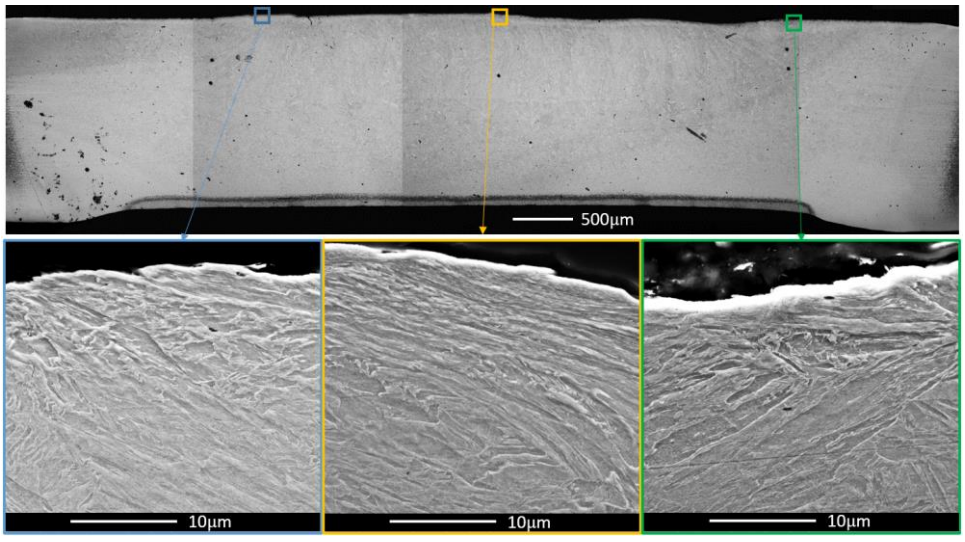

(b)

Figure 4.23. Fracture surfaces (a) and microstructural morphology (b) of DPTS-L samples showing domination of shear failure.

In contrast to DPTS-L samples, elongated dimples are along different directions at the most area of the fracture surface in DPTS-M samples (highlighted blue ellipse in Figure 4.24a), which indicate that out-of-plane shear dominates the failure. Elongated dimples with voids are observed that also indicates a mixed tensile-shear state, which is likely to be caused by cooperation of tensile and shear stress. In-plane shear dimples are observed near the edge of free surface, highlighted in blue, yellow and green squares in Figure 4.24a adjacent to the corona bond tips of nugget, which is also observed in free surface of the nugget (highlighted in blue and green squares in Figure 4.24b).

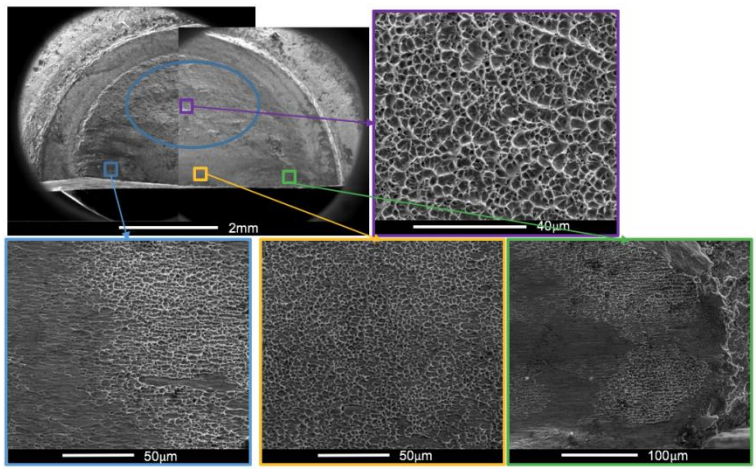

(a)

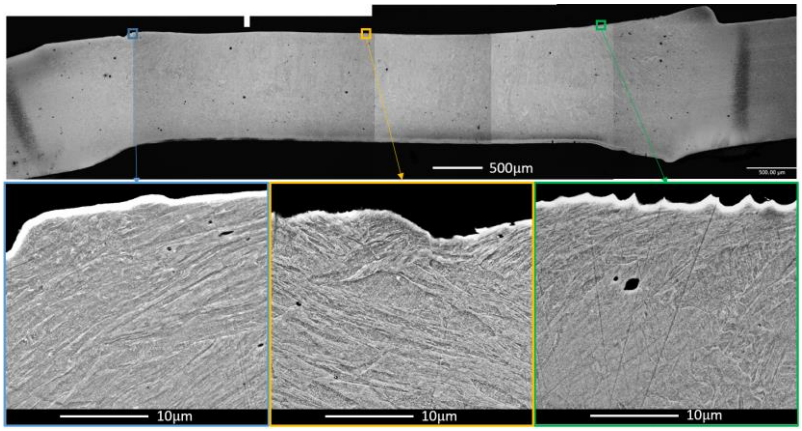

(b)

Figure 4.24. Fracture surfaces (a) and microstructural morphology (b) of DPTS-M samples showing domination of shear failure.

Figure 4.25 shows the fracture surface and microstructural morphology of DPTS-H sample. Ductile dimples are observed in the centre of fracture surface (highlighted in yellow squares in Figure 4.25a) while shear dimples are observed within the upper and bottom of fracture surface (highlighted in blue and purple squares in Figure 4.25a). In addition, local necking is observed around HAZ/BM around the crack path, indicated in white arrows in Figure 4.25a. Therefore, fracture of sample with high welding current could be due to local necking.

Individual grains at left and right side along the crack path are elongated and deflected to the same side, highlighted in blue and green squares in Figure 4.25b, while that in the middle is elongated massively, confirms the failure is caused by necking.

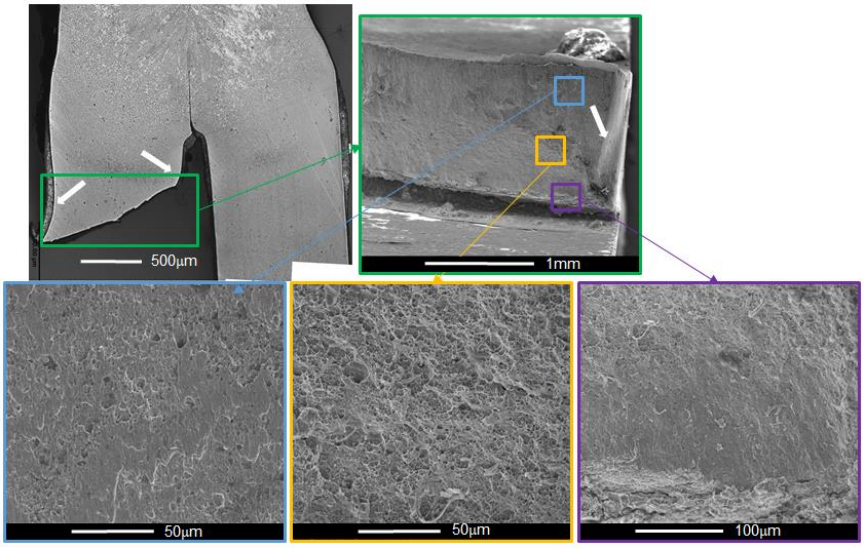

(a)

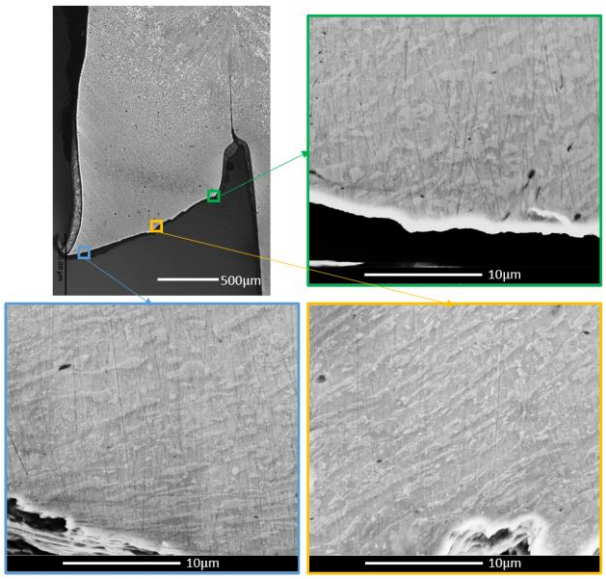

(b)

Figure 4.25. Fracture surfaces (a) and microstructural morphology (b) of DPTS-H samples showing domination of local necking failure.

4.5.3 Discussion

It is known that crack initiation and propagation usually depends on the microstructure of the sample and its loading condition [104], thus a fractography analysis, in combination with deformation evolution analysis have been carried out in order to analyse the failure mechanism of spot weld under

tensile-shear loading condition.

All LCTS samples, which are reference samples failed through PF mode. This could be due to the microstructure within the weld. Since the ultra-low carbon content within the material, there is no phase transformation during welding process in HAZ and nugget wherein only contains ferrite leading to relatively low hardness, this was also reported in the literature for spot weld of a ultralow carbon steel DC54D [220], Figure 4.8. This situation indicates the weld in low carbon steel is more ductile than that in DP1000, thus the nugget in low carbon steel might require more plastic strain to fail. The developed bending and tension in HAZ results in necking in HAZ decreasing the stress in nugget leading to failure in HAZ before the developed strain in nugget is sufficient to induce the failure, Figure 4.18x.

Fractography and microstructural morphology analysis of LCTS samples shown in Figure 4.20b, 4.19b and 4.20b indicates that failure occurs in HAZ at where closer to the nugget as the welding current decreases. Because the mechanical properties of weld is not affected by welding current due to the full ferrite microstructure shown in Figure 4.8, it could be due to that larger nugget by higher welding current changes the position of strain concentration of HAZ from close to nugget to close to BM. Necking and subsequent ductile failure within HAZ dominates the PF mode of LCTS samples, which is in agreement with the observation reported by Zuniga et al. [8] and Pouranvari [228].

Although, the nugget size of samples in low carbon steels is almost same with samples in DP1000, samples in DP1000 shows different failure behaviour.

The evolution of local strain at the centre of the nugget and around the corona bond tip is shown in Figure 4.26 for the DPTS samples welded with selected currents, the loading direction and coordinate are shown in Figure 4.13. The comparison of maximum principal strain at centre of nugget and around corona bond tip within the nugget under low, medium and high welding currents is shown in Figure 4.26g. In DPTS-L sample, the shear strain curve is almost identical with maximum principal strain curve at location 1 (centre of nugget) and 2 (within nugget adjacent to corona bond tip) indicating that shear deformation dominates the failure as expected, Figure 4.26d.

However, in DPTS-M sample, e_{yy} and e_{xy} strain evolutions are similar and much larger than e_{xx} strain at location 2 while there is almost no deformation in the material within centre of the nugget. This is due to higher welding current results in softer HAZ and nugget transferring the deformation localisation from the centre of the nugget to HAZ leading to necking in HAZ. However, the samples still failed via IF mode by shear due to the maximum principal strain in HAZ is insufficient to induce the failure.

In DPTS-H sample, e_{yy} strain evolution is almost consistent with maximum principal strain curve at location 2 and there is almost no sign of deformation due to shear mode indicating tensile deformation developed in Y direction dominates the failure, Figure 4.26f. In contrast to other samples, the compressive e_{xx} strain evolution at location 2 indicates the necking phenomenon, Figure 4.26f. The critical maximum principal strain increases from around 5% to around 8% at location 2 just before crack initiation as welding current increases indicating material within the nugget can withstand larger plastic deformation and consequently require more applied energy (higher failure load and longer elongation), Figure 4.26g.

Moreover, maximum principal strain in the centre of nugget of DPTS-L sample just before crack initiation is around 2% while that of DPTS-M and DPTS-H samples are closed to zero indicating that the material within the centre of nugget is no longer deformed. This transition could lead to different failure modes, maximum principal strain values in location 1 and 2 indicate that HAZ softening could dominates the transition. Microhardness analysis in HAZ, Figure 4.4, indicates that HAZ becomes softer when increasing the welding current making this section weaker and weaker, especially the SCHAZ, while the nugget is much harder than HAZ, thus HAZ with higher welding current is much easier to deform shown in Figure 4.26a, b and c. In addition, a larger and softer nugget is achieved by higher welding current, it was reported that the nugget with lower hardness had higher fracture toughness[229], this means the nugget needs higher stress to fail. Meanwhile the localisation in HAZ offloads the rest of the material leading to lower stresses in the nugget, thus, the nugget with higher welding current is harder to fail.

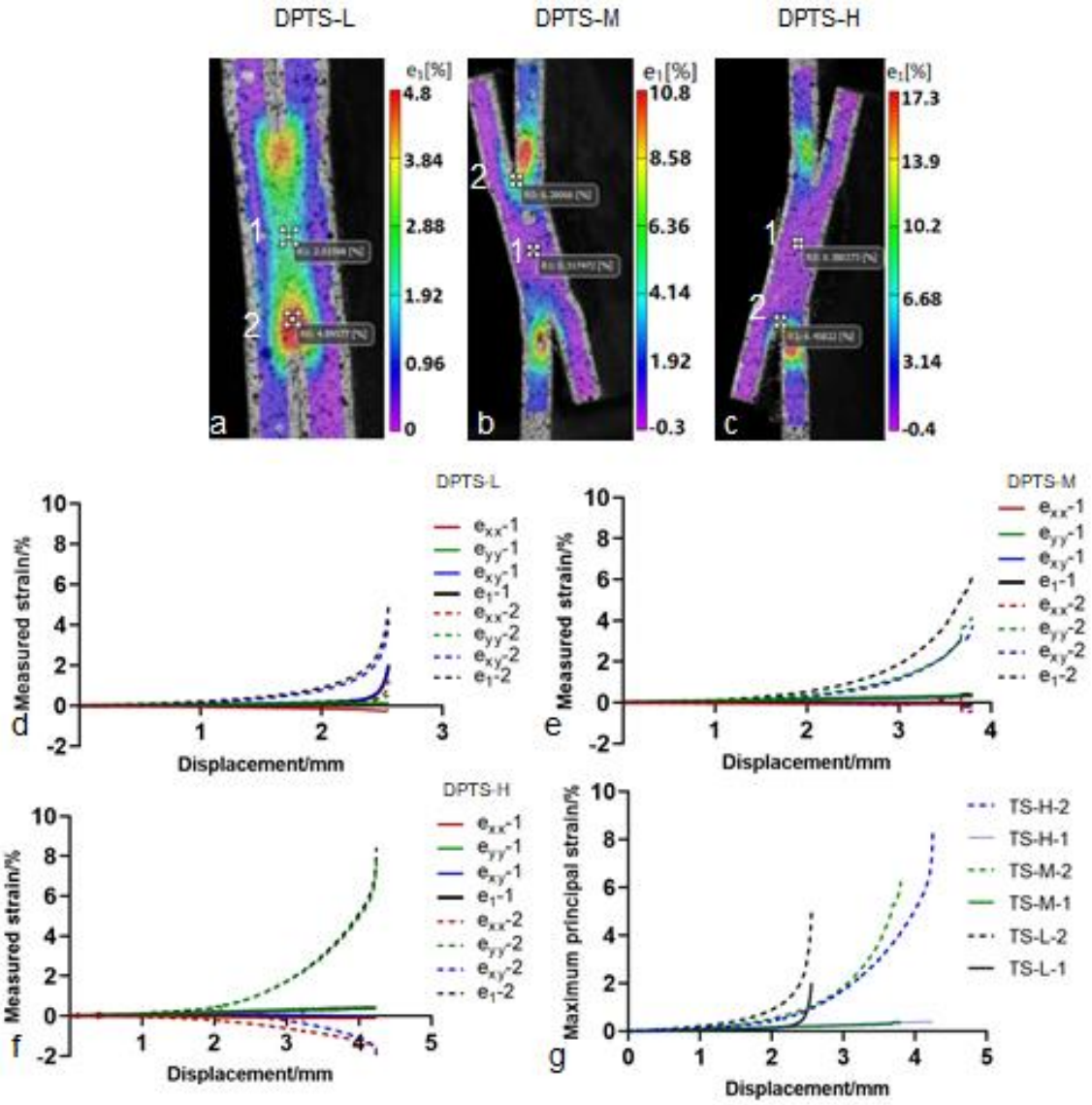

Figure 4.26. Measured strain evolution curves between start point of deformation and start of failure of (a) and (d) DPTS-L, (b) and (e) DPTS-M, (C) and (f) DPTS-H samples and (g) comparison of maximum principal strain at centre of nugget and around corona bond tip within the nugget under low, medium and high welding currents.

Elongated dimples observed in most region of fracture surface in DPTS-L sample in Figure 4.23a, indicates that shear fracture dominates interfacial failure confirming shear stress is the dominated stress of IF mode in DPTS-L samples. Shear dimples have also been observed at the central part of the nugget section for full weld in DP980 [108][11], and out-of-plane shear at circumference of nugget fracture surface in DP980 was reported by researchers [108][11] which is same with that observed in the fracture surface of DPTS-L.

However, quasi-cleavage fracture was reported to be the dominant fracture mode of IF failure in B1500 steel[109], which is different with the observed fracture mechanism in DPTS-L sample. This could be due to the material in the nugget of B1500 steel is much harder that makes the nugget harder to be plastically deformed. Although, DPTS-M sample shows a similar fracture mechanism with DPTS-L sample, larger bending and stretch in HAZ/nugget, Figure 4.24, could apply more complex bending, tensile and shear stress state to the nugget leading to larger portion of out-of-plane shear fracture. In DPTS-H sample, necking occurred in HAZ/ BM where has lowest hardness due to tempering effect in SCHAZ is the main reason to induce Pull-out failure, Figure 4.25. Moreover, it was reported that the conditional fracture toughness K_{IQ} of FGHAZ in DP1000 is the highest, this is owing to the refinement of martensite grains in FGHAZ as it can generate more grain boundaries leading to higher energy requirement for the crack propagation [43]. Meanwhile, the ICHAZ and BM has a lower conditional fracture toughness than FG/CGHAZ [43]. In this case the failure is most likely to take place around the boundary of BM/HAZ when it undergoes large plastic deformation, as shown in Figure 4.25b. This mechanism is also reported by Liu et al. and Nikoosohbat et al. in spot weld under tensile-shear loading condition in DP780 and DP980 steel due to the softening of HAZ [111][230]. In conclusion, welds in DP980 steels also show same failure mechanisms for IF and PF modes.

The microstructure difference of each region of the welds in DP1000 leads to different failure behaviour with LCTS samples. The high volume fraction of martensite in welds of DPTS samples results in higher strength and worse ability to deform. Therefore, DPTS samples could have higher failure load and the nugget of DPTS samples could fail through IF mode when being applied a relatively smaller strain. It is clear that as welding currents increases the weld section become softer, leading to higher plasticity and fracture toughness in nugget, the failure is more likely to occur outside the nugget in DPTS-H samples. This is also confirmed according to the results of LCTS samples. Thus, the improvement of formability in welds could lead to the weld failed through an expected failure mode.

A failure mechanism can be suggested for the studied materials under

tensile-shear loading condition, according to the observed strain evolution. Figure 4.27 shows a simple model of stress analysis at the circumference and interface of weld nugget under tensile-shear loading condition, similar to those observed in low carbon steels in literature[104]. At the start of loading, shear stress τ_1 at the nugget around the corona bond tip dominates the nugget area due to relative motion between upper and lower sides of the nugget by loading in opposite directions, as shown in Figure 4.26d e_{xy}-2. Additionally, stress σ_x caused by rotation of the weld due to unsymmetrical loading tends to open the nugget from the notch tip at where the stress concentrates, as shown by strain component e_{xx}-2 in Figure 4.26d. The nugget of DPTS-L sample is the smallest and least deformable results in shear stress during loading process transferring from the corona bond tips to the centre of the nugget reaching the critical failure strain (around 4.8%) leading to IF mode, e_1-2 in Figure 4.26d. At this stage, the bending is small and tensile stress is small and there almost no plastic deformation in HAZ

In further loading, bending stress could evolved according to equation 4.1, leading to larger bending deformation in HAZ, which cooperates with tensile stress σ_y leading to necking in HAZ , especially around the SCHAZ as it is the weakest region, reducing the stress transferred to nugget. A shear stress τ could occur after the bending of HAZ due to relative motion between HAZ and nugget, Figure 4.19w. However, the nugget of DPTS-M sample is not enough ductile enough to bear the deformation in Y direction caused by bending and tension as well as shear deformation, leading to failure occurred in the nugget. Furthermore, in DPTS-H sample, bending and tension keep increasing leading to larger necking within a softer HAZ than lower current cases. The nugget is the most deformable and largest, meanwhile necking in HAZ reduces the stress transferring into nugget, stress applied to nugget is not sufficient to lead to plastic deformation, therefore, failure occurred in HAZ.

$$\sigma_{bending} = \frac{M}{S} = \frac{6F_y l}{bh^2}$$

Equation 4.1

where F_y is load, $\sigma_{bending}$ is bending stress at corona bond tip, M is bending moment, S is section modulus, l Is width between loading point and

tip of corona bond, b is width of metal sheet and h is thickness of metal sheet.

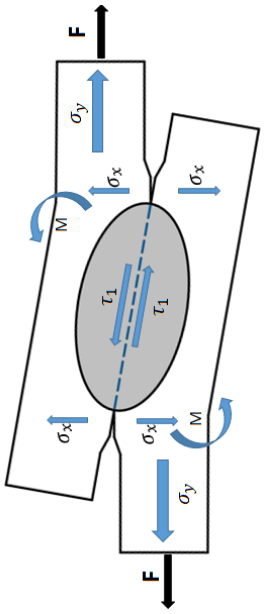

Figure 4.27. Stress analysis at the circumference and interface of the weld nugget during loading.

4.6 Failure mechanism analysis of spot weld under mixed tensile/bending loading condition

4.6.1 Deformation and failure analysis of welds under mixed tensile/bending loading condition (results)

Figure 4.28a and b shows the load-displacement curves of coach-peel samples where lines in black show the CP-L samples while lines in yellow and green indicate CP-M and CP-H samples. Figure 4.28c shows average maximum load and corresponding average displacement with standard deviation for samples with each welding current. Small standard deviations on load and displacement are observed for DPCP and LCCP samples, which might indicate the produced CP samples are repeatable. However, difference is viewed with respect to DPCP samples such as DPCP-L1 and DPCP-H1 sample, Figure 4.28b. This could be due to difference in bending radius of two legs, Figure 4.28d, leading to difference on whole stiffness of different samples. It can be seen that displacement of LCCP samples is much longer than that of DPCP samples, it is

because the much larger bending deformation occurs in HAZ and two legs in LCCP samples, indicated with white arrows in Figure 4.29a. Samples of higher welding current DPCP-H have higher failure load and longer elongation which indicates higher current samples requires more plastic energy, Figure 4.28c. The drop of load of DPCP-L samples might indicate a different failure mode. A higher load is also observed in LCCP samples with applied higher welding current, however, the elongation shows a reverse trend, Figure 4.28b, and this difference is small, Figure 4.28c. This could be due to sample with higher welding current has larger nugget leading to slightly earlier bending in HAZ.

Figure 4.29 shows the failed CP samples, three samples of each welding current were painted with speckle patterns while one sample was tested without speckle patterns.

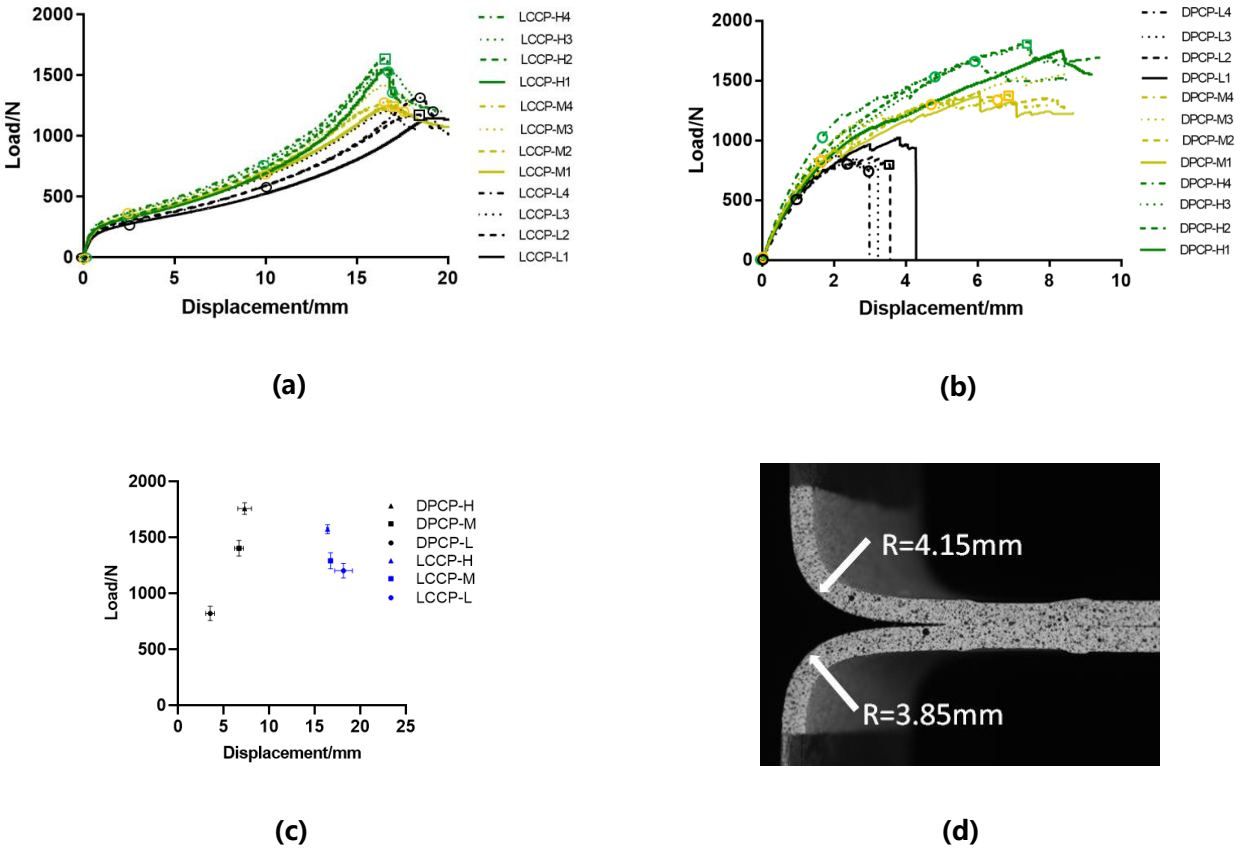

(a) (b)

(c) (d)

Figure 4.28. Load-displacement curves of coach-peel samples in (a) Low carbon steel, (b) DP1000 steel with low medium and high welding currents. The highlighted circles show evolution of failure of the samples without paints while highlighted squares

show the final fracture point of DPCP samples and highest load before failure of LCCP samples, (c) average maximum load vs average displacement with standard deviation for samples with each welding current and (d) difference of bending radius of legs.

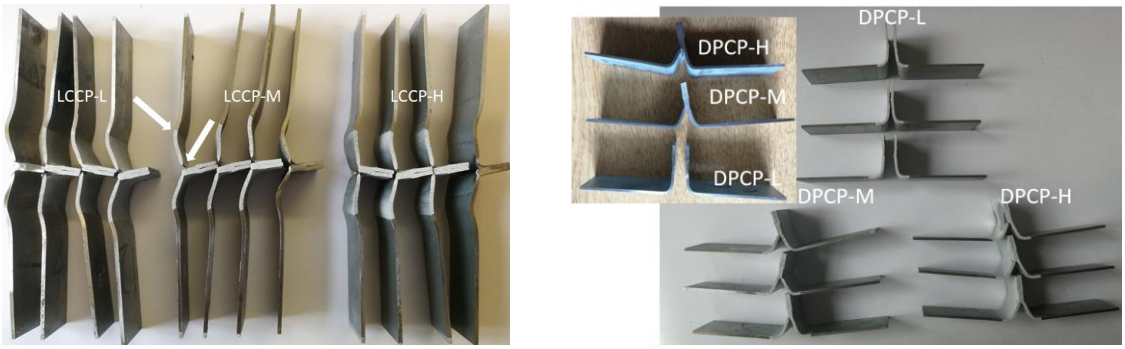

(a) **(b)**

Figure 4.29. Failed coach-peel samples in (a) low carbon steel and (b) DP1000.

Figure 4.30 shows deformation and failure process of spot welds of LCTS-L4, LCTS-M4 and LCTS-H4 samples, images a, b, c and d are highlighted in black (low), yellow (medium) and green (high) circles in load-displacement curves, Figure 4.28b. All samples are failed via PF mode.

The failure process of samples with applied low, medium and high welding currents are similar. Local deformation first occurs around corona bond tips in nugget, white arrows in Figure 4.30b, g and l and bending within HAZ resulting in large plastic deformation, highlighted in yellow arrows in Figure 4.30b, g and l. Local necking is observed within HAZ/nugget for all samples caused by bending and tension leads to fracture within HAZ/nugget leading to PF mode, yellow ellipses in Figure e, j and o.

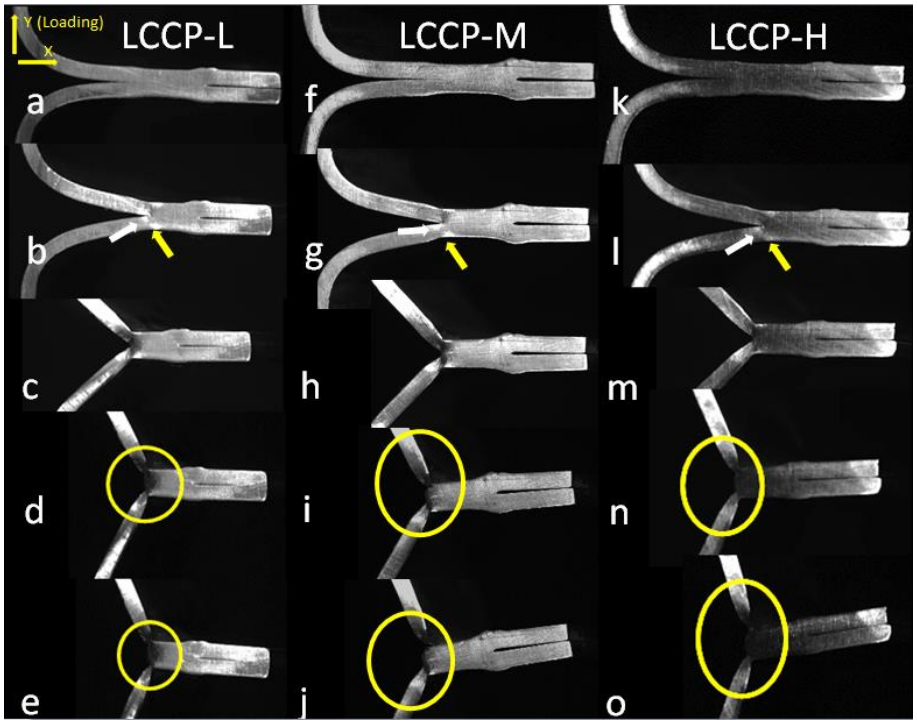

Figure 4.30. Images of deformation and failure process of LCCP samples without paint, (a), (f) and (k), before testing, (b), g) and (l) around start of plastic deformation, (c), (h) and (m) plastic deformation and (d), (i) and (n) highest load before failure and (e), (j) and (o) failure.

Figure 4.31 shows deformation evolution and failure of tested samples indicated in load-displacement curves with black (low), yellow (medium) and green (high) circles as shown in Figure 4.28b representing before test, around yielding, just before final failure and final failure. DPCP-L4 sample fails through IF, while DPCP-M4 and DPCP-H4 samples fail through PIF and PF as observed.

Figure 4.31 a, b c and d show deformation evolution and failure of DPCP-L sample. The local deformation initially occurs around the tip of corona bonds and boundary of HAZ, blue and yellow arrows in Figure 4.31b, and then crack propagates through the interface of nugget from the corona bond tip resulting in IF mode, Figure 4.31c. DPCP-M sample fails via PIF as shown in Figure 4.31h. Local deformation firstly occurs around corona bond tip adjacent to the nugget same with DPCP-L sample, Figure 4.31f. And then, it propagates into the nugget along interface for a certain distance until deflecting its path to the sheet thickness direction, highlighted in yellow circle in Figure 4.31g, leading to

PIF mode. Local necking is observed in the loading leg according to deformation band highlighted in yellow circle in Figure 4.31h, and bending is observed within HAZ in Figure 4.31g. DPCP-H fails through PF mode as shown in Figure 4.31l. The materials also starts to deform around the corona bond, Figure 4.31j. However, localized necking propagates the crack along around 45° instead of passing through the nugget, highlighted in yellow circles in Figure 4.31 k and l.

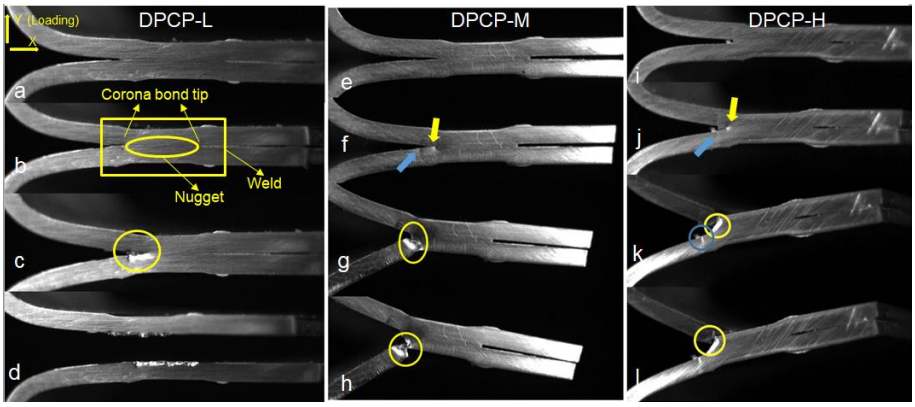

Figure 4.31. Images of deformation and failure process of DPCP samples without paint, (a), (e) and (i), before testing, (b), (f) and (j) around yield point, (c), (g) and (k) during testing and (d), (h) and (l) final failure.

Figure 4.32 reveals the associated measured out-of-plane displacement at the onset of failure. The maximum out of displacement at onset of failure is around 0.07mm in DPCP samples while out-of-plane displacement around position of failure is around 0.2mm in LCCP samples, the corresponding in-plane displacement are around 0.2mm and 0.65mm, much larger than out-of-plane displacement. This indicates a small image distortion which is due to the same reason with TS samples and 2D maximum principal strain could indicator of failure.

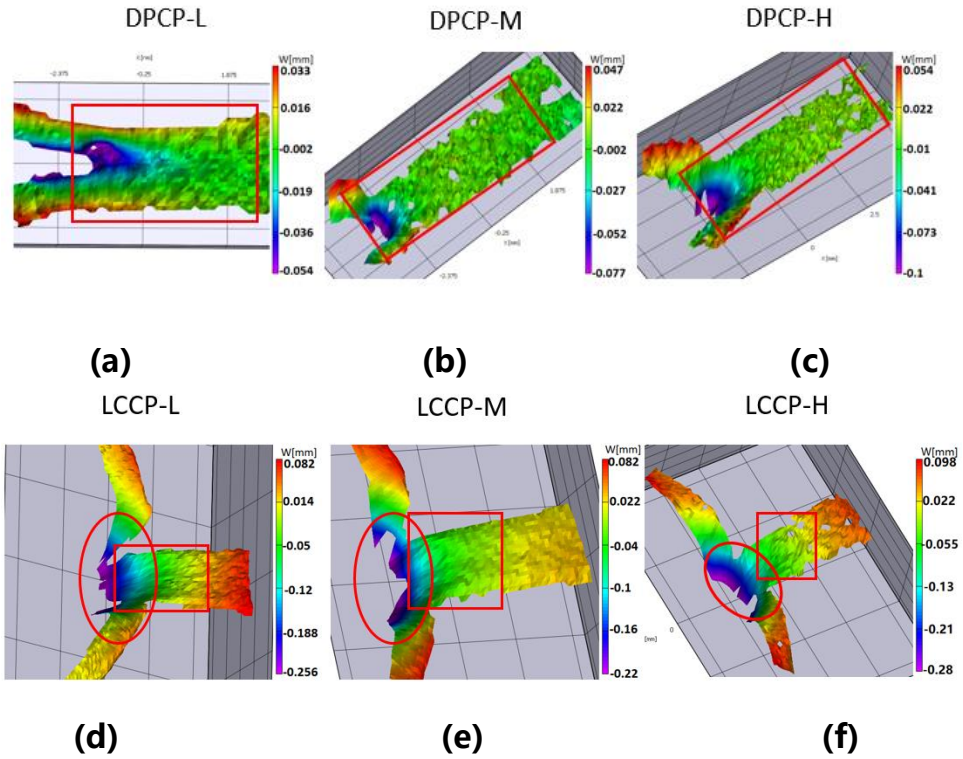

Figure 4.32. (a), (b) and (C) out-of-plane displacement of DPCP-L, DPCP-M and DPCP-H samples while (d), (e) and (f) out-of-plane displacement of LCCP-L, LCCP-M and LCCP-H samples.

The strain dependency curves with respect to the selected subset size of DPCP and LCCP samples are shown in Figure 4.33. A convergence criteria same with TS samples was used. Maximum principal strain keeps increasing as subset size decreases, and subsequently comes to convergence when subset size decreases to around 23 pixels. Thus, a subset size of 23 pixels was selected for DPCP and LCCP samples with physical size of 322 micron and 300 micron as well as spatial resolution of 14 micron/pixel and 13 micron/pixel. Additionally, systematic error of strain measurements were analysed for DPCP and LCCP samples, Figure 4.34. Ten images of unloaded sample were used to carry out the analysis. The maximum strain values are around 0.004% indicating an ignorable systematic error in strain measurement.

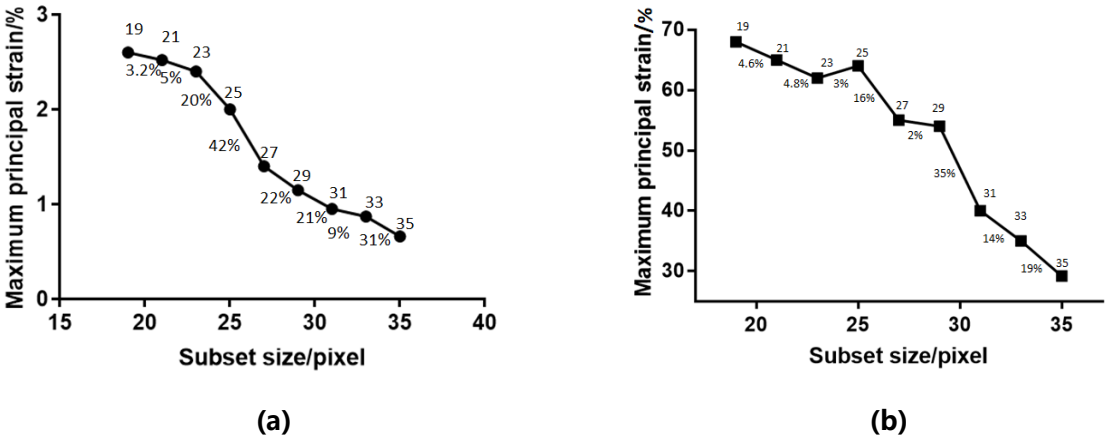

(a) (b)

Figure 4.33. Strain dependency of (a) DPCP and (b) LCCP samples.

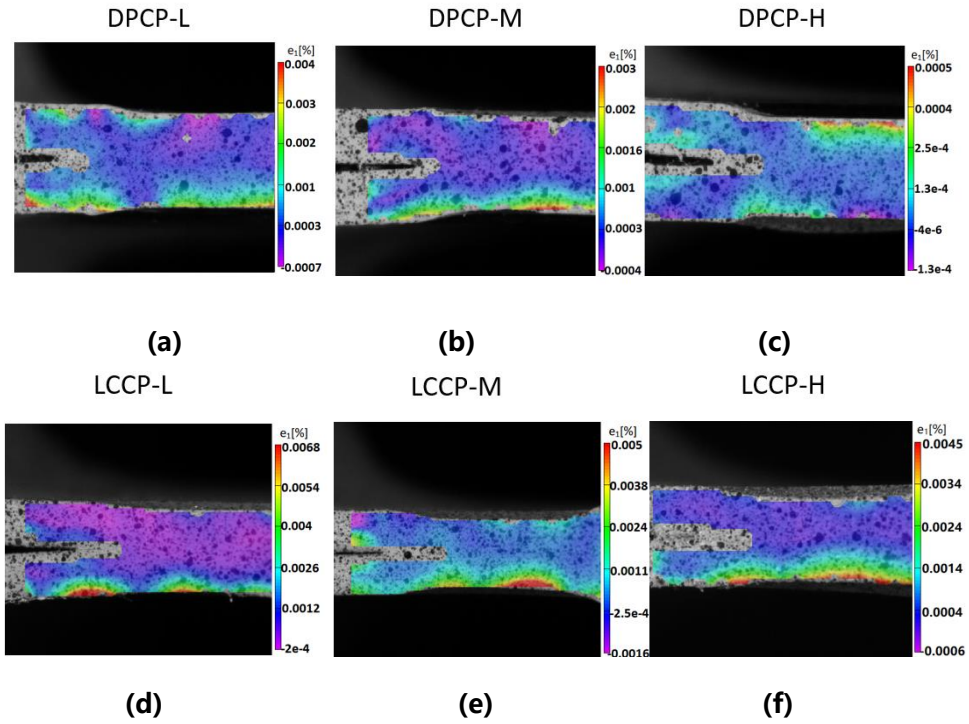

(a) (b) (c)

(d) (e) (f)

Figure 4.34. Uncertainty analysis, systematic error of maximum principal strain of (a) DPCP-L, (b) DPCP-M, (c) DPCP-H, (d) LCCP-L, (e) LCCP-M and (f) LCCP-H samples.

Figure 4.35 shows the distribution and evolution of measured strain components of LCCP samples (LCCP-L2, M2 and H2) based on the selected points of displacement, indicated in Figure 4.35 and black, yellow and green squares in Figure 4.28a.

Strain patterns of LCCP-L, LCCP-M and LCCP-H samples are similar with each other. For instance, in LCCP-L samples, bending occurs in HAZ and

becomes larger as longer displacement. This is indicated by strain concentration in X direction shown in Figure 4.35a_1, a_5 and a_9, which is the main factor leading to PF mode according to maximum principal strain at failure, Figure a_{12}. Shear deformation in HAZ also becomes larger, Figure 4.35a_3, a_7 and a_{11}, which also contributes to the failure. Compression deformation is observed in nugget in Y direction through the whole process before failure and necking is observed within HAZ, which could be due to the bending deformation in HAZ squeezes the material near the indents toward nugget and stretch the material around corona bond tips, indicated in yellow and white arrows in Figure 4.32a_6. Moreover, the failure strain could be determined based on the maximum principal strain at the location of strain concentration before failure, which is around 58%, 56.5% and 54.5% for LCP-L/M/H samples, Figure 4.32a_{12}, b_{12} and c_{12}.

Increasing the welding current does not have any influence on the failure behaviour of LCCP samples according to the above analysis.

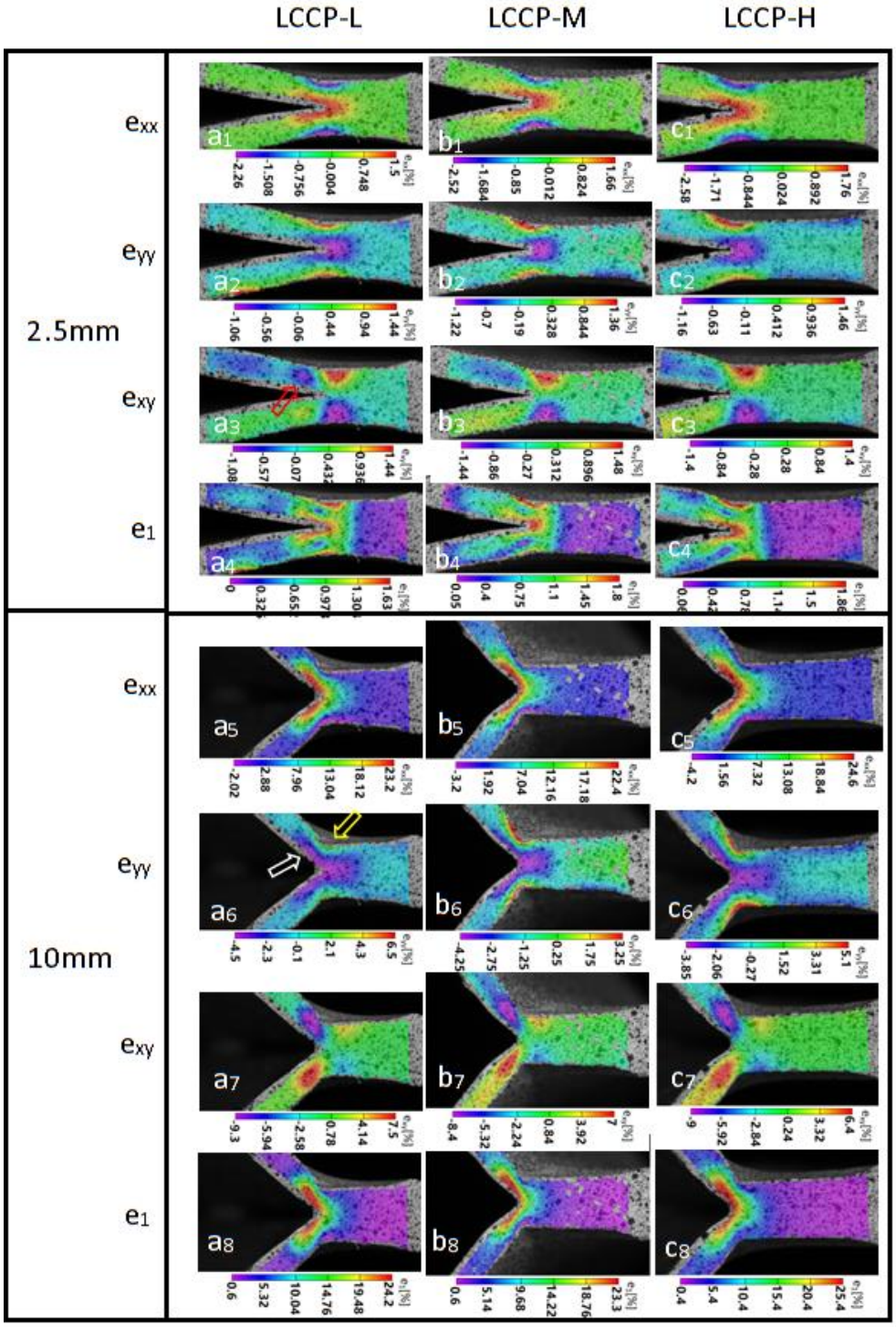

Figure 4.35. Distribution and evolution of strain components of various loading stages for (a) LCCP-L2, (b) LCCP-M2 and (c) LCCP-H2 samples, showing strain components normal to loading direction, e_{xx}, align to loading direction e_{yy}, shear strain component e_{xy}, and maximum principal strain e_1.

Continue to next page

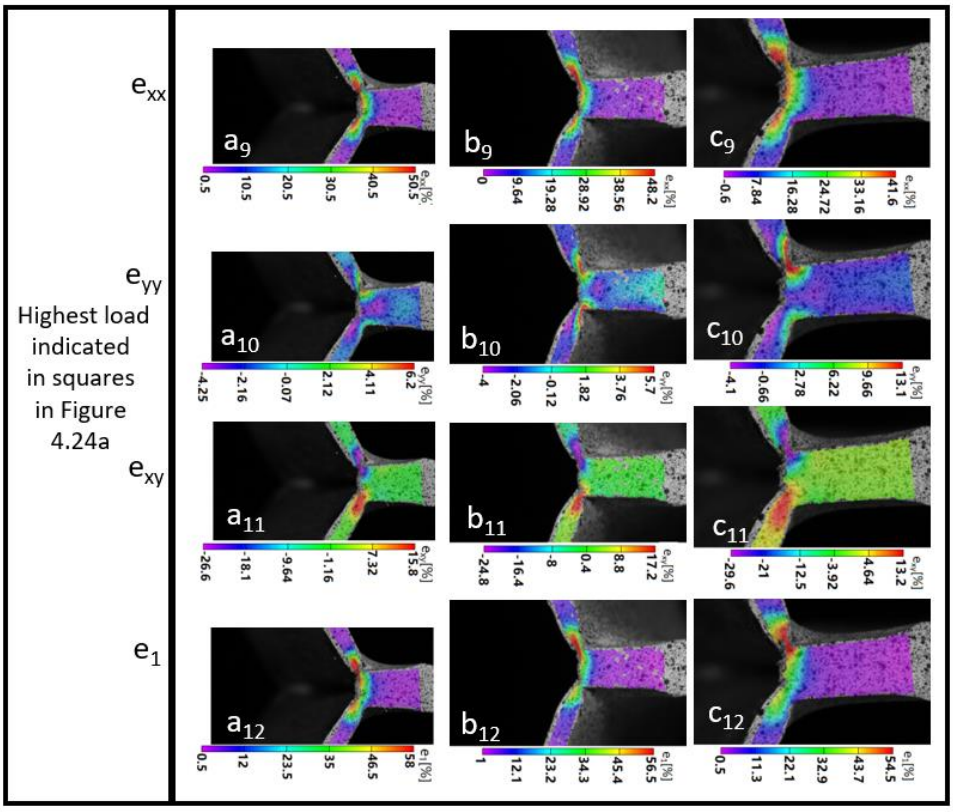

Figure 4.36 shows the distribution and evolution of measured strain components of DPCP-L2/M2/H2 samples based on the selected displacement points, indicated in Figure 4.36 and black, yellow and green squares in Figure 4.28b.

Figure 4.36a shows the strain evolution of DPCP-L sample. At 1.5mm where is the around the beginning of deformation, it is clear that strain in X, Y and shear directions concentrates around the corona bond tips , Figure 4.36a_1, a_2 and a_3, which might has great contribution to maximum principal strain, shown in Figure 4.36a_3. However, strain e_{yy} keeps concentrating around the crack path and grows much faster than strain e_{xx} and shear strain e_{xy}, shown in Figure 4.36a_5, a_6, a_7, a_9, a_{10}, and a_{11}, it becomes more and more critical in maximum principal strain, and subsequently leads to IF mode, Figure 4.36a_8 and a_{12}. The crack initiates when the maximum strain reaches 2.54% which might be the strain at the onset of failure, 4.36a_8.

In contrast, different strain patterns are observed in DPCP-M samples leading to PIF mode. At 1.5 and 2.2mm, considering maximum principal strain

distribution in Figure 4.36b_4 and b_8, strain concentration in X and shear direction play more important role while only compression is observed ahead of the corona bond tip, Figure 4.36b_1-b_3 and b_5-b_7, showing a delay of tensile deformation in Y direction. In further loading up to crack initiation shown in Figure 4.36b_9-b_{16}, strain concentration occurs in Y direction around the corona bond tip, and become the domination of crack initiation according to maximum strain distribution shown in Figure 4.36b_{16}. Meanwhile, compression deformation Y direction moves from around the corona bond tips towards the nugget. Figure 4.36b_{17}-b_{20}, at 5.8mm shows that the crack propagates into the nugget along the faying face indicating IF mode, and strain concentration in Y direction around the crack makes the greatest contribution to maximum principal strain shown in Figure 4.36b_{20}. Thus, considering the strain evolution of DPCP-L sample, strain concentration in Y direction is most likely to dominate the IF mode. Figure 4.36b_{21}-b_{24} shows the strain distribution before final failure, strain concentration observed in X around crack tip in nugget are likely to lead to crack deflection to thickness direction resulting in PF mode according to maximum principal strain, Figure 4.36b_{21} and b_{24}. Bending around the crack is observed increasing through the whole process of deformation evolution and failure, which could be the reason leading to increase of strain in X direction. Moreover, the failure starts when the maximum strain is around 4.28% at the corona bond tip, Figure 4.36b_{16}.

Figure 4.36c shows the strain evolution of DPCP-H sample. Compression deformation around the corona bond tip is also observed until the crack initiates at 5.8mm displacement indicating that opening of nugget takes place even later than that of DPCP-M sample, Figure 4.36c_{18}. This could be due to larger deformation in HAZ in X direction caused by bending delaying the opening of corona bond tip in Y direction, as indicated with red arrows in Figure 4.36a_5, b_5 and c_5. Moreover, strain concentration in X direction contributes the most to maximum principal strain, leading to crack initiation and propagation in HAZ before strain e_{yy} is sufficient to open the nugget, causing PF mode, Figure 4.36C_{17}, c_{20}, c_{21} and c_{24}. The maximum principal strain at crack initiation is larger than low and medium current samples, which is around 4.52% at the corona bond tip, Figure4.36c_{20}.

In addition, compressive strain is observed within nugget of samples in each welding current which might resist the crack from passing through the nugget. The failure strain initiating the cracks could be determined based on the maximum principal strain at corona bond tip, which is around 2.54%, 4.28% and 4.52% for DPCP-L/M/H samples, Figure 4.36$a_{8,}$ b_{16} and c_{20}. The crack opening mode is the dominant factor causing IF of DPCP-L and IF phase of DPCP-M samples. Increasing the welding current reduces the deformation in loading direction in nugget, and deformation localisation along loading legs as well as shear strain localisation in HAZ becomes the dominant factor leading to PF phase of DPCP-M and PF of DPCP-H samples.

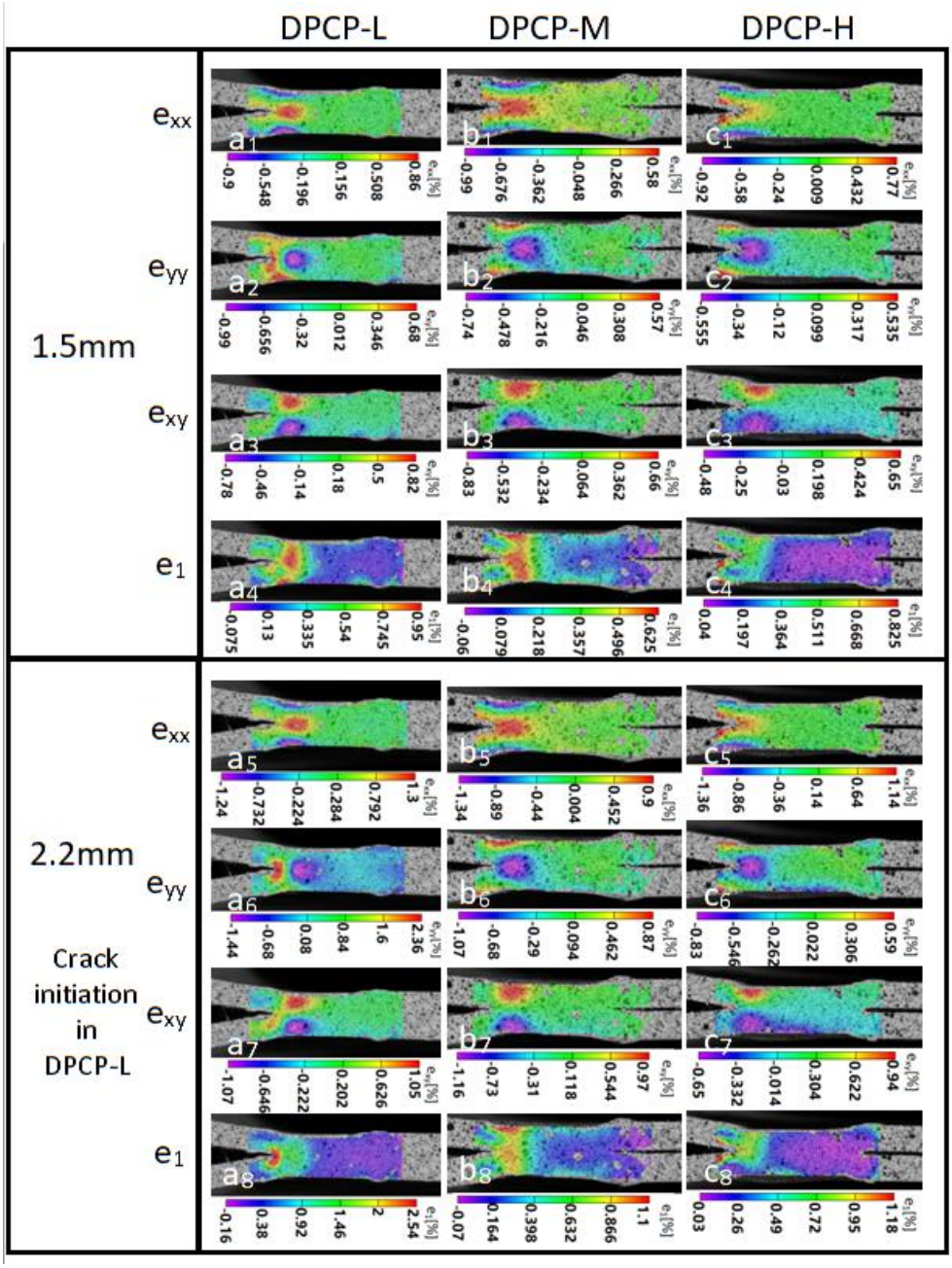

Figure 4.36. Distribution and evolution of strain components of various loading stages for (a) DPCP-L2, (b) DPCP-M2 and (c) DPCP-H2 samples, showing strain components normal to loading direction, e_{xx}, align to loading direction e_{yy}, shear strain component e_{xy}, and maximum principal strain e_1.

Continue to next page.

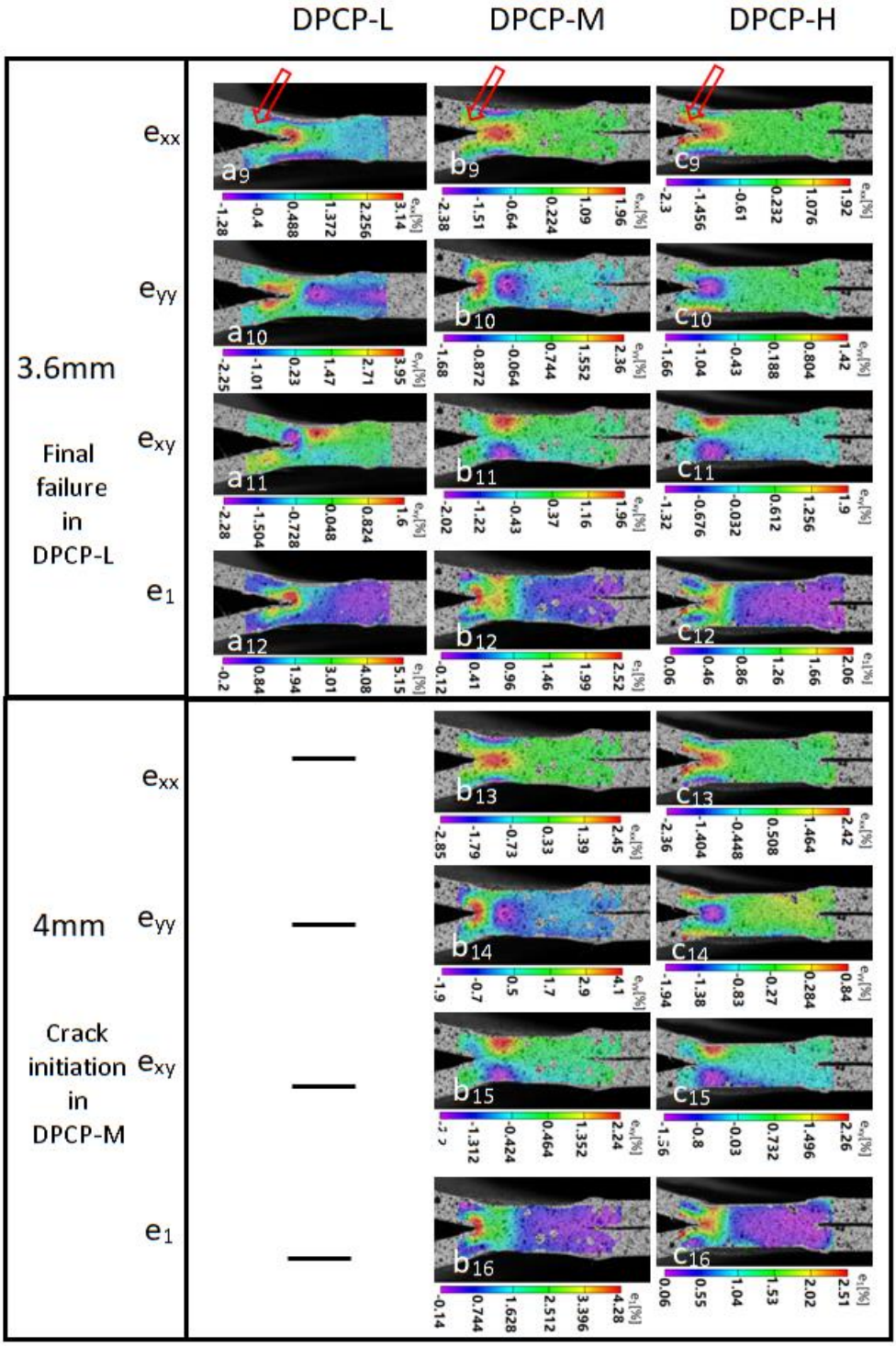

Continue to next page.

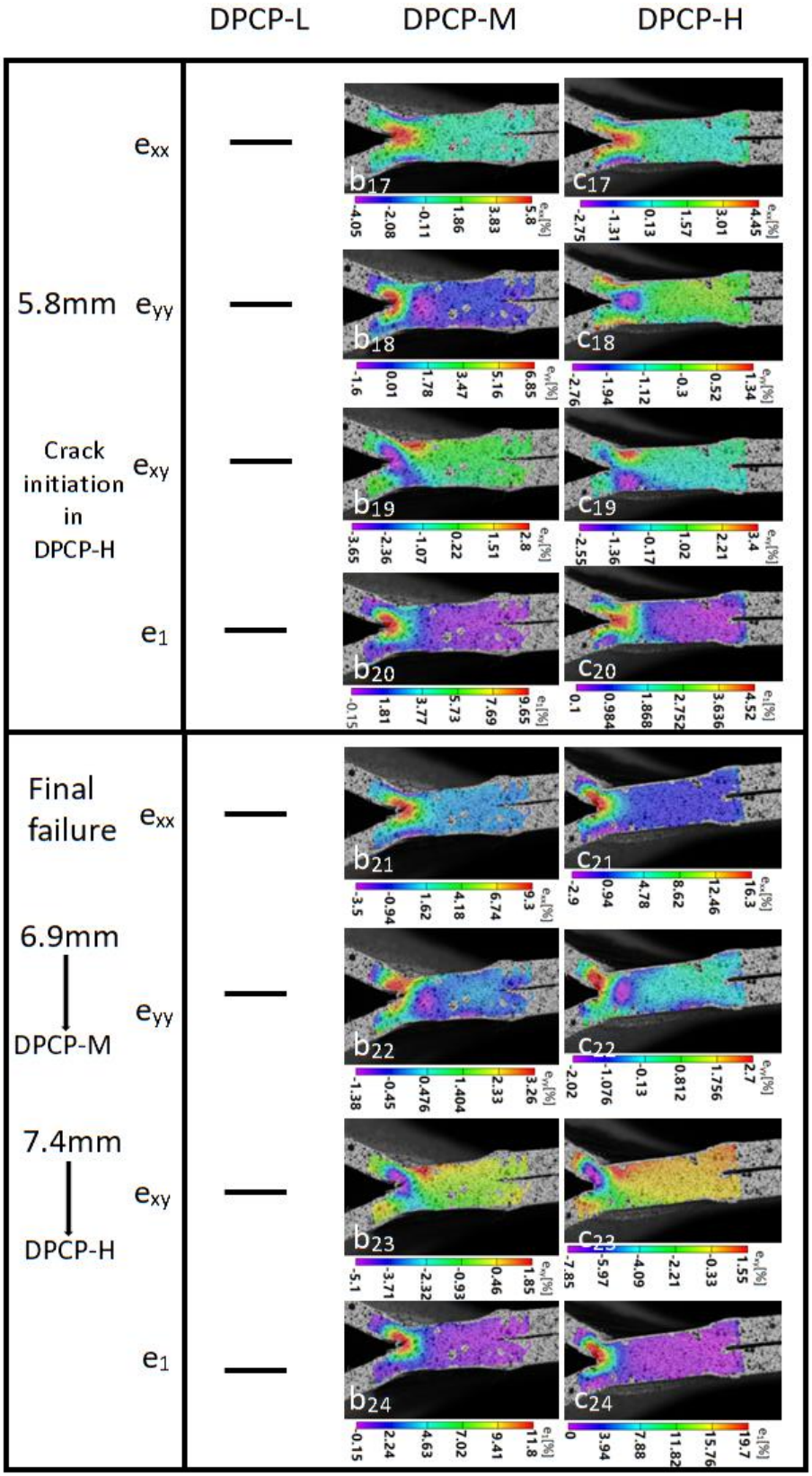
DPCP-L
DPCP-M
DPCP-H
exx
eyy
exy
e1
5.8mm
Crack initiation in DPCP-H
Final failure
6.9mm
DPCP-M
7.4mm
DPCP-H
b17
c17
b18
c18
b19
c19
b20
c20
b21
c21
b22
c22
b23
c23
b24
c24

4.6.2 The effect of welding current on fracture mechanism of welds under mixed tensile /bending loading (results)

Figure 4.37 shows fracture surfaces and morphology of cut surfaces of LCCP-L sample. Deformation bands observed around the corona bond tip beneath cut surface indicates substantial stretch, highlighted in blue and yellow squares in Figure 4.37a. Elongated dimples are observed in top part of nugget indicating shear fracture surface. Out-of-plane deformation is observed in nugget highlighted in red square in Figure 4.37a, which might be due to necking in HAZ highlighted red square in Figure 4.37b. Morphology of cut surface shows the failure occurs at HAZ/nugget boundary. The ferrite within nugget along the crack path are massively stretched and elongated indicating that failure could be caused by tension highlighted in blue, green and yellow squares in Figure 4.37b. The fracture mechanisms of LCCP-M and LCCP-H sample are same with LCCP-L sample according to the observation in Figure 4.38 and 4.39.

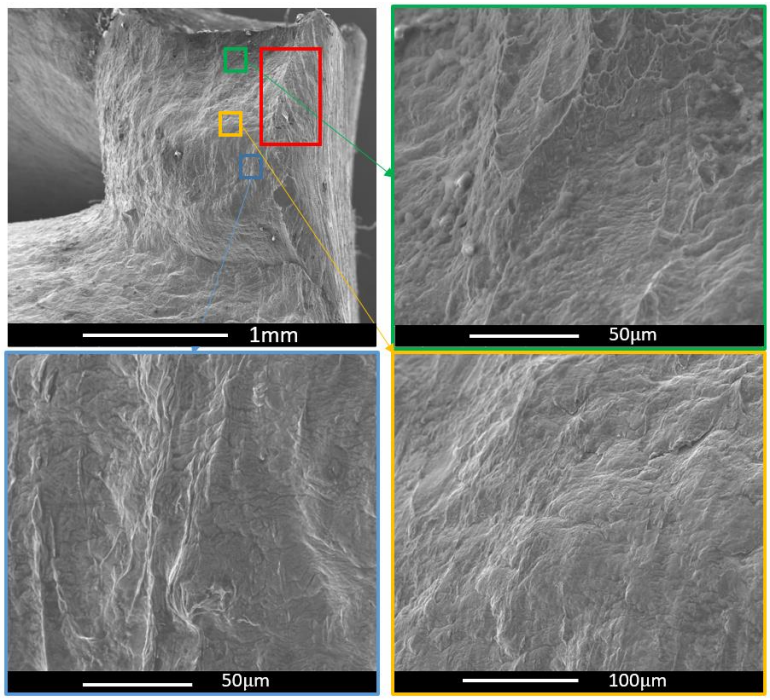

(a)

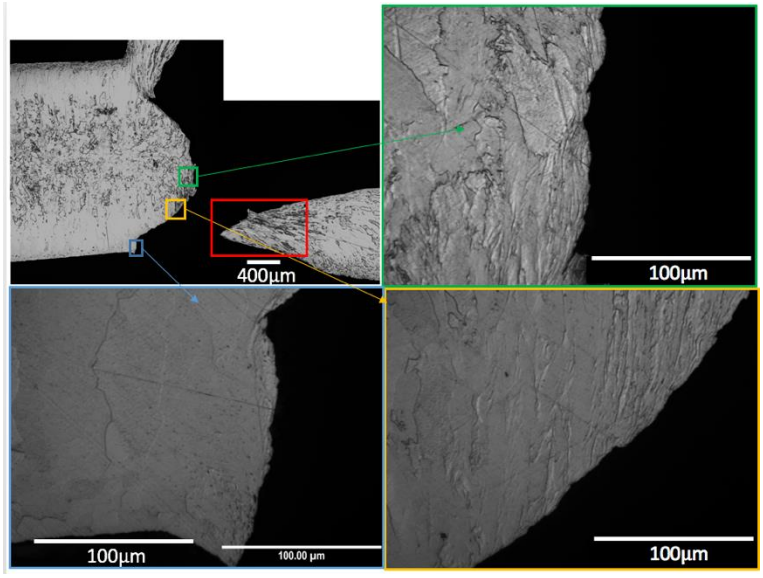

(b)

Figure 4.37. Fracture surfaces (a) and microstructural morphology of LCCP-L samples showing domination of necking.

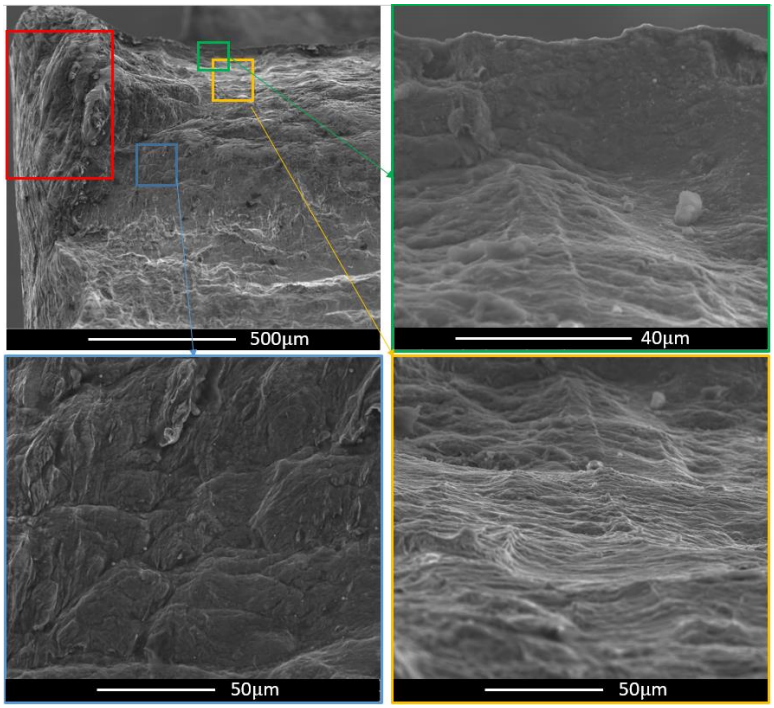

(a)

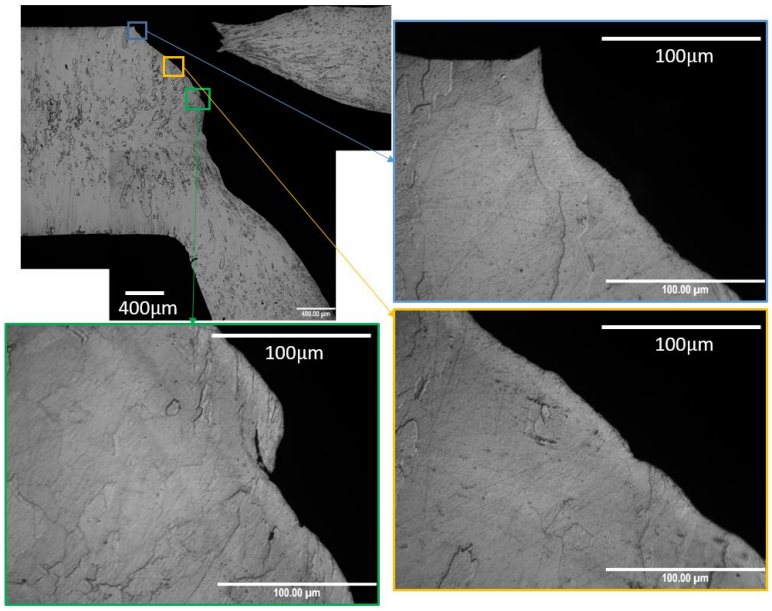

(b)

Figure 4.38. Fracture surfaces (a) and microstructural morphology of LCCP-M samples showing domination of necking.

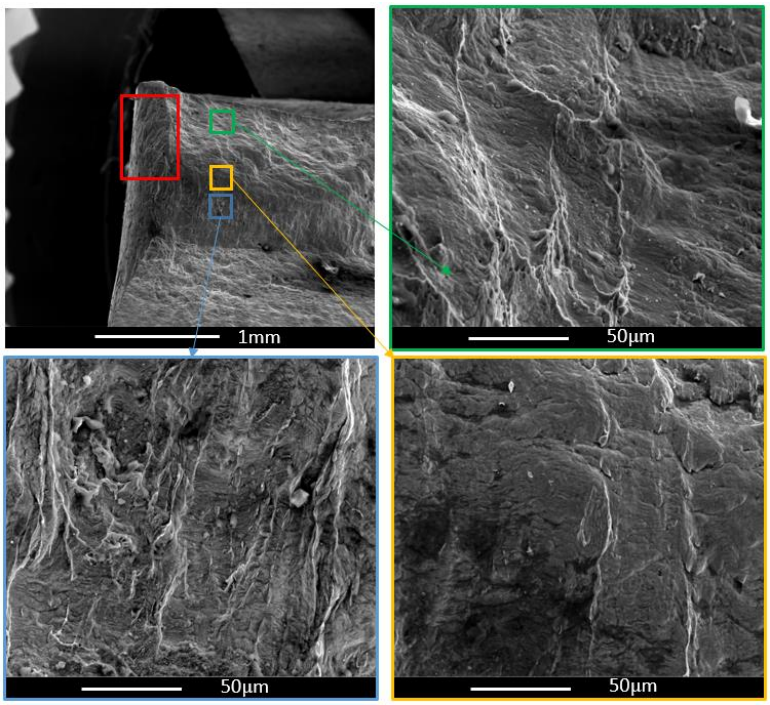

(a)

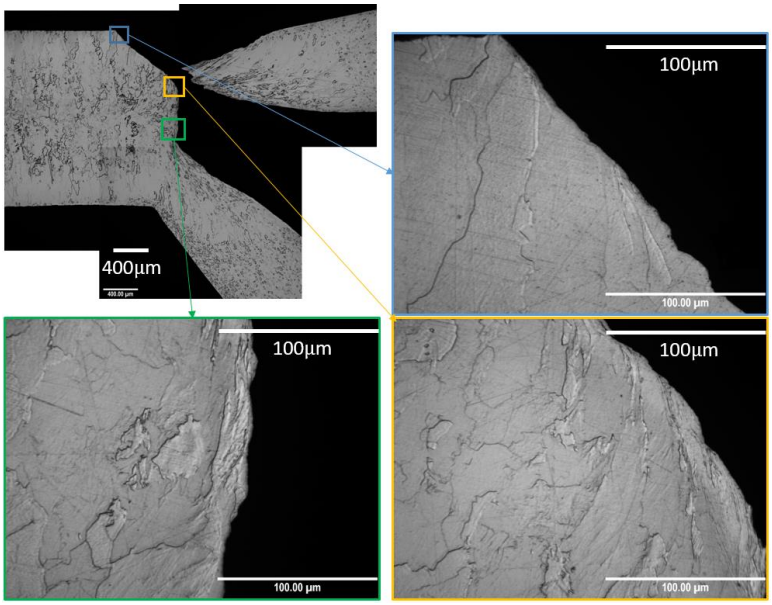

(b)

Figure 4.39. Fracture surfaces (a) and microstructural morphology of LCCP-H samples showing domination of necking.

Figure 4.40 shows the fracture surface of nugget is in IF mode. Ductile fracture mainly locates at where close to the edge of cut section, highlighted in blue square in Figure 4.40a. The multifaceted fracture surface with ductile

dimples indicates quasi-cleavage fracture [231], highlighted in yellow square in Figure 36a, dominating IF mode, which might be caused by stress normal to the fracture surface. This mechanism could be confirmed by the morphology of cut surface shown in Figure 4.40b. The zigzag crack cuts through the almost undeformed martensite and continuously changes its direction, which might indicate cleavage fracture caused by stress normal to fracture surface.

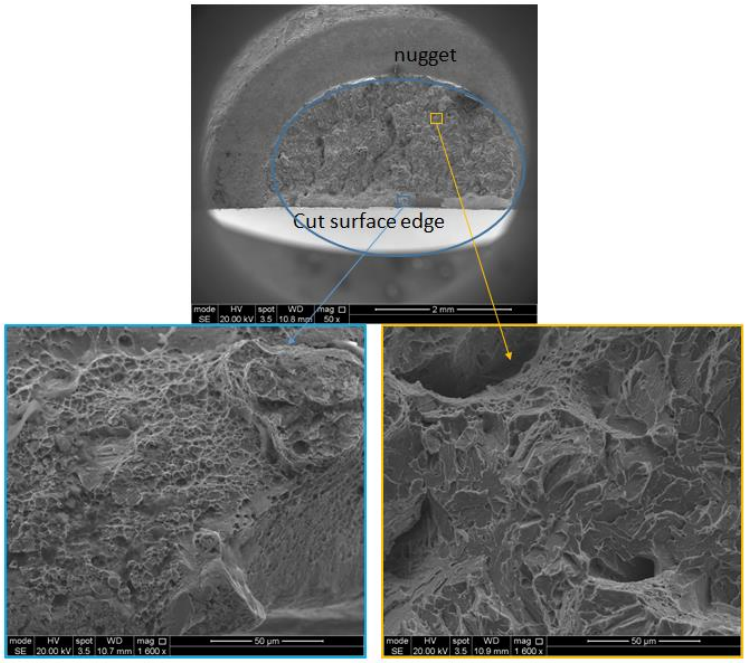

(a)

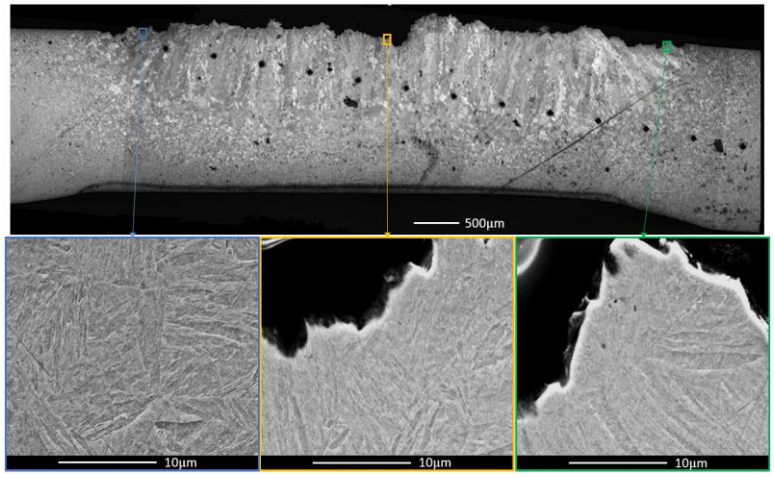

(b)

Figure 4.40. Fracture surfaces (a) and microstructural morphology (b) of DPCP-L samples showing domination of quasi-cleavage fracture.

In contrast to DPCP-L sample, fracture surfaces of DPCP-M sample contain two phases, IF and PF, highlighted in blue and dark green squares in Figure 4.41. Brittle facets with ductile dimples indicates quasi-cleavage dominating the IF phase, highlighted in yellow square in Figure 4.41, while ductile dimples are also observed near the cut surface, highlighted in light green squares in Figure 4.41. However, fracture surface of PF phase shows two different fracture modes, highlighted in dashed red and purple rectangles in Figure 4.41, quasi-cleavage fracture dominates the first part (highlighted in red square in Figure 4.41) while elongated dimples indicate that pure shear fracture dominates the second part, purple squares in Figure 4.41.

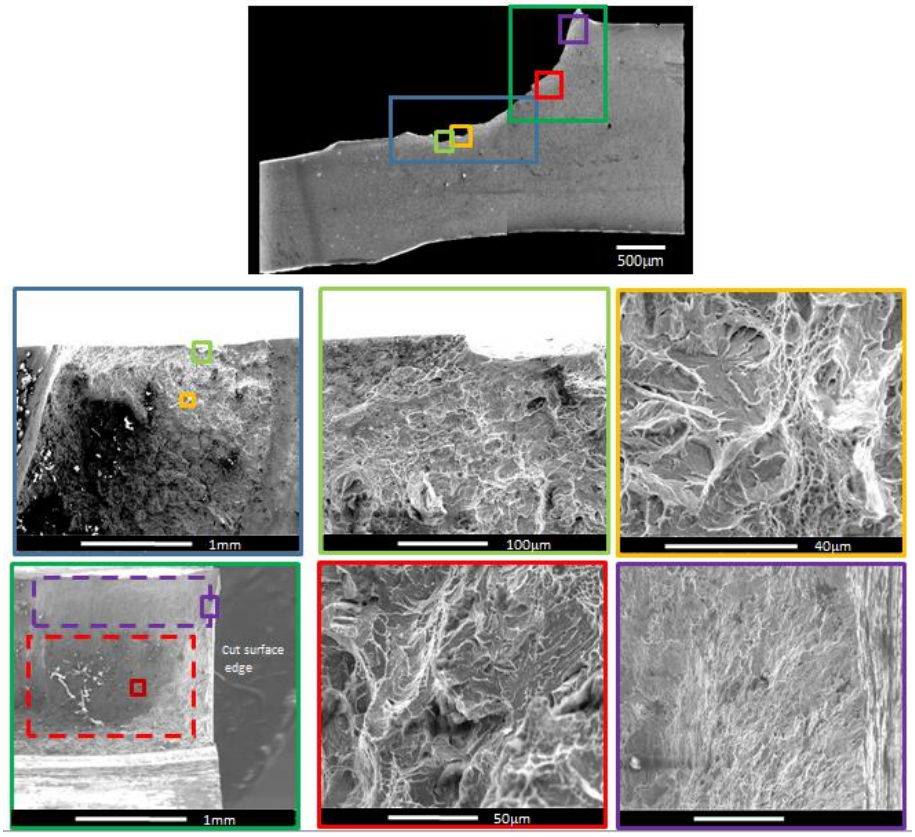

Figure 4.41. Fracture surfaces of DPCP-M samples showing domination of shear and quasi-cleavage failure.

Figure 4.42 reveals fracture surfaces of DPCP-H samples failed through PF mode due to the crack path is around the nugget and cut into CGHAZ along thickness direction, shown in top left image. The failure also includes two parts, highlighted with blue and purple dashed rectangular in Figure 4.42, ductile dimples with less portion of brittle facets indicates that ductile fracture

dominates the first part, while pure shear failure dominates the second part, highlighted in blue, yellow and purple squares in Figure 4.42. The observed fracture surface might indicate that ductile and shear fracture leads to PF mode of DPCP-H samples.

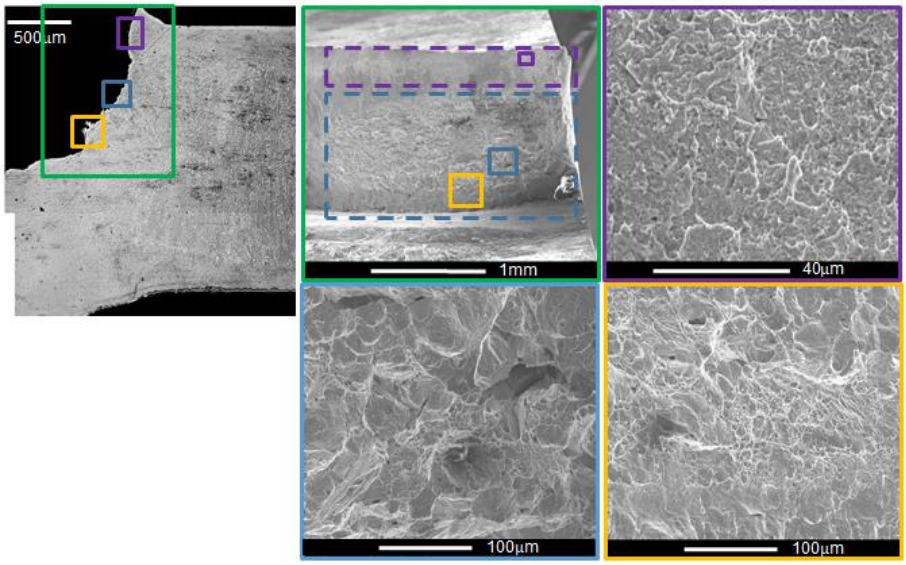

Figure 4.42. Fracture surfaces of DPCP-H samples showing domination of shear and ductile failure.

4.6.3 Deformation and failure analysis of welds under mixed tensile/bending loading (DPMiCP samples results)

Figure 4.43 shows the load-displacement curves for the micro CP samples. The black lines show DPMiCP-L samples with low welding current, lines in green indicate DPMiCP-M samples with medium welding current while Lines in yellow indicate DPMiCP-H samples with high welding current. Due to the limited cross head movement of in-situ tensile machine, samples were loaded to end of travel rather than final fracture as shown in Figure 4.45, 4.46 and 4.47. The load-displacement curves show a good consistency in the tested samples. A higher load was obtained for samples with applied higher welding current might indicate samples with higher welding current require higher plastic energy. The load drops in the curves are due to the stress relaxation of the system during the interval when the tensile machine is stopped. Figure 4.44 shows the tested samples.

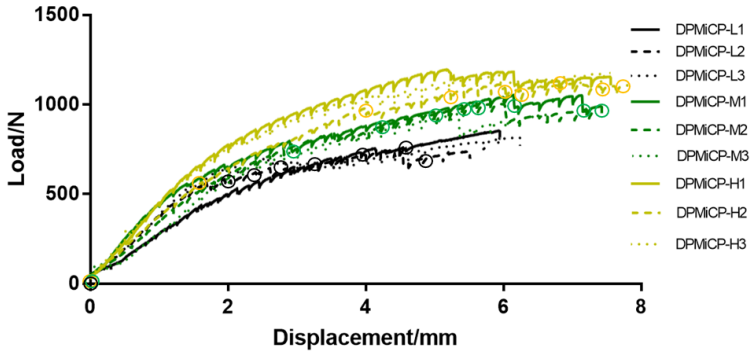

Figure 4.43. Load-displacement curves of samples with low (DPMiCP-L), medium (DPMiCP-M) and high (DPMiCP-H) welding currents. The highlighted circles show process of failure of the samples.

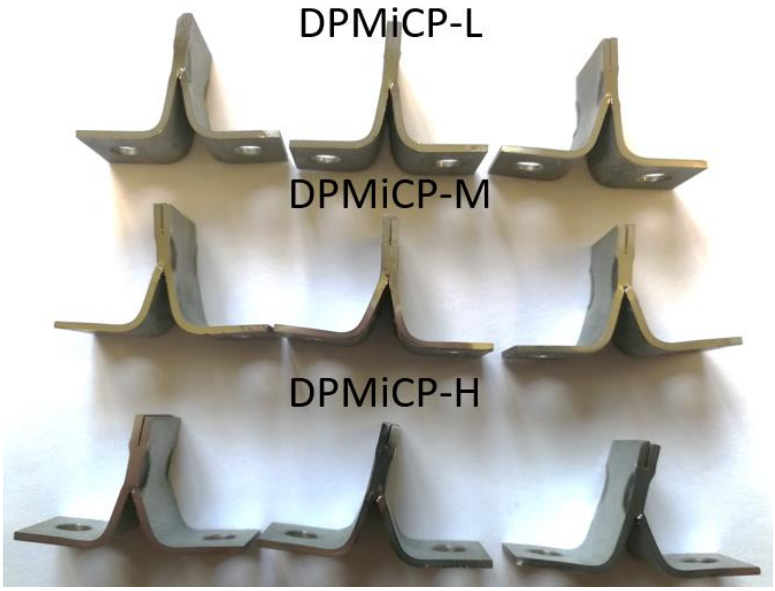

Figure 4.44. Failed DPMiCP samples under three different welding currents.

Micrographs of the sample corresponding to the selected points, indicated by circles, of load-displacement curves are shown in Figure 4.45, 4.46 and 4.47. These images show crack initiation and propagation of samples with applied low, medium and high welding currents, which are used to investigate the failure mechanism of welds.

Figure 4.45 shows the crack initiation and propagation of DPMiCP-L sample. It starts with the opening of corona bond followed by localized deformation around the tip at the boundary between CGHAZ and nugget, indicated by white and yellow arrows in Figure 4.45b and c. The loading

direction is shown in Figure 4.45a. Deformation bands are observed due to plastic deformation ahead of the corona bond tip within nugget leading to formation of two cracks indicated with black and red arrows in the enlarged image, Figure 4.45d, the subordinate crack, black arrow, forms in CGHAZ, Figure 4.45e and f, while the dominate crack, which is normal to the loading direction, red arrows, cut into the nugget along the plastic localised deformation bands resulting in interfacial failure of the weld, Figure 4.45e to 4.45i. This dominate crack is possibly induced by mode I fracture (opening) leading to plastic deformation of martensite in the nugget due to the loading direction is at horizontal direction which is perpendicular to the crack path. The subordinate crack stopped propagating which might because the small martensite grains in CGHAZ are greater dislocated leading to larger resistance to the crack propagation.

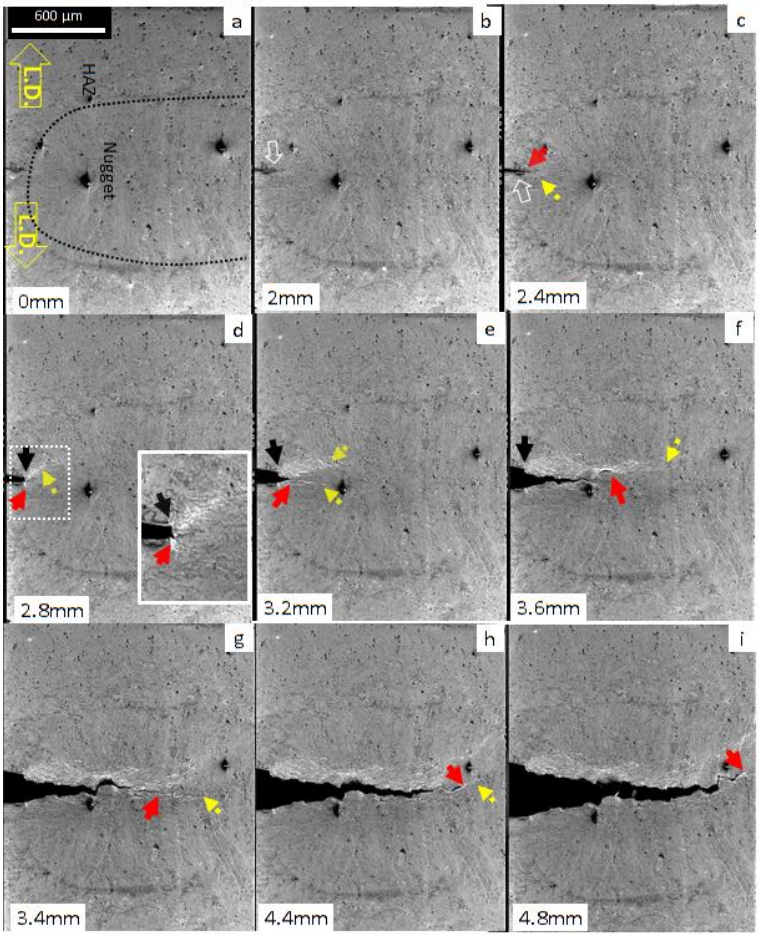

Figure 4.45.Microscopic images show crack initiation and propagation of DPMiCP-L sample indicating IF mode, white arrows indicate corona bond, yellow arrows show localized deformation bands, black arrows show subordinate crack and red arrows show dominate crack.

For DPMiCP-M samples, Figure 4.46, the opening of corona bond tip is observed in Figure 4.46b which is same with DPMiCP-M sample. The loading direction is shown in Figure 4.46a.The large stress concentration at the corona bond tip results in formation of two sharp cracks, black and red arrow, in Figure 4.46c. The subordinate crack, stops developing after a certain propagation, black arrows in Figure 4.46d and e. The dominate crack, red arrows, cuts into the nugget through the martensite grains until its deflection to about 45° towards the thickness direction of the nugget showing IF phase, Figure 4.46d to 4.46f. It is then open up following the deformation bands, yellow arrow, Figure 4.46g to 4.46i, and expected to pass through the red dashed line by a

shearing process leading to PF phase, Figure 4.46i.

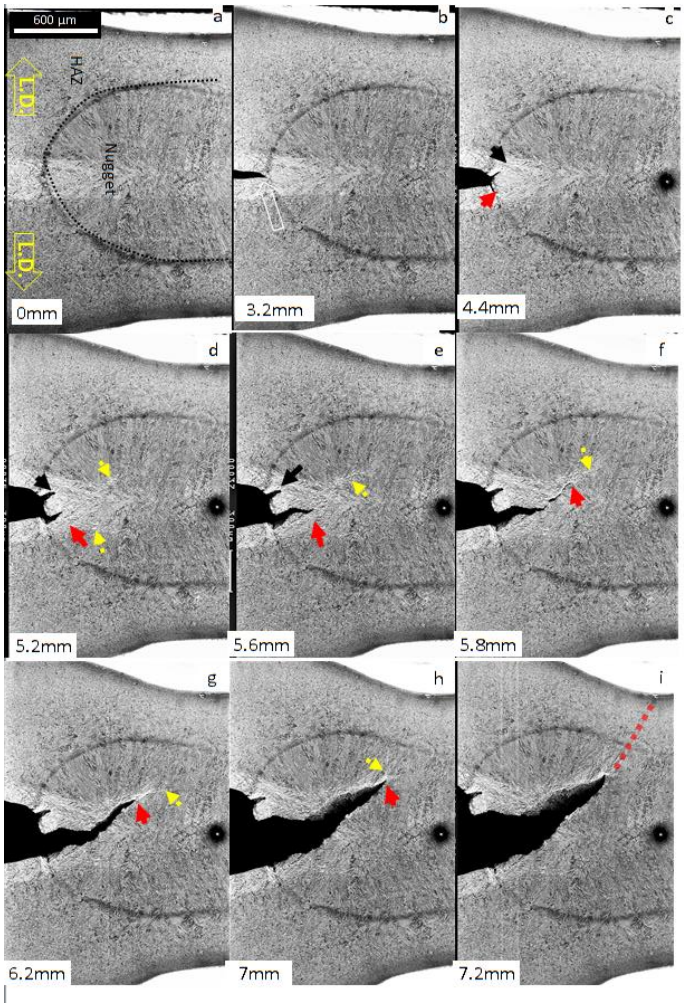

Figure 4.46.Microscopic images show crack initiation and propagation of DPMiCP-M sample indicating PIF mode, the yellow arrows show localized deformation bands, black arrows show subordinate crack and red arrows show dominate crack, while the red dashed line indicate potential subsequent crack path.

Figure 4.47 shows the failure process of DPMiCP-H sample failed through PF mode. The loading direction is shown in Figure 4.47a. Same with samples with applied low and medium welding current, the failure process starts with opening of corona bonds, white arrow in Figure 4.47b and c, followed by two cracks formed at the boundary of the nugget due to large plastic deformation caused by stress concentration at the crack tip, black and red arrows in Figure 4.47d. The subordinate crack is slightly open up without propagating into the nugget, black arrows in Figure 4.47d to 4.47 f, though deformation bands are

observed in the nugget, yellow arrows in Figure 4.47d to 4.47f. Meanwhile, the dominant crack (red arrows) propagates into CGHAZ along deformation bands (blue arrows), Figure 4.47 e and f. Although the deformation bands indicate that the crack could propagate into FGHAZ, blue arrow in Figure 4.47f, the crack changes its path to CGHAZ which might be due to finer martensite grains in FGHAZ resist the crack development, Figure 4.47g.The following crack propagation is expected to follow the red dashed line in Figure 4.47i through shear fracture leading to PF mode.

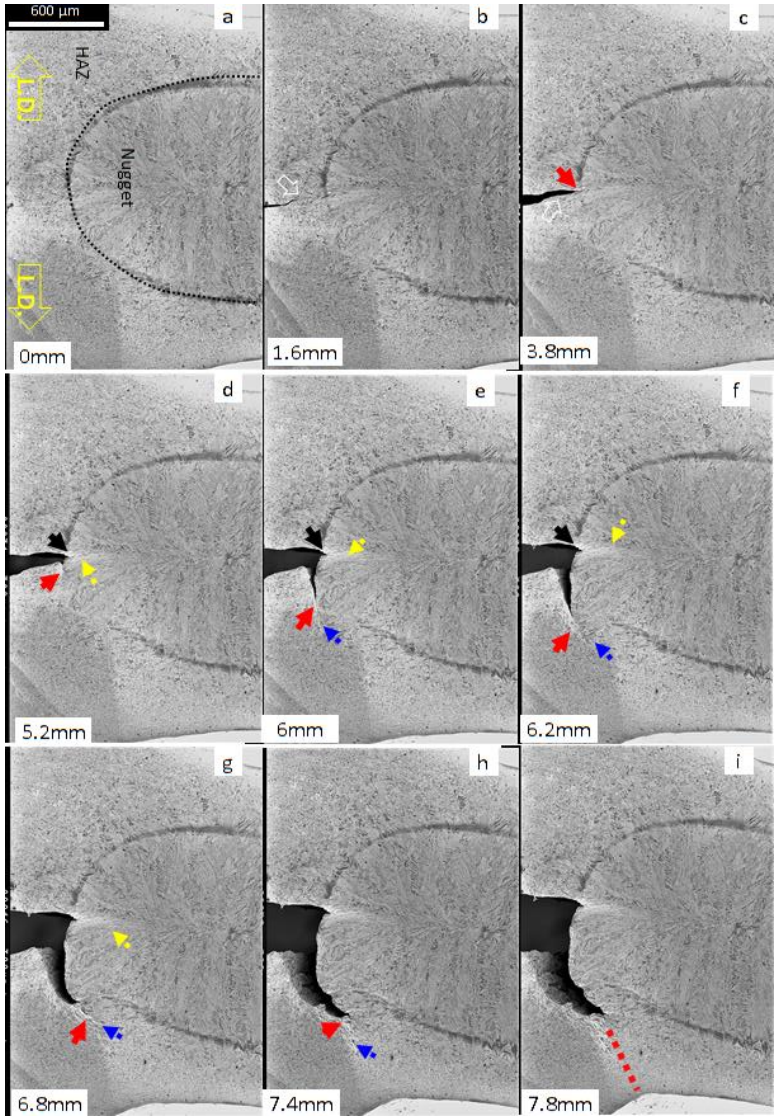

Figure 4.47.Microscopic images show crack initiation and propagation of DPMiCP-H sample indicating PF mode, the yellow and blue arrows show localized deformation bands, black arrows show subordinate crack and red arrows show dominant crack, while the red dashed line indicate potential subsequent crack path.

Figure 4.48 shows the strain dependency curve in relation to subset size. Assume that when the error between each two subset is smaller than 3%, the corresponding subset size is acceptable to be used for strain calculation. Measured maximum principal strain keeps decreasing as subset size decreases and subsequently comes to convergence when subset size decreases to around 31 pixels, an error of 2% was obtained compared to a subset size of 29 pixels. Further decreasing the subset size cannot improve the accuracy because there are no enough distinctive patterns around the corona bond tip for DIC to track leading to subset deletion before crack initiation. A subset size of 31 pixels was selected for computing the strain distribution, and the physical size is 62 micron as well as the spatial resolution is 2 micron/pixel. Additionally, systematic error of strain measurements were analysed for DPMiCP –L, DPMiCP -M and DPMiCP-H sample. Ten images of unloaded samples were used to carry out the analysis, Figure 4.49. The maximum strain value is around 0.01% indicating an ignorable error in strain measurement.

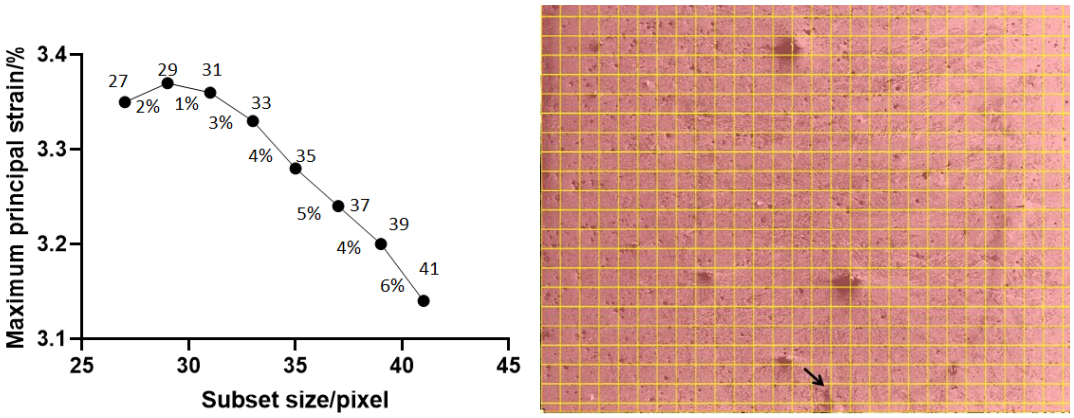

Figure 4.48. (a) Subset size dependency and (b) subset size selected for strain measurement.

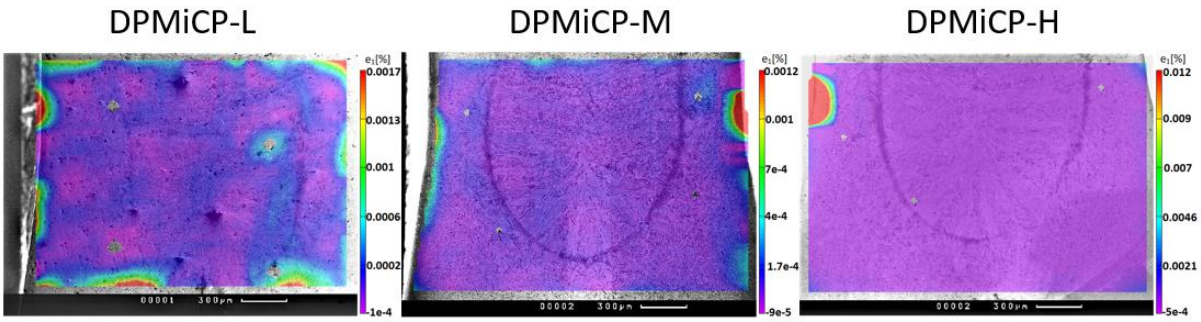

(a) **(b)** **(c)**

Figure 4.49. Uncertainty analysis, systematic error of maximum principal strain of (a) DPMiCP-L, (b) DPMiCP-M and (c) DPMiCP-H samples.

Figure 4.50 to 4.52 show deformation evolution as well as crack initiation and propagation of DPMiCP-L, DPMICP-M and DPMiCP-H samples based on the same loading stage shown in Figure 4.45 to 4.47. Although there is some strain patterns loss around the crack path due to no enough distinguishable patterns around the crack to be tracked by DIC technique, the lost portion does not affect the failure mechanisms analysis. It is worth noting that the loading direction is in X direction while loading direction of DPCP samples is in Y direction. In order to be consistent with DPCP samples, the strain maps of DPMiCP samples were rotated 90 degree.

In samples with low welding current, DPMiCP-L, strain e_{xx} concentrates around the corona bond tip and its value increases as the opening of corona bond, Figure 4.50a_2 and a_3. Subsequently, strain in X direction is observed concentrating around the crack tip, Figure 4.50a_4 to a_9. Meanwhile, the strain in Y direction is observed localized around the crack path and in the nugget, Figure 4.50b_2 to b_7, and then concentrates around the crack tip, Figure 4.50b_8 and b_9. Shear strain also concentrates around the crack tip shown in Figure 4.50c_8 and c_9. However, according to maximum principal strain concentration shown in Figure d4 to d_9, strain concentration in X (loading) direction is most likely to dominate the crack initiation and propagation leading to IF mode.

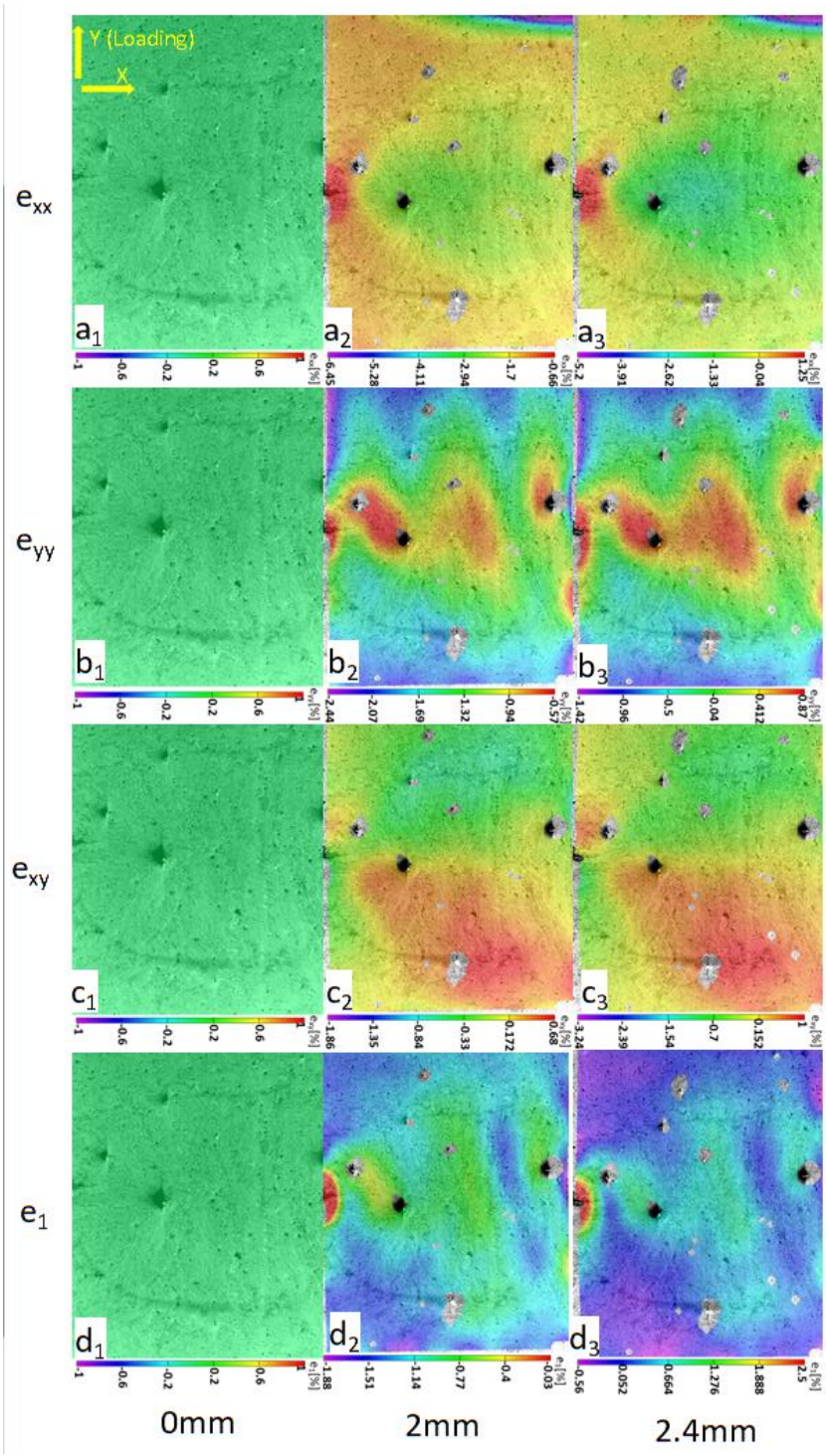

Figure 4.50. Distribution and evolution of strain components for DPMiCP-L sample, (a_z-a_9) strain evolution parallel to loading direction, e_{xx}, (b_1-b_9) strain evolution normal to loading direction, e_{yy}, (c_1-c_9) strain evolution at shear direction, e_{xy}, and (d_1-d_9) maximum principal strain evolution, e_1.

Continue to next page.

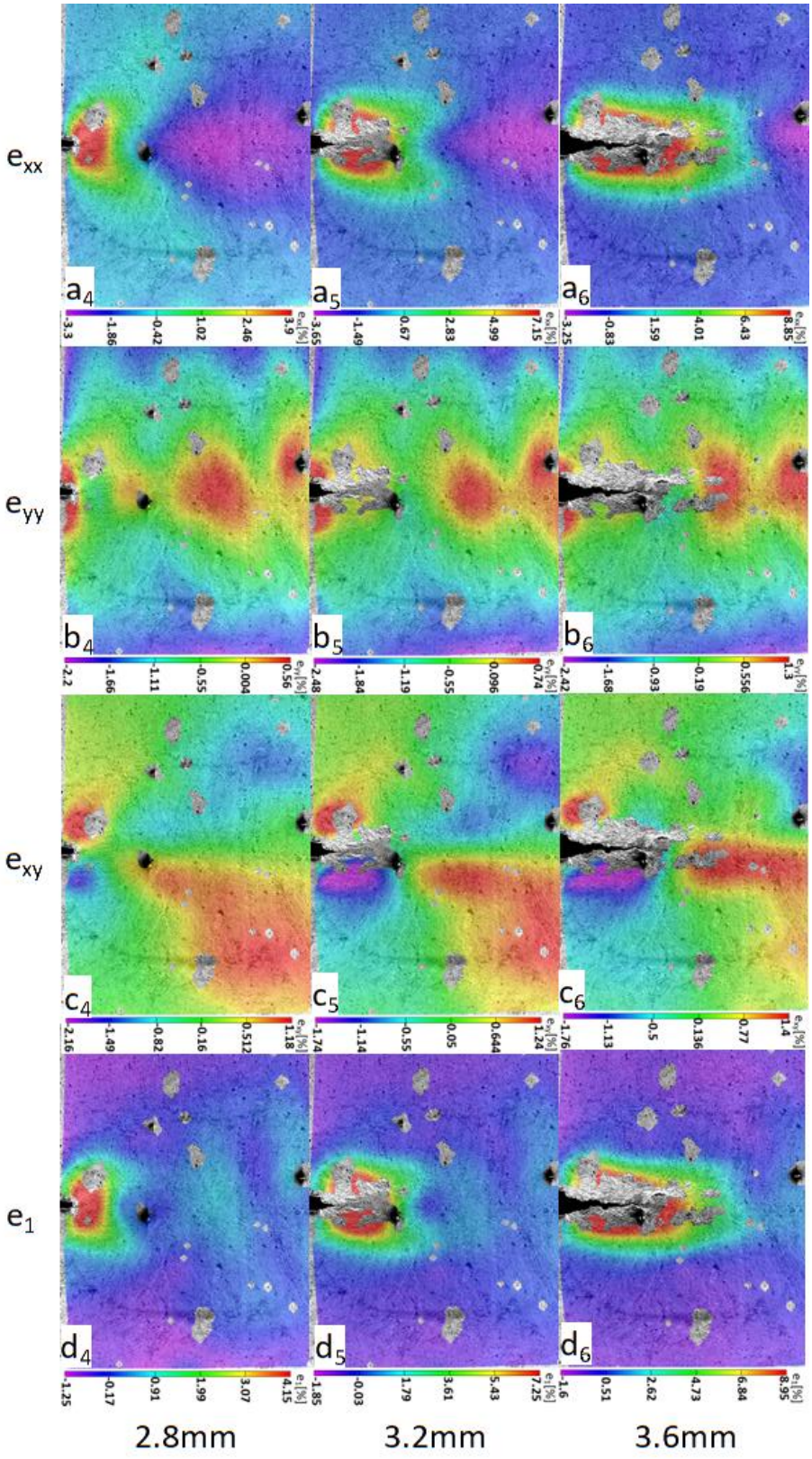

Continue to next page.

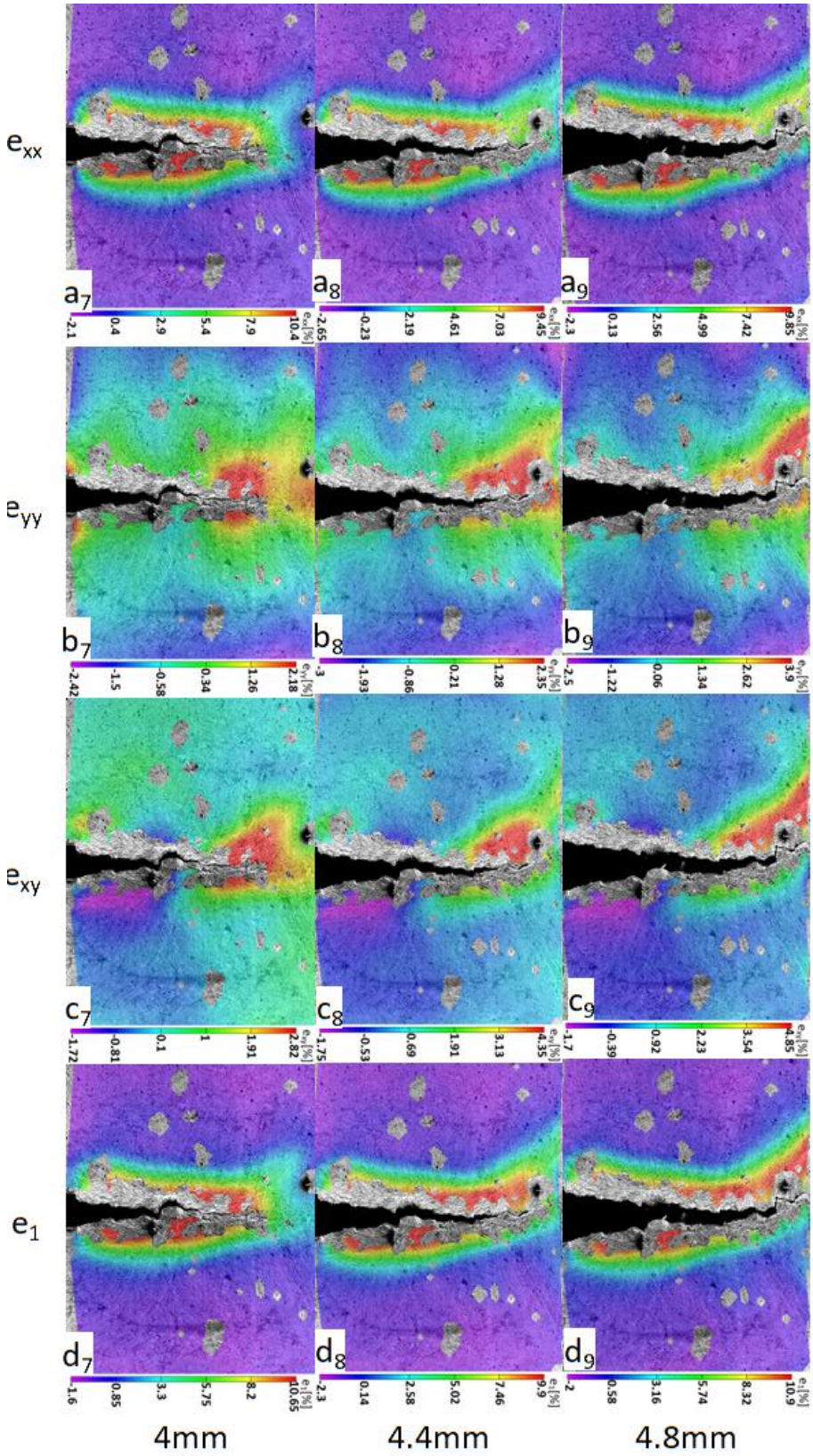
e_{xx}
e_{yy}
e_{xy}
e_1
a_7
a_8
a_9
b_7
b_8
b_9
c_7
c_8
c_9
d_7
d_8
d_9
4mm
4.4mm
4.8mm

Figure 4.51 shows strain evolution of DPMICP-M sample failed through PIF mode. For strain evolution in X direction, strain concentrates around the crack tip and passes into the nugget as the crack propagates, which plays the most important role in crack propagation according to maximum strain concentration, leading to IF mode, Figure 4.51a_2 to a_5 and 4.51$d2_2$ to d_5, Additionally, strain concentration in Y direction is observed at two sides of corona bond in HAZ while compression is observed ahead of the tip in the nugget, red and black arrows in Figure 4.51b_2 and b_3. This could be due to bending of HAZ squeezes the material ahead of the tip. However, strain concentration around the crack tip in Y direction (normal to loading) becomes dominant instead of strain e_{xx} leading to crack path deflection, according to maximum principal strain concentration, red arrows in Figure 4.51a_6, b_6 and d_6. Subsequently, shear strain concentration and strain concentration in Y direction ahead of the crack tip are observed, black and red arrows in Figure 4.51b_9 and c_9, which are most likely to result in the following failure leading to PF mode, because they make the greatest contribution to maximum principal strain concentration ahead of the crack tip, red and black arrows in Figure 4.51d_9.

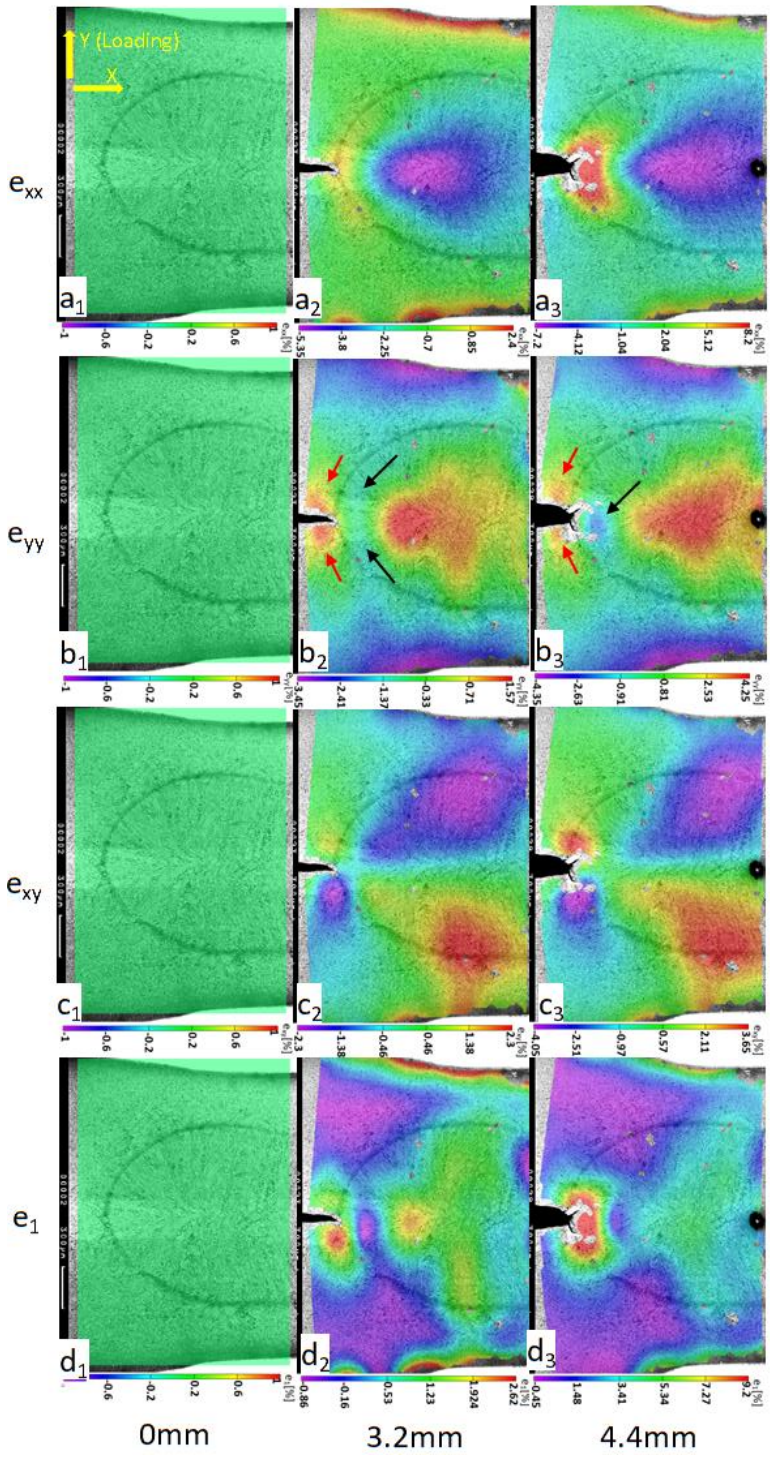

Figure 4.51. Distribution and evolution of strain components for DPMiCP-M sample, (a_z-a_9) strain evolution parallel to loading direction, e_{xx}, (b_1-b_9) strain evolution normal to loading direction, e_{yy}, (c_1-c_9) strain evolution at shear direction, e_{xy}, and (d_1-d_9) maximum principal strain evolution, e_1.

Continue to next page.

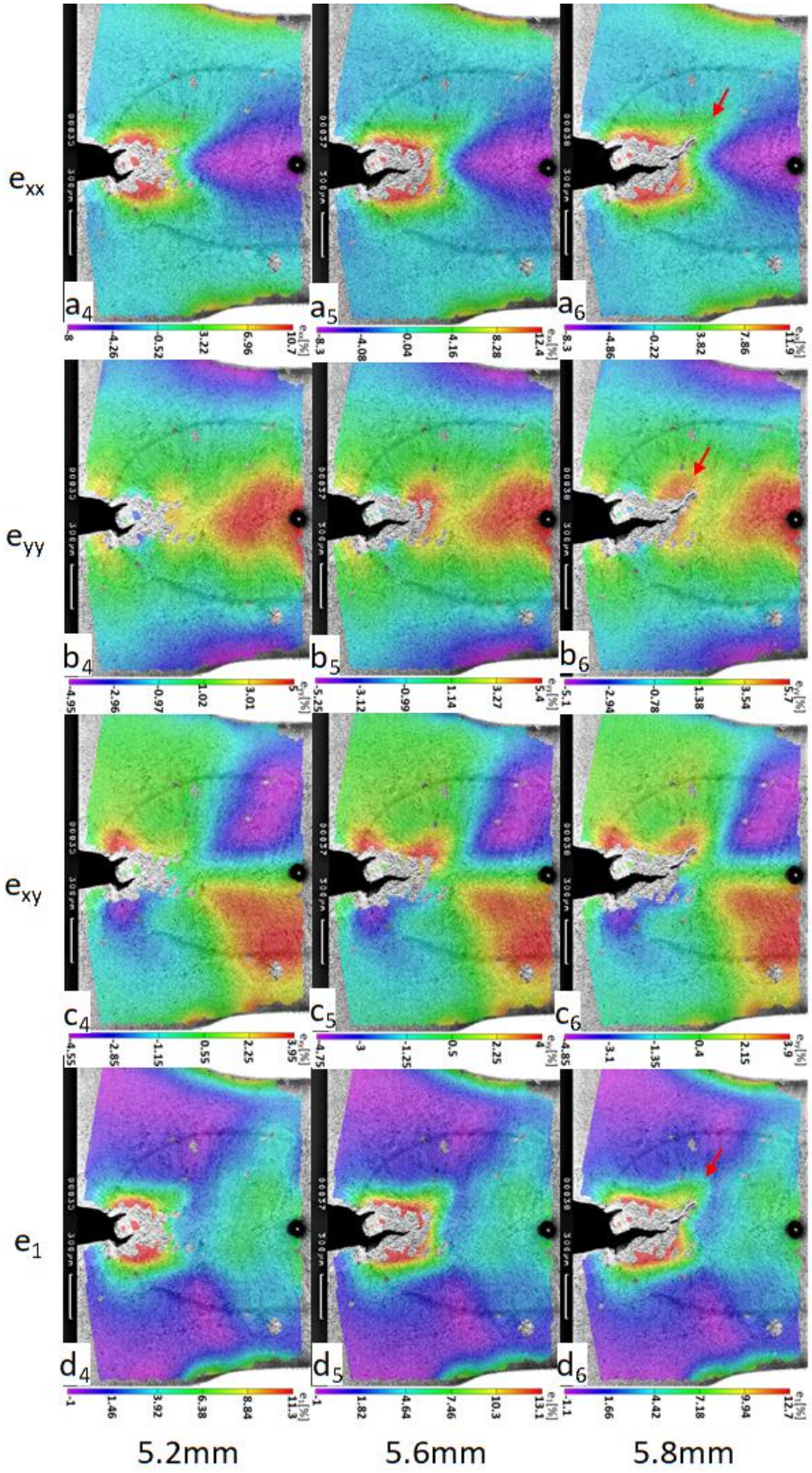

Continue to next page.

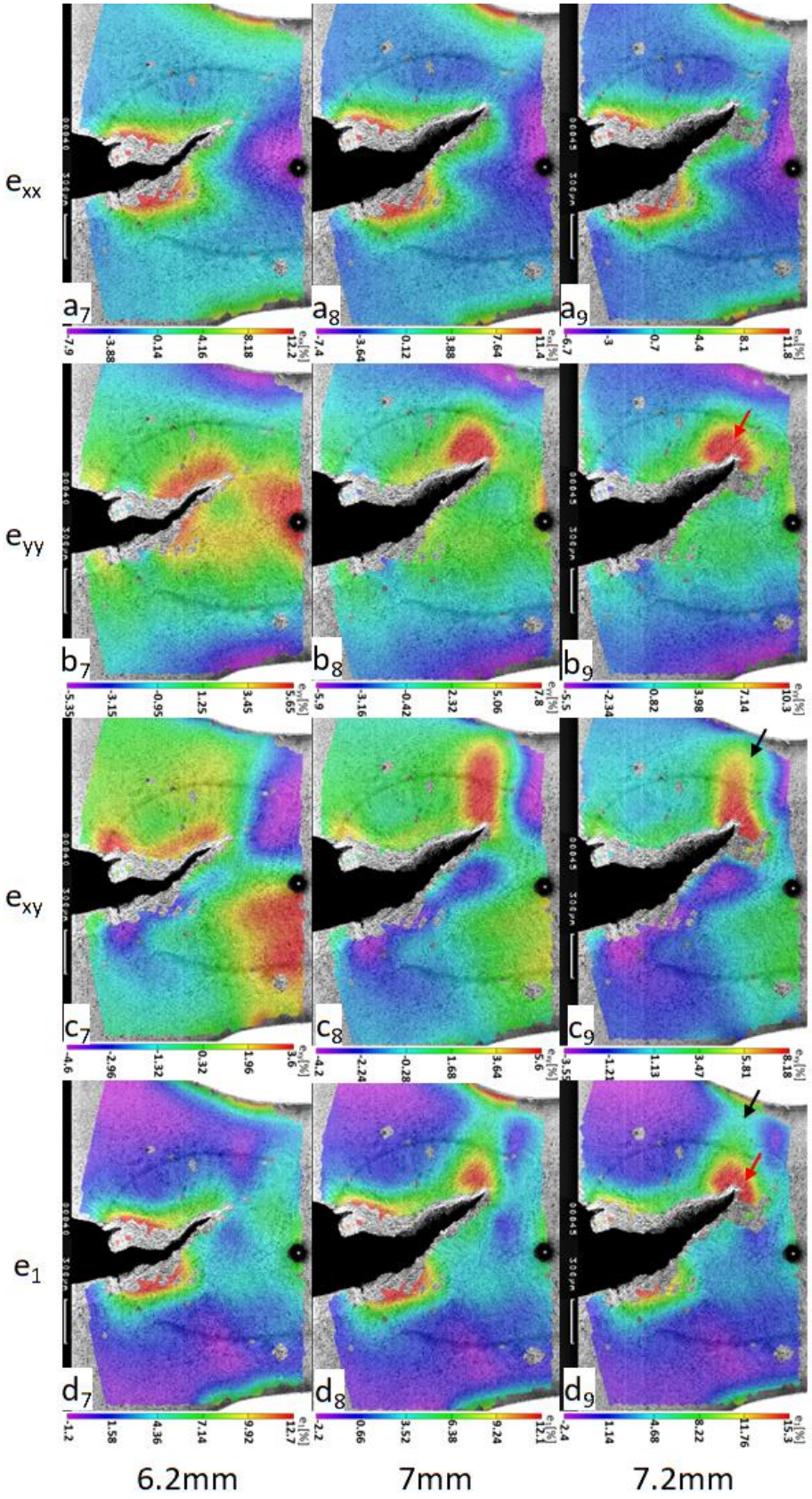
e_{xx}
e_{yy}
e_{xy}
e_1
a_7
a_8
a_9
b_7
b_8
b_9
c_7
c_8
c_9
d_7
d_8
d_9
6.2mm
7mm
7.2mm

Strain evolution of DPMiCP-H sample is show in Figure 4.52, indicating PF mode. Strain evolution in X (loading) direction shows that e_{xx} concentrates around the subordinate crack, black arrow in Figure 4.52a_4, and grows to high measured value as further loading, Figure 4.52a_5 to a_9. Compression is observed by side of the dominant crack in X direction, white arrow in Figure 4.52a_4, and becomes larger as further loading, 4.52a_5 to a_9, which might indicate local necking in HAZ. However, strain concentration in Y (normal to loading) and shear direction are most likely to lead to dominant crack propagation within HAZ according to maximum principal strain concentration around the dominant crack tip, Figure 4.52b_4 to b_9, c_4 to c_9 and d_4 to d_9. Additionally, according to maximum principal strain concentration around the crack tip indicated in red arrow in Figure 4.52d_9, the strain concentration in shear direction and Y direction ahead of the crack tip might lead to the subsequent failure, red arrow in Figure 4.52c_9.

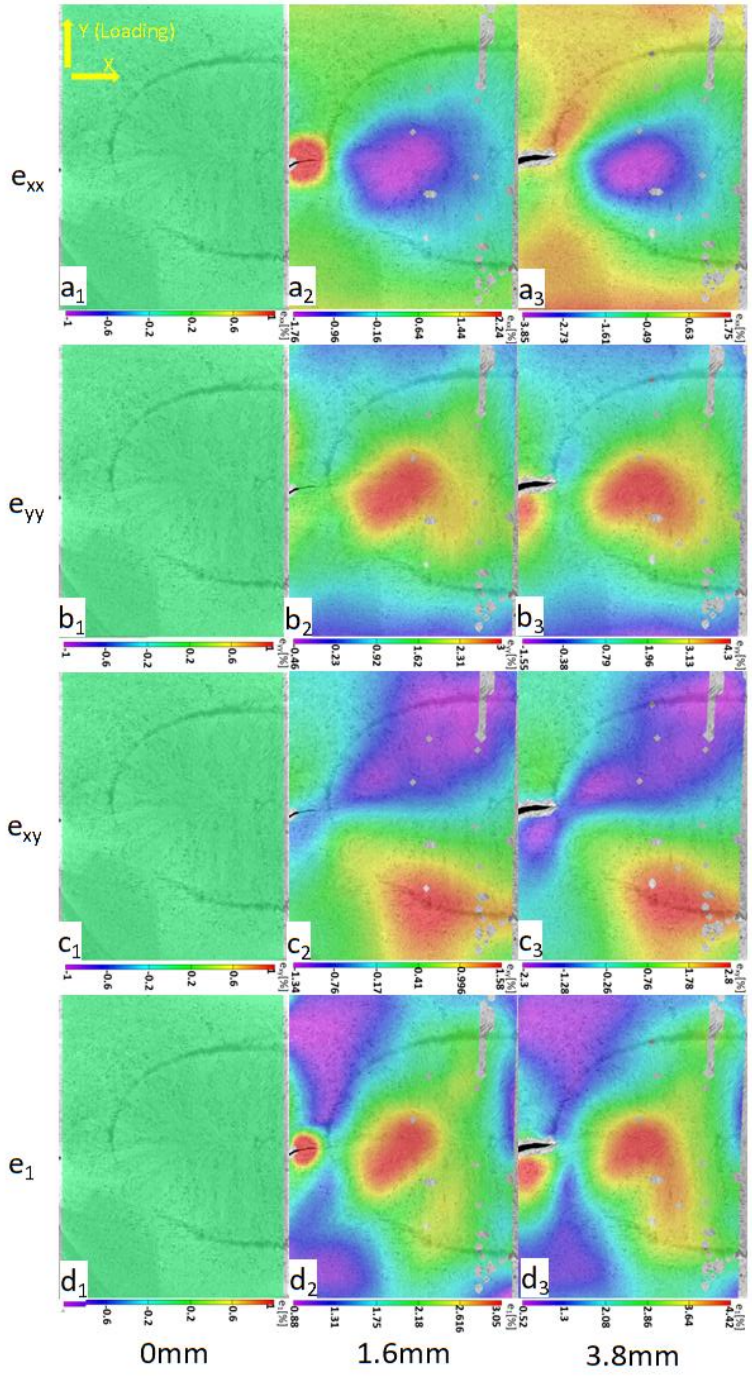

Figure 4.52. Distribution and evolution of strain components for DPMiCP-H sample, (a_z-a_9) strain evolution parallel to loading direction, e_{xx}, (b_1-b_9) strain evolution normal to loading direction, e_{yy}, (c_1-c_9) strain evolution at shear direction, e_{xy}, and (d_1-d_9) maximum principal strain evolution, e_1.

Continue to next page.

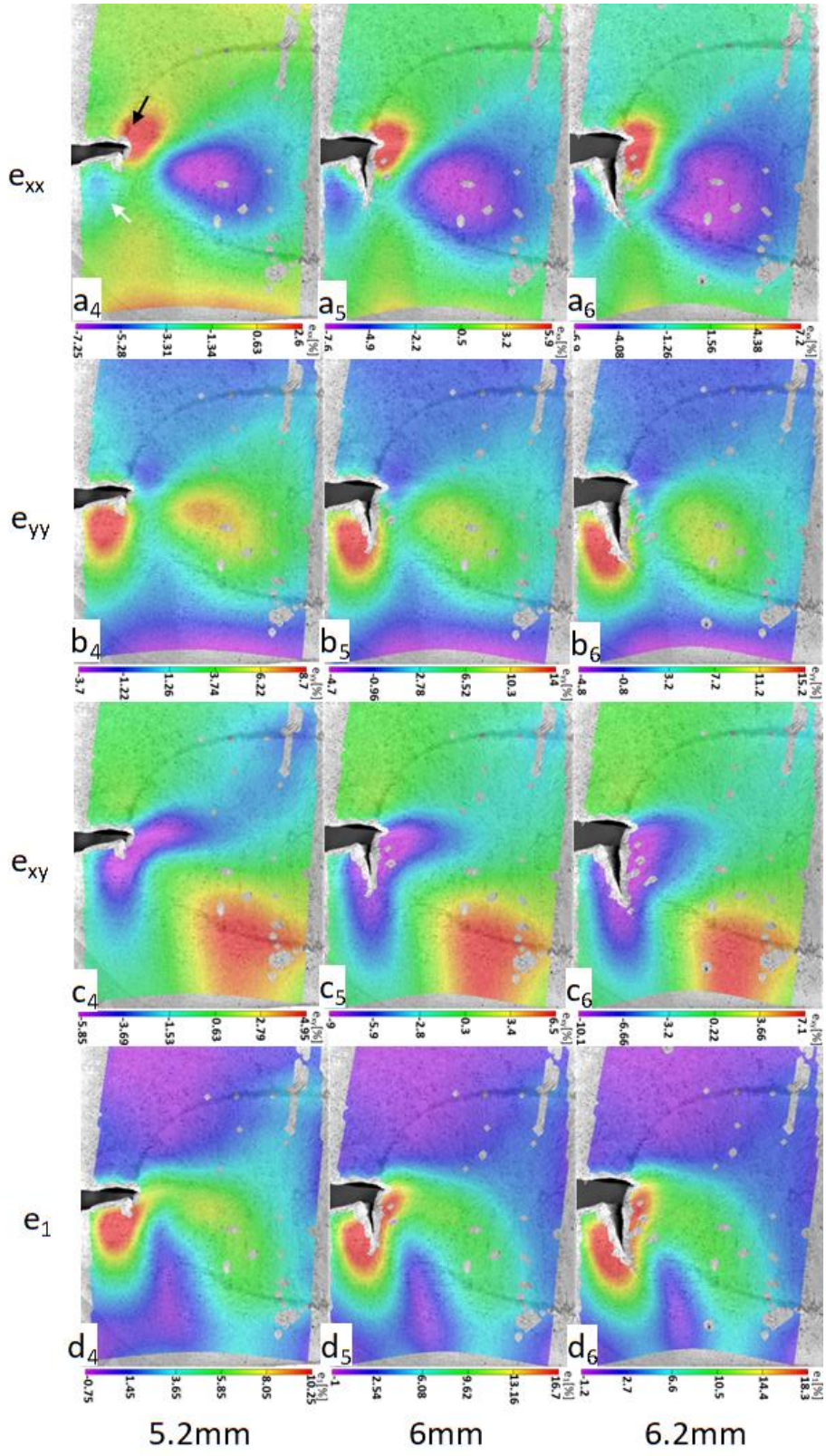

Continue to next page.

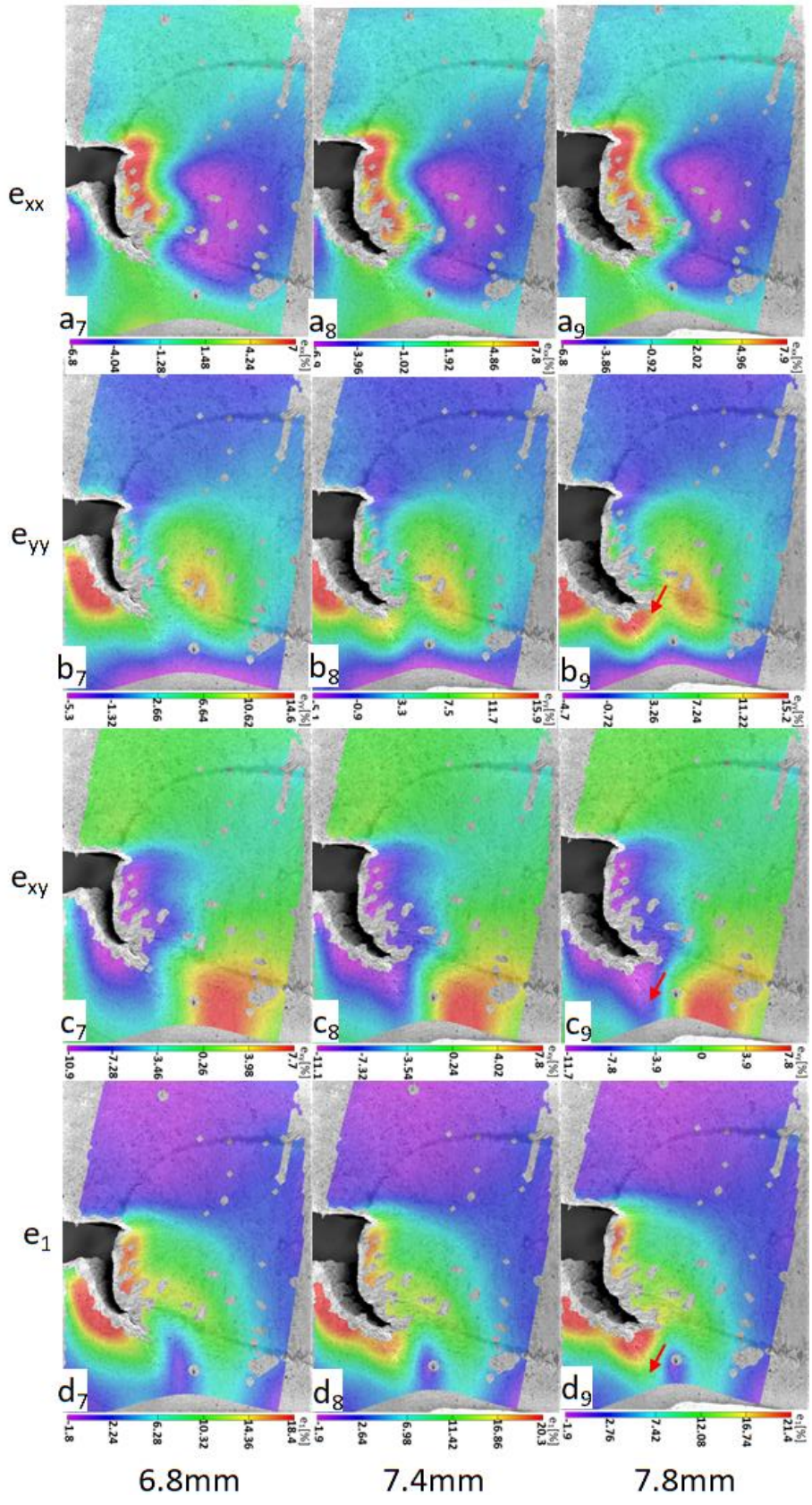
e_{xx}
e_{yy}
e_{xy}
e_1
a_7
a_8
a_9
b_7
b_8
b_9
c_7
c_8
c_9
d_7
d_8
d_9
6.8mm
7.4mm
7.8mm

4.6.4 Discussion

The failure of LCCP samples is due to the large bending within HAZ. According to the hardness profile shown in Figure 4.8, the ferrite grains within HAZ results in low yield strength and high plasticity. Thus, the applied bending and tensile stress state could easily bend the HAZ leading to large tensile strain concentration along the loading leg and shear strain concentration in loading direction around the corona bond tip, Figure 4.35a_9 and a_{11}. Meanwhile, it was reported that material with higher yield strength could have lower fracture toughness[229], the boundary of nugget/HAZ has higher hardness than rest of the HAZ and BM, which indicates this region could have lower fracture toughness. Moreover, the compression in nugget could provide resistance to the crack initiation within nugget, Figure 4.35a_{12}. Therefore, the failure takes place in the boundary of nugget/HAZ.

Figure 4.53 shows the measured strain evolution curves between the beginning of loading and crack initiation of DPCP-L, DPCP-M and DPCP-H samples at the tips of corona bonds in the nuggets (highlighted in white squares marked with d e and f in Figure 4.53a, b and c).

It is found that value of e_{yy} is the largest at the onset of crack initiation for the samples failed via IF mode (DPCP-L and IF phase of DPCP-M), therefore leading to the crack passing through the nugget due to mode I fracture, Figure 4.53d and e. The strain in Y direction increases rapidly from compression to tension while the e_{yy} strain increasing point of DPCP-L sample is around 1mm. However, as it was also shown in strain maps of Figure 4.36b_{21} and b_{22}, the subsequent bending deformation in DPCP-M sample stretched the material in X direction leading to larger concentrated strain in X direction but smaller concentrated strain in Y direction in the nugget comparing to strain e_{xx} and e_{yy} at the point of crack initiation in Figure 4.53e. Thus, deformation in X direction is more likely to open the crack along Y direction deflecting the crack path from passing through the nugget to sheet thickness direction in DPCP-M sample, and then leads to PIF mode. In addition, Figure 4.53d and e show that e_{yy} strain evolution is similar to the maximum principal strain evolution for DPCP-L and DPCP-M samples confirming that deformation along Y direction

dominates IF mode and the driving force is stress normal to the interface of the nugget.

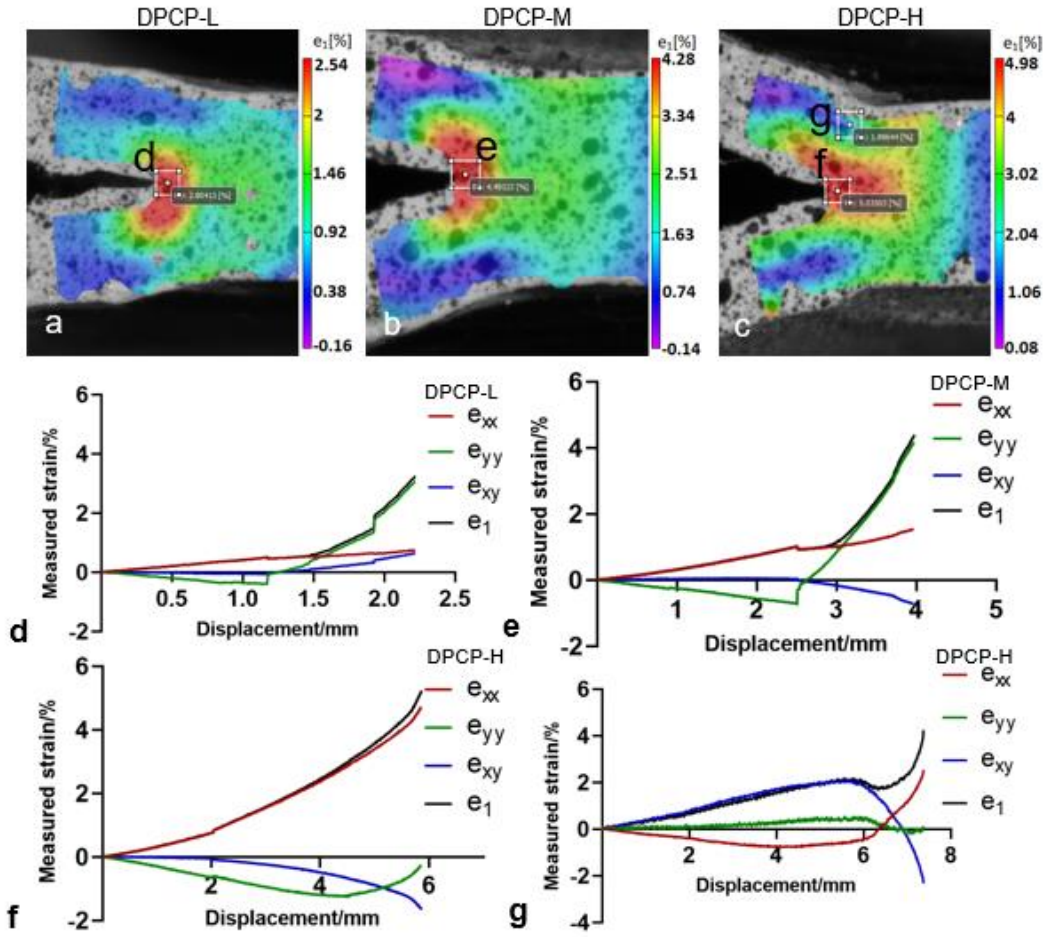

Figure 4.53. Maximum principal strain distribution, (a) DPCP-L, (b)DPCP-M and (c)DPCP-H, indicating the extracted positions of measured strain evolution curves between start point of deformation and crack initiation of (d) DPCP-L, (e) DPCP-M and (f) DPCP-H samples while (g) measured strain evolution curves between start point of loading and final failure of second part of PF mode in DPCP-H samples.

The strain evolution of DPCP-H sample shown in Figure 4.53f, which is the first part of failure (highlighted in white square marked with 'f'), indicates that material at the corona bond tip goes under tension in X direction while strain e_{yy} is in compression mode. This might lead to delay of crack propagation through the nugget caused by compressive stress and strain field in Y direction, while the material within HAZ and nugget around the corona bond tip in X directioin is stretched to localised plastic deformation leading to

mode I fracture and necking, Figure 4.42. Additionally, strain of e_{yy} starts increasing at around 4mm, Figure 4.53f, which might be due to the fact that the tensile stress caused by loading at this point overcomes the compressive stress and is large enough to induce tensile deformation. However, negative e_{yy} indicates that the material in nugget around the crack tip is still in compression, Figure 4.53f. Thus, e_{xx} strain concentration caused by bending stress dominates first part of PF mode.

Figure 4.53g shows strain evolution curves between start point of loading and final failure of second part of PF mode in DPCP-H samples, the extracted position is on the crack path, within HAZ highlighted in white square marked with letter 'g' in Figure 4.53c. For the second part of PF mode shown in Figure 4.53g, the shear strain curve is almost consistent with maximum principal strain curve indicating that shear deformation dominates the second part of PF mode until 6 mm of elongation and then shear strain and normal strain in X direction become dominant leading to shear fracture. The shear strain was caused by relative motion between material in HAZ and nugget. Because of bending within HAZ, material around position 'g' in Figure 4.53c was compressed in X direction until around 6mm of elongation, at where started being stretched when the crack almost researched this position. This is also the reason of changing the direction of shear strain. Thus, stress along X direction and shear stress dominates PF mode of DPCP-H sample. The strain evolution curves given in Figure 4.53 might also give critical failure strain for DPCP-L/M/H samples, according to the maximum principal strain at the point of crack initiation.

According the deformation evolution DPCP samples, as welding current increases, the compression strain e_{yy} ahead of corona bond tips makes great contribution to transition from IF to PF modes. This compression strain is caused by bending within HAZ and last for longer elongation in samples with applied higher welding current, e_{yy} evolution shown in Figure 4.53d, e and f. Hardness analysis shows the softening effect in HAZ and nugget due to a lower cooling rate increases the size of prior austenite grains and reduce the dislocation density [232] and tempering effect in SCHAZ. Thus, the material in HAZ and nugget is easier deformed leading to larger bending in HAZ and

subsequently larger compression in nugget adjacent to corona bond tip under coach-peel loading, as shown in Figure 4.53a, b and c. Additionally, a larger plasticity around corona bond tip in nugget and FGHAZ was observed by increasing the welding current, this was better observed in DPMiCP samples that the crack propagates further into CGHAZ instead of into nugget, Figure 4.45-4.47. Therefore, the softening of weld section, compression deformation in nugget and plasticity in nugget and FGHAZ affect the failure mode transition from IF to PF for DPCP samples.

Edge effect due to half weld geometry is observed causing a different fracture mechanism in the fracture surface adjacent to the cut surface edge highlighted in blue square in Figure 4.40. Material loaded near the cut surface could be assumed under plane stress state which could have lower stress triaxiality compared to the material inside the nugget leading to different fracture mechanisms. It is clear that stress triaxiality around the crack tip of full weld sample is much larger than that of half weld sample, Figure 4.54a_1 and b_1. In the cross section surface shown in Figure 4.54a_2 and b_2, although the stress triaxiality of most area in nugget of the half weld sample is similar with that of full weld sample, the stress triaxiality of half weld sample closed to the cut surface is around 0.4 which is much smaller than that around the centre line of full weld sample (around 1.2), therefore different fracture mechanism could occur.

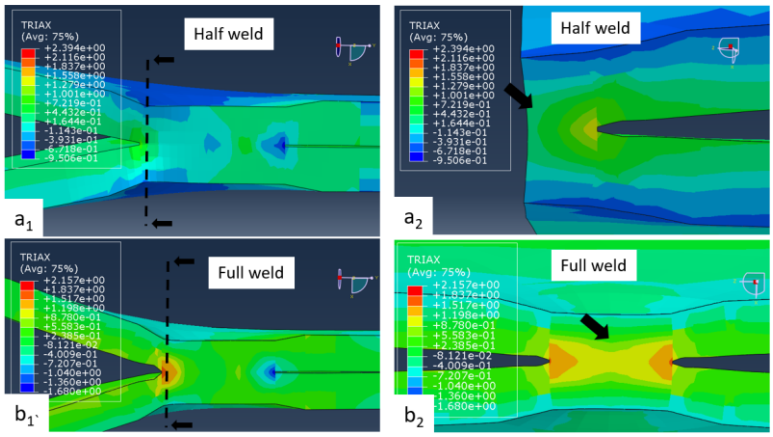

Figure 4.54 Stress triaxiality of the nugget before failure, (a_1) and (a_2) half weld CP sample, (b_1) and (b_2) full weld CP sample.

Microstructural morphology analysis along the crack path of half failed

DPCP samples with applied low, medium and high welding currents was carried out in order to better understand the influence of microstructure of the weld to the failure modes, Figure 4.55, the samples were prepared by removing deformed portion. As shown in Figure 4.55c and d, in DPCP-L, the crack first initiates from the sharp tip of the corona bond due to analysis as mentioned and cut through the martensitic laths along a relatively flat path and then deflect its path. The crack path deflection could be owing to the region of smaller and shorter martensite , highlighted in yellow squares in Figure 4.55b and c, it was reported that finer martensite laths has higher strength, as founded by Wang [233], which may resist the crack from cutting through. Then the crack path deflects back along around 45° angle as the tensile loading is sufficient to force the crack to propagate along horizontal direction.

In DPCP-M, the path deflection also occurs when crack propagates to the area that has finer martensite. The crack first cuts through the longer columnar grains without much path deflection, this might be due to the fact that low energy crack path could form along the direction of grain growth due to interdendritic microsegregation of the solutes [221], Figure 4.55f. Then, the crack deflects its path when reaching the region of smaller martensite grains shown in Figure 4.55f, as this region might retard the crack propagation. Additionally, as mentioned that the low energy crack path might form along the grain growth direction (vertical direction), it could help the crack propagate through thickness direction, Figure 4.55h.

In PF mode of DPCP-H sample, crack initiates at the tip of corona bond and propagates along circumference of the nugget and CGHAZ as shown in Figure 4.55k. Several factors based on the microstructure may result in the failure mode transition: grain growth makes the nugget more ductile thereby the nugget has sufficient fracture toughness to resist the crack from cutting into the nugget; hardness measurement indicates that the material within the CGHAZ and at exterior of nugget is harder than that within the nugget which could be due to this region was first solidified results in higher dislocation density, thus crack is more likely to initiate in CGHAZ when the concentrated stress around the tip of corona bond is not sufficient to crack into the nugget. Moreover, Bouzekri et al. indicated that microcracks formed in CGHAZ due to

low-melting point element and microsegregation at grain boundaries in weld of DP780 [221], this may also be the reason help crack propagation in CGHAZ.

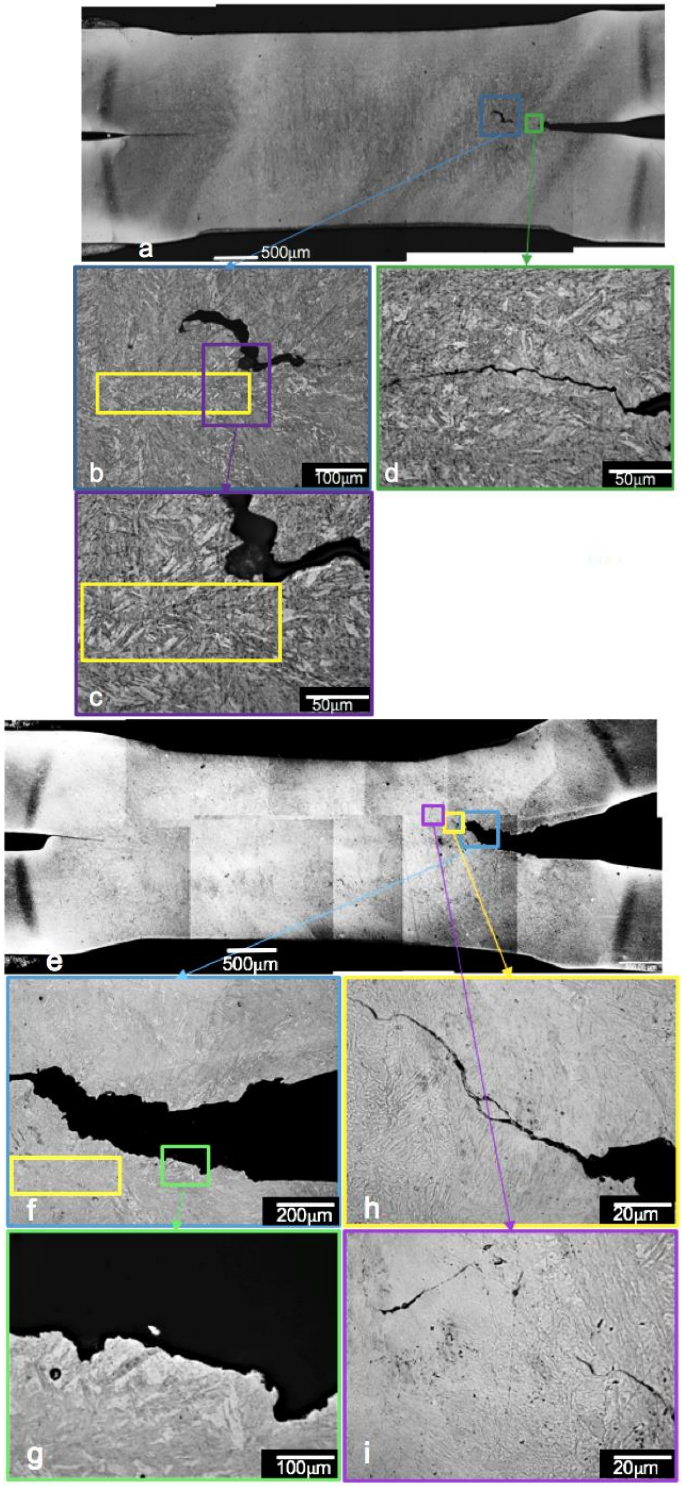

Figure 4.55. Microstructural morphology along the crack path of half failed (a-d) DPCP-L, (e-i) DPCP-M as well as (j) and (k) DPCP-H samples.

Continue to next page.

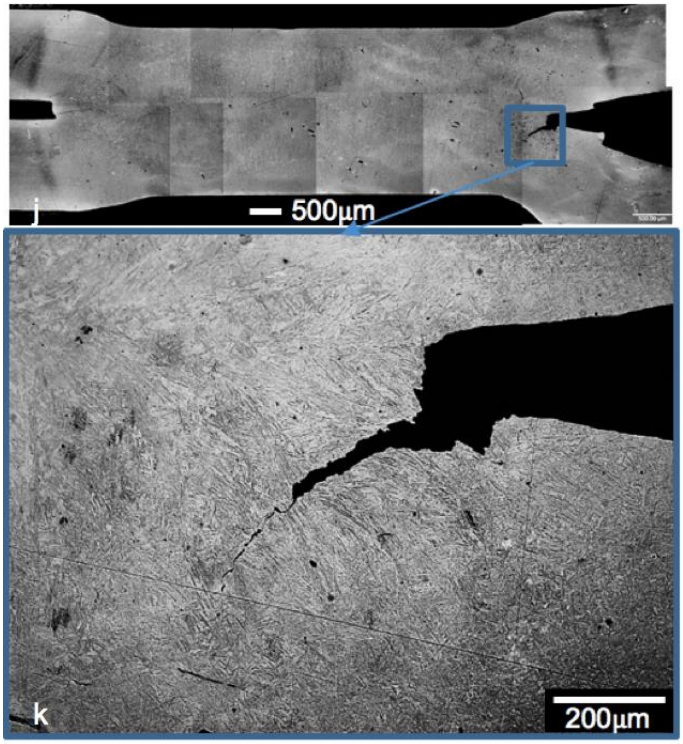

Although the weld size of LCCP samples are similar with DPCP samples, all LCCP samples failed through PF mode. This is due to the weld of LCCP is much more deformable than DPCP samples, therefore much larger bending deformation was induced by the bending moment compared to DPCP-H sample leading to failure in HAZ, Figure 4.35a_9 and 4.36c_{21}. The failure of LCCP samples confirms the deformation evolution analysis of DPCP samples that softer HAZ could lead to larger bending deformation prompting transition of failure mode from IF to PF.

Figure 4.56 shows a possible stress model of CP samples based on the achieved strain evolution and fractography analysis in previous chapter 4.6 and a failure mechanism can be concluded.

At start of deformation, angular motion of two legs results in bending in HAZ (between the highlighted blue and green circles Figure 4.56). The bending deformation adjacent to the notch tip tends to stretch the material within the nugget resulting in stress σ_x in HAZ along two loading legs, meanwhile bending at exterior (highlighted in blue circles in Figure 4.56) of HAZ tends to compress the material in HAZ and nugget ahead of the corona bond tip towards the nugget, and consequently causes compressive stress σ_c within the nugget ahead of the corona bond tip, according to e_{xx} and e_{yy} shown in

Figure 4.53d. Stress σ_y normal to interface of the nugget around corona bond tip caused by loading tends to open up the nugget, resulting in a tensile-bending stress state with bending stress σ_x. Shear stress might occur within HAZ/nugget between the highlighted blue and green circles due to relative motion of the loading legs and nugget, Figure 4.56. In further loading, bending stress increases according to Equation 4.2 as the increase of load F, it is noted that the reducing rate of the length l is much smaller than increasing rate of load before crack initiation in the weld. This results in increase of compressive stress σ_c, , meanwhile, stress $\sigma_y$and shear stress τ also increase due to the increase of load F resulting in the rise of strain e_{yy} and e_{xy}, Figure 4.53d, e and f.

$$\sigma_x = \frac{M}{S} = \frac{6F_y l}{bh^2}$$

Equation 4.2

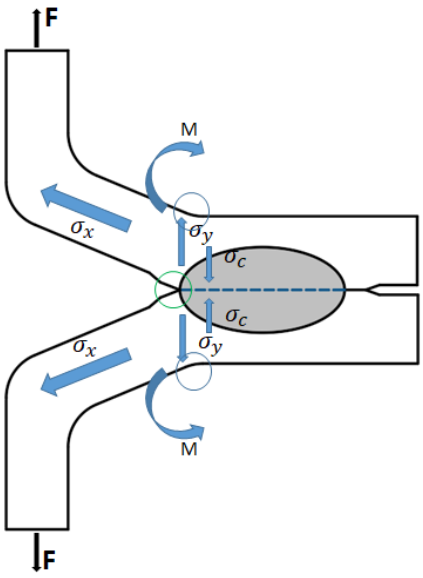

Figure 4.56. Stress analysis at the circumference and interface of the weld nugget in coach-peel sample.

According to section 4.1.3, the weld section with low welding current, DPCP-L, is the least deformable, at the start of loading, the bending stress σ_x is too small to induce sufficient bending deformation in HAZ around the crack tip before the amount of deformation induced by stress σ_y is enough to propagate the crack into the nugget along the interface of the nugget, leading to IF mode, as shown in crack initiation and propagation of DPMiCP-L sample,

Figure 4.45. This is also confirmed by the observation of strain evolution of DPMiCP-L sample, Figure 4.50.

However, sample with higher welding current, DPCP-H, shows different mechanism, fracture surface shown in Figure 4.42 indicates that the fracture is caused by bending stress σ_x and shear stress. As the material witin HAZ is more ductile than samples with low welding current, therefore leading to larger bending deformation in HAZ under bending stress. It induces increase of compressive stress σ_c leading to larger compressive deformation ahead of the crack tip, e_{yy} in Figure 4.53d, e and f, retarding the crack initiation and propagation from the corona bond tip towards the nugget. Meanwhile, plastic deformation in horizontal direction around the corona bond tip in HAZ and nugget develops caused by bending stress, leading to strain concentration and following localised necking in HAZ, resulting in mode I crack initiation at the interface between HAZ and nugget, further loading will increase such strain caused by bending leading to crack propagation in HAZ, as shown in Figure 4.47. Maximum principal strain evolution of DPMiCP-H sample shows that the strain concentration is at CGHAZ around the corona bond tip, Figure 4.52d$_4$. Although similar strain value is observed at vicinity of the tip in nugget, the failure occurs in CGHAZ. This is due to larger martensite grains in nugget which has better plasticity and can take more plastic deformation, meanwhile the smaller grains in FGHAZ resist the crack propagation, as observed in crack propagation in DPMiCP-H sample in Figure 4.47. As further loading, the shear stress developed ahead of the crack is sufficient to induce shear fracture, consequently pulling the nugget off the sheet.

IF and PF phases of DPCP-M samples have similar failure mechanism with those of DPCP-L and DPCP-H samples.

Additionally, load around yielding and highest load of DPTS samples with each welding current is much higher than DPCP samples, which could be affected by bending in DPCP samples. A rough stress calculation was carried out to obtain the shear stress τ of DPTS-L sample within nugget and bending stress σ_x of DPCP-L sample according to equations 4.2 and 4.3, since DPCP sample and DPTS sample can be assumed to be a cantilever beam problem and

a simple shear problem. It was found that, shear stress is about 785MPa for DPTS-L sample which is similar with bending stress for DPCP-L sample of about 840MPa, thus a small load is required to obtain a large stress due to bending of DPCP samples.

$$\tau = \frac{F_y}{A}$$

Equation 4.3

Where τ is shear stress of nugget in TS sample, F_y is load around yielding, σ_x is bending stress in CP sample at corona bond tip, M is bending moment, S is section modulus, l Is length between loading point and tip of corona bond, b is width of metal sheet and h is thickness of metal sheet.

4.7 Failure mechanism analysis of spot weld under tensile loading condition

4.7.1 Deformation and failure analysis of welds under tensile loading (results)

Figure 4.57 shows the load-displacement curves for the U-shape samples in DP1000 and low carbon steel. Lines in black indicate the U-L samples with high welding current, lines in yellow indicate the U-M samples with medium welding current while the green lines show U-H samples with a lower welding current. As indicated by black arrows in Figure 4.57a, and b, the load dramatically drops and then increases, which is similar with unloading and loading phenomenon. This indicates the two half welds didn’ t fail at the same time. According to the weld size measurement at the beginning of this section, no significant difference is observed between the two half welds, thus it could be due to the geometry difference of samples. Because of the spring back effect of DP1000, it is difficult to perfectly fabricate the U-shape samples. As shown in Figure 4.57c, which is an example showing the geometry difference of DPU sample, the angle difference of the notches at two sides of the weld are around 2°, and the loading legs are not perfectly aligned, which could lead to asymmetric loading leading to such unexpected failure. For LCU samples, the

large plastic deformation around loading legs could also affect symmetric loading of two welds, indicated in blue arrow in Figure 4.58b, thus the load-displacement curves of LCU samples might not be that reliable. Although such situation is observed, higher plastic energy is needed for DPU samples with applied higher welding current Figure 4.57b.

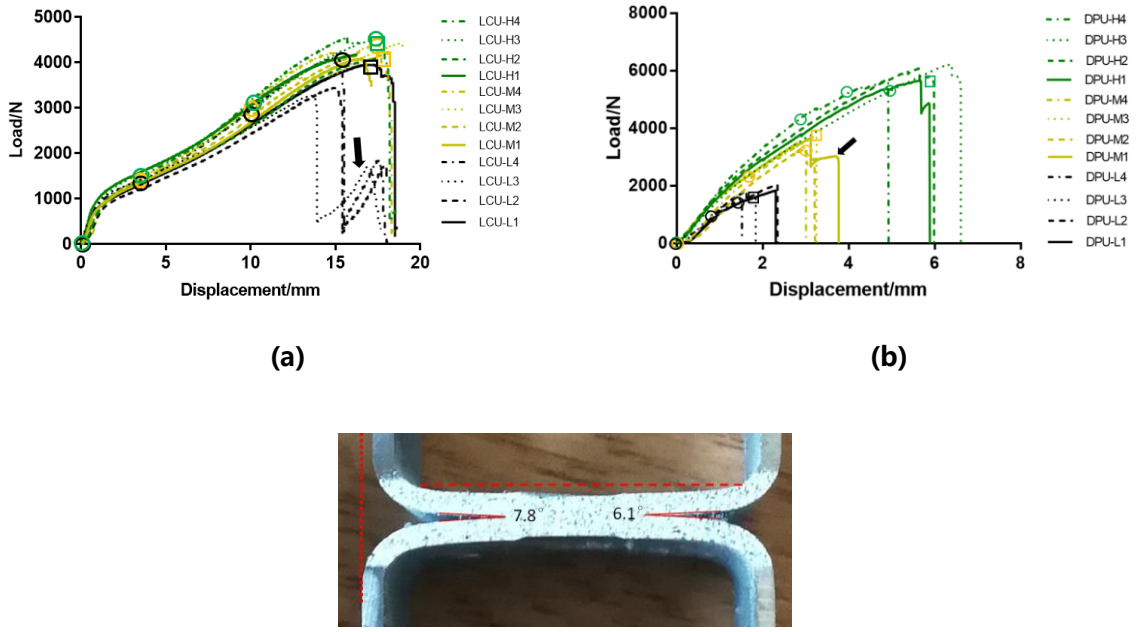

(a) **(b)**

(c)

Figure 4.57. Load-displacement curves of U-shape samples with low, medium and high welding currents in (a) low carbon, (b) DP1000 and (c) example showing geometry difference of U-shape sample. The highlighted squares show the failure point of the painted samples, the highlighted circles show deformation evolution and failure of the samples without paint.

Figure 4.58 shows the failed U-shape samples, all LCU samples failed through PF mode, Figure 4.58b while DPU-L and DPU-M samples failed through IF and DPU-H failed via PIF, Figure 4.58a. It can be seen that the loading legs of LCU samples are severely plastically deformed, blue arrows in Figure 4.58b. This could be due to the nugget is the strongest part of the sample caused by welding process, and it is harder to deform than the rest of the sample.

(a) **(b)**

Figure 4.58. Failed U-shape samples in (a) DP1000 and (b) low carbon steel under three different welding currents.

Figure 4.59 shows deformation evolution and failure of spot welds of LCU-L4, LCU-M4 and LCU-H4 samples indicated in black, green and yellow circles in Figure 4.57a. All samples fail via PF mode.

The failure process of samples with applied low, medium and high welding currents are similar. Local deformation first occurs around corona bond tips within nugget in Figure4.59b, g and l, and then HAZ are dramatically stretched and bended resulting in a great mount of plastic deformation causing necking within HAZ, highlighted in yellow ellipses in Figure 4.59d, i and n, subsequently pulling the nugget off the sheets resulting in PF mode as shown in Figure 4.59e, j and o. In this case, though the load-displacement curves are not reliable, the strain evolution could be a good indicator to study deformation evolution and failure of the samples.

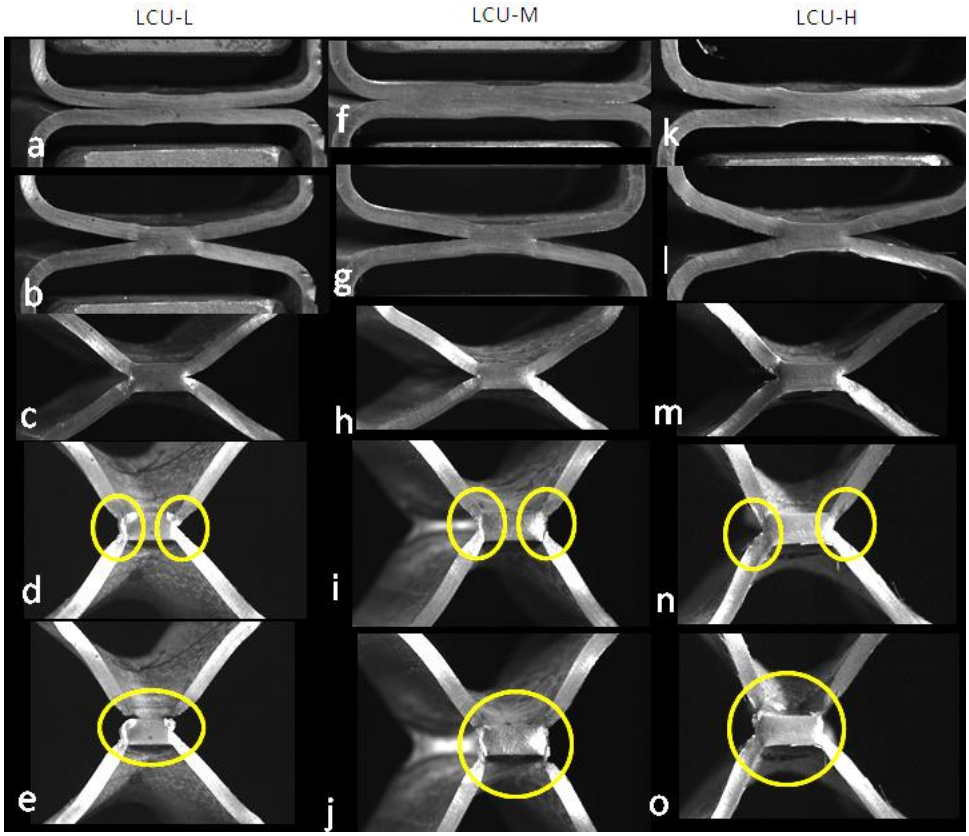

Figure 4.59. Images of deformation evolution and failure of LCU-L4, LCU-M4 and LCU-H4 samples without paint, deformation in various stages highlighted in black, yellow and green circles in Figure 4.57 (a) (f) and (k) before testing, (b) (g) and (l) around start of plastic deformation, (c) (h) and (m) during plastic deformation, (d) (i) and (n) highest load before failure, (e) (j) and (o) failure.

Figure 4.60 shows deformation evolution and failure of DPU-L2/M2/H2 samples indicated in load-displacement curves with black, yellow and green circles, Figure 4.57b. DPU-L and DPU-M samples fail via IF (Figure 4.60d and h) while DPU-H samples fail via PIF (Figure 4.60 m).

Figure 4.60 a, b, c and d shows the deformation and failure process of DPU-L sample. Deformation localises around the corona bond tip highlighted in yellow circles in Figure 4.60c and spreads through the nugget in a sudden leading to IF mode, Figure 4.60d. DPU-M sample failed via IF mode which has similar mechanisms with DPU-L sample, Figure 4.60h. Larger plastic deformation is observed in the nugget (highlighted in yellow circles in Figure 4.60g) comparing to DPU-L sample just before final failure according to the

size of deformation bands. In DPU-H sample, the cracks initiate within nugget adjacent to corona bond tips, indicated by blue arrows in Figure 4.60j and propagate along the interface of the nuggets, indicated in blue arrows in Figure 4.60k, and then change their paths to the thickness direction leading to PIF mode, Figure 4.60l and m. Additionally, bending can be observed for all three types of samples within HAZ in upper and lower legs, Figure 4.60c,g and k.

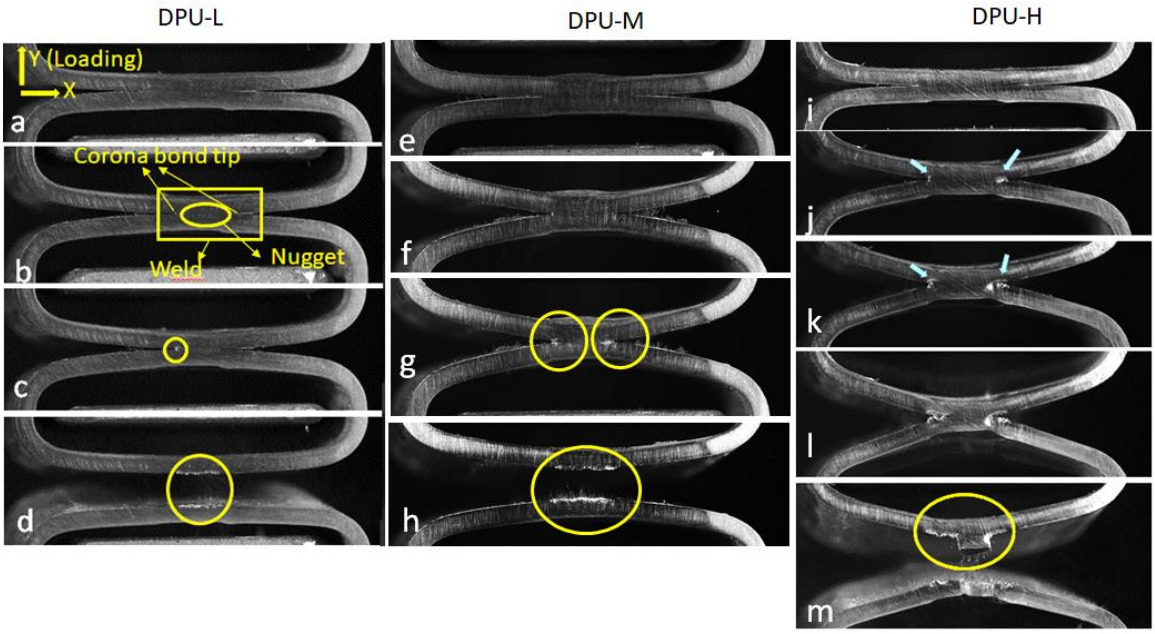

Figure 4.60. Images of deformation evolution and failure of DPU-L4, DPU-M4 and DPU-H4 samples without paint, deformation in various stages highlighted in black, yellow and green circles in Figure 4.57, (a) (e) and (i) before testing, (b) (f) and (j) yielding, (k) during crack propagation of DPU-H4 sample(c) (g) and (l) just before final failure and (d) (h) and (m) final failure.

Figure 4.61 shows the associated measured out-of-plane displacement at the weld zones before final failure indicated in black, yellow and green squares in Figure 4.57. The maximum out-of-plane displacement in DPU samples is around 0.046mm while that of LCU samples is around 0.13mm at the onset of failure, red squares in Figure4.61, and the corresponding in-plane displacement are 0.2mm and 0.7mm, which are much larger. This indicates that 2D maximum principal strain could be the indicator of failure.

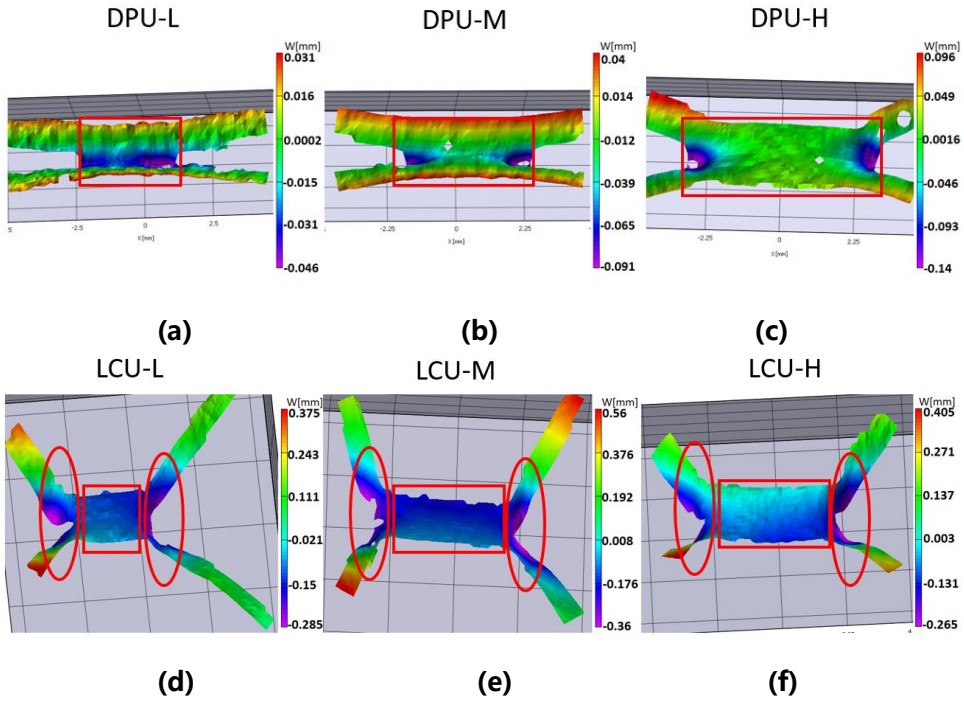

Figure 4.61. Out-of-plane displacement maps before failure of (a) DPU-L, (b) DPU-M, (c)DPU-H samples, (d) LCU-L, (e) LCU-M and (f) LCU-H samples.

The strain dependency curves with respect to the selected subset size of DPU and LCU samples are shown in Figure 4.62. Same convergence criteria with CP samples. A same converge criteria with TS samples was used. Maximum principal strain keeps increasing for DPU samples and LCU samples as subset size decreases, and subsequently comes to convergence when subset sizes are around 31 and 25 pixels. Thus, subset sizes of 27 pixels and 25 pixels were selected for DPU and LCU samples with physical sizes of 340 micron and 330 micron and spatial resolution of 12.6 micron/pixel and 12.2micron/pixel. Additionally, same with TS and CP samples, systematic error of strain measurements were analysed for DPU and LCU samples, Figure 4.63. The maximum strain values are around 0.004% indicating an ignorable error in strain measurement.

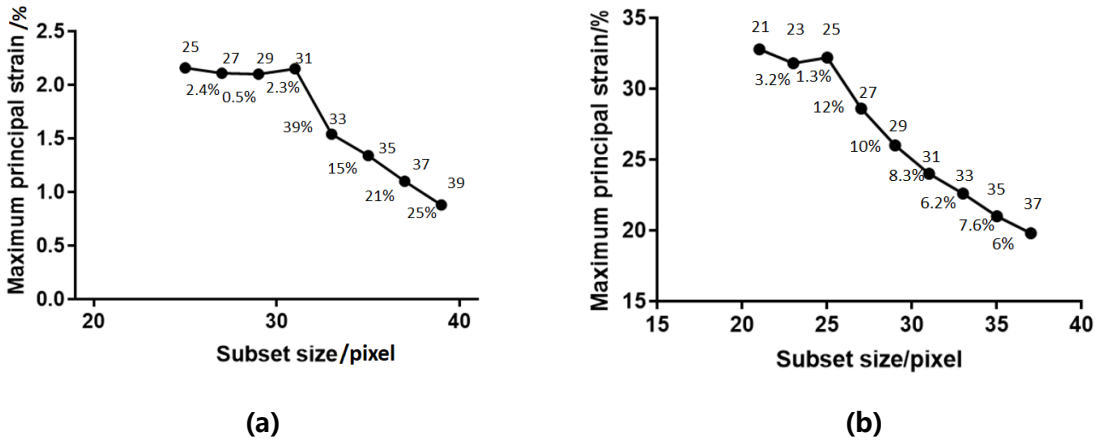

(a) (b)

Figure 4.62. Strain dependency of (a) DPU and (b) LCU samples.

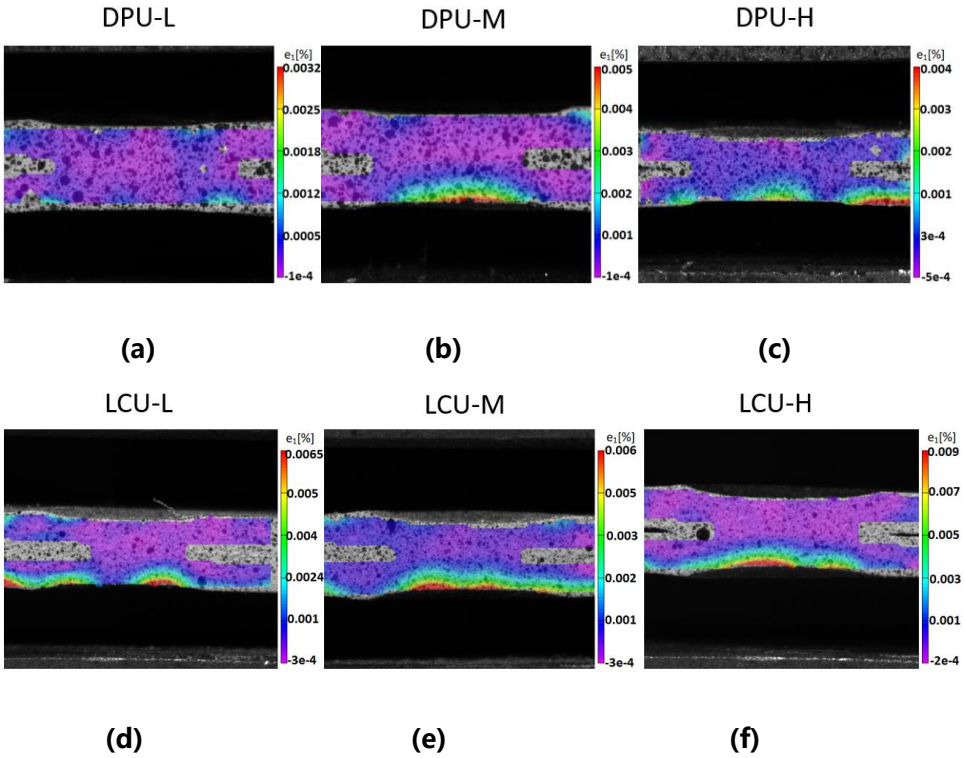

(a) (b) (c)

(d) (e) (f)

Figure 4.63. Uncertainty analysis, systematic error of maximum principal strain of (a) DPU-L, (b) DPU-M , (c) DPU-H samples, (d) LCU-L, (e) LCU-M and (f) LCU-H samples.

Figure 4.64 shows strain distribution and evolution in X, Y and shear direction as well as maximum principal strain distribution of LCU-L1/M2/H2 samples, of several stages in load-displacement curves, the displacement shown in Figure 4.64 reflects each stage in the load-displacement curves in Figure 4.57a. In LCU-L sample, strain e_{xx} concentrates within HAZ and nugget adjacent to the corona bond tip caused by bending, Figure 4.64a$_1$. It becomes

larger as longer displacement and grows much faster leading to larger plastic deformation in X direction, Figure 4.64a_9. Such stretch in X direction results in local necking in HAZ indicated by blue arrows in Figure 4.64$a_{10.}$ According to maximum principal strain concentration in Figure 4.64a_{12}, the concentrated strain in X direction in HAZ is most likely to be the dominant strain component leading to PF failure. The strain evolution of LCU-M and LCU-H samples is similar with LCU-L sample. Additionally, the measured maximum principal strain values at HAZ where the strain concentrates are similar for each welding current and the strain values in the nugget are close to zero, Figure 4.64a_{12}, b_{12} and c_{12}, this might reveal that the welding current has almost no effect on the weld deformation of LCU samples.

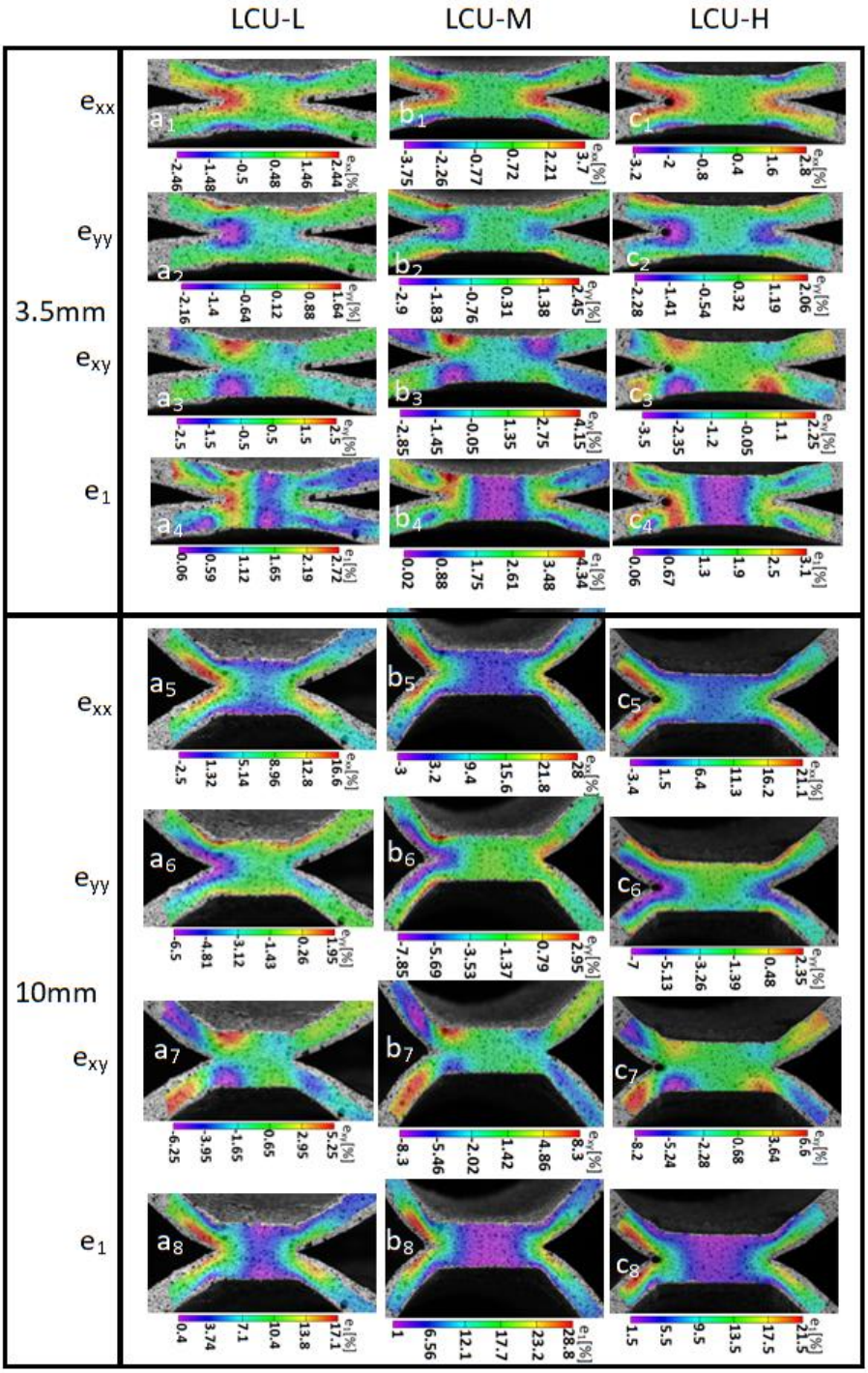

Figure 4.64. Distribution and evolution of strain components of various loading stages for (a) LCU-L1, (b) LCU-M2 and (c) LCU-H2 samples, showing strain components normal to loading direction, e_{xx}, align to loading direction e_{yy}, shear strain component e_{xy}, and maximum principal strain e_1.

Continue to next page.

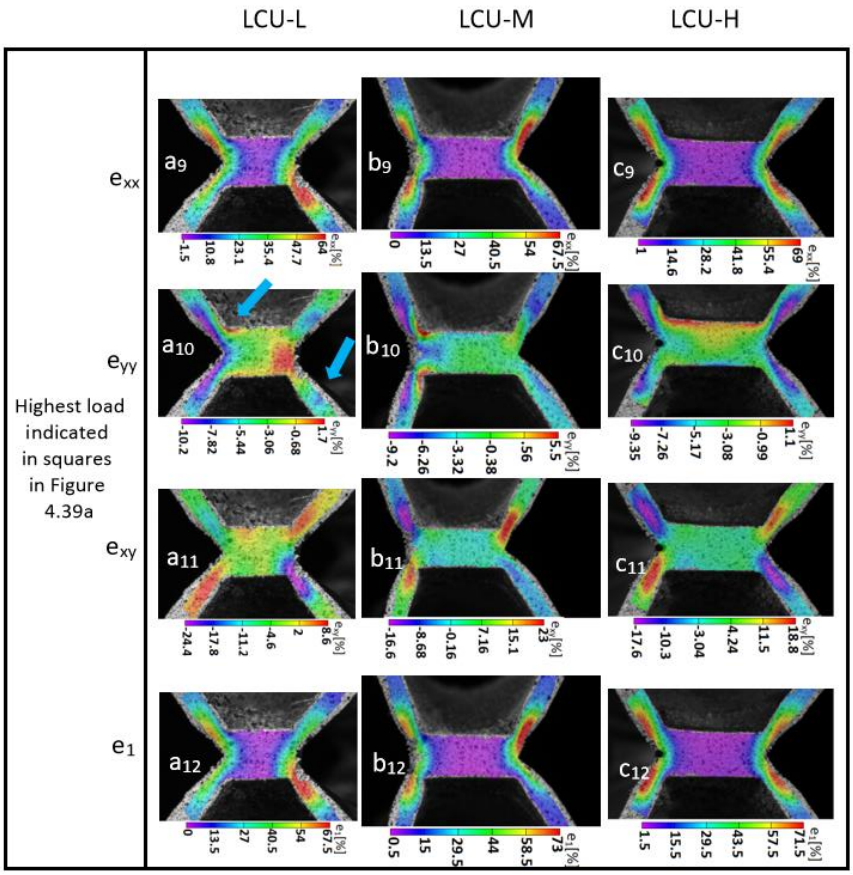

Figure 4.65 shows strain distribution and evolution in X, Y and shear direction as well as maximum principal strain distribution of DPU-L3/M3/H2 samples, of several stages based on displacement in load-displacement curves, Figure 4.57b. In DPU-L sample, e_{yy} strain concentrates in nugget around the corona bond tip makes the greatest contribution to maximum principal strain leading to mode I opening of the nugget and subsequently IF failure, Figure 4.65a_6 and a_8. It can be observed that the maximum principal strain only concentrates at one side of the nugget, indicated by red arrow in Figure 4.65a_8, this could be due to that the loading on two sides of nugget is not symmetric caused by the geometry difference leading to asymmetric stress state.

Figure 4.65b_1-b_{16} shows strain evolution of DPU-M samples. It has similar mechanism with DPU-L sample that strain concentration in Y direction dominates the failure. However, unlike DPU-L sample that strain e_{xx} concentrates in the centre of the nugget at 1.85mm, it concentrates in HAZ and nugget around two corona bond tips, red arrows in Figure 4.65a_5 and b_5, and develops to the centre of the nugget, this could be due to larger and softer

nugget slow the stress transfer.

Strain patterns of DPU-H samples shows different mechanism. The strain e_{xx} concentrates at two sides of the weld rather than the centre before final failure, red arrows in Figure 4.65c$_{13}$. The crack propagates into the nugget at left side, yellow arrow in Figure 4.65c$_{14}$, while it propagates along the boundary of nugget at right side, yellow arrow in Figure 4.65c$_{13,}$ and then leading to PIF mode. Similar with DPCP-H sample, strain concentration in X direction in HAZ dominates the right side which shows a PF failure, while strain concentration Y direction dominates the IF failure at left side, Figure 4.65c$_{17}$-c$_{20.}$

The failure strain inducing the crack initiation can be obtained according to measured maximum principal strain, which is 1.15%, 1.95% and 3.02% for DPU-L/M/H samples, Figure4.65a$_{4,}$ b$_{12,}$ c$_{12}$. The effect of welding current on failure behaviour is similar with DPCP samples.

The observed failure modes and associate strain evolution of U shape samples are similar with symmetric CP samples. However, design of U-shape samples aimed to replicate the cross-tension sample, aiming to reduce the effect of bending to the failure of the weld and investigate the failure mechanism of weld section under tensile loading. Therefore, U-shape sample is not proper to be applied in such investigation.

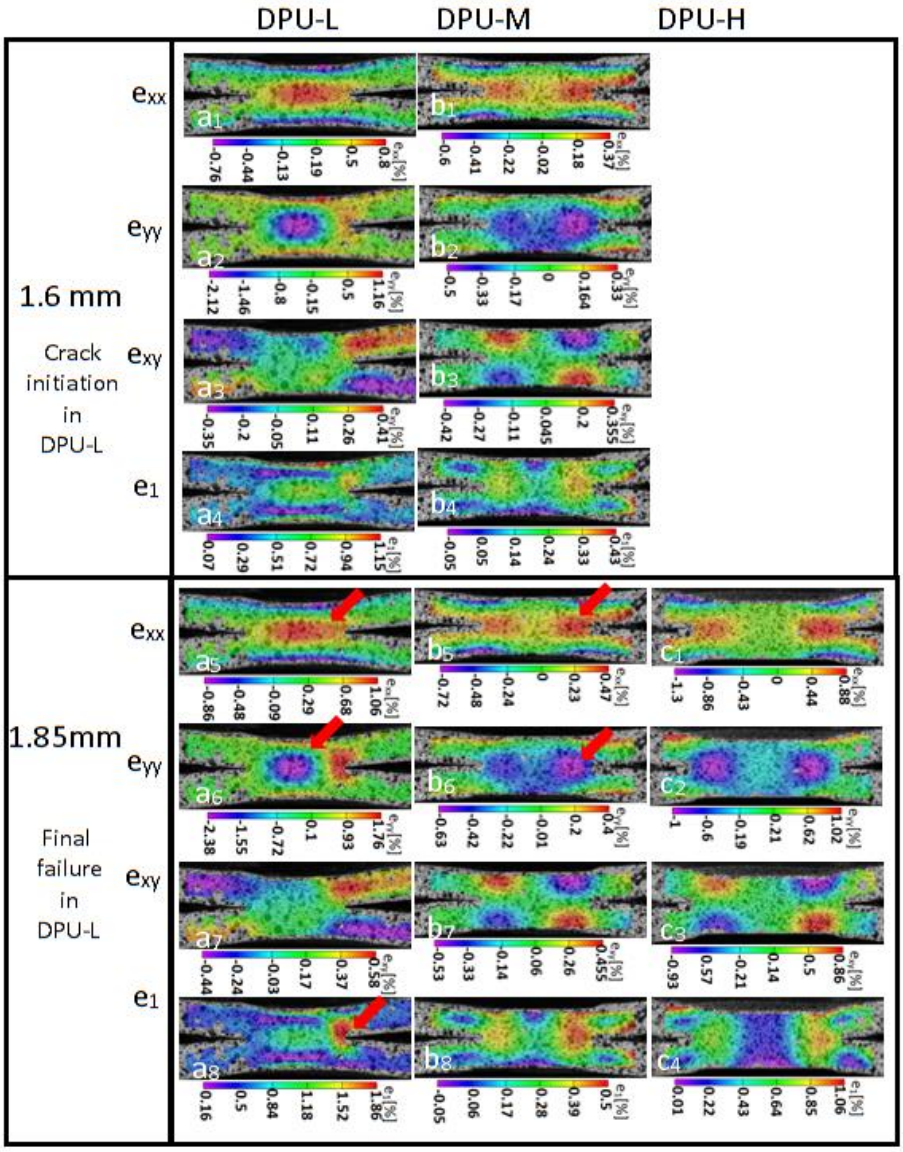

Figure 4.65. Distribution and evolution of strain components of various loading stages indicated by displacement corresponding to Figure 4.57b for (a) DPU-L3, (b) DPU-M3 and (c) DPU-H2 samples, showing strain components normal to loading direction, e_{xx}, align to loading direction e_{yy}, shear strain component e_{xy}, and maximum principal strain e_1.

Continue to next page

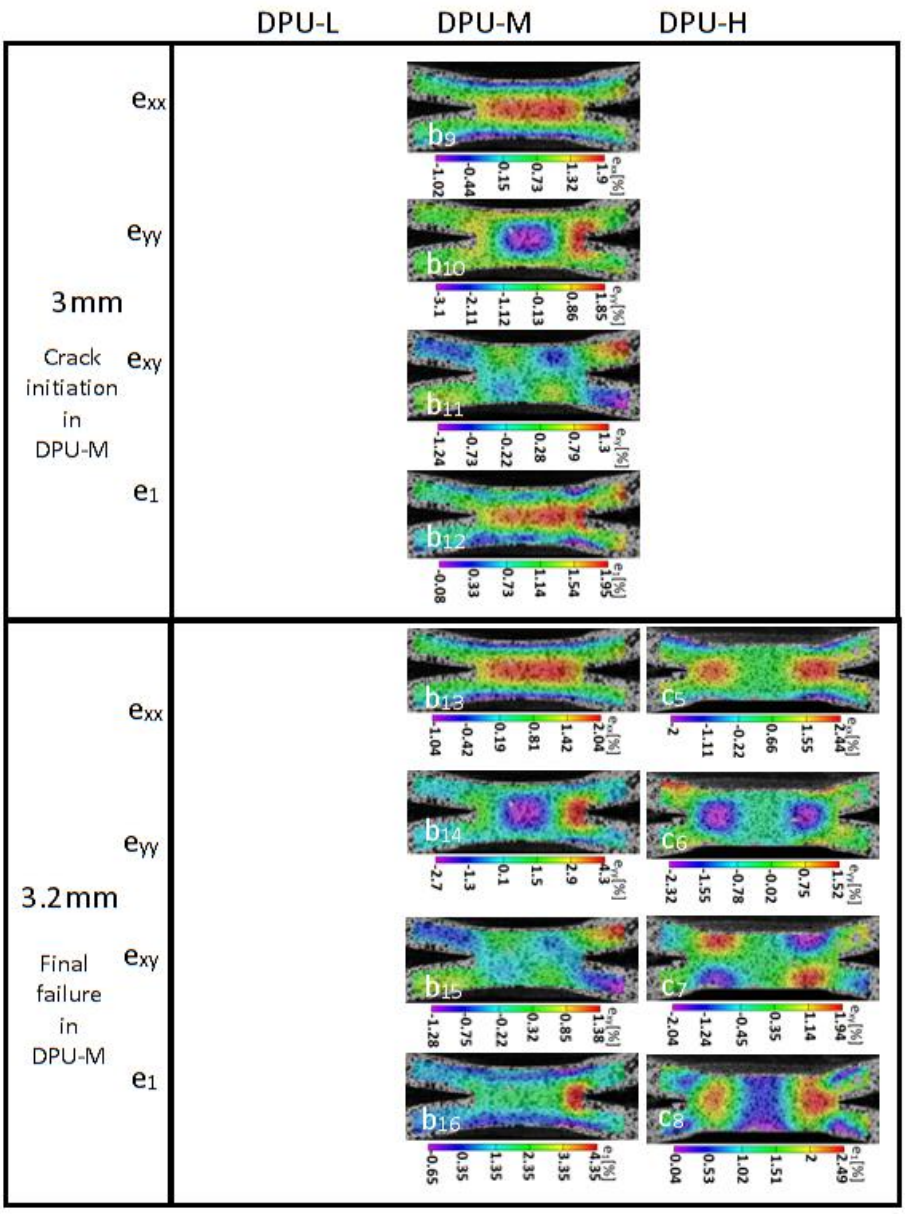

Continue to next page

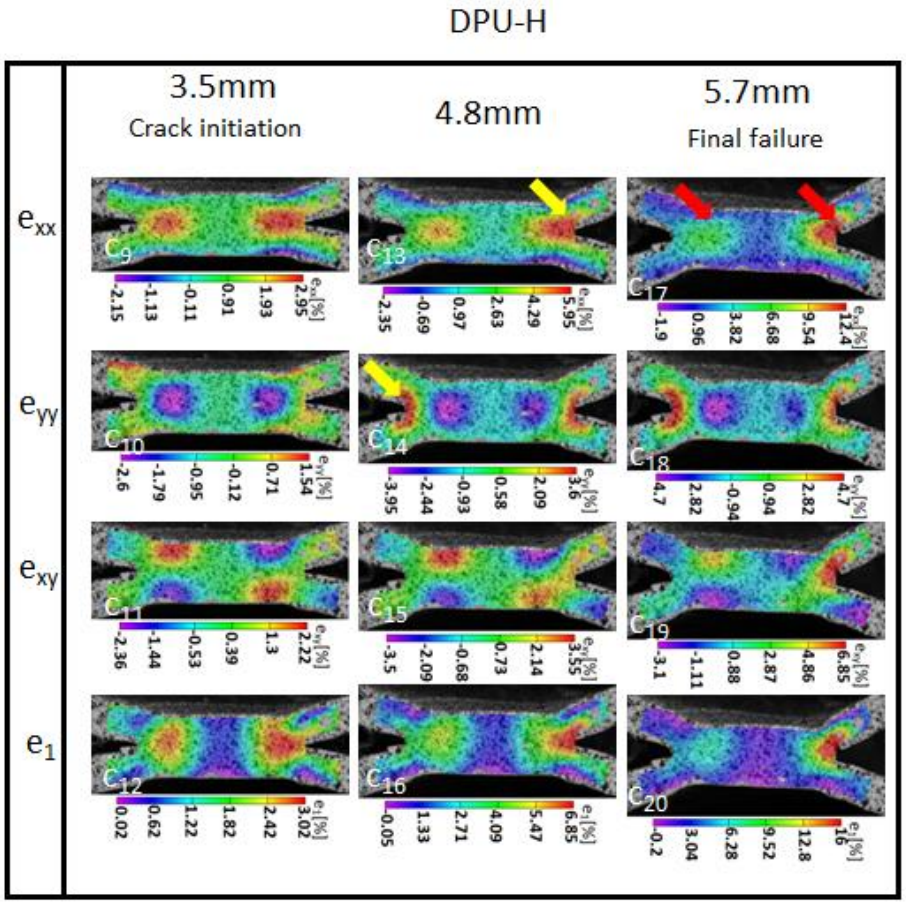

4.7.2 The effect of welding current on fracture mechanism of welds under tensile loading (results)

Morphology of LCU samples is shown in Figure 4.66. Necking is observed within HAZ wherein larger ferrite grains can be observed for samples with each welding current. There is almost no plastic deformation in the nugget. The ferrite grains along the crack path are substantially elongated to loading direction highlighted in green squares in Figure 4.66a, b and c might indicate necking and subsequent ductile failure. The failure could be prompted by the deformation discontinuity at HAZ and nugget.

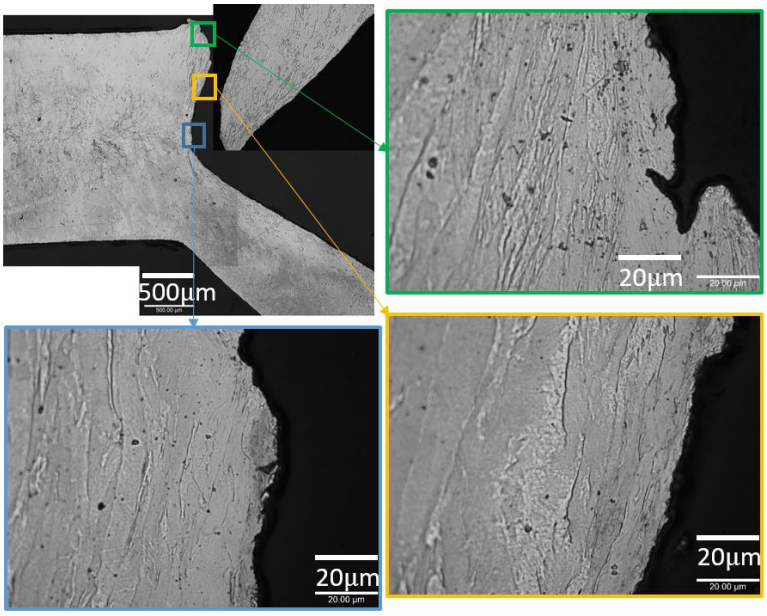

(a)

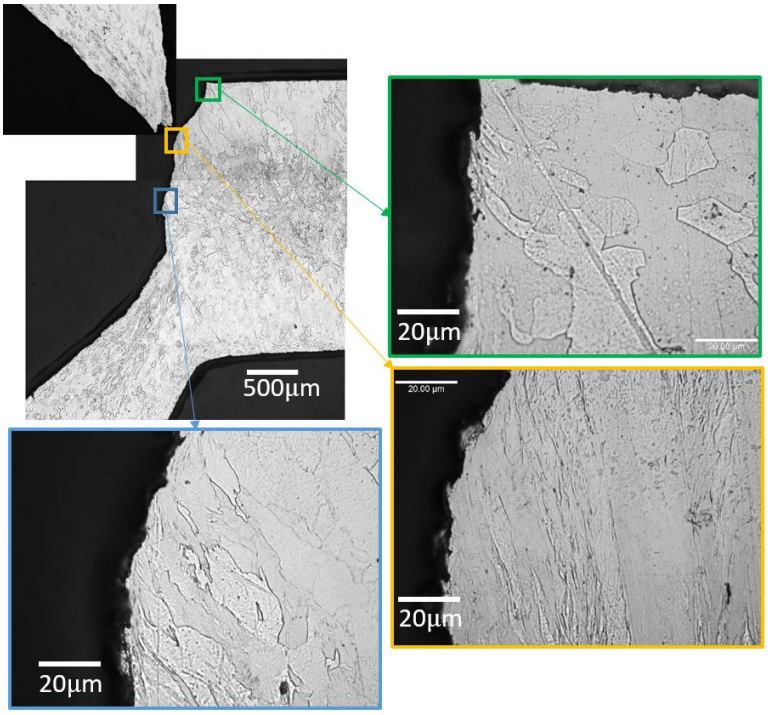

(b)

Figure 4.66. Microstructure in cross section surface of failed spot weld under (a) low welding current (LCU-L), (b) medium welding current (LCU-M) and (c) high welding current (LCU-H).

Continue to next page.

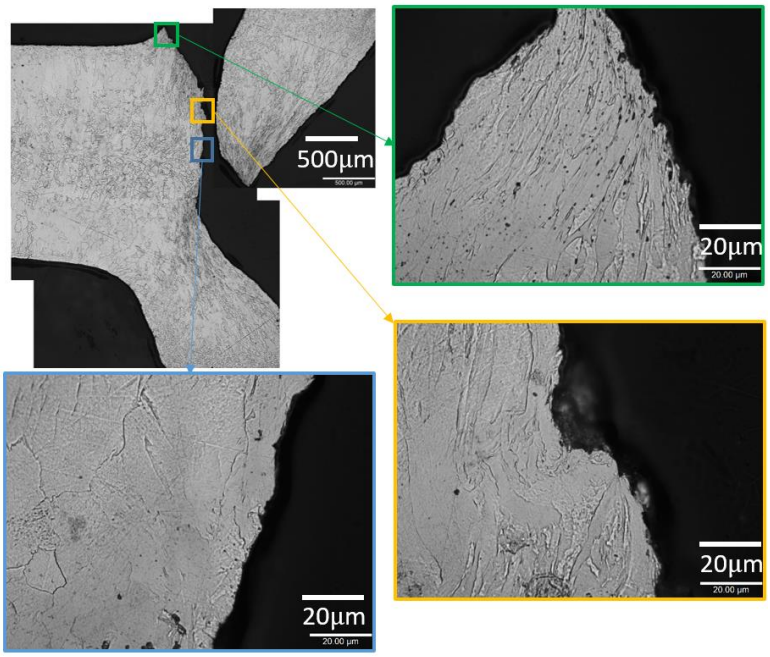

(c)

Figure 4.67a shows fracture surface of DPU-L sample. The brittle fracture surface with flat and reflective facets and some ductile dimples indicates quasi-cleavage fracture which might be caused by stress normal to the fracture surface, highlighted in blue squares in Figure 4.67a. Ductile dimples along the cut surface edge indicate ductile fracture, highlighted in yellow squares in Figure 4.67a. This mechanism could be confirmed by the morphology of cut surface shown in Figure 4.67b. The zigzag crack path is observed in Figure 4.67b, which might indicate the failure is caused by mode I fracture.

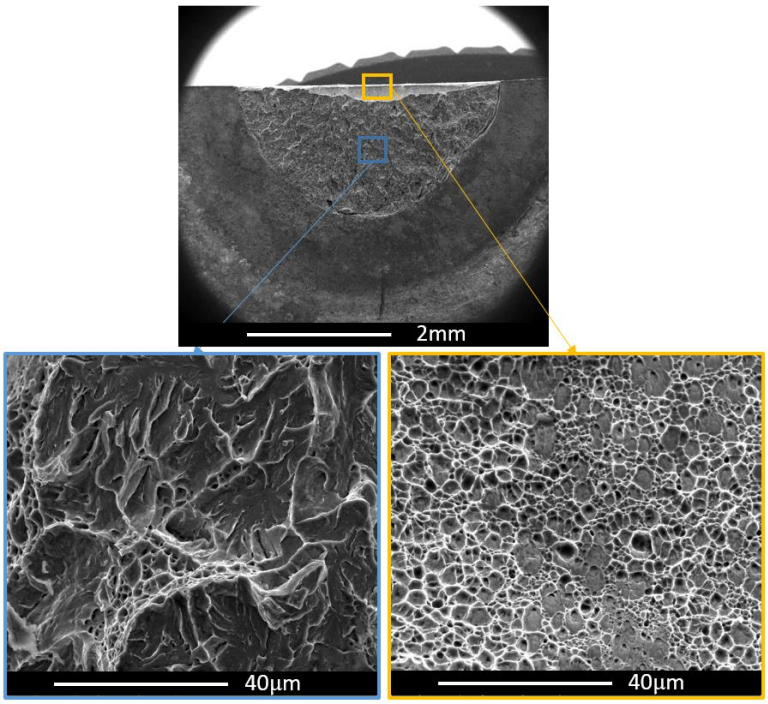

(a)

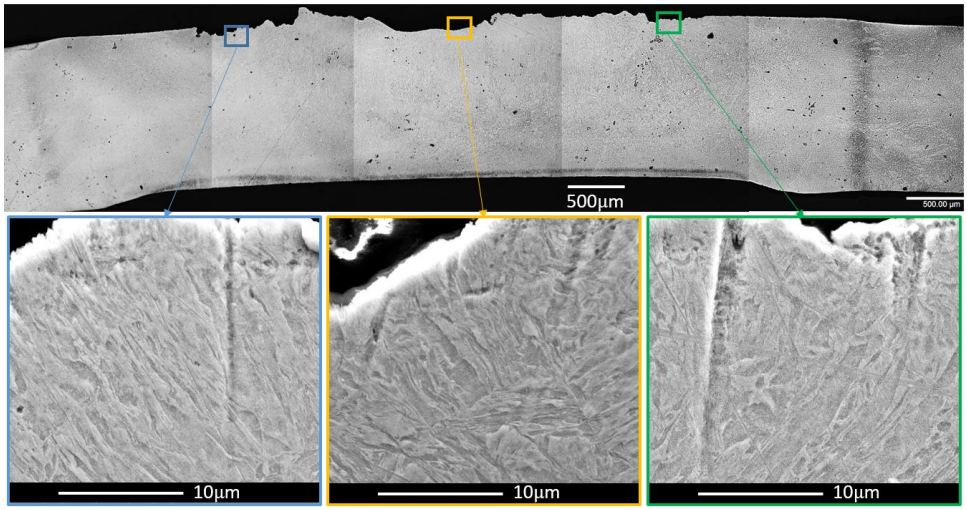

(b)

Figure 4.67. Fracture surfaces (a) and microstructural morphology (b) of DPU-L samples showing domination quasi-cleavage fracture.

It is clear that fracture mechanism of DPU-M sample is same with DPU-L sample according to the micrographs of fracture surfaces and morphology shown in Figure 4.68.

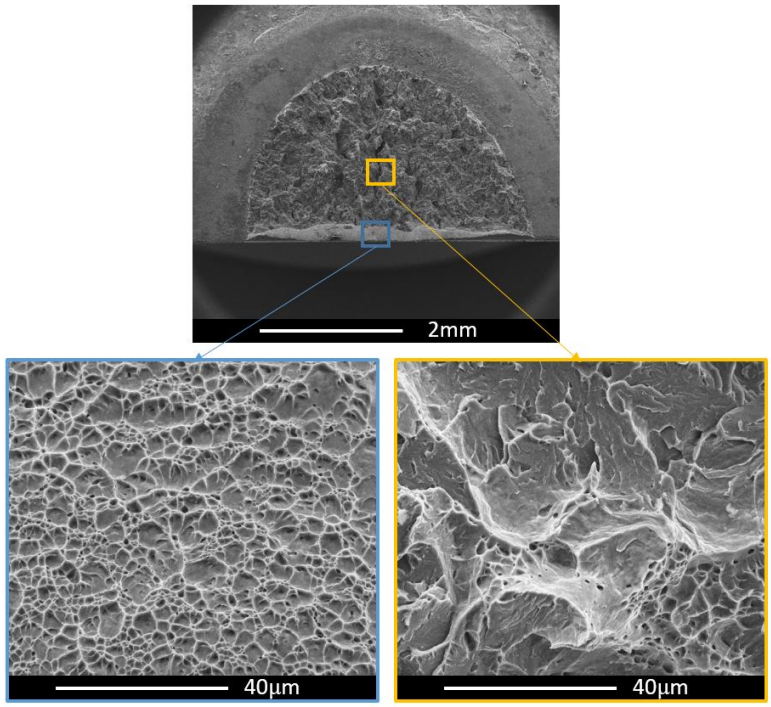

(a)

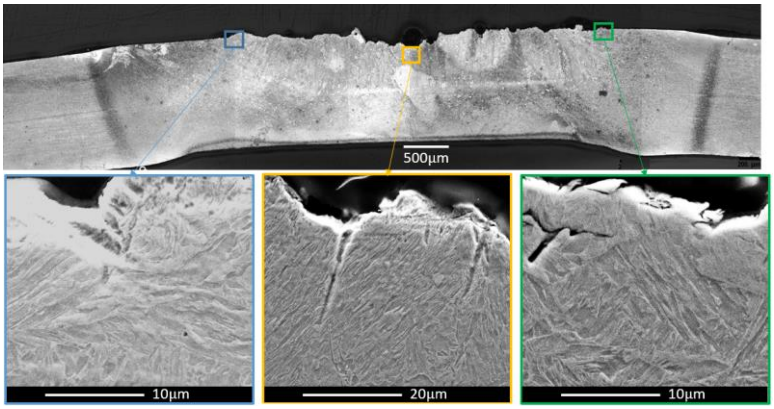

(b)

Figure 4.68. Fracture surfaces (a) and microstructural morphology (b) of DPU-M samples showing domination quasi-cleavage fracture.

The IF phase of DPU-H sample, highlighted in dashed yellow rectangular in Figure 4.69a, shows same fracture mechanisms with DPU-M sample, highlighted in green and yellow squares in Figure 4.69a. However, shear fracture dominates the PF phase according to the slipping bands and elongated dimples highlighted in blue and purple squares in Figure 4.69a. The flat crack path and elongated and deflected martensite laths along the path

highlighted in green and purple squares in Figure 4.69b confirms that shear fracture leads to PF phase.

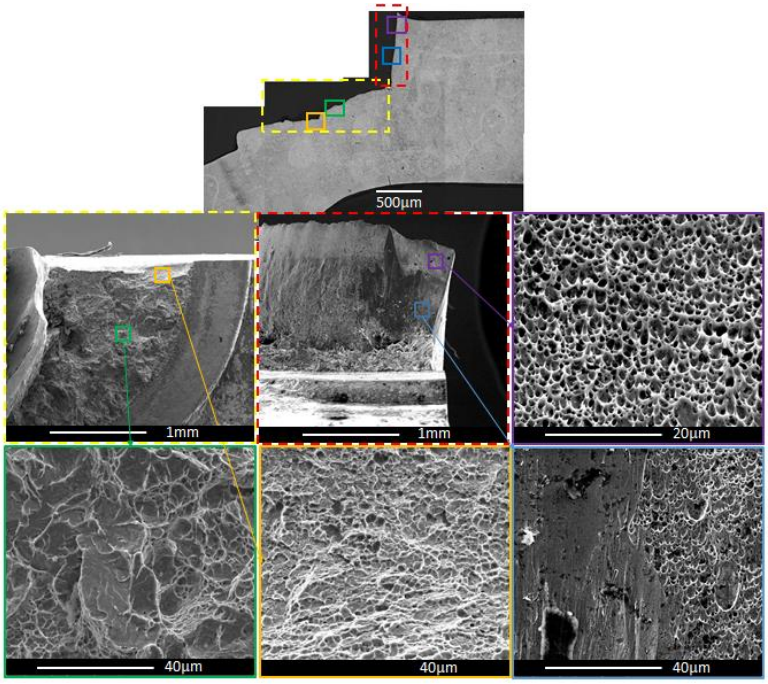

(a)

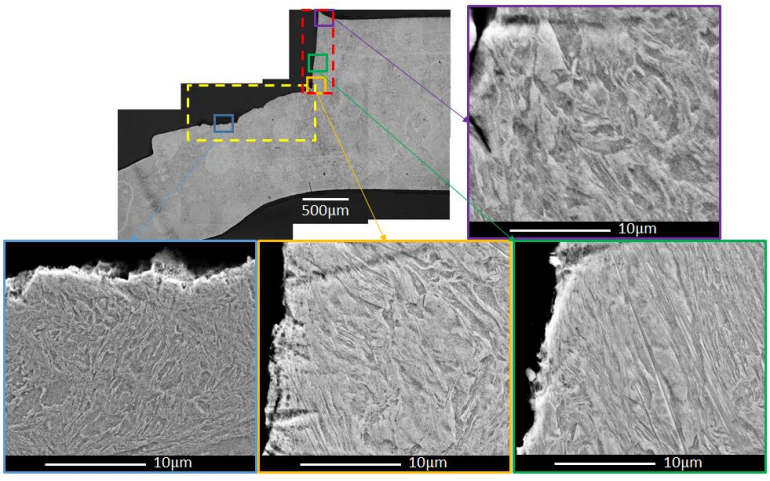

(b)

Figure 4.69 Fracture surfaces (a) and microstructural morphology (b) of DPU-H samples showing domination of quasi-cleavage (IF phase) and shear fracture (PF phase).

4.7.3 Discussion

Similar mechanisms with LCTS and LCCP samples, all LCU samples failed via PF modes due to necking caused by substantial bending deformation in HAZ because of the high ductility of ferrite grains.

Figure 4.70 shows the measured strain evolution of DPU-L, DPU-M and DPU-H samples from beginning of loading to crack initiation within nugget adjacent to corona bond tips highlighted in white squares in Figure 4.70a, b and c. In DPU-L and DPU-M samples, strain evolution in x direction is consistent with maximum principal strain up to about 1.5mm elongation and 3mm elongation, and then strain e_{yy} start increasing up to initiation of failure, which could be due to the end of bending leading to IF mode. It is interesting that left side of weld in DPU-H sample fails via PIF while right side of weld fails via PF. The curves shown in Figure 4.70f and g indicates the difference, at left side of the weld, measured strain in X direction is smaller than that in Y direction at point of crack initiation, at right side of the weld, and measured strain in X direction is much larger than that in Y direction. Thus, this phenomenon might result in different failure modes. The difference of curves in Figure 4.70 f and g is due to that the geometry of DPU sample is not totally symmetric resulting in the different stress state within the nugget adjacent to two corona tips of the weld. The material within HAZ/nugget around tips with smaller angles could have longer bending arm leading to larger bending moment, strain evolution shown in Figure 4.70g. Similar with DPCP samples, increase delay of measured strain in Y direction is also observed, which is due to the same reason that materials in HAZ with higher welding current around the corona tips is more ductile and easier bended. The effect of welding current and microstructure on failure is also similar with DPCP samples.

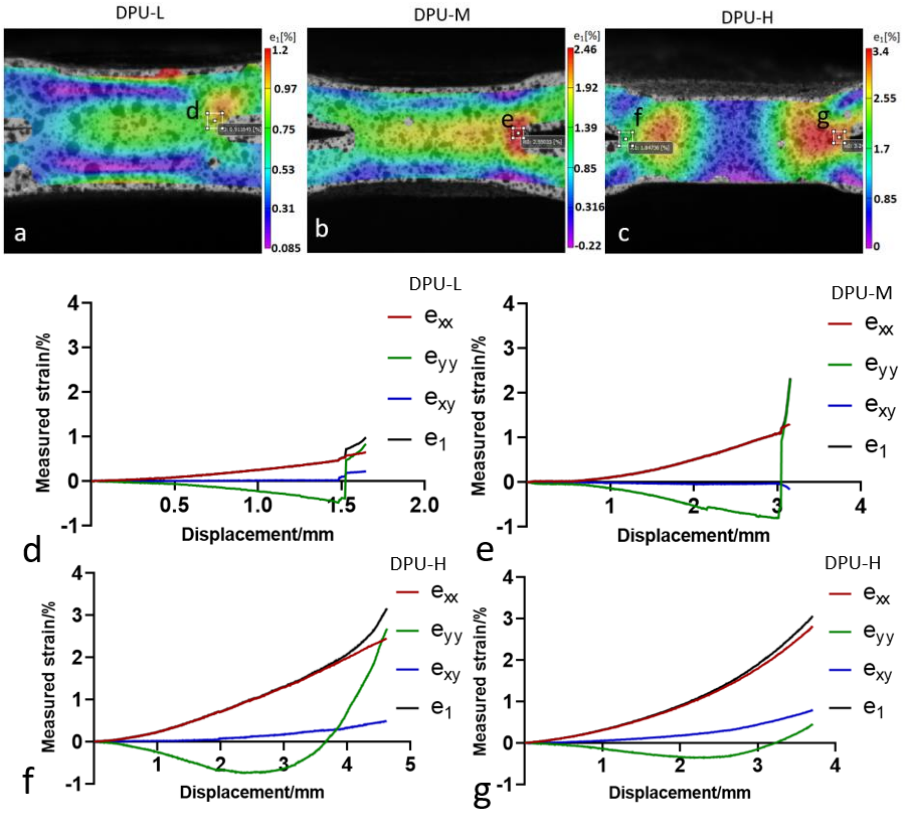

Figure 4.70. Maximum principal strain evolution at crack initiation, (a) DPU-L, (b)DPU-M and (c)DPU-H, indicating the extracted position of strain evolution curves between start point of loading and crack initiation of (d) IF mode in DPU-L, (e) IF and PF modes in DPU-M as well as (f) and (g) IF and PF modes in DPU-H samples.

According to the strain evolution and fractography analysis, the failure mechanism of IF mode of DPU sample is similar with DPCP sample. However, DPU-M sample failed via IF mode while DPCP-M sample failed through PIF mode, this could be due to the bending arm of U-shape sample is smaller than CP samples, causing that the bending stress is not large enough to induce sufficient bending deformation in HAZ in horizontal (X) direction before stress σ_y prompts the crack goes through the nugget. DPU-H sample failed through PIF mode and shear fracture surface is observed in PF phase, Figure 4.69. This could also be due to the load in loading direction resulted in sufficient shear stress before the bending stress is enough to open the crack along loading direction in PF phase.

Figure 4.71 shows the simple model of stress analysis at the circumference

and interface of weld nugget of the U-shape samples. Design of U-shape samples aims to replicate the stress state of cross-tension samples which is under tensile stress along loading direction as reported by Pouranvari et al. [234], specifically, reducing the influence of bending on the weld and make the welds under tension along loading direction. However, according to the strain evolution analysis in the results section, Figure 4.35, 4.36, 4.64, 4.65 and 4.53, bending still greatly affects the failure leading to the stress state similar with symmetric CP sample. Therefore, U-shape samples is not proper to meet the requirement.

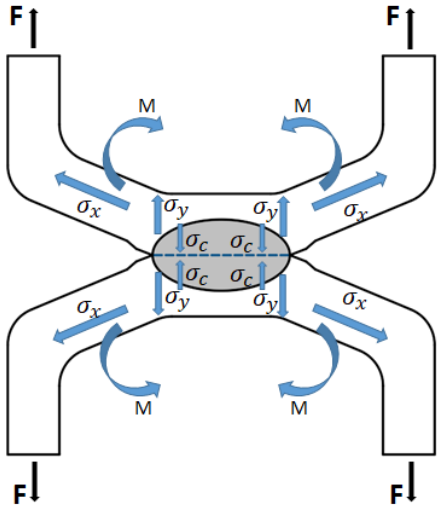

Figure 4.71. Stress analysis at the circumference and interface of the weld nugget.

4.8 Summary

In this chapter, microstructure characterisation and microhardness measurement of weld section in two types of materials was carried out. The hardness was found varying due to the difference in microstructural morphology in BM, HAZ and nugget. Moreover, Welding current showed negative correlation with hardness profile of weld of DP1000, while it had almost no effect on that of low carbon steels, this could also be due to the microstructure difference in welds of two types of materials. The stress state of de design sample geometries were validated according to the conventional samples. Deformation behaviour could be similar for TS and CP samples, but larger difference was found for U-shape samples. Deformation evolution of welds under TS, CP and U-shape samples under three levels of welding currents

was quantified using DIC technique, and the associated fractography analysis was conducted. It was found that deformation evolution under different loading conditions and welding currents greatly affect the failure mechanisms of samples in DP1000 steel, but shows less effect on failure of samples in low carbon steel. This could also be related to the presence of microstructural morphology difference of weld section of two types of materials. In situ tensile test of DPMiCP samples was done and crack development and deformation evolution were obtained. Results showed the effect of microstructure on crack initiation and propagation. Moreover, according to the obtained measured maximum principal strain, it is possible to determine the failure strain at the initiation of failure which could be used to identify a failure criterion for 2D FE damage modelling.

According to the obtained results, the analysis of deformation and failure behaviour of welds and the effect of welding current on failure mechanisms of the weld under different loading conditions were conducted.

In the next chapter, the local mechanical properties of the weld section were characterised with the proposed approaches and validated using FE method, aiming to validate the achieved experimental data and propose a potential and possible way for the future FE modelling development.

5 CHARACTERISATION OF MECHANICAL PROPETIES OF WELD SECTIONS FOR FUTURE WORK IN FE MODELLING DEVELOPMENT

Several approaches were proposed in this chapter in order to characterise local mechanical properties of the weld section including true stress-strain curves and stress triaxiality. The approaches were then validated through comparing the load-displacement curves of FE model using obtained mechanical properties and corresponding experiment. A commercial finite element package Abaqus/explicit was used to create the FE model. A 3D stress 8-node linear brick, reduced integration Hex element, C3D8R, was applied into the simulation in order to reduce the computation time. The sample used for the validation was DPCP sample with applied high welding current. Johnson-Cook failure model was selected as the damage model to simulate the initiation of damage. Mesh refinement was implemented in order to enhance the simulation accuracy.

5.1 Constitutive properties characterisation

The constitutive properties of base metal, heat affected zone and nugget of the welds were obtained using different approaches, including uniaxial tensile test, DIC technique and nanoindentation.

Engineering stress-strain curve of the given DP1000 material (base metal) was obtained using uniaxial tensile test and DIC technique. The standard subsize uniaxial tensile sample was selected and designed based on the tensile testing standard ASTM E8-13a [46], Figure 5.1. Two samples were made along the rolling direction using the given 1.2mm steel sheet and tested to ensure the consistency of the results. The area of interest of the samples was painted with random speckle patterns, Figure 5.2a, and 2D DIC technique was applied to achieve the deformed images with the corresponding load and crosshead displacement of each image frame during the test. The images were processed using the Davis software with a subset size of 21 pixels and a step size of 7

pixels after the strain measurement sensitivity analysis, Figure 5.2a. A virtual extensometer was applied along the gauge length, which is 25mm, according to the standard [46] in order to extract the displacement variation of the gauge, Figure 5.2b. Then, the engineering stress-strain curve can be calculated using the load, displacement of the gauge and area of the gauge. The true stress – strain curve was calculated based on the obtained engineering stress-strain curve and shown in Figure 5.3.

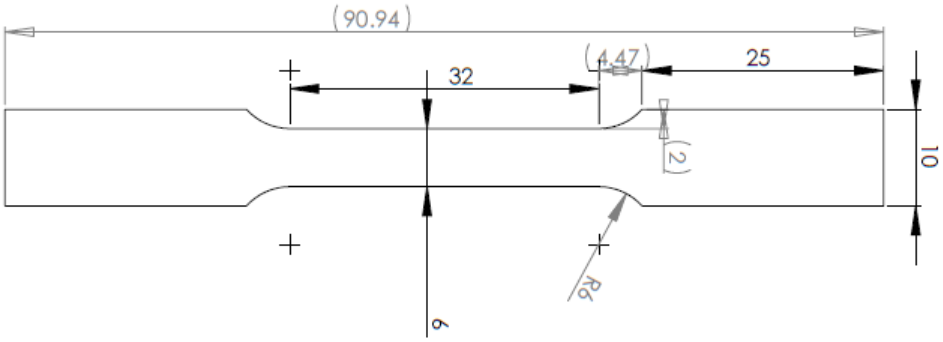

Figure 5.1. Drawing of subsize standard uniaxial tensile sample [46]**.**

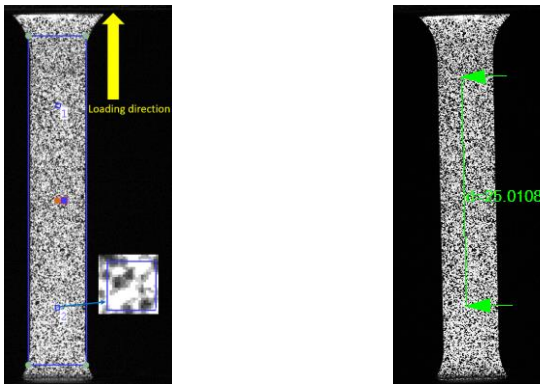

(a) **(b)**

Figure 5.2. (a) Unaxial tensile sample showing the loading direction, speckle pattern and selected subset size, (b) uniaxial tensiel sample showing the virtual extensometer and gauge length.

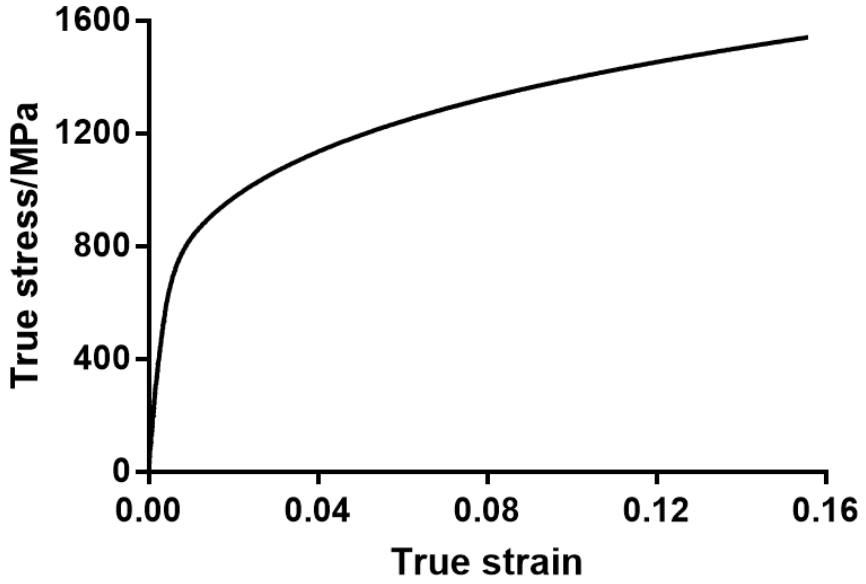

Figure 5.3. True stress-strain curve of DP1000.

The nugget of resistance spot weld has a quasi-cylindrical structure and tiny volume as mentioned in the previous sections. In addition, the HAZ has various regions (SGHAZ, ICHAZ, FGHAZ and CGHAZ) with different mechanical properties within the small ring structure as mentioned in literature review. It is hardly determining the constitutive properties of the spot weld using standard uniaxial tensile testing method. In this case, nanoindentaion and numerical calculation were introduced to obtain the flow stress curves of nugget and HAZ. As mentioned in section 2.2, Young' s modulus E, strain hardening exponent n, yield strength σ_y and strength coefficient K can be calculated according to the Nanoindentation data. Flow stress curve of the material is able to be obtained with these three parameters by the flow stress equation:

$$\boldsymbol{\sigma = k\varepsilon^n}$$

Equation 5.1

Where σ is true stress and ε is true strain.

Several steps were conducted to determine the parameters. Firstly, the weld section of DPCP-H sample was cold mounted, grinded to the centreline and polished properly in order to smooth out the cut surface of the weld and avoid any influence of the rough surface to the indentation results. Secondly, Nanoindentation was performed onto the sample surface using a Premier

nanoindenation machine with Berkovich indenter to get the necessary parameters including maximum indentation load P_{max} GPa, indenter contact area A, nm^2, maximum indentation depth h_{max}, nm, reduced modulus E_r, GPa, curvature of the loading curve $C = \frac{P_{max}}{h_{max}^2} \times 1000$ (17), GPa and unloading slope $\frac{dP_u}{dh}$ when $h_{max} = h, N/m$, thirdly, Young' s modulus, strain hardening exponent n and yield strength σ_y can be calculated by substituting the parameters in step 2 into the following equations 5.2-5.6 from literatures [42]–[44], lastly, strength coefficient K can be calculated by substituting $\sigma_{0.033}$, true strain $\varepsilon_{0.033} = 0.033$ and n into equation 5.1.

$$\frac{C}{\sigma_{0.033}} = -0.1 \times \{-1.131[\ln(\frac{E_r}{\sigma_{0.033}})]^3 + 13.635\left[\ln\left(\frac{E_r}{\sigma_{0.033}}\right)\right]^2 - 30.594\left[\ln\left(\frac{E_r}{\sigma_{0.033}}\right)\right] + 29.267\}$$

Equation 5.2

$$\begin{aligned}\frac{1}{E_r h_{max}}\frac{dP_u}{dh} = {} & (-1.40557n^3 + 0.77526n^2 + 0.15830n - 0.06831)\left[\ln\left(\frac{E_r}{\sigma_{0.033}}\right)\right]^2 \\ & + (-79.99715n^3 + 40.55620n^2 + 9.00157n - 2.54543)\left[\ln\left(\frac{E_r}{\sigma_{0.033}}\right)\right] \\ & + (122.65069n^3 - 63.88418n^2 - 9.58936n + 6.20045)\end{aligned}$$

Equation 5.3

$$E_r = \frac{1}{2.12}\frac{\sqrt{\pi}}{\sqrt{A}}\frac{dP_u}{dh}$$

Equation 5.4

$$\frac{1}{E_r} = \frac{1 - v^2}{E} + \frac{1 - v_i^2}{E_i}$$

Equation 5.5

$$\sigma_{0.033} = \sigma_y(1 + \frac{E}{\sigma_y}0.033)^n$$

Equation 5.6

Where v is the Poisson ratio of the material and v_i is the Poisson ratio of the indenter.E_i is the Young' s modulus of indenter. $\sigma_{0.033}$ is the true stress when true strain is equal to 0.033.

A Matlab (refer to appendix) code was developed to solve the unknown

parameters mentioned above.

The flow stress curves of BM, HAZ and nugget were calculated based on the Nanoindentation data. The HAZ was divided into 7 regions averagely with an interval of around 0.15mm considering the area of indentation pattern and enough distance between each pattern, Figure 5.4a and b. Twelve indents were performed in each pattern to get an average value as the indent is too small to cover both ferrite and martensite. The flow stress curves of BM, nugget and HAZ of DPCP-H sample made of DP1000 are shown in Figure 5.5. The flow stress curves of BM calculated according to the Nanoindentation data was compared with that obtained from uniaxial tensile test as shown in Figure 5.4. The two curves are almost consistent which indicates that the flow stress curves calculated by the method mentioned is reliable. The calculated Young' s Modulus of BM, HAZ and nugget of DPCP-H sample in DP1000 are shown in Table 5.1.

Table 5.1. Calculated Young' s Modulus of BM, HAZ and nugget of DPCP-H sample according to Nanoindentation data.

	HAZ-1	HAZ-2	HAZ-3	HAZ-4	HAZ-5	HAZ-6	HAZ-7	BM	nugget
E/GPa	205.5	208.4	208.7	210.1	205.4	209.6	209.1	204	211.5

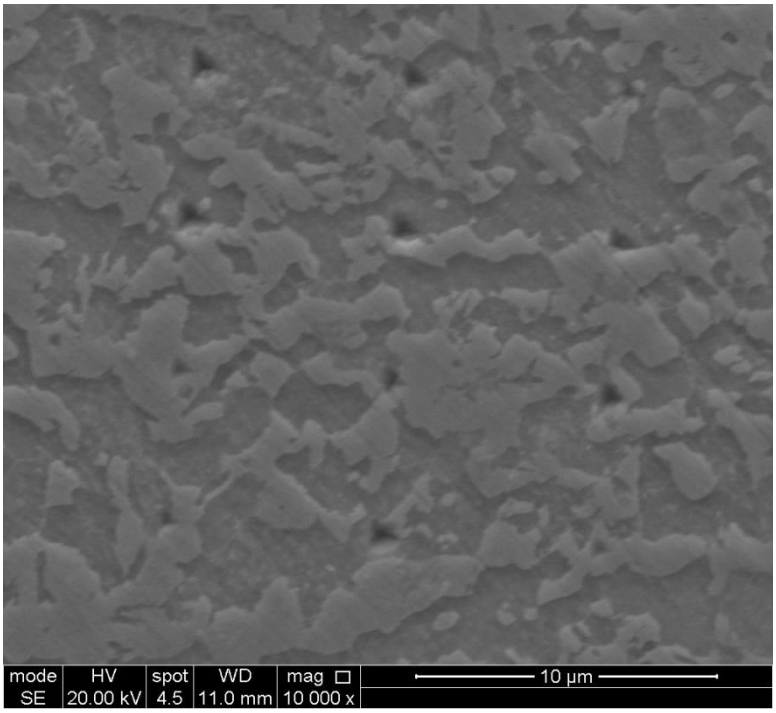

(a)

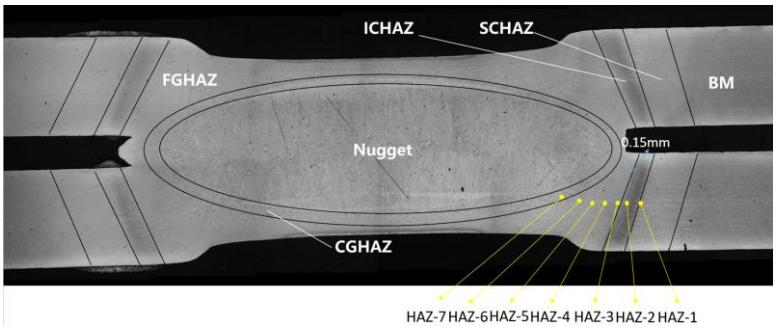

(b)

Figure 5.4. (a) 12 indents in HAZ of weld of DPCP-H sample in DP1000, (b) 7 regions of HAZ of weld in DPCP-H sample in DP1000.

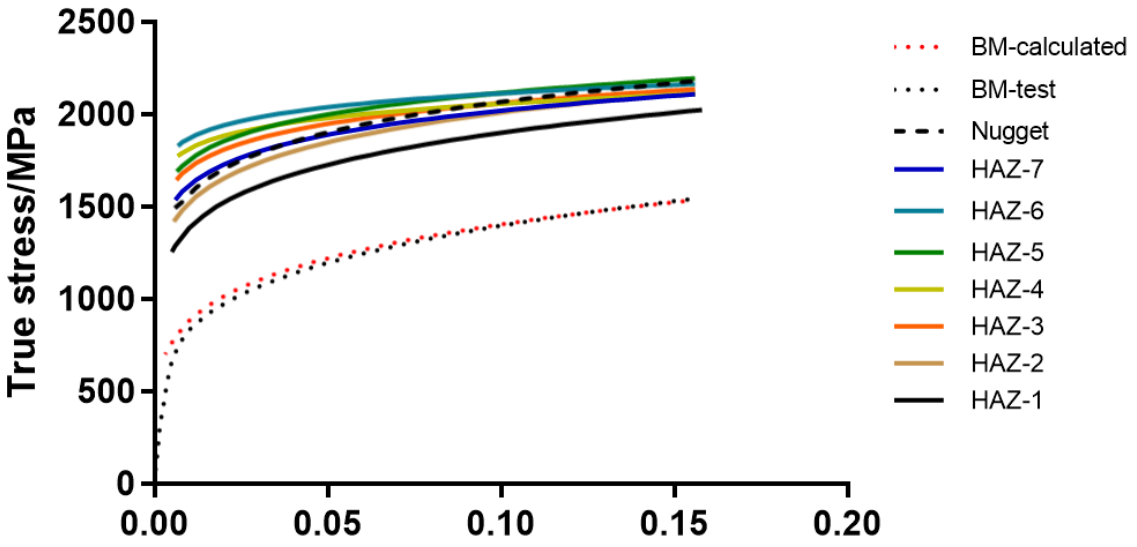

Figure 5.5. Flow stress curves of BM, HAZ (7 regions) and nugget calculated according Nanoindentation data and flow stress curve of BM obtained from uniaxial tensile test for the spot weld of DPCP-H sample in DP1000.

5.2 Material constants characterisation of J-C failure model

Johnson-cook failure model, which has been built in Abaqus, was selected to simulate the damage initiation of spot weld as this model does not have many unknown parameters needed to be calibrated and is proved to provide realistic solutions to damage of metals[235]. Johnson-cook failure model was proposed by John and Cook [129] and given in the following equation:

$$\varepsilon_f = [D_1 + D_2 \exp(D_3\sigma^*)]\left[1 + D_4 \ln\left(\dot{\varepsilon_p}^*\right)\right][1 + D_5 T^*]$$

Equation 5.7

where $D_1 - D_5$ are material constants ε_f is fracture strain, σ^* is stress triaxiality, $\dot{\varepsilon_p}^*$ is strain rate and T^* is temperature [130].

As D_4 and D_5 are the constants related to strain rate and temperature which were kept constant in the coach-peel test, thus D_4 and D_5 were assumed to be zero and only D_1, D_2 and D_3 were needed to be determined. In hence, equation 3.7 can be simplified as equation 5.8:

$$\varepsilon_f = [D_1 + D_2 \exp(D_3\sigma^*)]$$

Equation 5.8

In order to determine D_1, D_2 and D_3, it is necessary to get failure strain

and corresponding stress triaxiality at failure point of three different sample geometries. Thus, macro CP, TS and U-shape samples of high welding current were selected. Measured von mises strain of DPCP-H, DPTS-H and DPU-H samples using DIC technique at the point just before crack initiation was selected as the failure strain, Figure 5.6 d, e and f. Finite element models of DPCP-H, DPTS-H and DPU-H samples were created using Abaqus/explicit to get stress triaxility. The applied properties of flow stress of the weld were assumed to be same for DPCP-H, DPTS-H and DPU-H samples. The stress triaxiality of three types of geometries was obtained based on the same time point and displacement with experiment when the crack initiation started, highlighted in Figure 5.6 a, b and c. Table5.2 shows the failure strain and corresponding stress triaxiality and calculated constants D_1, D_2 and D_3.

The obtained mechanical properties and damage constants of J-C damage model were then applied into the FE model to obtain the load-displacement curve of DPCP-H sample.

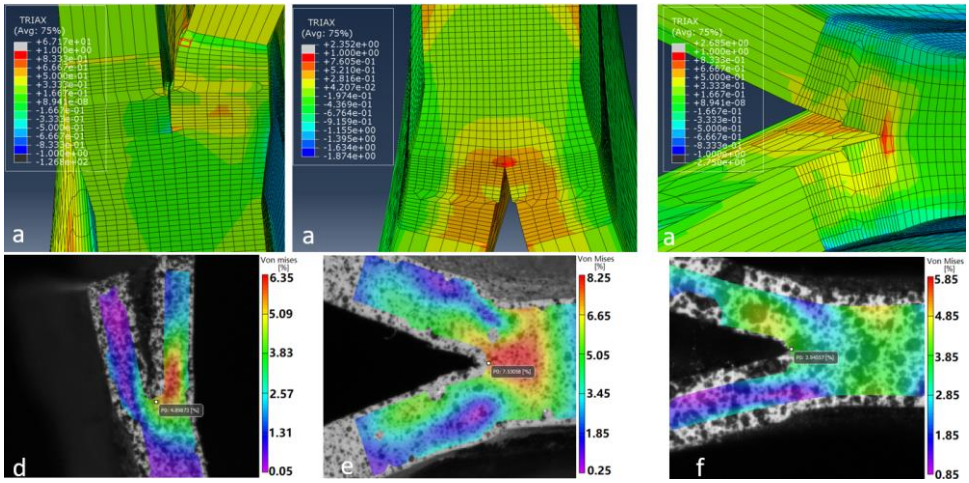

Figure 5.6. (a, b and c) Stress triaxiality of the position where the crack initiated of FE model and (d, e and f) strain maps in DPCP-H, DPTS-H and DPU-H samples.

Table 5.2. Failure strain and corresponding stress triaxiality of DPCP-H, DPTS-H and DPU-H samples and calculated constants D_1, D_2 and D_3.

Sample types	Failure strain	Stress triaxiality	Constants
DPCP-H	0.075	0.91	$D_1 = 0.0714$
DPTS-H	0.049	0.275	$D_2 = 0.00156$
DPU-H	0.04	0.874	$D_3 = 3.03$

5.3 Geometry and mesh

The geometries of macro CP sample were created in terms of the dimensions of the fabricated samples. The details of the created weld section are shown in Figure 5.7. Simplification was made to the nugget section (highlighted in yellow square, Figure 5.7) to simplified the simulation, unlike the real nugget which has an ellipsoid shape, it was created as cylindrical shape between two electrode indents (highlighted in blue square, Figure 5.7). Seven HAZ regions were generated adjacent to the nugget. Two pre-cracks (indicated in green lines in Figure 5.7) were made around the nugget using contour integral method between HAZ of two sheets to represent corona region of the weld.

Figure 5.8a shows the created geometries and mesh of DPCP sample. An 8-node linear brick element C3D8R was used to mesh the three types of geometries. Additionally, element deletion was on for failure simulation of high welding current DPCP sample (DPCP-H). Mesh was refined in the weld section to increase the simulation accuracy, Figure 5.8b.

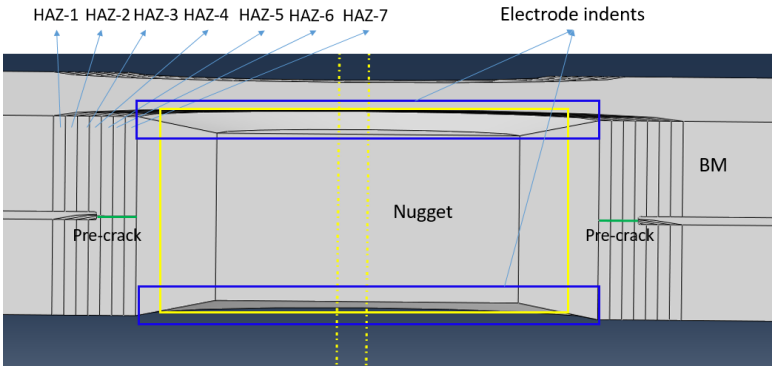

Figure 5.7. Structure of the spot weld model.

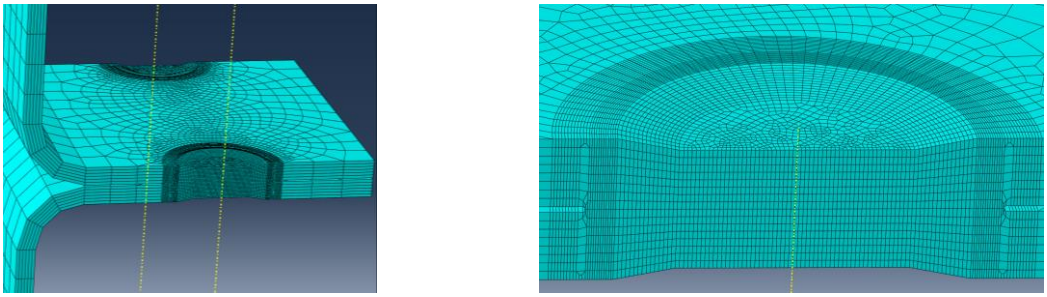

(a) **(b)**

Figure 5.8. Geometry and mesh, (a) macro-CP and (b) mesh refinement of weld.

5.4 Interaction and boundary conditions

All the contacts were created between each contact surface using kinematic contact method without friction. Boundary conditions were created according to experiments of macro CP samples, Figure 5.9. Two legs of macro CP samples were sectioned into two parts in order to model the clamped section of two legs, Figure 5.9. Upper and lower surfaces of the loading leg (highlighted in yellow square, Figure 5.9) were constrained to the reference point (RP-1) and a tension rate of 1mm/s was assigned to the point RP-1. Upper and lower surfaces of the fixed leg were fixed.

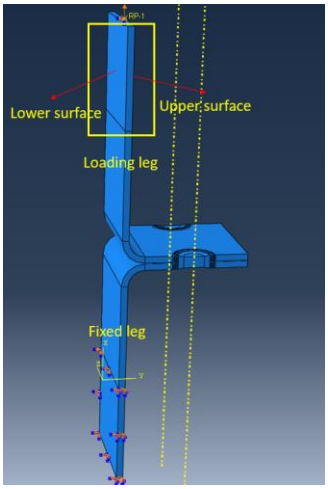

Figure 5.9. Boundary conditions of the simulation macro-CP sample.

5.5 Local mechanical properties validation of the weld section (macro coach-peel sample in DP1000)

As mentioned in methodology section, the flow stress curves of different areas of HAZ and nugget were obtained based on nanoindentation method. The damage constants of J-C damage model were calculated. The following results are obtained using the material properties of macro coach-peel sample with applied high welding current, DPCP-H, was obtained as an example to validate the achieved flow stress properties. Figure 5.10 shows the mesh refinement curve of the model, the maximum load of load –displacement curve of the model was selected for the refinement, highlighted in yellow square in Figure 5.10. It is clear that there is a big drop of maximum load for element number around 40000, and then a convergence is observed when the element number is around 130000. Thus, an element number of around 130000 was select to get the results.

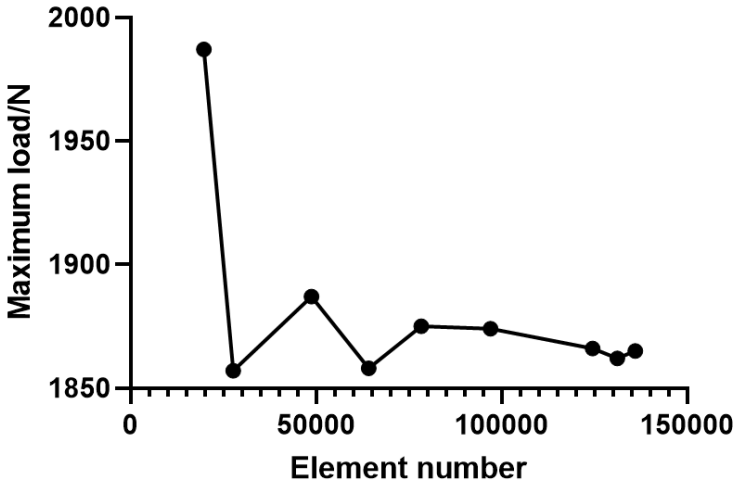

Figure 5.10. Mesh refinement based on the point highlighted in yellow circle in Figure 5.11.

A comparison has been made between displacement curves of FE model and experiment as shown in Figure 5.11. Rigid body motion of tensile machine has been removed through DIC technique for load-displacement curves of DPCP-H samples. An error analysis of maximum load before crack initiation and corresonding displacement between FE model and experiment has been carried out, highlighted in black and yellow circles in Figure 5.11, an average of load and displacement of tested samples was calculted, table 5.3. The errors of load of FE model is around 15.4% and the error of displacement is aournd 16.7%, which are acceptable, proving that the proposed approach is reasonable to characterise the local mechanical properties of different sections of a spot weld.

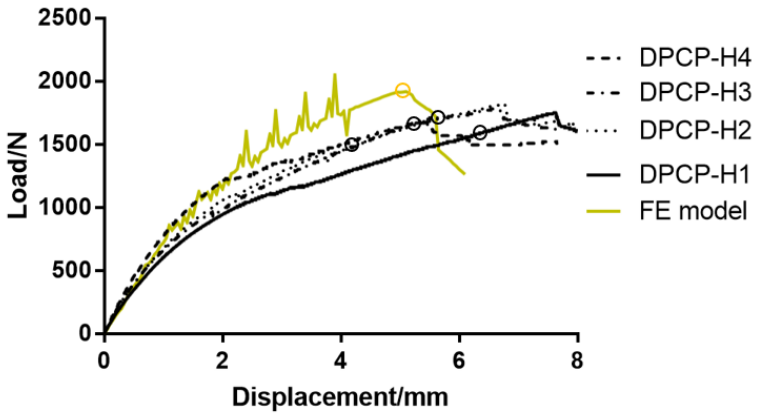

Figure 5.11. Comparison between displacement curves of FE model and experiment with respect to DPCP-H sample.

Table 5.3. Error analysis of load and displacement before crack initiation between FE model and experiment.

Load of FE model	1925	**Corresponding displacement of FE model**	5.59
Avg. load of test	1628	Avg. displacement of test	6.52
Error	15.4%	Error	16.8%

5.6 Summary

A validation was made with respect to the finite element modelling method using the experimental results. The errors of load and displacement before crack initiation are acceptable indicating the proposed mechanical property characterisation method is reasonable. However, challenges also exist, because of the difficulty of determining the damage constants of J-C material model as reported [236] for HAZ and nuggets of the welds, thus the flow stress obtained according to nanoindentation data was used for the determination. The constants regarding of strain rate and temperature were ignored in the J-C damage model used in the simulation. Other factors, including geometry difference between simulation and tested samples, errors of constitutive

relations of HAZ and nugget will also influence the results. These issues need to be resolved to optimise the current modelling method in the future work.

6 CONCLUSIONS AND CONTRIBUTION

6.1 Conclusions

Although full weld samples in DP1000 were not tested, the stress state analysis showed that the designed sample geometries could be acceptable to investigate the deformation evolution and effect of welding current on failure mechanism of spot weld in AHSS. Specifically, some conclusions can be obtained as follow:

1. Increasing welding current results in increase of weld size and softening of weld section in samples in DP1000 due to a higher applied thermal energy leading to longer cooling rate. However, it only increase the weld size and has rare effect on the hardness of the low carbon steel samples.

2. For welds under mixed tensile/shear loading, HAZ and nugget softening as well as larger nugget size is induced by higher welding current according to hardness analysis of welding section, it results in change of strain concentration from within the nugget to HAZ leading to necking in HAZ, and subsequently offloading of the nugget, thus leading to the transition of failure modes from IF mode to PF mode of DPTS samples. Shear stress within the nugget causes IF mode and stress along loading direction in HAZ and BM dominates PF mode. Only PF mode was observed in LCTS samples due to necking within HAZ. Moreover, DPTS samples with each welding current have higher energy absorption capacity.

3. Higher welding current results in HAZ and nugget softening in samples under mixed tensile/bending loading leading to larger compression normal to interface of nugget, larger plasticity in HAZ and nugget and larger bending in HAZ, causing transition from IF mode to PF mode. Strain normal to the interface of the nugget caused by stress along loading direction makes the greatest contribution to IF, resulting in mode I fracture in nugget. The failure mechanism of PF mode contains two parts, bending stress dominates the first part , leading to strain concentration at corona bond tip along the loading legs and subsequently mode I (opening) fracture in CGHAZ; shear stress and

bending stress dominates the second part leading to mode mode II (in-plane shear) fracture. Meanwhile, larger bending leads to larger compression within nugget retarding to crack initiation in nugget. LCCP samples all failed through PF mode caused by necking within HAZ due to bending and tensile stress. Larger bending could be induced within a more ductile HAZ when comparing samples in DP1000 and low carbon steels.

4. The U-shape samples are not proper to be used for investigation of tensile loading condition. The failure mechanisms are similar with CP samples. The unsymmetrical sample geometry results in unsymmetrical deformation and failure. The loading condition is similar to CP samples, and it is not valid to be used to investigate the failure of weld under pure tension loading.

5. The smaller martensitic laths within centre of the nugget might resist the crack from passing through the nugget in DPCP samples leading to crack path deflection.

6. The maximum principal strain around the corona bond tips at the critical point of crack initiation under each loading condition could be used as the threshold of failure. Since, the measured maximum principal strain is in-plane strain, the obtained failure strain could be used for helping develop 2D FE damage model.

6.2 Contributions to the knowledge

Based on the conventional testing methods and testing sample geometries for spot welds, this Ph.D. project proposed new sample geometries and testing methods to have a deeper investigation on failure mechanisms of spot weld under different loading conditions, and provided experimental data for further FE model development. The contribution of this research to the knowledge lies in：

- Developing new sample geometries, including CP, TS and U-shape samples with double half welds to make the deformation of weld section visible.
- Proposing new testing methods to comprehensively investigate the

failure mechanisms of spot weld under different loading conditions as well as the effects of welding current on failure mechanisms.

- Validating the experimental data and proposing an initial FE simulation method to predict the failure of spot weld.

Additionally, the proposed testing method and sample geometries could be applied in industries to investigate the failure and enhance the performance of spot weld. The experimental data could be used in the future FE model development.

7 FUTURE WORK

Some work is required to be done in the future.

- The geometries of U-shape sample will be optimised to make it proper for investigation of weld under tension loading.
- The FE damage model will be developed based on the data achieved in the project, and to determine the local plasticity and damage in the materials.
- As only microstructure of weld section and fracture surface were characterised using SEM. It is necessary to carry out a more comprehensive and in-depth analysis of microstructure and investigate the effect of stress state as well as microstructure on the fracture propagation in weld section in order to have some more understanding of the failure mechanisms.
- Since the time was limited, the designed geometries was validated only based on the stress state of designed half weld samples and conventional full weld samples. Therefore, comparison of failure mechanism between full weld samples and designed half weld samples will be carried out to have a better validation of the designed samples.

8 REFERENCE

[1] H. Ghadbeigi, C. Pinna, S. Celotto, and J. R. Yates, “Local plastic strain evolution in a high strength dual-phase steel,” *Mater. Sci. Eng. A*, vol. 527, no. 18–19, pp. 5026–5032, 2010, doi: 10.1016/j.msea.2010.04.052.

[2] M. K. Singh, “Application of Steel in Automotive Industry,” *Acta Mech. Slovaca*, vol. 6, no. 7, pp. 246–253, 2016, doi: 10.21496/ams.2017.001.

[3] S. Brauser, L. A. Pepke, G. Weber, and M. Rethmeier, “Deformation behaviour of spot-welded high strength steels for automotive applications,” *Mater. Sci. Eng. A*, vol. 527, no. 26, pp. 7099–7108, 2010, doi: 10.1016/j.msea.2010.07.091.

[4] M. Pouranvari, “Fracture toughness of martensitic stainless steel resistance spot welds,” *Mater. Sci. Eng. A*, vol. 680, no. August 2016, pp. 97–107, 2017, doi: 10.1016/j.msea.2016.10.088.

[5] M. I. Khan, M. L. Kuntz, E. Biro, and Y. Zhou, “Microstructure and Mechanical Properties of Resistance Spot Welded Advanced High Strength Steels,” *Mater. Trans.*, vol. 49, no. 7, pp. 1629–1637, 2008, doi: 10.2320/matertrans.MRA2008031.

[6] M. T. D.J.Radakovic, “An Evoluation of the Cross-Tension Test of Resistance Spot Welds in High-Strength Dual-Phase Steels,” *Weld. J.*, vol. 91, pp. 8–15, 2012.

[7] K. Kishore, P. Kumar, and G. Mukhopadhyay, “Resistance spot weldability of galvannealed and bare DP600 steel,” *J. Mater. Process. Technol.*, vol. 271, pp. 237–248, 2019, doi: 10.1016/j.jmatprotec.2019.04.005.

[8] S. Zuniga and S. Sheppard, “Resistance Spot Weld Failure Loads and Modes in Overload Conditions,” *Fatigue Fract. Mech. 27th Vol.*, vol. 27, pp. 469–489, 1997, doi: 10.1520/stp16249s.

[9] I. Hajiannia, R. Ashiri, M. R. Pakmanesh, M. Shamanian, and M. Atapour, “Evaluation of Performance of Resistance Spot Welded Joints with Different Parameters in Advanced High Strength TRIP Steel,” vol. 3, no. 1, pp. 9–16, 2019.

[10] T. Huin, S. Dancette, D. Fabrègue, and T. Dupuy, “Investigation of the failure of advanced high strength steels heterogeneous spot welds,” *Metals (Basel).*, vol. 6, no. 5, pp. 1–19, 2016, doi: 10.3390/met6050111.

[11] S. Dancette, V. Massardier, J. Merlin, D. Fabrègue, and T. Dupuy, “Investigations on the mechanical behavior of advanced high strength steels resistance spot welds in cross tension and tensile shear,” *Adv. Mater. Res.*, vol. 89–91, pp. 130–135, 2010, doi: 10.4028/www.scientific.net/AMR.89-91.130.

[12] N. Baluch, “Advanced High Strength Steel in Auto Industry : an Overview,” *Eng. Technol. Appl. Sci. Res.*, vol. 4, no. 4, pp. 686–689, 2014.

[13] A. Chabok, E. van der Aa, J. T. M. De Hosson, and Y. T. Pei, “Mechanical behavior and failure mechanism of resistance spot welded DP1000 dual phase steel,” *Mater. Des.*, vol. 124, pp. 171–182, 2017, doi: 10.1016/j.matdes.2017.03.070.

[14] A. Chabok, E. van der Aa, I. Basu, J. De Hosson, and Y. Pei, “Effect of pulse scheme on the microstructural evolution, residual stress state and mechanical performance of resistance spot welded DP1000-GI steel,” *Sci. Technol. Weld. Join.*, vol. 23, no. 8, pp. 649–658, 2018, doi: 10.1080/13621718.2018.1452875.

[15] Roland Berger, “Automotive metal components for car bodies and chassis,” *Glob. Mark. study*, no. February, p. 39, 2017.

[16] Z. Li, Q. Yu, X. Zhao, M. Yu, P. Shi, and C. Yan, “Crashworthiness and lightweight optimization to applied multiple materials and foam-filled front end structure of auto-body,” *Adv. Mech. Eng.*, vol. 9, no. 8, pp. 1–21, 2017, doi: 10.1177/1687814017702806.

[17] K. M. Keeler. S, *Advanced High Strength Steel Application Guidelines Version 5.0*. 2014.

[18] J. Zrník, I. Mamuzić, and S. V. Dobatkin, “Recent progress in high strength low carbon steels,” *Metalurgija*, vol. 45, no. 4, pp. 323–331, 2006.

[19] “Carbon Steel and Mild Steel: The Basics,” *Reliance Foundry*, 2017. [Online]. Available: https://www.reliance-foundry.com/blog/carbon-steel-mild-steel#gref.

[20] J. G. Speer and D. K. Matlock, “Recent Developments In Low-carbon sheet steels,” *JOM*, pp. 19–24, 2002.

[21] S. Hoile, “Processing and properties of mild interstitial free steels,” *Mater. Sci. Technol.*, vol. 16, no. 10, pp. 1079–1093, 2000, doi: 10.1179/026708300101506902.

[22] L. J. Baker, S. R. Daniel, and J. D. Parker, “Metallurgy and processing of ultralow carbon bake hardening steels,” *Mater. Sci. Technol.*, vol. 18, no. 4, pp. 355–368, 2002, doi: 10.1179/026708302225002452.

[23] H. Alloys, “Classification and Designation of Carbon and Low-Alloy Steels,” *Prop. Sel. Irons, Steels, High-Performance Alloy.*, vol. 1, pp. 140–194, 2018, doi: 10.31399/asm.hb.v01.a0001009.

[24] D. Gutiérrez, L. Pérez, A. Lara, D. Casellas, and J. M. Prado, “Toughness evaluation of high strength steels sheets by means of the essential work of fracture,” *19th Eur. Conf. Fract. Fract. Mech. Durability, Reliab. Safety, ECF 2012*, no. June 2017, 2012.

[25] C. E. . Rashid.M.S, “Relationship between microstructure and formability in two high-strength, low-alloy steels,” *ASTM Spec. Tech. Publ.*, vol. 64, pp. 174–190, 1978.

[26] U. Liedl, S. Traint, and E. A. Werner, “An unexpected feature of the stress-strain diagram of dual-phase steel,” *Comput. Mater. Sci.*, vol. 25, no. 1–2, pp. 122–128, 2002, doi: 10.1016/S0927-0256(02)00256-2.

[27] H. Liu *et al.*, “Challenges in hot-dip galvanizing of high strength dual phase steel: Surface selective oxidation and mechanical property degradation,” *Surf. Coatings Technol.*, vol. 206, no. 16, pp. 3428–3436, 2012, doi: 10.1016/j.surfcoat.2012.02.001.

[28] Y. Zhang, Y. Ma, Y. Kang, and H. Yu, “Mechanical properties and microstructure of TRIP steels produced using TSCR process,” *J. Univ. Sci. Technol. Beijing Miner. Metall. Mater. (Eng Ed)*, vol. 13, no. 5, pp. 416–419, 2006, doi: 10.1016/S1005-8850(06)60084-4.

[29] P. E. Geck, *Automotive Lightweighting Using Advanced High-Strength Steels*. 2014.

[30] B. C. De Cooman, Y. Estrin, and S. K. Kim, “Twinning-induced plasticity (TWIP) steels,” *Acta Mater.*, vol. 142, pp. 283–362, 2018, doi: 10.1016/j.actamat.2017.06.046.

[31] T. Taylor, G. Fourlaris, P. Evans, and G. Bright, “New generation ultrahigh strength boron steel for automotive hot stamping technologies,” *Mater. Sci. Technol. (United Kingdom)*, vol. 30, no. 7, pp. 818–826, 2014, doi: 10.1179/1743284713Y.0000000409.

[32] S. Igarashi, A. Bentur, and S. Mindess, “Microhardness testing of cementitious materials,” *Adv. Cem. Based Mater.*, vol. 4, no. 2, pp. 48–57, 1996, doi: 10.1016/S1065-7355(96)90051-6.

[33] E. Broitman, “Indentation Hardness Measurements at Macro-, Micro-, and Nanoscale: A Critical Overview,” *Tribol. Lett.*, vol. 65, no. 1, pp. 1–18, 2017, doi: 10.1007/s11249-016-0805-5.

[34] “ISO 14577: Metallic materials — Vickers hardness test — Part 1: Test method,” vol. 3, no. 1. 2002.

[35] J. Lopez, “Microhardness testing of plastics: Literature review,” *Polym. Test.*, vol. 12, no. 5, pp. 437–458, 1993, doi: 10.1016/0142-9418(93)90016-I.

[36] M. Grzybicki and J. Jakubowski, “Comparative tests of steel car body sheet welds made using CMT and MIG/MAG methods,” *Weld. Int.*, vol. 27, no. 8, pp. 610–615, 2013, doi: 10.1080/09507116.2011.606147.

[37] “ASTM92-17: Standard Test Methods for Vickers Hardness and Knoop Hardness of Metallic Materials,” pp. 1–27, 2017, doi: 10.1520/E0092-17.2.

[38] Y. W. Bao, W. Wang, and Y. C. Zhou, “Investigation of the relationship between elastic modulus and hardness based on depth-sensing indentation measurements,” *Acta Mater.*, vol. 52, no. 18, pp. 5397–5404, 2004, doi: 10.1016/j.actamat.2004.08.002.

[39] A. E. Giannakopoulos and S. Suresh, “Determination of Elastoplastic Properties By Instrumented Sharp Indentation,” vol. 40, no. 10, pp. 1191–1198, 1999.

[40] J. Dean, J. M. Wheeler, and T. W. Clyne, “Use of quasi-static nanoindentation data to obtain stress-strain characteristics for metallic materials,” *Acta Mater.*, vol. 58, no. 10, pp. 3613–3623, 2010, doi: 10.1016/j.actamat.2010.02.031.

[41] G. Kermouche, J. L. Loubet, and J. M. Bergheau, “Extraction of stress-strain curves of elastic-viscoplastic solids using conical/pyramidal indentation testing with application to polymers,” *Mech. Mater.*, vol. 40, no. 4–5, pp. 271–283, 2008, doi: 10.1016/j.mechmat.2007.08.003.

[42] M. Dao, N. Chollacoop, K. J. Van Vliet, T. A. Venkatesh, and S. Suresh, “Computational modeling of the forward and reverse problems in instrumented sharp indentation,” *Acta Mater.*, vol. 49, no. 19, pp. 3899–3918, 2001, doi: 10.1016/S1359-6454(01)00295-6.

[43] A. Chabok, E. Galinmoghaddam, J. T. M. De Hosson, and Y. T. Pei, “Micromechanical evaluation of DP1000-GI dual-phase high-strength steel resistance spot weld,” *J. Mater. Sci.*, vol. 54, no. 2, pp. 1703–1715, 2019, doi: 10.1007/s10853-018-2886-z.

[44] W. C. Oliver and G. M. Pharr, “An improved technique for determining hardness and elastic modulus using load and displacement sensing indentation experiments,” *J. Mater. Res.*, vol. 7, no. 6, pp. 1564–1583, 1992, doi: 10.1557/JMR.1992.1564.

[45] “ISO 6892-1 2019(en) Metallic materials-Tensile testing-Part 1 Method of test at room temperature.” .

[46] ASTM E8, “ASTM E8/E8M standard test methods for tension testing of metallic materials,” *Annu. B. ASTM Stand. 4*, no. C, pp. 1–27, 2010, doi: 10.1520/E0008.

[47] D. Yao, L. Cai, and C. Bao, “A new approach on necking constitutive relationships of ductile materials at elevated temperatures,” *Chinese J. Aeronaut.*, vol. 29, no. 6, pp. 1626–1634, 2016, doi: 10.1016/j.cja.2016.10.011.

[48] Y. Ling, “Uniaxial True Stress-Strain after Necking,” *AMP J. Technol.*, vol. 5, no. 1, pp. 37–48, 2004.

[49] K. Mori and Y. Abe, “A review on mechanical joining of aluminium and high strength steel sheets by plastic deformation,” *Int. J. Light. Mater. Manuf.*, vol. 1, no. 1, pp. 1–11, 2018, doi: 10.1016/j.ijlmm.2018.02.002.

[50] C. Yuce, F. Karpat, N. Yavuz, and O. Dogan, “a Review on Advanced Joining Techniques of Multi Material Part Manufacturing for Automotive Industry,” *Int. J. Mech. Prod. Eng.*, no. 3, p. 63, 2015.

[51] Y. Chastel and L. Passemard, “Joining technologies for future automobile multi-material modules,” *Procedia Eng.*, vol. 81, no. October, pp. 2104–2110, 2014, doi: 10.1016/j.proeng.2014.10.293.

[52] E. Spišák, “Alternative Joining Methods in Car Body Production,” *Int. J. Eng. Sci.*, vol. 5, no. 11, pp. 42–46, 2016, doi: 10.9790/1813-0511024246.

[53] R. Rzasinski and L. Kochanski, “Joining methods in car body construction,” *IOP Conf. Ser. Mater. Sci. Eng.*, vol. 400, no. 2, 2018, doi: 10.1088/1757-899X/400/2/022051.

[54] D. Li, A. Chrysanthou, I. Patel, and G. Williams, “Self-piercing riveting-a review,” *Int. J. Adv. Manuf. Technol.*, vol. 92, no. 5–8, pp. 1777–1824, 2017, doi: 10.1007/s00170-017-0156-x.

[55] T. Grimm, M. Jäckel, T. Falk, and W. G. Drossel, “Technologies for the mechanical joining of aluminum die castings,” *AIP Conf. Proc.*, vol. 2113, 2019, doi: 10.1063/1.5112572.

[56] C. Sarda, “Review: Self Piercing Riveting in Automotive Industry,” *Int. J. Res. Appl. Sci. Eng. Technol.*, vol. V, no. VIII, pp. 1749–1755, 2017, doi: 10.22214/ijraset.2017.8249.

[57] L. Kaščák, E. Spišák, and J. Majerníková, “Joining three car body steel sheets by clinching method,” *Open Eng.*, vol. 6, no. 1, pp. 566–573, 2016, doi: 10.1515/eng-2016-0081.

[58] X. He, “Clinching for sheet materials,” *Sci. Technol. Adv. Mater.*, vol. 18, no. 1, pp. 381–405, 2017, doi: 10.1080/14686996.2017.1320930.

[59] Y. Zhang, X. He, Y. Wang, Y. Lu, F. Gu, and A. Ball, “Study on failure mechanism of mechanical clinching in aluminium sheet materials,” *Int. J. Adv. Manuf. Technol.*, vol. 96, no. 9–12, pp. 3057–3068, 2018, doi: 10.1007/s00170-018-1734-2.

[60] S. Pang, W. Chen, and W. Wang, “A quantitative model of keyhole instability induced porosity in laser welding of titanium alloy,” *Metall. Mater. Trans. A Phys. Metall. Mater. Sci.*, vol. 45, no. 6, pp. 2808–2818, 2014, doi: 10.1007/s11661-014-2231-3.

[61] H. Zhao and T. DebRoy, “Macroporosity free aluminum alloy weldments through numerical simulation of keyhole mode laser welding,” *J. Appl. Phys.*, vol. 93, no. 12, pp. 10089–10096, 2003, doi: 10.1063/1.1573732.

[62] J. Stavridis, A. Papacharalampopoulos, and P. Stavropoulos, “Quality assessment in laser welding: a critical review,” *Int. J. Adv. Manuf. Technol.*, vol. 94, no. 5–8, pp. 1825–1847, 2018, doi: 10.1007/s00170-017-0461-4.

[63] L. Liu, *Welding and Joining of Magnesium Alloys*. 2010.

[64] J. Svenungsson, I. Choquet, and A. F. H. Kaplan, “Laser Welding Process - A Review of Keyhole Welding Modelling,” *Phys. Procedia*, vol. 78, no. August, pp. 182–191, 2015, doi: 10.1016/j.phpro.2015.11.042.

[65] “Advantage & disadvantage analysis of laser welding machine,” *HANZ LASER*. [Online]. Available: http://www.hanzlaser.com/service/laser-knowledge/311.htm.

[66] Y. Cho, S. J. Hu, and W. Li, “Resistance spot welding of aluminium and steel: A comparative experimental study,” *Proc. Inst. Mech. Eng. Part B J. Eng. Manuf.*, vol. 217, no. 10, pp. 1355–1363, 2003, doi: 10.1243/095440503322617126.

[67] M. Pouranvari, “Susceptibility to interfacial failure mode in similar and dissimilar resistance spot welds of DP600 dual phase steel and low carbon steel during cross-tension and tensile-shear loading conditions,” *Mater. Sci. Eng. A*, vol. 546, pp. 129–138, 2012, doi: 10.1016/j.msea.2012.03.040.

[68] B. Ma, C. Fan, D. Chen, H. Wang, and F. Zhou, “An investigation of the dynamic separation of spot welds under plane tensile pulses,” *J. Appl. Phys.*, vol. 116, no. 5, 2014, doi: 10.1063/1.4891639.

[69] L. Jeffus, *Welding Principles and Applications 7th edition*. 2012.

[70] H. Zhang and J. Senkara, *Resistance welding: Fundamentals and Applications*. CRC Press Taylor & Francis Group, 2006.

[71] F. Chen, S. Sun, Z. Ma, G. Q. Tong, and X. Huang, “Effect of weld nugget size on failure mode and mechanical properties of microscale resistance spot welds on Ti–1Al–1Mn ultrathin foils,” *Adv. Mech. Eng.*, vol. 10, no. 7, pp. 1–10, 2018, doi: 10.1177/1687814018785283.

[72] S. T. Wei, D. Lv, R. D. Liu, and L. Lin, “Similar and dissimilar resistance spot weldability of galvanised DP1000 and TWIP980 steels,” *Sci. Technol. Weld. Join.*, vol. 22, no. 4, pp. 278–286, 2017, doi: 10.1080/13621718.2016.1226569.

[73] N. Park, M. Park, J. Kwon, and H. Huh, “Material properties of the nugget zone in resistance spot-welded DP980 steel joint at various strain rates,” *Sci. Technol. Weld. Join.*, vol. 23, no. 1, pp. 7–12, 2018, doi: 10.1080/13621718.2017.1306015.

[74] S. S. Nayak, Y. Zhou, V. H. Baltazar Hernandez, and E. Biro, “Resistance spot welding of dual-phase steels: Heat affected zone softening and tensile properties,” *ASM Proc. Int. Conf. Trends Weld. Res.*, no. May 2014, pp. 641–649, 2013.

[75] V. H. Baltazar Hernandez, S. K. Panda, Y. Okita, and N. Y. Zhou, “A study on heat affected zone softening in resistance spot welded dual phase steel by nanoindentation,” *J. Mater. Sci.*, vol. 45, no. 6, pp. 1638–1647, 2010, doi: 10.1007/s10853-009-4141-0.

[76] K. Matsuda and S. Kodama, “Evaluation of corona bond strength of resistance spot welding,” *Sci. Technol. Weld. Join.*, vol. 25, no. 1, pp. 66–72, 2020, doi: 10.1080/13621718.2019.1613010.

[77] N. Bay, “Cold pressure welding—The mechanisms governing bonding,” *J. Manuf. Sci. Eng. Trans. ASME*, vol. 101, no. 2, pp. 121–127, 1979, doi: 10.1115/1.3439484.

[78] C. S. Obayi *et al.*, “Effect of grain sizes on mechanical properties and biodegradation behavior of pure iron for cardiovascular stent application,” *Biomatter*, vol. 6, no. 1, p. e959874, 2016, doi: 10.4161/21592527.2014.959874.

[79] X. Yuan, L. Chen, Y. Zhao, H. Di, and F. Zhu, “Dependence of grain size on mechanical properties and microstructures of high manganese austenitic steel,” *Procedia Eng.*, vol. 81, no. October, pp. 143–148, 2014, doi: 10.1016/j.proeng.2014.09.141.

[80] B. Białobrzeska, Ł. Konat, and R. Jasiński, “The influence of austenite grain size on the mechanical properties of low-alloy steel with boron,” *Metals (Basel).*, vol. 7, no. 1, pp. 1–20, 2017, doi: 10.3390/met7010026.

[81] X. Liu, F. Yuan, and Y. Wei, “Grain size effect on the hardness of nanocrystal measured by the nanosize indenter,” *Appl. Surf. Sci.*, vol. 279, pp. 159–166, 2013, doi: 10.1016/j.apsusc.2013.04.062.

[82] J.-C. Society, C. Depolymerization, L. View, and I. Z. Awan, “Recovery , Recrystallization , and Grain-Growth GENERAL AND,” *J.Chem.Soc.Pak*, vol. 41, no. 1, pp. 1–42, 2019.

[83] K. K. Alaneme and E. A. Okotete, “Recrystallization mechanisms and microstructure development in emerging metallic materials: A review,” *J. Sci. Adv. Mater. Devices*, vol. 4, no. 1, pp. 19–33, 2019, doi: 10.1016/j.jsamd.2018.12.007.

[84] J. Moravec, I. Novakova, J. Sobotka, and H. Neumann, “Determination of grain growth kinetics and assessment of welding effect on properties of s700mc steel in the HAZ of welded joints,” *Metals (Basel).*, vol. 9, no. 6, pp. 1–20, 2019, doi: 10.3390/met9060707.

[85] J. Knott, “Brittle fracture in structural steels: Perspectives at different size-scales,” *Philos. Trans. R. Soc. A Math. Phys. Eng. Sci.*, vol. 373, no. 2038, 2015, doi: 10.1098/rsta.2014.0126.

[86] P. Müllner, C. Solenthaler, P. J. Uggowitzer, and M. O. Speidel, “Brittle fracture in austenitic steel,” *Acta Metall. Mater.*, vol. 42, no. 7, pp. 2211–2217, 1994, doi: 10.1016/0956-7151(94)90300-X.

[87] G. Z. Wang, J. H. Chen, and Z. H. Li, “Further Study on the Mechanism of the Ductile-to-Brittle Fracture Transition in C-Mn Base and Weld Steel,” vol. 28, no. August, 1997.

[88] G. Gruben, D. Morin, M. Langseth, and O. S. Hopperstad, “Ductile Fracture of Steel Sheets under Dynamic Membrane Loading,” *Procedia Eng.*, vol. 197, pp. 185–195, 2017, doi: 10.1016/j.proeng.2017.08.095.

[89] C. Li, E. Daxin, and N. Yi, “Analysis on fracture initiation and fracture angle in ductile sheet metal under uniaxial tension by experiments and finite element simulations,” *J. Mater. Res.*, vol. 31, no. 24, pp. 3991–3999, 2016, doi: 10.1557/jmr.2016.412.

[90] V. N. Van Do, “The behavior of ductile damage model on steel structure failure,” *Procedia Eng.*, vol. 142, pp. 26–33, 2016, doi: 10.1016/j.proeng.2016.02.009.

[91] T. L. Anderson, *Fracture mechanics: fundermentals and applications*. Taylor & Francis, 2005.

[92] J.H. Chen and R. Cao, *Micromechanism of Cleavage Fracture of Metals*. 2015.

[93] C. Briant, C. B. Intergranular, F. In, M. Journal, and D. P. Colloques, “INTERGRANULAR FRACTURE IN METALS To cite this version :,” vol. 49, 1988.

[94] S. K. Bhambri, “Intergranular fracture in 13 wt% chromium martensitic stainless steel,” *J. Mater. Sci.*, vol. 21, no. 5, pp. 1741–1746, 1986, doi: 10.1007/BF01114734.

[95] C. Li and Z. Guangying, “Intergranular Fracture of Low-Alloy Cast Steel,” vol. 5803, no. 95.

[96] F. A. McClintock, “A criterion for ductile fracture by the growth of holes,” *J. Appl. Mech. Trans. ASME*, vol. 35, no. 2, pp. 363–371, 1964, doi: 10.1115/1.3601204.

[97] J. R. Rice and D. M. Tracey, “On the ductile enlargement of voids in triaxial stress fields*,” *J. Mech. Phys. Solids*, vol. 17, no. 3, pp. 201–217, 1969, doi: 10.1016/0022-5096(69)90033-7.

[98] R. Jamaati, M. R. Toroghinejad, H. Edris, and M. R. Salmani, “Fracture of steel nanocomposite made using accumulative roll bonding,” *Mater. Sci. Technol. (United Kingdom)*, vol. 30, no. 15, pp. 1973–1982, 2014, doi: 10.1179/1743284714Y.0000000634.

[99] O. Wall and A. Bergmark, “Ductile to brittle transition fracture behaviour of ductile steel at high strain rates,” *J. Phys. IV JP*, vol. 7, no. 3, pp. 1051–1056, 1997, doi: 10.1051/jp4:19973177.

[100] D.-Y. Kong and B. Yang, “Enhanced Voids Growth Model for Ductile Fracture Prediction of High-Strength Steel Q690D under Monotonic Tension: Experiments and Numerical Simulation,” *J. Struct. Eng.*, vol. 146, no. 6, p. 04020107, 2020, doi: 10.1061/(asce)st.1943-541x.0002658.

[101] S. Dancette, D. Fabrègue, V. Massardier, J. Merlin, T. Dupuy, and M. Bouzekri, “Experimental and modeling investigation of the failure resistance of Advanced High Strength Steels spot welds,” *Eng. Fract. Mech.*, vol. 78, no. 10, pp. 2259–2272, 2011, doi: 10.1016/j.engfracmech.2011.04.013.

[102] M. Pouranvari and S. P. H. Marashi, “Failure mode transition in AHSS resistance spot welds. Part I. Controlling factors,” *Mater. Sci. Eng. A*, vol. 528, no. 29–30, pp. 8337–8343, 2011, doi: 10.1016/j.msea.2011.08.017.

[103] M. Pouranvari and S. P. H. Marashi, “Critical review of automotive steels spot welding: Process, structure and properties,” *Sci. Technol. Weld. Join.*, vol. 18, no. 5, pp. 361–403, 2013, doi: 10.1179/1362171813Y.0000000120.

[104] M. Pouranvari and S. P. H. Marashi, “Failure of resistance spot welds: Tensile shear versus coach peel loading conditions,” *Ironmak. Steelmak.*, vol. 39, no. 2, pp. 104–111, 2012, doi: 10.1179/1743281211Y.0000000066.

[105] “BS EN ISO 14272: Specimen dimensions and procedure for cross tension testing resistance spot and embossed projection welds,” 2001.

[106] N. Chen, H. P. Wang, B. E. Carlson, D. R. Sigler, and M. Wang, “Fracture mechanisms of Al/steel resistance spot welds in coach peel and cross tension testing,” *J. Mater. Process. Technol.*, vol. 252, no. September 2017, pp. 348–361, 2018, doi: 10.1016/j.jmatprotec.2017.09.035.

[107] “BS EN ISO 14273: Specimen dimensions and procedure for shear testing resistance spot, seam and embossed projection welds,” 2001.

[108] S. Dancette, D. Fabrègue, V. Massardier, J. Merlin, T. Dupuy, and M. Bouzekri, “Investigation of the Tensile Shear fracture of Advanced High Strength Steel spot welds,” *Eng. Fail. Anal.*, vol. 25, pp. 112–122, 2012, doi: 10.1016/j.engfailanal.2012.04.009.

[109] Y. Zhao, Y. Zhang, and X. Lai, “Analysis of fracture modes of resistance spot welded hot-stamped boron steel,” *Metals (Basel).*, vol. 8, no. 10, pp. 1–15, 2018, doi: 10.3390/met8100764.

[110] K. Paveebunvipak and V. Uthaisangsuk, “Characterization of Static Performance and Failure of Resistance Spot Welds of High-Strength and Press-Hardened Steels,” *J. Mater. Eng. Perform.*, vol. 28, no. 4, pp. 2017–2028, 2019, doi: 10.1007/s11665-019-03988-2.

[111] C. Liu, X. Zheng, H. He, W. Wang, and X. Wei, “Effect of work hardening on mechanical behavior of resistance spot welding joint during tension shear test,” *Mater. Des.*, vol. 100, pp. 188–197, 2016, doi: 10.1016/j.matdes.2016.03.120.

[112] M. Pouranvari, A. Abedi, P. Marashi, and M. Goodarzi, “Effect of expulsion on peak load and energy absorption of low carbon steel resistance spot welds,” *Sci. Technol. Weld. Join.*, vol. 13, no. 1, pp. 39–43, 2008, doi: 10.1179/174329307X249342.

[113] H. L. Jaber, M. Pouranvari, R. K. Salim, F. A. Hashim, and S. P. H. Marashi, “Peak load and energy absorption of DP600 advanced steel resistance spot welds,” *Ironmak. Steelmak.*, vol. 44, no. 9, pp. 699–706, 2017, doi: 10.1080/03019233.2016.1229880.

[114] “BS EN ISO 10447: Resistance welding — Peel and chisel testing of resistance spot and projection welds,” *Management*, vol. 3, 2007.

[115] S. Burget and S. Sommer, “Modeling of deformation and failure behavior of dissimilar resistance spot welded joints under shear, axial and combined loading conditions,” *Icf13*, pp. 1–12, 2013.

[116] C. Sawanishi *et al.*, “Mechanical properties and microstructures of resistance spot welded DP980 steel joints using pulsed current pattern,” *Sci. Technol. Weld. Join.*, vol. 19, no. 1, pp. 52–59, 2014, doi: 10.1179/1362171813Y.0000000165.

[117] H. Li, M. W. Fu, J. Lu, and H. Yang, “Ductile fracture: Experiments and computations,” *Int. J. Plast.*, vol. 27, no. 2, pp. 147–180, 2011, doi: 10.1016/j.ijplas.2010.04.001.

[118] R. Kiran and K. Khandelwal, “Fast-to-compute weakly coupled ductile fracture model for structural steels,” *J. Struct. Eng. (United States)*, vol. 140, no. 6, pp. 1–11, 2014, doi: 10.1061/(ASCE)ST.1943-541X.0001025.

[119] A. L. Gurson, “Continuum Theory of Ductile Rupture By Void Nucleation and Growth - 1. Yield Criteria and Flow Rules for Porous Ductile Media.,” *Am. Soc. Mech. Eng.*, no. 76-Mat-CC, 1976.

[120] V. Tvergaard, “On localization in ductile materials containing spherical voids,” *Int. J. Fract.*, vol. 18, no. 4, pp. 237–252, 1982, doi: 10.1007/BF00015686.

[121] “Abaqus 6.14 / Analysis User’s Guide,” p. 862, 2014, doi: 10.1017/CBO9781107415324.004.

[122] P. Haušild, I. Nedbal, C. Berdin, and C. Prioul, “The influence of ductile tearing on fracture energy in the ductile-to-brittle transition temperature range,” *Mater. Sci. Eng. A*, vol. 335, no. 1–2, pp. 164–174, 2002, doi: 10.1016/S0921-5093(01)01913-X.

[123] E. H. J. Lamouroux, D. Coutellier, N. Doelle, and P. Kuemmerlen, “Detailed model of spot-welded joints to simulate the failure of car assemblies,” *Int. J. Interact. Des. Manuf.*, vol. 1, no. 1, pp. 33–40, 2007, doi: 10.1007/s12008-007-0006-4.

[124] Y. R. Oh, J. S. Kim, and Y. J. Kim, “Determination of GTN Damage Parameters for Application to Pipe Ductile Fracture Simulation,” *Procedia Eng.*, vol. 130, pp. 845–852, 2015, doi: 10.1016/j.proeng.2015.12.208.

[125] W. Dang, “Finite element modelling of hybrid (spot welded / bonded) joints under service conditions To cite this version : HAL Id : tel-01296998 Thèse présentée pour l ’ obtention du grade de Docteur de l ’ UTC,” *Univ. Technol. Compiègne*, 2015.

[126] L. Schwer, “Optional Strain-Rate Forms for the Johnson Cook Constitutive Model and the Role of the Parameter Epsilon _ 0 AUTHOR Len Schwer Keywords parameter ε,” *6th Eur. LS-DYNA Users’ Conf.*, 2007.

[127] A. M. Rajendran and D. J. Grove, “A Dynamic Failure Model for Ductile Materials,” *AIR FORCE ARMAMENT Lab.*, no. February 1991, 1991.

[128] F. R. Dehgolan, M. Behzadi, and J. F. Sola, “Obtaining Constants of Johnson-Cook Material Model Using a Combined Experimental, Numerical Simulation and Optimization Method,” *Int. J. Mech. Mechatronics Eng.*, vol. 33, no. 39, pp. 1615–1622, 2016.

[129] G. R. Johnson and W. H. Cook, “Fracture characteristics of three metals subjected to various strains, strain rates, temperatures and pressures,” *Eng. Fract. Mech.*, vol. 21, no. 1, pp. 31–48, 1985, doi: 10.1016/0013-7944(85)90052-9.

[130] A. Banerjee, S. Dhar, S. Acharyya, D. Datta, and N. Nayak, “Determination of Johnson cook material and failure model constants and numerical modelling of Charpy impact test of armour steel,” *Mater. Sci. Eng. A*, vol. 640, pp. 200–209, 2015, doi: 10.1016/j.msea.2015.05.073.

[131] G. H. Majzoobi and F. Rahimi Dehgolan, “Determination of the constants of damage models,” *Procedia Eng.*, vol. 10, pp. 764–773, 2011, doi: 10.1016/j.proeng.2011.04.127.

[132] M. Sadhinoch, E. H. Atzema, E. S. Perdahcioglu, and A. H. Van Den Boogaard, “Numerical and Experimental Validation of a New Damage Initiation Criterion,” *J. Phys. Conf. Ser.*, vol. 896, no. 1, 2017, doi: 10.1088/1742-6596/896/1/012080.

[133] M. Grédiac, “The use of full-field measurement methods in composite material characterization: Interest and limitations,” in *Composites Part A: Applied Science and Manufacturing*, 2004, vol. 35, no. 7–8, pp. 751–761, doi: 10.1016/j.compositesa.2004.01.019.

[134] A. Vautrin, J. R. Lee, J. Molimard, and Y. Surrel, “Full-field optical techniques : Applications to strain measurement and mechanical identification,” *10Th Eur. Conf. Compos. Mater.*, no. 388, pp. 1–10, 2002.

[135] M. Grédiac, F. Hild, and A. Pineau, *Full-Field Measurements and Identification in Solid Mechanics*, vol. 2. 2012.

[136] M. Grédiac, F. Sur, and B. Blaysat, “The Grid Method for In-plane Displacement and Strain Measurement: A Review and Analysis,” *Strain*, vol. 52, no. 3, pp. 205–243, 2016, doi: 10.1111/str.12182.

[137] H. T. Goldrein, S. J. P. Palmer, and J. M. Huntley, “Automated fine grid technique for measurement of large-strain deformation maps,” *Opt. Lasers Eng.*, vol. 23, no. 5, pp. 305–318, 1995, doi: 10.1016/0143-8166(95)00036-N.

[138] H. Ghadbeigi, C. Pinna, and S. Celotto, “Quantitative Strain Analysis of the Large Deformation at the Scale of Microstructure: Comparison between Digital Image Correlation and Microgrid Techniques,” *Exp. Mech.*, vol. 52, no. 9, pp. 1483–1492, 2012, doi: 10.1007/s11340-012-9612-6.

[139] M. Obata, H. Shimada, and A. Kawasaki, “Fine-grid method for large-strain analysis near a notch Tip,” *Exp. Mech.*, vol. 23, no. 2, pp. 146–151, 1983, doi: 10.1007/bf02320402.

[140] A. Karimi, “Plastic flow study using the microgrid technique,” *Mater. Sci. Eng.*, vol. 63, no. 2, pp. 267–276, 1984, doi: 10.1016/0025-5416(84)90128-9.

[141] P. F. Koshelev, V. L. Sanderov, V. N. Tsarev, and V. V Grot, “Investigation of Deformations by a Grid Method,” *Ind. Lab.*, vol. 42, no. 6, pp. 963–965, 1976.

[142] F. Delaire, J. L. Raphanel, and C. Rey, “Plastic heterogeneities of a copper multicrystal deformed in uniaxial tension: Experimental study and finite element simulations,” *Acta Mater.*, vol. 48, no. 5, pp. 1075–1087, 2000, doi: 10.1016/S1359-6454(99)00408-5.

[143] S. Sun, M. Grédiac, E. Toussaint, J. D. Mathias, and N. Mati-Baouche, “Applying a Full-Field Measurement Technique to Characterize the Mechanical Response of a Sunflower-Based Biocomposite,” *Exp. Mech.*, vol. 55, no. 5, pp. 917–934, 2015, doi: 10.1007/s11340-015-9988-1.

[144] J. McKelvie, “Moire strain analysis: an introduction, review and critique, including related techniques and future potential,” *J. Strain Anal. Eng. Des.*, vol. 33, no. 2, pp. 137–151, 1998, doi: 10.1243/0309324981512878.

[145] C. A. Walker, “A historical review of moiré interferometry,” *Exp. Mech.*, vol. 34, no. 4, pp. 281–299, 1994, doi: 10.1007/BF02325143.

[146] B. Han, D. Post, and P. Ifju, “Moire interferometry for engineering mechanics: current practices and future developments,” *J. Strain Anal. Eng. Des.*, vol. 36, no. 1, pp. 101–117, 2001, doi: 10.1243/0309324011512568.

[147] C. A. Walker, “Moir Interferometry for Strain Analysis,” *Opt. Lasers Eng.*, vol. 8, pp. 213–262, 1988.

[148] B. Pan, H. Xie, Z. Wang, K. Qian, and Z. Wang, “Study on subset size selection in digital image correlation for speckle patterns,” *Opt. Express*, vol. 16, no. 10, pp. 7037–7048, 2008, doi: 10.1364/oe.16.007037.

[149] W. H. Peters and W. F. Ranson, “Digital Imaging Techniques In Experimental Stress Analysis,” *Opt. Eng.*, vol. 21, no. 3, pp. 427–431, 1982, doi: 10.1117/12.7972925.

[150] T. C. Chu, W. F. Ranson, and M. A. Sutton, “Applications of digital-image-correlation techniques to experimental mechanics,” *Exp. Mech.*, vol. 25, no. 3, pp. 232–244, 1985, doi: 10.1007/BF02325092.

[151] M. Sutton, C. Mingqi, W. Peters, Y. Chao, and S. McNeill, “Application of an optimized digital correlation method to planar deformation analysis,” *Image Vis. Comput.*, vol. 4, no. 3, pp. 143–150, 1986, doi: 10.1016/0262-8856(86)90057-0.

[152] T. Chu, W. H. Peters, W. F. Ranson, and M. A. Sutton, “Application of Digital Correlation Methods To Rigid Body Mechanics.,” *Proceedings of the Society for Experimental Stress Analysis*. pp. 73–76, 1982, doi: 10.1117/12.7973231.

[153] B. Pan, K. Qian, H. Xie, and A. Asundi, “Two-dimensional digital image correlation for in-plane displacement and strain measurement: A review,” *Meas. Sci. Technol.*, vol. 20, no. 6, 2009, doi: 10.1088/0957-0233/20/6/062001.

[154] B. Pan, “Recent Progress in Digital Image Correlation,” *Experimental Mechanics*, vol. 51, no. 7. pp. 1223–1235, 2011, doi: 10.1007/s11340-010-9418-3.

[155] F. Chen, X. Chen, X. Xie, X. Feng, and L. Yang, “Full-field 3D measurement using multi-camera digital image correlation system,” *Opt. Lasers Eng.*, vol. 51, no. 9, pp. 1044–1052, 2013, doi: 10.1016/j.optlaseng.2013.03.001.

[156] Y. L. Dong and B. Pan, “A Review of Speckle Pattern Fabrication and Assessment for Digital Image Correlation,” *Exp. Mech.*, pp. 1161–1181, 2017, doi: 10.1007/s11340-017-0283-1.

[157] B. Pan and K. Li, “A fast digital image correlation method for deformation measurement,” *Opt. Lasers Eng.*, vol. 49, no. 7, pp. 841–847, 2011, doi: 10.1016/j.optlaseng.2011.02.023.

[158] M. Bornert *et al.*, “Assessment of digital image correlation measurement errors: Methodology and results,” *Exp. Mech.*, vol. 49, no. 3, pp. 353–370, 2009, doi: 10.1007/s11340-008-9204-7.

[159] H. A. Bruck, S. R. McNeill, M. A. Sutton, and W. H. Peters, “Digital image correlation using Newton-Raphson method of partial differential correction,” *Exp. Mech.*, vol. 29, no. 3, pp. 261–267, 1989, doi: 10.1007/BF02321405.

[160] P. Reu, “Stereo-rig Design : Stereo-Angle Selection — Part 4,” vol. 37, pp. 1–2, 2013.

[161] R. Huňady, M. Hagara, and F. Trebuňa, “The Measurement of Standing Wave Patterns by using High-speed Digital Image Correlation,” *Am. J. Mech. Eng.*, vol. 2, no. 7, pp. 247–251, 2014, doi: 10.12691/ajme-2-7-15.

[162] X. Xu, Y. Su, Y. Cai, T. Cheng, and Q. Zhang, “Effects of Various Shape Functions and Subset Size in Local Deformation Measurements Using DIC,” *Exp. Mech.*, vol. 55, no. 8, pp. 1575–1590, 2015, doi: 10.1007/s11340-015-0054-9.

[163] H. W. Schreier and M. A. Sutton, “Systematic errors in digital image correlation due to undermatched subset shape functions,” *Exp. Mech.*, vol. 42, no. 3, pp. 303–310, 2002, doi: 10.1177/001448502321548391.

[164] M. Guizar-Sicairos, S. T. Thurman, and J. R. Fienup, “Efficient subpixel image registration algorithms,” *Opt. Lett.*, vol. 33, no. 2, p. 156, 2008, doi: 10.1364/ol.33.000156.

[165] K. C. Mertens, B. de Baets, L. P. C. Verbeke, and R. R. de Wulf, “A sub-pixel mapping algorithm based on sub-pixel/pixel spatial attraction models,” *Int. J. Remote Sens.*, vol. 27, no. 15, pp. 3293–3310, 2006, doi: 10.1080/01431160500497127.

[166] D. Zhang and M. Luo, “Displacement/strain measurements using an optical microscope and digital image correlation,” *Opt. Eng.*, vol. 45, no. 3, p. 033605, 2006, doi: 10.1117/1.2182108.

[167] S. Yoneyama, “Lens distortion correction for digital image correlation by measuring rigid body displacement,” *Opt. Eng.*, vol. 45, no. 2, p. 023602, 2006, doi: 10.1117/1.2168411.

[168] P. Reu, “All about speckles: Aliasing,” *Exp. Tech.*, vol. 38, no. 5, pp. 1–3, 2014, doi: 10.1111/ext.12111.

[169] P. Reu, “All about speckles: contrast,” *Exp. Tech.*, vol. 39, no. 3, pp. 1–2, 2015, doi: 10.1111/ext.12161.

[170] P. Reu, “All about speckles: Edge sharpness,” *Exp. Tech.*, vol. 39, no. 2, pp. 1–2, 2015, doi: 10.1111/ext.12139.

[171] P. Reu, “All about speckles: Speckle density,” *Exp. Tech.*, vol. 39, no. 3, pp. 1–2, 2015, doi: 10.1111/ext.12161.

[172] P. Reu, “All about speckles: Speckle size measurement,” *Exp. Tech.*, vol. 39, no. 3, pp. 1–2, 2015, doi: 10.1111/ext.12161.

[173] B. Pan, H. Xie, and Z. Wang, “Equivalence of digital image correlation criteria for pattern matching,” *Appl. Opt.*, vol. 49, no. 28, pp. 5501–5509, 2010, doi: 10.1364/AO.49.005501.

[174] R. Roncella, E. Romeo, L. Barazzetti, M. Gianinetto, and M. Scaioni, “Comparative analysis of digital image correlation techniques for in-plane displacement measurements,” *2012 5th Int. Congr. Image Signal Process. CISP 2012*, no. Cisp, pp. 721–726, 2012, doi: 10.1109/CISP.2012.6469731.

[175] A. Giachetti, “Matching techniques to compute image motion,” *Image Vis. Comput.*, vol. 18, no. 3, pp. 247–260, 2000, doi: 10.1016/S0262-8856(99)00018-9.

[176] B. Pan, “Full-field strain measurement using a two-dimensional Savitzky-Golay digital differentiator in digital image correlation,” *Opt. Eng.*, vol. 46, no. 3, p. 033601, 2007, doi: 10.1117/1.2714926.

[177] W. Tong, “An evaluation of digital image correlation criteria for strain mapping applications,” *Strain*, vol. 41, no. 4, pp. 167–175, 2005, doi: 10.1111/j.1475-1305.2005.00227.x.

[178] M. A. Jinyuan Liu, P.E., M.ASCE, and Magued Iskander, P.E. and Abstract:, “Adaptive Cross Correlation for Imaging Displacements in Soils,” *J. Comput. Civ. Eng*, vol. 18, no. 1, pp. 46–57, 2004, doi: 10.1061/(ASCE)0887-3801(2004)18.

[179] J. C. Yoo and T. H. Han, “Fast normalized cross-correlation,” *Circuits, Syst. Signal Process.*, vol. 28, no. 6, pp. 819–843, 2009, doi: 10.1007/s00034-009-9130-7.

[180] W. Förstner, “On the geometric precision of digital correlation,” *Int. Arch. Photogramm. Proc. ISPRS Symp. ISPRS Comm. III*, pp. 176–189, 1982.

[181] F. Ackermann, “Digital Image Correlation: Performance and Potential Application in Photogrammetry,” *Photogramm. Rec.*, vol. 11, no. 64, pp. 429–439, 1984, doi: 10.1111/j.1477-9730.1984.tb00505.x.

[182] A. Grün, “Adaptive Least-Squares Correlation: A Powerful Image Matching Technique,” *South African J. Photogramm. Remote Sens. Cartogr.*, vol. 14, no. 3, pp. 175–187, 1985.

[183] B. Birgisson, A. Montepara, E. Romeo, R. Roncella, R. Roque, and G. Tebaldi, “An optical strain measurement system for asphalt mixtures,” *Mater. Struct. Constr.*, vol. 42, no. 4, pp. 427–441, 2009, doi: 10.1617/s11527-008-9392-8.

[184] S. Yaofeng and J. H. L. Pang, “Study of optimal subset size in digital image correlation of speckle pattern images,” *Opt. Lasers Eng.*, vol. 45, no. 9, pp. 967–974, 2007, doi: 10.1016/j.optlaseng.2007.01.012.

[185] R. Bigger *et al.*, “A Good Practices Guide for Digital Image Correlation,” *Int. Digit. Image Correl. Soc.*, p. 94, 2018, doi: 10.32720/idics/gpg.ed1.

[186] B. Pan, H. M. Xie, B. Q. Xu, and F. L. Dai, “Performance of sub-pixel registration algorithms in digital image correlation,” *Meas. Sci. Technol.*, vol. 17, no. 6, pp. 1615–1621, 2006, doi: 10.1088/0957-0233/17/6/045.

[187] B. Pan, B. Q. Xu, D. Chen, and J. Feng, “Sub-pixel registration using quadratic surface fitting in digital image correlation,” *Jiliang Xuebao/Acta Metrol. Sin.*, vol. 26, no. 2, pp. 128–134, 2005.

[188] B. Wattrisse, A. Chrysochoos, J. M. Muracciole, and M. Némoz-Gaillard, “Analysis of strain localization during tensile tests by digital image correlation,” *Exp. Mech.*, vol. 41, no. 1, pp. 29–39, 2001, doi: 10.1007/BF02323101.

[189] J. Zhang, G. Jin, S. Ma, and L. Meng, “Application of an improved subpixel registration algorithm on digital speckle correlation measurement,” *Opt. Laser Technol.*, vol. 35, no. 7, pp. 533–542, 2003, doi: 10.1016/S0030-3992(03)00069-0.

[190] J. Zhang, G. C. Jin, L. B. Meng, L. H. Jian, A. Y. Wang, and S. B. Lu, “Strain and mechanical behavior measurements of soft tissues with digital speckle method,” *Proc. SPIE*, vol. 10, no. 3, 2003, doi: 10.1117/12.477908.

[191] L. Oriat and E. Lantz, “Subpixel detection of the center of an object using a spectral phase algorithm on the image,” *Pattern Recognit.*, vol. 31, no. 6, pp. 761–771, 1998, doi: 10.1016/S0031-3203(97)00087-3.

[192] H. Jin and H. A. Bruck, “Pointwise digital image correlation using genetic algorithms,” *Exp. Tech.*, vol. 29, no. 1, pp. 36–39, 2005, doi: 10.1111/j.1747-1567.2005.tb00202.x.

[193] H. Jin, “Theoretical development for pointwise digital image correlation,” *Opt. Eng.*, vol. 44, no. 6, p. 067003, 2005, doi: 10.1117/1.1928908.

[194] M. Pitter, C. W. See, and M. Somekh, “Subpixel microscopic deformation analysis using correlation and artificial neural networks,” *Opt. Express*, vol. 8, no. 6, pp. 322–327, 2001, doi: 10.1364/oe.8.000322.

[195] Y. H. Wang *et al.*, “Whole field sheet-metal tensile test using digital image correlation,” *Exp. Tech.*, vol. 34, no. 2, pp. 54–59, 2010, doi: 10.1111/j.1747-1567.2009.00483.x.

[196] X.-D. K. & H. W. S. & M. A. S. & Y. Q. Wang, “Error Assessment in Stereo-based Deformation Measurements,” *Exp. Mech.*, vol. 51, pp. 423–441, 2011, doi: 10.1007/s11340-010-9449-9.

[197] H. Wang, H. Xie, Y. Ju, and Q. Duan, “Error analysis of digital speckle correlation method under scanning electron microscope,” *Exp. Tech.*, vol. 30, no. 2, pp. 42–45, 2006, doi: 10.1111/j.1747-1567.2006.00021.x.

[198] A. F. Bower, *Applied mechanics of solids*. 2009.

[199] J. Lubliner, *PLASTICITY THEORY*. 2006.

[200] V. P. Nguyen, *Finite elements for large deformation solid mechanics problems*. 2016.

[201] K. Alharbi *et al.*, “Damage in dual phase steel DP1000 investigated using digital image correlation and microstructure simulation,” *Model. Simul. Mater. Sci. Eng.*, vol. 23, no. 8, 2015, doi: 10.1088/0965-0393/23/8/085005.

[202] S. Daneshpour, A. H. Kokabi, A. A. Ekrami, and A. K. Motarjemi, “Crack initiation and kinking behaviours of spot welded coach peel specimens under cyclic loading,” *Sci. Technol. Weld. Join.*, vol. 12, no. 8, pp. 696–702, 2007, doi: 10.1179/174329307X238416.

[203] Q. Yin, C. Soyarslan, K. Isik, and A. E. Tekkaya, “A grooved in-plane torsion test for the investigation of shear fracture in sheet materials,” *Int. J. Solids Struct.*, vol. 66, no. November 2013, pp. 121–132, 2015, doi: 10.1016/j.ijsolstr.2015.03.032.

[204] C. Soyarslan, M. Malekipour Gharbi, and A. E. Tekkaya, “A combined experimental-numerical investigation of ductile fracture in bending of a class of ferritic-martensitic steel,” *Int. J. Solids Struct.*, vol. 49, no. 13, pp. 1608–1626, 2012, doi: 10.1016/j.ijsolstr.2012.03.009.

[205] S. Dancette, V. Massardier, D. Fabr[illegible]ue, J. Merlin, T. Dupuy, and M. Bouzerki, “HAZ Microstructures and Local Mechanical Properties of High Strength Steels Resistance Spot Welds,” *ISIJ Int.*, vol. 51, no. 1, pp. 99–107, 2011, doi: 10.2355/isijinternational.51.99.

[206] E. H. J. Lamouroux, D. Coutellier, and F. Seeger, “Detailed model of spot-welded joints to simulate the dynamical failure of car assemblies,” *5th Int. Ind. Simul. Conf. 2007, ISC 2007*, no. January 2007, pp. 119–128, 2007.

[207] K. L. Nielsen and V. Tvergaard, “Ductile shear failure or plug failure of spot welds modelled by modified Gurson model,” *Eng. Fract. Mech.*, vol. 77, no. 7, pp. 1031–1047, 2010, doi: 10.1016/j.engfracmech.2010.02.031.

[208] B. S. E. N. Iso, “BS EN ISO 18278-2： Resistance welding — Weldability —Alternative procedures for the assessment of sheet steels for spot welding,” vol. 3, 2004.

[209] “American National Standard, 1997.Weld button criteria, recommended practices for test methods for evaluating the resistance spot welding behavior of automotive sheet steel materials. ANSIAWSSAED8.9-97, Section 5.7,” *SMPTE Journal*, vol. 102, no. 4. doi: 10.5594/j03806.

[210] R. Choudhary, H. Kumar, and R. K. Garg, “Analysis and evaluation of heat affected zones in electric discharge machining of EN-31 die steel,” *Indian J. Eng. Mater. Sci.*, vol. 17, no. 2, pp. 91–98, 2010.

[211] C. Stjsao, “Analysis of Heat-Affected Zone Depth of Sample Surface at Electrical Discharge Machining with Brass Wire Electrode,” vol. 51, no. 6, pp. 633–640, 2009.

[212] *Vic-3 v7 Testing Guid*. .

[213] A. Acciaioli, G. Lionello, and M. Baleani, “Experimentally achievable accuracy using a digital image correlation technique in measuring small-magnitude (< 0.1%) homogeneous strain fields,” *Materials (Basel).*, vol. 11, no. 5, pp. 1–14, 2018, doi: 10.3390/ma11050751.

[214] R. Eriksen, C. Berggreen, S. W. Boyd, and J. M. Dulieu-Barton, “Towards high velocity deformation characterisation of metals and composites using Digital Image Correlation,” *EPJ Web Conf.*, vol. 6, no. September 2014, 2010, doi: 10.1051/epjconf/20100631013.

[215] A. J. Abdalla, T. M. Hashimoto, C. M. Neto, and M. S. Pereira, “Relationship between microstructure, mechanical properties and dislocation substructures in a multiphase steel,” *Rev. Bras. Apl. Vácuo*, vol. 23, no. 2, pp. 52–57, 2004.

[216] K. Hariharan, O. Majidi, C. Kim, M. G. Lee, and F. Barlat, “Stress relaxation and its effect on tensile deformation of steels,” *Mater. Des.*, vol. 52, pp. 284–288, 2013, doi: 10.1016/j.matdes.2013.05.088.

[217] M. A. Sutton, N. Li, D. C. Joy, A. P. Reynolds, and X. Li, “Scanning electron microscopy for quantitative small and large deformation measurements Part I: SEM imaging at magnifications from 200 to 10,000,” *Exp. Mech.*, vol. 47, no. 6, pp. 775–787, 2007, doi: 10.1007/s11340-007-9042-z.

[218] K. H. Kim, Z. Akase, T. Suzuki, and D. Shindo, “Charging effects on SEM/SIM contrast of metal/insulator system in various metallic coating conditions,” *Mater. Trans.*, vol. 51, no. 6, pp. 1080–1083, 2010, doi: 10.2320/matertrans.M2010034.

[219] A. Chabok, E. Van Der Aa, J. T. M. De Hosson, and Y. T. Pei, “Mechanical behavior and failure mechanism of resistance spot welded DP1000 dual phase steel,” *Mater. Des.*, vol. 124, pp. 171–182, 2017, doi: 10.1016/j.matdes.2017.03.070.

[220] C. Li, X. Yuan, K. Wu, H. Wang, Z. Hu, and X. Pan, “Nugget formation and its mechanism of resistance spot welded joints in DP600 dual-phase and DC54D ultralow carbon steel,” *Met. Mater. Int.*, vol. 23, no. 3, pp. 1–11, 2017, doi: 10.1007/s12540-017-6557-4.

[221] H. Bouzekri, M, Dancette, SDupuy, T, Lens, A, Massardier, V, Fabrègue, D, Klocker, “An Investigation of Failure Types in High- Strength Steel Resistance Spot Welds,” *Weld. World*, vol. 54, no. 3\4, pp. 3–14, 2010.

[222] A. Ghosh, “Segregation in cast products,” *Sadhana - Acad. Proc. Eng. Sci.*, vol. 26, no. 1–2, pp. 5–24, 2001, doi: 10.1007/BF02728476.

[223] X. Zhang, F. Yao, Z. Ren, and H. Yu, “Effect of welding current on weld formation, microstructure, and mechanical properties in resistance spot welding of CR590T/340Y galvanized dual phase steel,” *Materials (Basel).*, vol. 11, 2018, doi: 10.3390/ma11112310.

[224] E. J. Pavlina and C. J. Van Tyne, “Correlation of Yield strength and Tensile strength with hardness for steels,” *J. Mater. Eng. Perform.*, vol. 17, no. 6, pp. 888–893, 2008, doi: 10.1007/s11665-008-9225-5.

[225] Y. Wei *et al.*, “Evading the strength-ductility trade-off dilemma in steel through gradient hierarchical nanotwins,” *Nat. Commun.*, vol. 5, 2014, doi: 10.1038/ncomms4580.

[226] I. Masumoto and H. Suga, “Effect of Cooling Rate on the Dislocation Densities of Mild Steel and High Tensile Strength Steel Weld Metals,” *J. Japan Weld. Soc.*, vol. 52, no. 7, pp. 585–591, 1982.

[227] D. Lecompte, S. Bossuyt, S. Cooreman, H. Sol, and J. Vantomme, “Study and generation of optimal speckle patterns for DIC,” *Proc. SEM Annu. Conf. Expo. Exp. Appl. Mech. 2007*, vol. 3, no. February 2015, pp. 1643–1649, 2007.

[228] M. Pouranvari, “Analysis of Fracture Mode of Galvanized Low Carbon Steel Resistance Spot Welds,” *Int. J. Multidiscip. Sci. Eng.*, vol. 2, no. 6, pp. 36–40, 2011.

[229] I. Sevim, “Effect of hardness to fracture toughness for spot welded steel sheets,” *Mater. Des.*, vol. 27, no. 1, pp. 21–30, 2006, doi: 10.1016/j.matdes.2004.09.008.

[230] F. Nikoosohbat, S. Kheirandish, M. Goodarzi, M. Pouranvari, and S. P. H. Marashi, “Microstructure and failure behaviour of resistance spot welded DP980 dual phase steel,” *Mater. Sci. Technol.*, vol. 26, no. 6, pp. 738–744, 2010, doi: 10.1179/174328409X414995.

[231] X. Shi *et al.*, “Light and electron microscopy of microstructure and fractography of an ultrahigh-strength martensitic steel,” vol. 2, no. January, pp. 7–10, 2014, doi: 10.1038/35094560.

[232] M. Ali, D. Porter, J. Kömi, M. Eissa, H. El Faramawy, and T. Mattar, “Effect of cooling rate and composition on microstructure and mechanical properties of ultrahigh-strength steels,” *J. Iron Steel Res. Int.*, vol. 26, no. 12, pp. 1350–1365, 2019, doi: 10.1007/s42243-019-00276-0.

[233] C. Wang, H. Qiu, Y. Kimura, and T. Inoue, “Morphology, crystallography, and crack paths of tempered lath martensite in a medium-carbon low-alloy steel,” *Mater. Sci. Eng. A*, vol. 669, pp. 48–57, 2016, doi: 10.1016/j.msea.2016.05.041.

[234] M. Pouranvari, S. P. H. Marashi, and H. L. Jaber, “Dp780 dual-phase-steel spot welds: Critical fusion-zone size ensuring the pull-out failure mode,” *Mater. Tehnol.*, vol. 49, no. 4, pp. 579–585, 2015, doi: 10.17222/mit.2014.184.

[235] C. Kiran Sagar, A. Chilukuri, and A. Priyadrashini, “Determination of johnson cook material model constants for 93% WHA and optimization using genetic algorithm,” *Mater. Today Proc.*, vol. 5, no. 9, pp. 18911–18919, 2018, doi: 10.1016/j.matpr.2018.06.240.

[236] M. Murugesan and D. W. Jung, “Johnson cook material and failure model parameters estimation of AISI-1045 medium carbon steel for metal forming applications,” *Materials (Basel).*, vol. 12, no. 4, pp. 1–18, 2019, doi: 10.3390/ma12040609.

9 APPENDIX

```
% Nonlinear equations solver
% for more details, check the help for fsolve function
clc;
clear;
W = xlsread('DP1000CPHC.xlsx');
X = zeros(length(W));
for ii = 1:length(W)
   A = W(ii,1); %reduced modulus  GPa
   B = W(ii,2); %constant c GPa
   C = W(ii,3); %hmax nm
   D = W(ii,4); %elastic modulus GPa
   E = W(ii,5); %dPu/dh N/m
    fun = @(x)roots5segma(x, A, B, C, D, E);
%       options.FiniteDifferenceStepSize = 0.1;
   options = optimset('MaxFunEvals',500);
   options=optimset('Display','on');
    x0 = [0.5;0.1;0.5];
    x = fsolve(fun,x0,options);
    y(ii,1) = x(1); %segma0.033
    y(ii,2) = x(2); %n
    y(ii,3) = x(3); %segmay
end

function F=roots5segma(x, A, B, C, D, E)
F(1)=-0.1*(-1.131*(log(A/x(1)))^3+13.635*(log(A/x(1)))^2-30.594*(log(A/x(1)
)+29.267))*x(1)-B;
F(2)=-1+((((-1.40557*(x(2))^3+0.77526*(x(2))^2+0.1583*x(2)-0.06831)*(log(A/
x(1)))^3+(17.93006*(x(2))^3-9.22091*(x(2))^2-2.37733*x(2)+0.86295)*(log(A/x
(1)))^2+(-79.99715*(x(2))^3+40.5562*(x(2))^2+9.00157*x(2)-2.54543)*(log(A/x
(1)))+(122.65069*(x(2))^3-63.88418*(x(2))^2-9.58936*x(2)+6.20045))*A*C)/E);
F(3)=x(3)*(1+D*0.033/x(3))^(x(2))-x(1);
F=[F(1);F(2);F(3)];
end
```